

Copyright

by

James Burkhardt Biemiller

2020

The Dissertation Committee for James Burkhardt Biemiller Certifies that this is the approved version of the following dissertation:

Multi-timescale Mechanics of an Active Low-angle Normal Fault

Committee:

Luc Lavier, Supervisor

Laura Wallace, Co-Supervisor

Susan Ellis

Demian Saffer

Omar Ghattas

Multi-timescale Mechanics of an Active Low-angle Normal Fault

by

James Burkhardt Biemiller

Dissertation

Presented to the Faculty of the Graduate School of

The University of Texas at Austin

in Partial Fulfillment

of the Requirements

for the Degree of

Doctor of Philosophy

The University of Texas at Austin

December 2020

Dedication

For my husband and my family.

Acknowledgements

This work would not have been possible without the incredible support and guidance I received from so many people. First and foremost, I would like to extend my sincere gratitude to my advisors, Luc Lavier and Laura Wallace, who have gone above and beyond the call of duty. Thank you for patiently answering my countless questions and emails, for encouraging me every step of the way, and for showing me what it means to be a researcher. Luc, thank you for all the equation-scribbling whiteboard sessions, the impromptu chats about the future of our planet, the many cans of tuna shared in the field, and for reminding me to laugh along the way. Laura, thank you for showing me how to take GPS data all the way from laying rebar and mixing concrete to modeling interseismic fault locking, for encouraging me to approach research questions from many different angles and perspectives, and for the best Tex-Mex in all of New Zealand.

Thank you to everyone who collaborated on the Mai'iu fault – Dayman Dome projects. To Susan Ellis, Tim Little, Marcel Mizera, Jurgen Österle, Sam Webber, Danny Stockli, and Fred Taylor for their dauntless efforts in the face of fieldwork challenges in Papua New Guinea. To Susan, in particular, for the kind mentorship and long conversations about fault friction and geodynamics. To Fred, for introducing me to coral paleogeodesy and showing me the ropes of fossilized coral sampling. To Ann Chen for patiently teaching me how to process and interpret InSAR interferograms. To Adrien Arnulf for the discussions of shallow subduction zone dynamics and for showing me how to run multiple MATLAB sessions at one time. To River Shen and Helen Yu for dating the fossilized coral samples in Chapter 4. To Carolyn Boulton for the interesting conversations about deformation mechanisms and for the incredible laboratory friction

experiments in Chapter 5. To my committee members, Omar Ghattas, Demian Saffer, and Whitney Behr.

I extend my deepest gratitude and thanks to our many friends in Papua New Guinea who welcomed us into their land and communities and went out of their way to help with our fieldwork. In particular, I would like to thank Paul & Ethel Gardebo (Rako Point), Colin Egairo (Biniguni), McLaren & Bob (Moibiri), John, Rex, & Denis (Alotau), Willie Solomon (Alotau), Lulu Osembo (Milne Bay Research Authority), and John Kwazi (National Mapping Bureau). Thank you to my UT colleagues, officemates, and roommates for your friendship and support: Dennis Tong, Wanying Wang, Simone Puel, Kunpeng Liao, Nicholas Montiel, Brooklyn Gose, Xian Wu, Simon Scarpetta, Lily Serach, Kelly Hattori, Evan Ramos, Tom Etzel and Nick Ettinger. Thank you to my undergraduate professors and advisors for introducing me to research and to the wonders of geology: Lisa Greer, Dave Harbor, Jeff Rahl, Chris Connors, and Elizabeth Knapp.

Most of all, I would like to thank my husband, Adam Fiss. I could not have weathered the storms of graduate school without your love, laughter, and unwavering support. Thank you for being my rock.

Abstract

Multi-timescale Mechanics of an Active Low-angle Normal Fault

James Burkhardt Biemiller, PhD

The University of Texas at Austin, 2020

Co-Supervisors: Luc Lavier & Laura Wallace

Detachment faults dipping $< 30^\circ$ commonly accrue 10's of kms of offset and accommodate a large portion of crustal extension in moderately-to-highly extended regions. Slip on these high-offset low-angle normal faults remains perplexing due to their apparent misorientation relative to Andersonian principal stress directions. Classic fault mechanical theory predicts that normal faults should frictionally lock up and become abandoned at dips $< 30^\circ$, yet geologic, seismological, and geodetic evidence shows that some low-angle normal faults slip actively. Despite evidence for actively slipping low-angle normal faults, few large earthquakes have been recorded on these structures. The scarcity and low long-term slip rates of active low-angle normal faults make it difficult to determine whether these faults rupture in large earthquakes based solely on seismological or geodetic records. In this dissertation, multi-disciplinary studies of the world's most rapidly slipping low-angle normal fault are integrated to better understand the structural and tectonic evolution of detachment faults as well as to determine whether these faults slip in large earthquakes or predominantly creep aseismically.

Bounding the actively exhuming Dayman-Suckling metamorphic core complex, the Mai'iu fault in Papua New Guinea dips $16-24^\circ$ at the surface and has been estimated to slip at dip-slip rates of 8.6 ± 1.0 mm/yr to 11.7 ± 3.5 mm/yr. Geodynamic models suggest that weak zones and thermomechanical heterogeneities inherited from a previous

subduction phase may have facilitated the formation of this long-lived detachment fault system (Chapter 2). Models of seismic-cycle deformation governed by rate-and-state friction show that the spatial distribution of fault rock frictional stability parameters strongly controls whether low-angle normal faults creep aseismically, slip in periodic large earthquakes, or slip in a mix of episodic creep events and earthquakes (Chapter 3). Surveying and U/Th dating of emerged coral reef platforms along the Goodenough Bay coastline show that tectonic uplift is episodic and imply that this segment of the detachment system slips in infrequent (440 – 1520 year recurrence) large ($M_w > 7.0$) earthquakes (Chapter 4). Velocities from a newly installed network of densely spaced campaign GPS sites reveal horizontal extension rates of 8.3 ± 1.2 mm/yr (~ 8 -11 mm/yr dip-slip) on the Mai'iu fault (Chapter 5). Laboratory friction experiments on exhumed Mai'iu fault rocks showing depth-dependent transitions in frictional stability help constrain inversions of kinematic models of the GPS velocities indicating that the Mai'iu fault is more strongly locked at ~ 5 -16 km depth and creeping interseismically above 5 km depth. This result suggests that large ($M_w > 7.0$) earthquakes nucleate downdip of the low-angle portion of the Mai'iu fault and can propagate to the surface along the shallowly-dipping segment and/or more steeply-dipping splay faults in its hanging wall. In contrast to previous studies suggesting that active low-angle normal faults predominantly creep aseismically, this work implies that the active Mai'iu low-angle normal fault slips in infrequent large earthquakes accompanied by some shallow interseismic creep.

Table of Contents

List of Tables	xv
List of Figures.....	xix
Chapter 1: Introduction.....	1
1.1. Low-angle normal faults.....	1
1.2. Low-angle normal fault seismicity.....	4
1.3. The Mai'iu Fault, Papua New Guinea.....	7
1.4. Summary of research chapters.....	7
Chapter 2: Tectonic inheritance following failed continental subduction: a model for core complex formation in cold, strong lithosphere	12
Abstract.....	12
2.1. Introduction	13
2.1.1. Lithospheric conditions for MCC formation.....	15
2.1.2. Inheritance of collisional features following jammed subduction	16
2.1.3. This study: high-resolution modeling of cold post-collision MCC formation	17
2.2. General model of post-collisional extension	18
2.2.1. Numerical methods.....	18
2.2.2. Model setup	21
2.2.3. Results: three extensional modes.....	24
2.2.3.1. Mode 1: High-angle inherited shear zone develops a rolling-hinge	26
2.2.3.2. Mode 2: Low-angle inherited shear zone leads to 'domino'-style faulting.....	28
2.2.3.3. Mode 3: Near-symmetric rifting of thickened crust	30

2.2.4. Discussion of general model results	31
2.2.4.1. Shear zone strength and geometry	31
2.2.4.2. Removal of mantle lithosphere allows localization of extension	32
2.2.4.3. Rift width and mechanical decoupling in cold, strong lithosphere	34
2.2.4.4. Elastic thickness, isostatic rebound and initial topography	35
2.3. Natural case study: Dayman-Suckling metamorphic core complex.....	36
2.3.1. Tectonic & geologic setting.....	38
2.3.2. Application of our model to the Dayman-Suckling MCC.....	41
2.3.2.1. DSM-specific model.....	41
2.3.2.2. DSM model results	44
2.3.3. Comparison of DSM model to geological and geophysical observations.....	45
2.3.4. Implications for Woodlark Rift development.....	46
2.4. Conclusion.....	47
Chapter 3: Earthquake supercycles as part of a spectrum of normal fault slip styles	48
Abstract.....	48
3.1. Introduction	49
3.1.1 Background.....	49
3.1.2. Examples of slip transients on normal fault systems.....	51
3.1.3. Frictional properties of normal fault zones	52
3.1.4. General slip behaviors of normal faults.....	53
3.2. Methods	55
3.2.1. Rate-and-State Constitutive Equations.....	55

3.2.2. General numerical procedure	56
3.2.3. Model Geometry & Parameters.....	59
3.2.3.1. Typical Model Parameters & Spatial Discretization	59
3.2.3.2. Normal Fault Model Setup	62
3.3. Results	66
3.3.1. Parameter Tests	66
3.3.2. Earthquake Clustering & Aseismic Slip Transients	71
3.4. Discussion.....	74
3.4.1. Earthquake clusters and creep events	74
3.4.2. Control on slip response by shear zone composition	76
3.4.3. Shear zone composition and W/h^*	79
3.4.4. Future work	80
3.5. Conclusions	81
Chapter 4: Emerged Coral Reefs Record Holocene Low-angle Normal Fault	
Earthquakes	83
Abstract.....	83
Plain Language Summary.....	83
4.1. Introduction	84
4.1.1. LANF seismicity	85
4.1.2. Tectonic setting	86
4.2. Methods	89
4.2.1. General approach.....	89
4.2.2. Surveying and sampling	92
4.2.3. U-Th dating	93

4.3. Results	95
4.3.1. Coral ages	95
4.4. Discussion.....	95
4.4.1. Coral ages and coastal morphology record episodic tectonic uplift... 95	
4.4.2. Uncertainties.....	97
4.4.3. Maximum recurrence intervals and coseismic uplifts	98
4.4.4. Low-angle normal fault earthquakes	99
4.5. Conclusions	102
Chapter 5: Mechanical Implications of Creep and Partial Coupling on the World's Fastest Slipping Low-angle Normal Fault in Southeastern Papua New Guinea	103
Abstract.....	103
Plain Language Summary.....	104
5.1. Background & Introduction.....	104
5.1.1. Introduction	104
5.1.2. Tectonic and geological setting of the Mai'iu fault.....	107
5.1.3. Mai'iu fault rock sequence and deformation mechanisms	111
5.2. Campaign GPS experiment	113
5.2.1. GPS data and velocities	113
5.2.3. Elastic block and dislocation modeling approaches.....	115
5.2.3. Elastic block model results.....	117
5.2.4. 2-D Dislocation modeling	120
5.2.4.1. Model 1: Locked-to-surface models.....	120
5.2.4.2. Model 2: Consideration of shallow creep and splay fault activity	121

5.3. Mai'iu fault frictional strength and stability from rock deformation experiments.....	126
5.3.1. Fault rock sample descriptions	126
5.3.2. Experimental methods and materials.....	129
5.3.3. Frictional strength results	132
5.3.4. Rate-and-state frictional stability results	134
5.4. Discussion.....	137
5.4.1. Experimental constraints on fault slip behavior	137
5.4.1.1. Evidence for frictional strain-weakening of a rolling-hinge detachment.....	137
5.4.1.2. Depth-dependent frictional stability	138
5.4.2. Contemporary slip behavior in the context of geological and experimental evidence	140
5.4.3. Mechanical implications for LANFs	144
5.5. Conclusions	145
Chapter 6: Conclusion	147
Appendices	150
Appendix A: Supplementary Material for Chapter 2	150
A.1. Numerical procedure	150
A.2. Model description	151
A.3. Additional Model Results.....	154
Appendix B: Supplementary Material for Chapter 3	166
B.1. Benchmarks	166
B.2. Parameter Testing	168
Appendix C: Supplementary Material for Chapter 4	170

Appendix D: Supplementary Material for Chapter 5	178
D.1. GPS uncertainty calculations.....	178
D.2. Earthquake offset corrections	178
D.3. Block modeling (TDEFNODE).....	180
D.4. Dislocation modeling of vertical velocities.....	180
D.5. Quantitative X-ray diffraction methods.....	181
D.6. Hydrothermal Friction Experiments.....	182
D.7. Supplementary Figures.....	184
D.8. Supplementary Tables	195
References	202

List of Tables

<p>Table 2.1. a.) Mechanical parameter values used in thermomechanical models shown in sections 2.2 and 2.3. Thermal parameters are shown in Figure 2.1. b.) List of model experiments discussed in Section 2.2. The final column lists the predicted extensional mode for each of the three model variants described in each row, respectively.</p>	23
<p>Table 5.1. List of sampled fault rocks and experiments performed with experimental conditions (effective normal stress, pore fluid pressure, and temperature) and values of friction (=shear stress / effective normal stress, ignoring cohesion) at the end of each run-in (at 1 mm/s). The sliding velocity was 1 mm/s initially and then stepped to 0.3-1-3-10-30 mm/s with 0.5-1.5-1.5-1.5-1.5 mm of displacement. Steady state friction (mss) is determined at the end of the run-in at 1 mm/s at each sneff-T-Pf condition. * Run-in at 10 mm/s, step from 0.3 to 1 mm/s omitted, step from 30-100 mm/s included, ^ experiment terminated prematurely due to pore fluid leak, # indicates peak value of stick-slip.</p>	131
<p>Table C.1. List of all sampled corals with GPS coordinates, elevations, tidal adjustments and tidally corrected elevations. ALC = Above Living Coral. ACWL = Above Current Water Level.....</p>	175

Table C.2. Th/U isotopic results from ICPMS analysis of coral samples. Analytical errors are 2σ of the mean. ^a $[^{238}\text{U}] = [^{235}\text{U}] \times 137.77 (\pm 0.11\%)$ (Hiess et al., 2012); $\delta^{234}\text{U} = ([^{234}\text{U}/^{238}\text{U}]_{\text{activity}} - 1) \times 1000$. ^b $\delta^{234}\text{U}_{\text{initial}}$ corrected was calculated based on ²³⁰Th age (T), i.e., $\delta^{234}\text{U}_{\text{initial}} = \delta^{234}\text{U}_{\text{measured}} X e^{\lambda^{234}T}$, and T is corrected age. ^c $[^{230}\text{Th}/^{238}\text{U}]_{\text{activity}} = 1 - e^{-\lambda^{230}T} + (\delta^{234}\text{U}_{\text{measured}}/1000)[\lambda_{230}/(\lambda_{230} - \lambda_{234})](1 - e^{-(\lambda_{230} - \lambda_{234})T})$, where T is the age. Decay constants are $9.1705 \times 10^{-6} \text{ yr}^{-1}$ for ²³⁰Th, $2.8221 \times 10^{-6} \text{ yr}^{-1}$ for ²³⁴U (Cheng et al., 2013), and $1.55125 \times 10^{-10} \text{ yr}^{-1}$ for ²³⁸U. ^dAge corrections, relative to chemistry date on October 31st, 2018, were calculated using an estimated atomic ²³⁰Th/²³²Th ratio of $4 (\pm 2) \times 10^{-6}$ 177

Table D.1. GPS sites and observation years used in this study (below)..... 195

Table D.2. (below) Coordinates, velocities, and uncertainties for each GPS site.

VNIT14 and VEIT14 are the North and East components of velocity in the ITRF14 reference frame. VNAUS and VEAUS are the North and East components of velocity relative to the Australian Plate. σ_{Nf} and σ_{Ef} are the formal uncertainties for the North and East velocity components. σ_{Nrwn} and σ_{Erwn} are the uncertainties of the North and East velocity components after correcting for random-walk noise (Section D.1). 197

Table D.3. Poles of rotation of crustal blocks relative to the Australian Plate.

Cartesian coordinates are shown in the lower section. Ω_x , Ω_y , and Ω_z are the Cartesian angular velocity vector components; σ_x , σ_y , and σ_z are the uncertainties of the respective components. The final columns give the covariances of component pairs. WDLK = Woodlark Plate; TROB = Trobriand Block; DEI = D’Entrecasteaux Islands block; GOOD = Goodenough Bay block; NORM = Normanby Island block; PP = Papuan Peninsula block..... 199

Table D.4. Events and fault parameters used in regional earthquake corrections, based on USGS finite fault models (U.S. Geological Survey, 2019).

Latitude and longitude are given for the lower corner of the fault farthest along the strike direction. d_h is the hypocentral depth. d_1 and d_2 are the upper and lower depths of the fault, respectively. Str is the fault strike. L is the along-strike length of the slipping fault and slip is the total slip. For the events from 2016-2018 (during our Mai’iu fault campaign experiment), D is the approximate distance from the earthquake to our GPS sites near the Mai’iu fault, dE is the average magnitude of the eastward offset at our campaign sites due to each event, and dN is the average magnitude of the northward offset at our campaign sites due to each event. Red events had no available USGS finite fault model as of publication. * = events with non-planar or multi-segment sources (Section D.2). Individual fault segment parameters are listed below these events, except for the 2007 Solomon Islands earthquake, for which the modeled slip distribution from Wallace et al. (2015) is shown in Figure D.2. 200

Table D.5. Results of F test for block independence based on GPS velocities in Table D.2 and block boundary configurations in Figure D.3. N_{data} = number of data; N_{params} = number of free parameters; DOF = degrees of freedom. ‘VOGE + DEI + GOOD’ refers to models where Cape Vogel (VOGE), Goodenough Bay (GOOD), and D’Entrecasteaux Islands (DEI) blocks are treated as one unified block rotating about one pole. F tests cannot statistically distinguish between models where VOG E and GOOD are considered individual blocks (configuration 1) and ones where they are one unified block (configuration 2). Therefore, we treat them as one block in all TDEFNODE block models.....	201
Table D.6. Description and quantitative mineralogy of fault rock samples.	201

List of Figures

Figure 1.1. Schematics comparing styles of metamorphic core complex formation and low-angle detachment fault development from Little et al. (2019). A.) Rolling-hinge model with rider blocks. The active detachment fault dips more steeply at depth and rotates to dip at lower angles near the surface due to arching and back-rotation of the exhuming domal footwall complex. Slices of hanging wall crust are captured as ‘rider blocks’ atop the back-rotating footwall complex by sequential generations of splay faults in the shallowest hanging wall above the active detachment. See sections 4.1, 4.4, 5.2 and 5.4 for further discussion of splay faults and rider blocks as they relate to the Mai’iu fault and Dayman-Suckling metamorphic core complex. B.) Rolling-hinge model without rider blocks. Splay faults initiate in the hanging wall but do not cut rider blocks of hanging wall material that are subsequently transported with the rotating footwall. Instead, the detachment fault surface exhumes continuously atop the smooth domal footwall. C.) Composite domino faulting model. The detachment forms by continued slip and interconnection of the downdip portions of individual listric normal faults bounding ‘domino’ blocks in the upper plate.3

Figure 1.2. a.) Tectonic map with present (orange; Wallace et al., 2014) and 3.6—0.5 Ma (blue; Taylor et al., 1999) poles of rotation of the Woodlark Plate relative to the Australian Plate. Northward subduction at the New Britain and San Cristobal trenches accompanies counter-clockwise rotation of the Woodlark Plate and predominantly N-S extension at the Woodlark Spreading Center and along the southeastern portion of the Papuan Peninsula. b.) Local tectonic map with faults from Little et al. (2019) highlighting the active Mai'iu fault. The Mai'iu-Gwoira-Goodenough (MGG) fault system is mapped in three segments: the 16-24° dipping Mai'iu fault (red), the more steeply dipping Gwoira fault (orange) and the inferred offshore continuation through Goodenough Bay (dashed red). c.) Oblique view of the Mai'iu fault and DSM with topography from 90-m SRTM data and GeoMapApp (<http://www.geomapapp.org>). 6

Figure 2.1. a. Conceptual model of failed continental subduction margin undergoing extension, with numerical model domain outlined in red. b. Typical numerical model geometry, boundary conditions, and initial thermal structure. White lines show isotherms in 100 °C increments. Black dashed line and DLC indicate depth below which lower crust is weakened, which is 20 km in the models shown in Figure A.5 (Appendix A). c. Initial mechanical strength contrasts for the model shown in Figure 2.2. Colored shading shows Log10 of the effective dynamic viscosity η_{eff} , defined as: $\eta_{eff} = \tau / 2\varepsilon$, where τ is the principal in-plane shear stress and ε is the principal in-plane shear strain rate (Ranalli, 1995). This value quantifies how easily deformed an area is, and is useful for tracking relative strength in both the brittle and ductile deformation regimes. d. Initial geothermal structure from a vertical profile taken near the left edge of the model in b, with thermal properties for each layer listed; c is specific heat capacity; k is thermal conductivity; α is thermal expansivity coefficient; and h_r is radiogenic heat productivity (see Appendix A.1 for details).20

Figure 2.2. Mode 1 extension with initial shear zone dip of 60°. Crustal rheology follows a dislocation creep plagioclase flow law from Ranalli (1995) and initial brittle strength is given by cohesion of 40 MPa and internal friction angle of 30°, softening linearly to 15° over strains of 0.1. The pre-existing shear zone’s activation energy is lowered by 15% and its cohesion is lowered to 4 MPa. Other material properties are in Table 1. Log10 of effective viscosity is plotted after a. 100 kyr; b. 1 Myr; c. 2.5 Myr. White lines outline regions of different material properties. Dashed blue line shows position of the brittle-ductile transition (BDT), estimated by the depth at which the minimum yield stress transitions from plastic failure to dislocation or diffusion creep. Yellow arrows show sense of offset on faults between dome and breakaway. d,e,f) Cumulative strain overlain by strain rate (for strain rate > 10⁻¹⁴) at 100 kyr, 1 Myr, and 2.5 Myr. e) Interpretative schematic cartoon of Mode 1 style deformation. 26

Figure 2.3. a,b) Representative Mode 2 example after 1 and 3 Myr of extension, respectively, showing log10 of effective viscosity. White lines outline regions of different material properties and dashed white lines outline material originally in the inherited shear zone. Dashed blue line shows position of the brittle-ductile transition (BDT). The shear zone initially dips 30° with an internal friction angle of 25°, cohesion of 4 MPa, and viscous activation energy 25% lower than that of the surrounding crust. c,d) Cumulative strain overlain by strain rate (for strain rate > 10⁻¹⁴) at 1 and 3 Myr e) Interpretative schematic cartoon of Mode 2 style deformation..... 28

Figure 2.4. a,b) Representative Mode 3 example after 1 and 3 Myr of extension, respectively, showing log₁₀ of effective viscosity. White lines outline regions of different material properties and dashed white lines outline material originally in the inherited shear zone. Dashed blue line shows position of the brittle-ductile transition (BDT). The outlined ‘shear zone’ in this example dips 60° but has identical frictional and rheological properties to the surrounding crust. All other material properties and model parameters are as described in Table 2.1. c,d) Cumulative strain overlain by strain rate (for strain rate > 10⁻¹⁴) at 1 and 3 Myr. e) Interpretative schematic cartoon of Mode 3 style deformation. 30

Figure 2.5. a. Regional tectonic map showing active and extinct subduction zones and spreading centers, microplate poles of rotation and Woodlark Plate velocities relative to a fixed Australian Plate (Wallace et al., 2014). Dashed orange and blue boxes show regions of Figure 5b and 5c, respectively. AUS = Australian Plate; PAC = Pacific Plate; DSM = Dayman-Suckling MCC; DEI = D’Entrecasteaux Islands; b. Interpretive cross-section through the DSM, drawn after Little et al. (2019); c. Interpretive cross-section through DEI drawn after Ellis et al. (2011). Black arrows show possible upwelling and flow patterns of upper mantle or lower crust. 37

Figure 2.6: a. Simplified map showing spatial relationship between Woodlark spreading centers and the DSM. b. Hillshade DTM of Mt. Dayman area from Figure 2.6a showing mapped antithetic and locally synthetic faults cutting the footwall of the DSM, adapted from Mizera et al. (2018); c. Elevation profile of transect A'-A from Figure 2.6b with representative mapped footwall faults and back-warped footwall foliations; d. Oblique view of the DSM and Mai'iu fault, from 90m SRTM data and GeoMappApp (<http://www.geomappapp.org>)..... 40

Figure 2.7. a.) Cartoon of inferred pre-extensional configuration for SE Papua. b.) Numerical model setup of a. c) and d): Plots of (c) modeled strain (colors) and maximum compressive principal stress (σ_1) directions (white lines) and (d) material properties overlain by strain rate (for strain rate $> 10^{-15}$) at 200 kyr, 2 Myr, and 3.4 Myr. White lines show isotherms in 100 °C increments. Inferred shear band orientations shown by yellow dashed lines in c. e. Slip-parallel topographic profile of Mt. Dayman, location shown in 2.6b. f.) Modeled topography at 3.4 Myr extracted from 2.7c..... 43

Figure 3.1. Representative displacement vs. time plot showing three orders of slip behavior distinguished by their timescales. Drawn after Friedrich et al. (2003)..... 55

Figure 3.2. a. Realistic geometry of a Wasatch Fault Zone segment at depth. b. Modeled fault geometry. c. Associated model normal stress distribution. d. Associated a-b profile showing location of velocity-weakening zone along the fault. The orange star 5.3 km downdip on the fault denotes the location of point P1 where velocities and cumulative displacements are tracked in Figures 3.4, 3.6, and 3.8..... 61

Figure 3.3. a. Schematic of two-member theoretical fault zone model with ~95% brittle velocity-weakening clasts and ~5% low-viscosity velocity-strengthening matrix (dashed lines). b. Corresponding a-b profile along the fault; $\kappa = 0$. c. Schematic of fault zone model with ~50% brittle velocity-weakening phacoids and ~50% low-viscosity velocity-strengthening matrix. d. Corresponding a-b profile along the fault; $\kappa = 5$. Shear direction from bottom-right to top-left. The higher proportion of ductile matrix to brittle clasts in c allows for aligned fracture networks to form, facilitating aseismic creep. In our models, scenario a is represented by a small κ and scenario c by a large κ or bulk velocity-strengthening a-b. Drawn after Fagereng & Sibson (2010). 65

Figure 3.4. Representative characteristic slip responses of point P1 (see Figure 3.1 for its location) shown by slip-velocity vs. time plots. Red dashed lines denote 1 mm s^{-1} slip rates for reference. Green dashed lines denote the loading plate-velocity of $V_p = 3 \text{ mm yr}^{-1}$. a. No smoothing, pure seismic cycle slip. b. $\kappa = 3$, mostly seismic slip separated by few aseismic slip transients. c. $\kappa = 5$, earthquake clusters separated by periods of aseismic slip transients lasting up to 1 kyr. d. $\kappa = 6$, aseismic periodic slip transients..... 68

Figure 3.5. a. Schematic diagram to provide context for where the velocity-weakening patch is along the fault. b. Slip behavior phase diagram showing thresholds of minimum a-b in the weakening patch for each slip regime. The blue profile represents higher $\kappa = 5$, corresponding to a shear zone with more ductile velocity-strengthening material. The red profile represents lower $\kappa = 0$, corresponding to a shear zone with more brittle velocity-weakening material. 69

Figure 3.6. a-c. Modeled cumulative slip over time plots at point P1 for three characteristic regimes: a. pure seismic cycle, b. earthquake clustering, and c. aseismic slip transients (creep events). d-f. Cumulative slip vs. time plots for a section of the fault extending from 3.5 to 6.5 km downdip, which includes the velocity-weakening patch. Note that the total fault domain extends 3.5 km updip and 28.5 km downdip from the section plotted. When the maximum velocity of any point on the fault is greater than 1 mm/s slip is contoured every 1 second with a dashed red line. When the maximum velocity is less than 1 mm/s but greater than $100V_p$, slip is contoured every 15 minutes with a dashed green line. When the maximum velocity is less than $100V_p$, slip is contoured every 20 years with a solid blue line. Orange stars and lines indicated the location of the point P1, for which cumulative slip is tracked in a-c. Colored boxes and labels indicate the occurrence of an earthquake cluster and aseismic slip transients in e. These plots correspond to the three characteristic regimes: d. pure seismic cycle, e. earthquake clustering, and f. aseismic slip transients. 70

Figure 3.7. a. $(W/h^*)_{\max}$ vs. minimum a-b for a typical normal fault model, each blue dot represents one model run with a different κ . Green dashed lines show the slip response regimes from Figure 3.5. b. Predominantly tightly-packed brittle competent shear zone, corresponding to seismic cycle slip. c. Shear zone with a higher proportion of incompetent ductile matrix, allowing some small interconnected matrix-filled fracture networks to form, facilitating a combination of seismic and aseismic slip. d. Shear zone with a sufficient proportion of ductile incompetent matrix to form large interconnected fracture networks, facilitating predominantly aseismic creep processes. 73

Figure 3.8. a. Slip velocity over time for the weakening patch (at point P1; see Figure 3.1 for its location) in the model setup described in section 3.3.2. Note the clustered seismic events separated by 1 kyr – timescale periods of aseismic slow-slip transients. b. Zoomed-in velocity vs. time plot showing complex periodic aseismic creep events occurring between earthquake clusters. Note the oscillation between slower and faster creep events. Red dashed line denotes 1 mm/s slip rates for reference. Green dashed lines denote the loading plate-velocity of $V_p = 3$ mm/yr..... 74

Figure 4.1. a.) Tectonic map with present (orange; Wallace et al., 2014) and 3.6—0.5 Ma (blue; Taylor et al., 1999) poles of rotation of the Woodlark Plate relative to the Australian Plate. b.) Local tectonic map with faults from Little et al. (2019). The MGG fault system is mapped in three segments: the 16-24° dipping Mai’iu fault (red), the more steeply dipping Gwoira fault (yellow) and the inferred offshore continuation through Goodenough Bay (dashed red). GPS velocity vectors from Wallace et al. (2014) and Biemiller et al. (2020b). c.) Emerged Holocene corals dated in this study; d.) Along-strike view of fault-bounded topography along the southern Goodenough Bay coastline; e-f.) Schematic crustal-scale cross-sections across the Dayman (e; A-A’) and Goodenough segments (f; B-B’) based on interpreted seismic lines (Fitz & Mann, 2013a; Fitz, 2011). Representative geometry of the Mai’iu fault (solid red) and potentially active synthetic splay faults (dashed red) are inferred from surface geology, seismic reflection, and microseismicity (Abers et al., 2016; Fitz & Mann, 2013a; Little et al., 2019; Mizera et al., 2019; Webber et al., 2020). Topography from 90-m SRTM data and GeoMapApp (<http://www.geomapapp.org>)..... 89

Figure 4.2. a.) Schematic modified from Thirumalai et al. (2015) showing growth and rapid emergence of a coral platform. b.) Predicted and measured tidal range over two days, showing estimated emergence required to preserve distinct platforms (section 4.4.1). c.) Sampled encrusting *Favia* sp. coral. d.) Emerged platform-notch-platform sequence with labeled mean tidal range..... 92

Figure 4.3. a.) Coral ages and along-strike sample locations colored by elevation ALC with lines showing along-strike correlations between emergence events. Plotted ages are offset laterally up to 500 m to show all samples in each cluster. b. All coral ages and elevations ALC colored by site. Dashed lines show reference uplift rates. c.) Coral ages and elevations with schematic topographic profile of individually numbered platform sequence at site D. d.) Inferred coseismic slip characteristics on the MGG detachment for near-surface splay fault dips of 60°, 45°, and 30° (no splay fault) based on 1.2 m of coseismic uplift, a splay-detachment intersection depth of 5 km, and the scaling relationships of Leonard (2010). e.) Mapview of representative rupture areas associated with slip distributions from d. Mai'iu fault depth contours (solid) drawn from Webber et al. (2020) and inferred (dashed) along-strike..... 94

Figure 5.1. a.) Regional tectonic map of PNG with main map area outlined, showing overall Australia-Pacific Plate convergence and Woodlark spreading (vectors). Ellipses show modern (orange; Wallace et al., 2014) and 3.6–0.5 Ma (cyan; Taylor et al., 1999) poles of rotation of the Woodlark Plate relative to the Australian Plate. b.) Topographic map with faults from Little et al. (2007, 2011, 2019) and GPS velocities relative to the Australian Plate (section 5.2; Wallace et al., 2014). Ellipses show 95% confidence intervals based on formal uncertainties. Stars indicate uplifted Holocene coral platforms. Dashed box shows area of 1c. c.) Enlarged map of dense GPS velocity field on the Mai'iu fault hanging wall. d.) Regional map showing seismicity and seismometer locations from Abers et al. (2016). e.) Oblique view of the Mai'iu fault and Dayman-Suckling Metamorphic Core Complex (Mt. Masasoru, Mt. Dayman, and Mt. Suckling). Black arrows show sense of motion across the fault. Ellipse colors show observation years at GPS sites near the fault (see key), and brown circles show fault rock sample locations. Samples from each site include: 1.) PNG-15-70; 2.) PNG-14-19E, PNG-14-19F, and PNG-16-17D2H; 3.) PNG-14-33A and PNG-14-33B; 4.) PNG-15-50B and PNG-16-151e from adjacent sites; see Appendix Figure D.7 for details. Topography from 90-m SRTM (Shuttle Radar Topography Mission) data and GeoMapApp (<http://www.geomapapp.org>). AUS = Australian Plate; PAC = Pacific Plate; NBP = North Bismarck Plate; SBP = South Bismarck Plate; WP = Woodlark Plate; NBT = New Britain Trench; SCT = San Cristobal Trench. MF = Mai'iu fault; GF = Gwoira fault; MS = Mt. Suckling; MD

= Mt. Dayman; MM = Mt. Masasoru; OSS = Owen-Stanley Suture zone;
 GI = Goodenough Island; FI = Fergusson Island; NI = Normanby Island;
 TB = Trobriand Block; WSR = Woodlark Spreading Ridge; WB =
 Woodlark Basin. 111

Figure 5.2. Best-fitting elastic block fault locking model results colored by kinematic fault coupling ratio Φ . Vectors indicate observed (white) and predicted (green) GPS velocities. a.) Preferred locking model. Dashed lines show preferred block boundaries (Appendix Figure D.3; Appendix Table D.3). b.) Enlarged view of GPS velocities near the modeled Mai'iu fault, which is predominantly uncoupled below 2 km depth. Labeled orange vectors show modeled rates and directions of relative motion between adjacent blocks across the fault. c.) Strike-perpendicular horizontal velocities relative to the Papuan Peninsula footwall block for sites in the Mai'iu fault network (Profile Y – Y' in 5.2a). Observed velocities (black), modeled velocities (green), and the modeled velocity contribution of elastic strain (pink) and block rotations (purple) are shown..... 119

Figure 5.3. Best-fitting two-dimensional planar elastic half-space dislocation locking models based on strike-perpendicular horizontal velocities projected onto profile X-X' of Figure 5.1b. Red labels show GPS site names. a-c.) Model 1; locked to 2 km depth. d-f.) Model 2; locked from 5 to 16 km depth, with creep and splay fault slip above 5 km depth. a,d): Observed (blue) and modeled strike-perpendicular velocities. b,e): Observed and modeled vertical velocities. c,f): Schematic of fault locking models.

Profile topography from 90-m SRTM data and GeoMapApp

(<http://www.geomapapp.org>)..... 124

Figure 5.4. Example of misfit (χ^2) tradeoffs for 2D dislocation models capped at $\chi^2=1.27$ (equivalent to 75% confidence interval for model 2 calculated with *F*-tests for statistical significance) to highlight those models that fit the data reasonably well. a.) Tradeoffs between locking depth and slip rate for locked from surface to depth models with different dip angles. Locked-at-surface models prefer shallow locking (<4 km depth) on a shallowly dipping ($\sim 26^\circ$) fault slipping ~ 9 -12 mm/yr, while steeply dipping faults ($\geq 40^\circ$) do not fit the data well ($\chi^2 > 1.0$). b.) Buried-dislocation models show tradeoffs between the updip depth of locking (depth P, Figure 5.3f) and slip rate with different depth ranges of locking (depth D, Figure 5.3f). Fault dip shown here is fixed to the best-fitting value of 35° ; however, P, D, slip rate, and dip were all varied in grid searches. These models prefer a more strongly locked zone from ~ 5 -16 km depth on a shallowly dipping ($\sim 35^\circ$) fault slipping ~ 10 -12 mm/yr..... 125

Figure 5.5. Summary of fault rocks analyzed. Sample locations are shown in Figure 5.1e and Appendix Figure D.7 and listed in Appendix Table D.6. (a) Exposure of the inactive Mai’iu fault showing the footwall fault rock sequence sharply overlain by unmetamorphosed hanging wall sedimentary rocks. (b) A schematic cross section through the fault core, including the structural position of the fault rocks sampled (after Little et al., 2019; Mizera et al., 2020). (c) Fault-exhumed exposure of the foliated cataclasite unit and a pseudotachylite vein. Inset: foliated serpentine schist (>10 m thick) entrained between the footwall and hanging wall of the Mai’iu fault, stranded atop the footwall north of Mt. Masasoru. (d) Outcrop of cohesive ultracataclasite unit structurally overlying foliated cataclasites. (e) Mafic fault gouges, and (f) corrensite-saponite fault gouge comprising the principal slip zone. 128

Figure 5.6. Friction measured during velocity-step experiments on Mai’iu fault rocks (Section 5.3.1; Figure 5.5; Table 5.1; Appendix Table D.6) including a.) corrensite-saponite gouges, b.) ultracataclasite and serpentinite schist; c.) mafic gouges; d.) foliated cataclasites. Colors indicate individual experiments (‘u368’) on numbered samples (‘PNG-14-19F’) under lower-temperature (LT) or higher-temperature (HT) conditions. 133

Figure 5.7. Rate-state-friction stability parameters (*a-b*) from velocity-stepping experiments on Mai’iu fault rocks (Section 5.3.1; Figure 5.5, Table 5.1; Appendix Table D.6) including a.) corrensite-saponite gouges, b.) ultracataclasite and serpentinite schist; c.) mafic gouges; d.) foliated cataclasites. 136

Figure 5.8. Inferred distribution of active Mai'iu fault rocks and deformation mechanisms, along with the resulting geodetic coupling and horizontal surface velocities. Stronger locking occurs in the velocity-weakening cataclastic units, while stable interseismic creep occurs updip and downdip of this zone in the saponite gouges and mylonites, respectively. Frictional stability and strength derived from experiments (Figures 5.6, 5.7) for all units except the mylonites, for which frictional behavior is inferred from microstructures (Little et al., 2019; Mizera et al., 2020) and microseismicity (Abers et al., 2016). The differential stress profile is based on frictional strength above the brittle-ductile transition zone (solid line) and inferred only schematically below (dashed line), but is consistent with preliminary peak differential stress estimates of ~140-185 MPa in the cataclasites from calcite twinning paleopiezometry (Mizera et al., 2020). 143

Figure A.1. Comparison of extensional style for varying slab dips of 30, 45, and 60° at times of 0.1, 1, and 4 Myr. Plots show log₁₀ of the second invariant of plastic strain in the crust. All models shown are 150 km wide and 30 km deep. Vertical exaggeration = 2. All other model properties are the same as in Table 2.1. Note that despite the low frictional and viscous strength of the initial shear zones in these models, high-angle normal faults initiate rifting above the pre-existing fault for the 30° case, while strain localizes on the pre-existing fault and exhumes a domal structure in the 60° case. In the intermediate 45° case strain localizes on the pre-existing fault, but significant activation of newly initiated high-angle fault through its footwall accommodate some extension and cut the hanging wall block that ends up stranded above the initial fault surface at 4 Myr. . 154

Figure A.2. Comparison of extensional style for varying shear zone cohesions of 4, 20, and 40 MPa at times of 0.1, 1, and 4 Myr, respectively. The viscous strength of the shear zone is lower than the surrounding crustal material. Initial shear zone and slab dip is 60°. Plots show log10 of the second invariant of plastic strain in the crust. All models shown are 150 km wide and 30 km deep. Vertical exaggeration = 2. All other model properties are the same as in Table 2.1. Note that the shear zone with higher cohesion and frictional strength predicts more distributed faulting through the footwall and does not exhume a domal core complex. Lower panels: initial strength profile with depth (log10(effective viscosity)) from within the actively deforming shear zone region and strength profiles after 100 kyr, as strain begins to localize (differential stress, log10(effective viscosity)) for the three models shown in the upper panels. 155

Figure A.3. Comparison of extensional style for varying shear zone viscous activation energies of 1.76×10^5 , 2.36×10^5 , and 2.76×10^5 J mol⁻¹ at times of 0.1, 1, and 4 Myr, respectively. Plots show log10 of the second invariant of plastic strain in the crust. All models shown are 150 km wide and 30 km deep. Vertical exaggeration = 2. All other model properties are the same as in Table 2.1. Lower panels: initial strength profile with depth (log10(effective viscosity)) from within the actively deforming shear zone region and strength profiles after 100 kyr, as strain begins to localize (differential stress, log10(effective viscosity)) for the three models shown in the upper panels. 156

Figure A.4. Comparison of extensional style for varying shear zone viscous activation energies of 2.26×10^5 , 2.76×10^5 , and $3.05 \times 10^5 \text{ J mol}^{-1}$ above weak lower crust at times of 0.1, 1, and 4 Myr. Lower crust is initially given as crustal material between 20 and 35 km depth. Plots show \log_{10} of the second invariant of plastic strain in the crust. All models shown are 150 km wide and 30 km deep. Vertical exaggeration = 2. Weak lower crust activation energy is $1.76 \times 10^5 \text{ J mol}^{-1}$ below 20 km. All other model properties are the same as in Table 2.1. Note that only the low-viscosity initial shear zone case predicts a single domal core complex, while higher viscosity shear zone configurations predict double domes and bivergent high-angle rift faulting..... 157

Figure A.5. Comparison of extensional style for varying lower crustal strengths with activation energies of 1.76×10^5 , 2.26×10^5 , and $2.76 \times 10^5 \text{ J mol}^{-1}$ at times of 0.1, 1, and 4 Myr. Lower crust is initially given as crustal material between 20 and 35 km depth. Shear zone viscous properties are identical to those of the upper crust. Plots show \log_{10} of the second invariant of inelastic strain in the crust. All models shown are 150 km wide and 30 km deep. Vertical exaggeration = 2. All other model properties are the same as in Table 2.1. Lower panels: initial strength profile with depth ($\log_{10}(\text{effective viscosity})$) taken from left of the actively deforming region and strength profiles after 100 kyr, as strain begins to localize (differential stress, $\log_{10}(\text{effective viscosity})$) for the three models shown in the upper panels, showing effect of weak lower crustal rheology. 158

Figure A.6. Full model domain of Mode 1 example shown in Figure 2.2 of the main text at model times 0.1, 1, and 3 Myr.....	159
Figure A.7. Full model domain of Mode 2 example shown in Figure 2.3 of the main text at model times 0.1, 1, and 3 Myr.....	160
Figure A.8. Full model domain of Mode 3 example shown in Figure 2.4 at model times 0.1, 1, and 3 Myr.....	161
Figure A.9. Strain rate plots of full model domain for DSM-specific model (Figure 2.7) at 200 kyr, 2 Myr, and 3.4 Myr.....	162
Figure A.10. Elastic strain for the three representative modal models from the text (Figures 2.2, 2.3, 2.4) at 100 kyr, 1 Myr, and 3 Myr.....	163
Figure A.11. Elastic strain in the preferred Dayman Dome model (Figure 2.7) at 1 Myr, 2 Myr, and 3.4 Myr, showing the distribution of bending and flexural elastic stresses in the footwall.....	163
Figure A.12. Model of Dayman Dome exhumation with continental crust in the upper plate hanging wall. All other model parameters are the same as the model in Figure 2.7 of the main text. a.) Initial model geometry, with weak zones as shown in Figure 2.7. b-d.) Strain after 200 kyr, 2 Myr, and 3.4 Myr.....	164
Figure A.13. Depth and temperature histories of particles shown in (a) at times 0 and 3.4 Myr for Dayman Dome model (Section 2.3). Note that depths plotted here are relative to modeled sea-level (elevation = 0) and therefore underestimate total vertical exhumational trajectory (change in depth of overlying rock column) by about 7 km due to the initial surface topography in the model setup.....	165

Figure B.1. Results of benchmark tests using the model setup of Liu & Rice (2007).
All four characteristic responses at the slip transition are obtained: a.
Decaying periodic. b. Simple periodic. c. Complex periodic. d. Seismic. . 168

Figure B.2. Characteristic slip response phase diagram for different κ and plate
velocities. The representative cases shown in Figure 3.6 are labeled with
letters a – d..... 169

Figure C.1. Detailed map of southern Goodenough Bay coastline showing coral
sample locations (white dots). The village of Rabaraba, offshore of
which our tide gauge was installed, is shown in red. 170

Figure C.2. Photos showing field examples of the coral platform sequences (top,
middle, lower right) and outcrop examples of intertidal echinoid burrows
above a platform level (lower left). 171

Figure C.3. Coral sample ages and elevations with schematic topographic profiles
(blue) of platform sequences at sites: a.) A; b.) B & C. See Figure 4.3c
for profiles at site D. c.) Average emergence rates for each site. 172

Figure C.4. Uplift-recurrence interval plots testing whether recorded earthquakes at Site D are a.) slip-predictable or b.) time-predictable. For a mean uplift rate of 1.5 mm/yr (dashed line), data should plot along the dashed line if the model holds. Earthquakes on the MGG fault system appear to be neither strictly slip-predictable nor strictly time-predictable, although the limited number of observed earthquake cycles may limit this interpretation. Additionally, removing smaller earthquakes from the maximum earthquake uplifts may shift some events towards the slip- or time-predictable lines, although this is beyond the resolution of the coral record. c.) Details of the calculated values plotted in a & b. ‘Age before 1950’ is the youngest coral age of each age cluster and ‘Age from:’ is the associated sample. ‘Elev.’ is the lowest sample elevation of each cluster and ‘Elev. from’ is the associated sample. ‘Recur. Int.’ is the time before the subsequent uplift event; ‘Max. Uplift’ is the maximum uplift of each event..... 173

Figure C.5. Extended measured (blue) and predicted (orange) tidal range from 4 – 9 July, 2018. Times are given in local time. During the study period, local tides were primarily diurnal with relatively stable mean high high-water (MHHW), mean sea-level (MSL), and mean low low-water (MLLW) levels..... 174

Figure D.1. Regional earthquakes of $M \geq 6.9$ corrected for using STATIC1D (Section D.2; U.S. Geological Survey, 2019). See Table D.4 and Section D.2 for a list and description of these events. Labeled numbers refer to event numbers in Table D.4..... 184

Figure D.2. Slip distribution for the 2007 M 8.1 Solomon Islands earthquakes from joint inversion of campaign GPS displacements (red vectors) and coastal uplift/subsidence recorded by coral reef platforms (Taylor et al., 2008; Wallace et al., 2015). Black vectors show the modeled fit to the horizontal component of GPS velocities. Larger black vectors show the rake of slip. 185

Figure D.3. Individual blocks tested for independence. *F* tests cannot statistically distinguish between models where VOGE and GOOD are considered individual blocks and ones where they are one unified block (Table D.5). Therefore, we treat them as one block in subsequent TDEFNODE block models (configuration 2 in Table D.5). TROB = Trobriand Islands block; SOLI = Solomon Islands block; WDLK = Woodlark Plate block; DEI = D’Entrecasteaux Islands block (Goodenough & Fergusson Islands); NORM = Normanby Island block; VOGE = Cape Vogel block; GOOD = Goodenough Basin block; PP = Papuan Peninsula block; AUST = Australian Plate block. 186

Figure D.4. Mai’iu fault locking results for different inversion constraints and locking depths in the elastic block models. We test models where the kinematic coupling ratio, Φ , is free to increase or decrease with depth (a), as well as models where the Mai’iu fault is prescribed to be fully creeping ($\Phi = 0$) or fully locked ($\Phi = 1$) at all depths (b, c, respectively), or fully locked at the surface (d) or from the surface to 2, 4, 9, or 14 km depth (e, f, g, h, respectively). We also test models that exclude the velocity at site YAMS: i.) coupling is required to decrease with depth; and j.) no prescribed spatial constraints on coupling..... 187

- Figure D.5.** Illustrated example of tradeoffs between locking depth, fault dip and predicted velocities for planar dislocation models with locking at the surface. Observed velocities are parallel to profile X-X' of Figure 5.1a and are relative to a fixed Australian plate. Fault dip has less effect on velocities for shallowly locked faults than for more deeply locked faults. 188
- Figure D.6.** Parameter sensitivity plots for locked-to-surface dislocation models showing data misfit (reduced χ^2) tradeoffs between: a.) slip rate and locking depth for dips of 15°, 28°, 45°, and 60°; b.) dip angle and slip rate for locking depths of 0.5, 2, 5, and 15 km; c.) dip angle and locking depth for slip rates of 8, 10, 12, and 14 mm/yr..... 189
- Figure D.7.** Tectonic setting (inset) and geological map showing the active and inactive strands of the Mai'iu Fault and the location of the fault rocks analyzed. Each fault rock is identified by its field sample number. Map after Little et al. (2019) and Mizera et al (2020). 191
- Figure D.8.** Images of the High Temperature and Pressure (HPT) Lab, Utrecht University, hydrothermal ring shear apparatus used to measure the frictional properties of Mai'iu fault rock samples. (a) is a labelled photograph of the apparatus, and (b) depicts the two pistons which, fitted together with an annulus of gouge between them, are inserted into the pressure vessel and sheared under controlled conditions of temperature, effective normal stress, and velocity. 192
- Figure D.9.** Parameter sensitivity plots for models with locking to the surface excluding the velocity at site YAMS. a-e.) Tradeoffs between locking depth and slip rate for locked from surface to depth models with different dip angles of 15°, 26°, 43° (best-fit), 40° and 55°, respectively.. 193

Figure D.10. Parameter sensitivity plots for buried dislocation models excluding the velocity at site YAMS. Buried-dislocation models show tradeoffs between the updip depth of locking (depth P, Figure 5.3f) and slip rate with different depth ranges of locking (depth D, Figure 5.3f). Fault dip shown here is fixed to the best-fitting value of 34° ; however, P, D, slip rate, and dip were all varied in grid searches. a-e.) Sensitivity plots for total depth ranges of locking of 3 km, 7 km, 8 km (best-fit), 11 km, and 15 km, respectively..... 194

Chapter 1: Introduction

Earthquakes and resulting tsunamis near population centers are among the deadliest and most destructive natural disasters on Earth. Major 21st-century disasters including the 2008 M_w 7.9 Wenchuan earthquake in China (>68,000 casualties; Wang, 2008), the 2010 M_w 7.0 Haiti earthquake (>135,000 casualties; Daniell et al., 2013), and the 2011 M_w 9.1 Tohoku-oki earthquake in Japan (>15,000 casualties; National Police Agency of Japan, 2020) serve as stark reminders of the immense human toll of earthquakes and their associated seismic hazards. Despite their intense societal impact, large earthquakes' infrequency, unpredictability, and uniqueness render them difficult to study and limit our collective preparedness for such events. The limited historical and instrumental record of earthquakes on major active faults necessitates the multi-disciplinary integration of geological, geophysical, historical, and modeling evidence in order to better understand which faults may slip in large earthquakes within the coming decades and centuries as well as to develop evidence-based rupture scenarios for these impending events. In this dissertation, I aim to advance our understanding of the slip behavior and seismic hazard potential of active low-angle normal faults (LANFs; dip < 30°) by studying the world's most rapidly slipping LANF, the Mai'iu fault in Papua New Guinea, using a variety of geodetic, paleoseismological, and numerical modeling techniques and linking these results to recently published geologic, seismological, and experimental evidence.

1.1. LOW-ANGLE NORMAL FAULTS

How do normal faults dipping < 30° form and do they slip at these dips? These questions have fueled a longstanding debate that stems from the classic LANF 'paradox.' Classical fault mechanical theory predicts that under Andersonian stresses (i.e., a vertical principal stress), normal faults cutting brittle crustal rocks with Byerlee friction (static friction coefficient $\mu = 0.6 - 0.85$) should initiate and slip at dips of 45-60° and should frictionally lock up and become inactive at

dips $< 30^\circ$ as new well-oriented higher-angle normal faults initiate and begin accommodating subsequent extension (e.g., Axen, 2004 and references within). However, the global geologic record contains abundant evidence of km-scale offsets on normal-sense detachment faults that today dip $< 30^\circ$ (e.g., Collettini, 2011 and references within), seemingly at odds with fault mechanical theory (hence, the ‘paradox’). Central to this paradox is the question of whether these LANFs initiate and slip at such shallow dips, or if they form and slip at higher angles and subsequently rotate back to shallower dips following abandonment. Early geodynamic models of lithospheric extension offered a mechanically feasible model for LANF formation known as the rolling-hinge model (Lavie et al., 1999, 2000), by which continued extension on a more steeply dipping normal fault causes it to rotate back to dip at shallower angles near the surface due to isostatic unloading and flexure of the footwall that concurrently develops a convex-up domal footwall (Figure 1.1). Section 2.1.1 describes these models in more detail and reviews more recent modeling results that further constrain the tectonic and thermomechanical conditions leading to localized detachment faulting rather than wide distributed rifting. Microstructural and paleomagnetic evidence of synextensional footwall rotations facilitated by detachment slip from oceanic (Garcés & Gee, 2007; Morris et al., 2009) and continental (Mizera et al., 2019; Watson, 2019) core complexes have verified the rolling-hinge model and helped reconcile the LANF paradox. Despite these important discoveries, many outstanding questions about the mechanics and deformation of these anomalous structures persist, including one with particular societal importance: do LANFs creep aseismically or slip in large earthquakes?

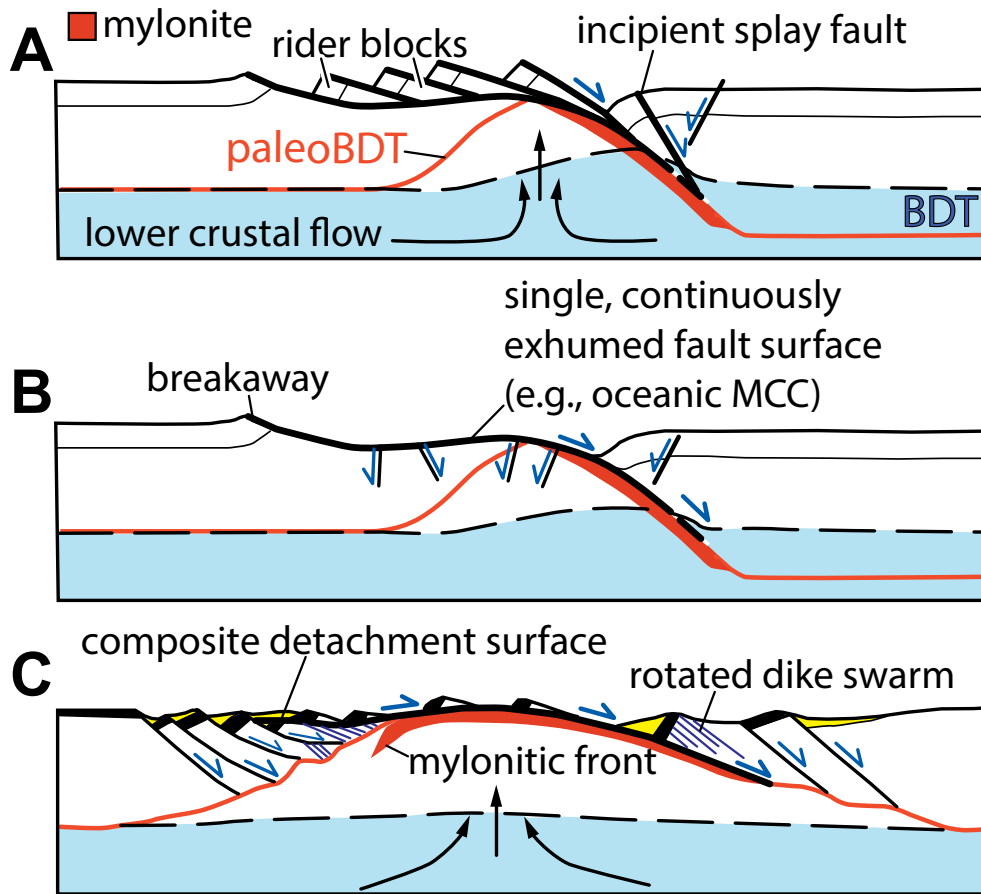


Figure 1.1. Schematics comparing styles of metamorphic core complex formation and low-angle detachment fault development from Little et al. (2019). A.) Rolling-hinge model with rider blocks. The active detachment fault dips more steeply at depth and rotates to dip at lower angles near the surface due to arching and back-rotation of the exhuming domal footwall complex. Slices of hanging wall crust are captured as ‘rider blocks’ atop the back-rotating footwall complex by sequential generations of splay faults in the shallowest hanging wall above the active detachment. See sections 4.1, 4.4, 5.2 and 5.4 for further discussion of splay faults and rider blocks as they relate to the Mai’iu fault and Dayman-Suckling metamorphic core complex. B.) Rolling-hinge model without rider blocks. Splay faults initiate in the hanging wall but do not cut rider blocks of hanging wall material that are subsequently transported with the rotating footwall. Instead, the detachment fault surface exhumes continuously atop the smooth domal footwall. C.) Composite domino faulting model. The detachment forms by continued slip and interconnection of the downdip portions of individual listric normal faults bounding ‘domino’ blocks in the upper plate.

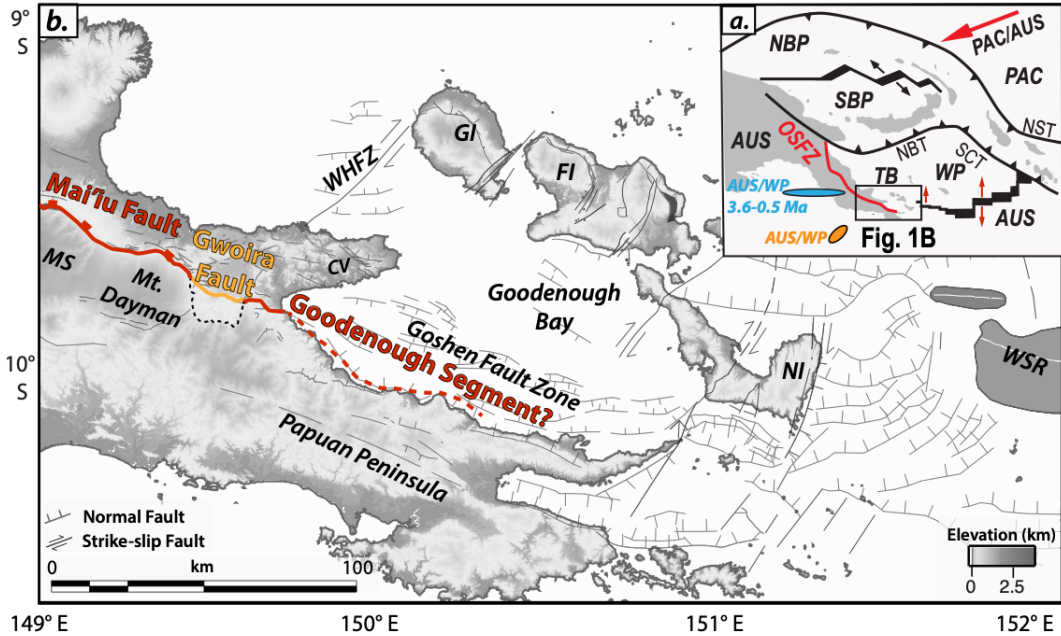
1.2. LOW-ANGLE NORMAL FAULT SEISMICITY

Few earthquakes of $M_w > 5.5$ with well-resolved low-angle normal-sense focal mechanisms have been recorded instrumentally (Collettini et al., 2019 and references within). The largest recorded unambiguously discriminated LANF earthquakes were M_w 5.9 and 6.2 events in the Gulf of Corinth with reported dips of 30° and 33° , respectively (Jackson & White, 1989). Larger earthquakes, such as the 29 October 1985 M_w 6.8 Woodlark Basin event, have been attributed to slip on LANFs based on the proximity of their hypocenters to well-known and seismologically imaged LANFs (Abers, 2001; Abers et al., 1997). Active LANFs are rare and typically slip at low long-term slip rates (<1 mm/yr to ~ 10 mm/yr; Webber et al., 2018), which may in part explain the lack of recorded moderate-to-large LANF earthquakes. However, it remains unclear whether the paucity of instrumentally recorded large ($M_w > 6.0$) LANF earthquakes reflects only the infrequency of these events or a fundamental difference in mechanical behavior between LANFs and more seismogenic higher-angle normal faults.

Wernicke (1995) proposed that their geometry allows LANFs to accumulate more interseismic strain than their steeper counterparts, implying that LANFs rupture less frequently but in larger earthquakes than high-angle normal faults. In contrast, Hreinsdóttir & Bennett (2009) studied GPS velocities across the Altotiberina LANF in the Northern Apennines and inferred that the Altotiberina fault predominantly creeps aseismically below a shallow locking depth of 4 km. This inferred aseismic LANF creep could be facilitated by numerous proposed mechanisms including: rotated non-Andersonian principal stress orientations (Axen, 1992, 2020), highly elevated pore fluid pressures (Axen, 1992; Collettini & Barchi, 2004; Ikari et al., 2009; Abers, 2009), and/or creep within frictionally stable gouge minerals (e.g., Collettini, 2011; Collettini et al., 2019) including serpentine (antigorite/lizardite) (Floyd et al., 2001), talc (Collettini et al., 2009a), and phyllosilicate-rich clays (Ikari et al., 2009; Ikari & Kopf, 2017). However, reevaluation and modeling of the GPS data from the Northern Apennines (Anderlini et al., 2016) showed that the data were better explained by spatially heterogeneous locking of the main Altotiberina fault as well as the splay faults in its hanging wall. Evidence from structural geology,

microseismicity and seismic reflection imaging support this emerging view that slip on the Altotiberina fault is more complex and involves both predominantly creeping and predominantly locked segments (Anderlini et al., 2016; Brozetti et al., 2009; Valoroso et al., 2017). Various hypothesized mechanical behaviors imply drastically different seismic hazard potentials of LANFs. Better understanding whether LANFs predominantly creep aseismically (e.g., Hreinsdóttir & Bennett, 2009;), slip in large earthquakes (e.g., Wernicke, 1995) or slip via spatiotemporally complex mixed-mode seismic and aseismic processes (e.g., Anderlini et al., 2016) is crucial to estimating the size and hazard potential of future LANF earthquakes.

Modern geodetic techniques such as GNSS (Global Navigation Satellite System) positioning and InSAR (interferometric synthetic aperture radar) have revolutionized our understanding of interseismic fault locking and the seismic cycle by providing measurements of the Earth's surface velocities that can be modeled to infer fault slip rates and locking distributions. Previous geodetic studies of active LANFs have been limited by the low long-term slip rates of these faults. For example, the Altotiberina fault in Italy is estimated to slip at long-term rates of 2.4 ± 0.3 mm/yr (Hreinsdóttir & Bennett, 2009) or 1.7 ± 0.3 mm/yr (Anderlini et al., 2016). For comparison, these rates are orders of magnitude slower than convergence rates at subduction zones which typically range from 1 – 10 cm/yr (e.g., Heuret et al., 2011 and references within). The low slip rates across LANFs make it more difficult to geodetically resolve reliable secular fault slip rates. In addition, spatial variations in surface velocities related to spatially heterogeneous fault locking are subtle and more difficult to model conclusively on faults with such low slip rates. Therefore, it is critical to study the most rapidly slipping LANFs to better understand the interseismic slip behavior of these faults.



PAC = Pacific Plate; AUS = Australian Plate; WP = Woodlark Plate; NBP = North Bismarck Plate; SBP = South Bismarck Plate; NBT = New Britain Trench; SCT = San Cristobal Trench; OSFZ = Owen-Stanley Fault Zone; MS = Mt. Suckling; WHFZ = Ward Hunt Fault Zone; CV = Cape Vogel; WSR = Woodlark Spreading Ridge; D'Entrecasteaux Islands: GI = Goodenough Island; FI = Fergusson Island; NI = Normanby Island.

Figure 1.2. a.) Tectonic map with present (orange; Wallace et al., 2014) and 3.6—0.5 Ma (blue; Taylor et al., 1999) poles of rotation of the Woodlark Plate relative to the Australian Plate. Northward subduction at the New Britain and San Cristobal trenches accompanies counter-clockwise rotation of the Woodlark Plate and predominantly N-S extension at the Woodlark Spreading Center and along the southeastern portion of the Papuan Peninsula. b.) Local tectonic map with faults from Little et al. (2019) highlighting the active Mai'iu fault. The Mai'iu-Gwoira-Goodenough (MGG) fault system is mapped in three segments: the 16-24° dipping Mai'iu fault (red), the more steeply dipping Gwoira fault (orange) and the inferred offshore continuation through Goodenough Bay (dashed red). c.) Oblique view of the Mai'iu fault and DSM with topography from 90-m SRTM data and GeoMapApp (<http://www.geomapapp.org>).

1.3. THE MAI'IU FAULT, PAPUA NEW GUINEA

Dipping 16-24° at the Earth's surface (Little et al., 2019; Mizera et al., 2019) and slipping at long-term dip-slip rates of 8.6 ± 1.0 mm/yr (Wallace et al., 2014) to 11.7 ± 3.5 mm/yr (Webber et al., 2018), the Mai'iu fault in Papua New Guinea (PNG) is one of the world's fastest-slipping active LANFs (Webber et al., 2018). Along the base of Mt. Dayman where the Mai'iu fault dips 16-24°, this fault is the main structure accommodating NNE-SSW tectonic extension between the Australian Plate and the Woodlark Plate related to northward subduction of Solomon Sea lithosphere at the San Cristobal and New Britain trenches (Figure 1.2; Wallace et al., 2014; Abers et al., 2016; Little et al., 2007, 2011, 2019; Baldwin et al., 2012). Along with Mt. Suckling, the ~3 km-tall smooth corrugated dome of Mt. Dayman comprises part of the Dayman-Suckling metamorphic core complex (DSM), one of the world's youngest and most rapidly exhuming metamorphic core complexes (Figure 1.2; Daczko et al., 2009, 2011; Whitney et al., 2013; Little et al., 2019; Mizera et al., 2019; Österle et al., 2020a). Metamorphic core complexes are structurally coherent exposures of mid-to-lower crustal rocks typically exhumed in the domal or convex-up footwalls of high-offset low-angle detachment faults (e.g., Whitney et al., 2013 and references within). More detailed descriptions of the tectonics, geology, structure, and kinematics of southeast Papua New Guinea and the Mai'iu fault are reserved for the background sections of the research chapters (sections 2.3, 4.1, 5.1), but it is important to note that the rapid rates of active LANF slip and MCC exhumation make southeast PNG an ideal and unique field area in which to study the dynamic tectonic processes driving and accommodating LANF slip and MCC formation.

1.4. SUMMARY OF RESEARCH CHAPTERS

This dissertation uses numerical modeling, GPS geodesy, and coral paleoseismology to unravel the deformation patterns related to slip on the Mai'iu fault as well as the (thermo)mechanical and geologic processes facilitating this slip and the exhumation of the DSM over an array of timescales ranging from the coseismic (seconds) and interseismic (years to

hundreds of years) to the tectonic (millions of years). The research chapters are organized according to the deformation timescales of interest, from longest to shortest: chapter 2 explores the Myr-timescale thermomechanical and structural evolution of the DSM and post-subduction MCCs with tectonic geodynamic models; chapter 3 develops numerical modeling techniques that integrate seismic-cycle deformation with kyr-timescale tectonic loading to model LANF seismic cycles under different frictional and mechanical conditions; chapter 4 examines the Holocene coral paleoseismological record of slip on the Goodenough Bay segment of the Mai'iu fault system to assess whether this segment slips seismically; and chapter 5 presents and models the results of a multi-year campaign GPS experiment across the Mai'iu fault to illuminate the distribution of interseismic creep and locking on this fault. Finally, chapter 6 summarizes the conclusions and offers suggestions for future work.

This dissertation represents the results of work performed in collaboration with the co-authors listed in the acknowledgments and references sections. It is important to note that these studies were undertaken in conjunction with other multidisciplinary and international projects studying the geology, tectonics, and mechanics of the Mai'iu fault and DSM. The geologic and experimental evidence from those projects (Webber et al., 2018, 2020; Little et al., 2019; Mizera et al., 2019, 2020; Mizera et al., in prep; Österle et al., 2020a, 2020b; section 3 of Biemiller et al., 2020b) informed and constrained the interpretation of the results in this dissertation, and vice-versa. I performed a primary role in the development and undertaking of the experiments, analysis and interpretation of the results, and writing of this dissertation and the associated manuscripts, with the exception of the laboratory friction experiments in chapter 5 section 3, which were primarily developed and performed by Carolyn Boulton. The subsequent introduction paragraphs briefly summarize each research chapter.

The tectonic history of New Guinea includes multiple phases of subduction, collisional orogenesis and rifting (e.g., Baldwin et al., 2012 and references within), and may have involved significant slab breakoff of subducted lithosphere at the end of one phase of subduction (Cloos et al., 2005). However, it has thus far remained unclear whether subduction cessation due to failed

subduction of continental lithosphere, with or without slab breakoff, leads to lithospheric conditions conducive to the formation of core complexes and/or LANFs. Chapter 2 presents a suite of geodynamic models testing the effects of post-subduction tectonically inherited thermomechanical heterogeneities on the structural style of subsequent lithospheric extension and rifting. Results of these models are compared with geologic and geophysical observations of the DSM to assess the pre-extensional regional lithospheric conditions and potential role of tectonically inherited features in the formation and exhumation of the DSM. Chapter 2 has been published in *Tectonics* as “Tectonic Inheritance Following Failed Continental Subduction: A Model for Core Complex Formation in Cold, Strong Lithosphere” (Biemiller et al., 2019).

Over the last two decades, geodetic and seismological studies have revealed that subduction megathrusts slip in a spectrum of slip behaviors ranging from steady aseismic creep to episodic large earthquakes following periods of interseismic locking (e.g., Schwartz & Rokosky, 2007; Peng & Gomberg, 2010; Saffer & Wallace, 2015; references within). The intermediate slip behaviors are commonly referred to as ‘slow earthquakes’ and include episodic periods of accelerated fault creep (slow-slip events), low-frequency and very-low-frequency earthquakes, and long-duration ‘tsunami earthquakes’ with higher surface displacements than predicted by their seismically determined magnitude. These observations show that strain release on active faults is more complex than the classical elastic rebound theory of earthquake faulting. It is less clear whether normal faults (including LANFs) slip via a similar spectrum of multi-timescale seismic and aseismic processes. Chapter 3 develops numerical modeling techniques to incorporate seismic-cycle deformation governed by rate-state friction into a long-term tectonic modeling framework based on the Fast-Lagrangian Analysis of Continua (FLAC) algorithms. These techniques are used to model seismic-cycle-timescale slip on LANFs with different distributions of rate-state friction parameters under different loading conditions. The models predict that normal faults may slip in periodic aseismic creep events akin to slow-slip events and help constrain the frictional and loading conditions leading to aseismic creep, large earthquakes, and intermediate slip behaviors on LANFs. Chapter 3 has been published in the *Journal of Geophysical Research: Solid Earth* as

“Earthquake supercycles as part of a spectrum of normal fault slip styles” (Biemiller & Lavier, 2017).

Along-strike to the east of Mt. Dayman (Figure 1.2), the hanging wall of the Mai’iu fault is cut by more steeply-dipping synthetic and antithetic splay faults, including the prominent $\sim 42^\circ$ -dipping Gwoira fault that soles into the Mai’iu fault at a depth of ~ 1 km (Webber et al., 2020). Further east, the active fault system follows the southern shoreline of Goodenough Bay and freshly faceted dip-slopes dipping $\sim 45^\circ$ suggest that near-surface slip occurs on a set of higher-angle splay faults rooted in the Mai’iu detachment. Fossil coral reefs exposed at >300 m elevations and reported Holocene uplift rates of >3 mm/yr (Mann & Taylor, 2002; Mann et al., 2004, 2009) indicate that this stretch of coastline is primarily located on the actively tectonically uplifting footwall of the detachment. Chapter 4 details mapping and U/Th dating results from emerged coral platforms along the Goodenough Bay coastline. These data are used to estimate coastal uplift rates and establish a coral paleoseismological record of Holocene earthquake slip on the Mai’iu-Goodenough detachment system. Chapter 4 is in press at *Geophysical Research Letters* as “Emerged Coral Reefs Record Holocene Low-angle Normal Fault Earthquakes” (Biemiller et al., 2020a).

Previous geodetic studies of active LANF slip and interseismic coupling have focused on faults with low long-term slip rates of ~ 2 mm/yr (Hreinsdóttir & Bennett, 2009; Anderlini et al., 2016). GPS velocities and cosmogenic isotope concentrations suggest that the Mai’iu fault slips actively at significantly faster long-term dip-slip rates of up to 1 cm/yr (Wallace et al., 2014; Webber et al., 2018). Building upon previous observations of a regional GPS network (Wallace et al., 2014), Chapter 5 presents results from a multi-year campaign GPS experiment with dense station spacing on the hanging wall of the Mai’iu fault. Velocities derived from GPS observations are used to estimate fault slip rates and constrain kinematic models of interseismic fault locking. Microstructural analyses (Little et al., 2019; Mizera et al., 2020) and laboratory friction experiments on exhumed Mai’iu fault rocks (performed by Carolyn Boulton; section 5.3) constrain the interpretation of non-unique kinematic models and help develop an integrated view of the

geologic and mechanical processes facilitating slip on the Mai'iu fault. Chapter 5 has been published at *Journal of Geophysical Research: Solid Earth* as “Mechanical Implications of Creep and Partial Coupling on the World’s Fastest Slipping Low-angle Normal Fault in Southeastern Papua New Guinea” (Biemiller et al., 2020b).

Chapter 2: Tectonic inheritance following failed continental subduction: a model for core complex formation in cold, strong lithosphere

Copyright statement: An edited version of this paper was published by AGU. Copyright 2019 American Geophysical Union.

Biemiller, J., Ellis, S., Mizera, M., Little, T., Wallace, L., & Lavier, L. (2019). Tectonic Inheritance Following Failed Continental Subduction: A Model for Core Complex Formation in Cold, Strong Lithosphere. *Tectonics*, 1742–1763.
<https://doi.org/10.1029/2018TC005383>

ABSTRACT

Inherited structural, compositional, thermal and mechanical properties from previous tectonic phases can affect the deformation style of lithosphere entering a new stage of the Wilson Cycle. When continental crust jams a subduction zone, the transition from subduction to extension can occur rapidly, as is the case following slab breakoff of the leading subducted oceanic slab. This study explores the extent to which geometric and physical properties of the subduction phase affect the subsequent deformation style and surface morphology of post-subduction extensional systems. We focus on regions that transition rapidly from subduction to extension, retaining lithospheric heterogeneities and cold thermal structure inherited from subduction. We present numerical models suggesting that following failed subduction of continental crust (with or without slab breakoff), the extensional deformation style depends on the strength and dip of the pre-existing subduction thrust. Our models predict three distinct extensional modes based on these inherited properties: 1) reactivation of the subduction thrust and development of a rolling-hinge detachment that exhumes deep crustal material in a domal structure prior to onset of an asymmetric rift; 2) partial reactivation of a low-angle subduction thrust, which is eventually abandoned as high-angle, ‘domino’-style normal faults cut and extend the crust above the inherited thrust; 3) no reactivation of the subduction fault, but instead localized rifting above the previous subduction margin as new rift-bounding, high-angle normal faults form. We propose that the first mode is well

exemplified by the young, rapidly exhumed Dayman-Suckling metamorphic core complex that is exhuming today in Papua New Guinea.

2.1. INTRODUCTION

Tectonic inheritance can exert an important control on the style of extension as continental crust rifts apart during the onset of a new Wilson cycle (e.g., Manatschal et al., 2015; Misra & Mukherjee, 2015; Salerno et al., 2016; Osmundsen & Peron-Pindivic, 2018; Salazar-Mora et al., 2018). One manifestation of rifting involves the formation and exhumation of a Metamorphic Core Complex (MCC). MCCs typically include coherent exposures of mid to lower crustal rocks exhumed as an arched or domed structure in the lower plate of a large-offset normal fault during extension. In the upper plate, a wedge of brittlely distended upper crust is displaced laterally away from that dome and from upwelling ductile material beneath, along a weak detachment fault (e.g., Lister and Davis, 1989). Although MCCs typically form under specific crustal conditions during extension of warm, mechanically weak crust, these conditions can arise from a variety of tectonic settings and thus MCCs are found in both oceanic and continental crust within oceanic spreading centers, continental margins, continental rifts, and continental collision zones (e.g., Baldwin et al., 2012; Whitney et al., 2013; Platt et al., 2015; Brun et al., 2018). Examples of collision-related MCCs include the Aegean Cyclades (Jolivet et al., 2010), the gneiss domes of Papua New Guinea (Baldwin et al., 1993; Little et al., 2011), and the Himalayan Gurla Mandhata (Murphy & Copeland, 2005).

MCC exhumation is largely accommodated by slip on normal faults that dip at a low angle at the surface. In common usage, a low-angle normal fault (LANF) is defined to be a normal fault that slips at a dip of $<30^\circ$, an attitude that is seemingly mis-oriented with respect to extensional Andersonian principal stress directions (e.g., Axen, 1992). As observed in many MCCs, a detachment fault is a normal fault—typically dipping $<30^\circ$ today—that has accrued large displacements of ≥ 10 's of km, though whether this slip accumulated on a fault that was dipping $<30^\circ$ at the time of its activity is often a subject of interpretation (e.g., Collettini, 2011; Whitney

et al., 2013). Major dip-slip on a detachment fault can accommodate focused exhumation of mid-to-lower crustal rocks in the footwall of that fault. Such localized extension contrasts with a case of distributed crustal extension accommodated by slip on numerous high-angle normal faults of more modest displacement (e.g., Axen 1992; Wernicke, 1995; Collettini, 2011). Although Andersonian fault mechanics for rocks with Byerlee friction predict that normal faults with dips $<30^\circ$ should not slip in the brittle crust (e.g., Axen, 1992; Collettini, 2011), active LANFs have been observed geodetically (Hreinsdóttir & Bennet, 2009; Wallace et al., 2014) and seismologically (e.g., Wernicke, 1995; Abers, 2001; Chiaraluce et al., 2007). One leading concept for LANF activity is that these faults slip at low angles in the brittle crust due to the presence of intrinsically low-friction gouge minerals and/or high pore-fluid pressure, and geological observations suggest such faults on the continents sole into low-angle mylonitic shear zones at or below the brittle-ductile transition (e.g., Lister & Davis, 1989; Axen, 1992; Collettini et al., 2009). In this case, the LANF may have been reactivated from a pre-existing low-angle structure, such as a thrust fault (e.g., Singleton et al., 2018), or it potentially may have nucleated in intact rock at a primary low-dip, with the latter phenomenon being harder to explain mechanically (e.g., Sibson, 1985; Collettini & Sibson, 2001). An alternative concept is that most LANFs initiate as high-angle normal faults through the brittle crust, and are later rotated back via a ‘rolling-hinge’ process to low angles at shallow depths as a result of tectonic unloading and consequent flexural and isostatic footwall uplift, possibly aided by focused lower crustal flow or asthenospheric upwelling (e.g., Lister & Davis, 1989; Lavier et al., 1999, 2000; Platt et al., 2015; Brun et al., 2018). Although paleomagnetic evidence of footwall rotation has confirmed the rolling-hinge mechanism for oceanic MCCs (e.g., Garcés & Gee, 2007), the origin and development of continental LANFs is still debated, in part because it is difficult to demonstrate geologically that large horizontal-axis rotations have affected deeply exhumed metamorphic rocks; and in part because the wide range of lithospheric conditions that may exist prior to continental extension can lead to diverse tectonic histories that are less uniform and more complex than those of relatively young oceanic lithosphere.

2.1.1. Lithospheric conditions for MCC formation

Physical and numerical modeling has improved our understanding of the mechanics and dynamics of MCC formation and exhumation, as well as the physical conditions under which these enigmatic structures form. For example, early geological studies recognized the importance of LANF detachments in exhuming deep crustal rocks in MCCs (e.g., Davis et al., 1980; Miller et al., 1983), but details of how such mechanically misoriented faults could form in the brittle crust remained unclear. Theoretical studies such as Buck (1988) and Buck (1993) showed that the shallow dip of LANFs could be explained by rotation of originally well-oriented high-angle normal faults during protracted extension, a process which was also observed in analogue models (Brun et al., 1994). Thermomechanical models confirmed the mechanical viability of the rolling-hinge process (Lavie et al., 1999) and showed that lithospheric thermal structure, crustal elastic thickness, and the degree of plastic strain-softening influenced whether LANFs formed and accommodated large offsets (Lavie et al., 1999; 2000; Lavie & Buck, 2002).

Further numerical modeling has shown that extension of relatively homogeneous lithosphere can lead to either narrow rifting, wide rifting, or localized slip on high-offset detachment faults that bound one or more MCCs (e.g., Buck, 1991; Rosenbaum et al., 2008; Tirel et al., 2008; Rey et al., 2009; Schenker et al., 2012). Although lithosphere-scale numerical models have successfully replicated structural and morphological features of MCCs, they typically model extension of undisturbed homogeneous crust above a flat Moho (e.g., Buck, 1991; Lavie et al., 1999; 2000; Rosenbaum et al., 2005; Whitney et al., 2013; Labrousse et al., 2016). Such initial conditions seem most applicable to continental settings where variations in pre-extensional crustal thickness and Moho relief are minimal (e.g., Whitney et al., 2013), but may not be appropriate where previous tectonic phases have altered the thickness or configuration of the lithosphere (e.g., Huisman & Beaumont, 2007); for example, by introduction of a subduction zone. Models incorporating different crustal rheological layerings have shown that the presence of a weak lower-

or middle-crustal layer that is decoupled from strong upper crust enhances the rate of lateral ductile crustal flow beneath detachment faults, and the upward focusing of flow (upwelling) beneath them; these crustal flow processes enhance localized exhumation of mid- to lower crustal rocks in the footwall of a detachment fault and can lead to the formation of an MCC (e.g., Le Pourhiet et al., 2004; Huet et al., 2011a; 2011b; Wu et al., 2015; Wu & Lavier, 2016; Labrousse et al., 2016). Many proposed mechanisms for MCC formation recognize that decoupling of the upper crust from the lower crust and mantle is essential to establish a localized and long-lived detachment.

2.1.2. Inheritance of collisional features following jammed subduction

Post-subduction extension is thought to initiate following jamming of a subduction zone by positively buoyant downgoing continental crust, which may be accompanied by slab breakoff of the denser, negatively buoyant leading oceanic lithosphere (e.g., Davies & von Blanckenburg, 1995; Leech et al., 2005). Slab breakoff can occur when the tensile stress in the downgoing slab due to the opposing buoyant forces of the subducted continental and oceanic lithosphere exceeds the yield stress needed to fully thin the subducted plate at depth over some time interval of detachment (e.g. Wong A Ton & Wortel, 1997; Duretz et al., 2011; 2012; van Hunen & Allen, 2011). Large-scale geodynamic models have shown that the net positive buoyancy of the remaining continental slab following breakoff can drive its uplift and local extension in the presence (Petersen & Buck, 2015) or absence (Duretz et al., 2011; Liao et al., 2018) of continued far-field convergence. These models have been invoked to explain pressure-temperature histories of (ultra)-high-pressure metamorphic rocks in the Alps, the Aegean Islands, the Dabie metamorphic complex in China, the Norwegian Caledonides and the D'Entrecasteaux Islands (e.g., Davies & von Blanckenburg, 1995; Duretz et al., 2012; Bottrill et al., 2014; Butler et al., 2015; Petersen & Buck, 2015; Liao et al., 2018).

Controls on breakoff-related collisional style have been investigated by large-scale geodynamic models, which simulate both the oceanic and continental subduction phases as well

as post-collisional exhumation of subducted continental crust (e.g., Duretz et al., 2011, 2012; Duretz & Gerya, 2013). Mechanical decoupling of rheologically distinct lithospheric layers can control whether slab breakoff occurs, and whether deeply subducted continental rocks are subsequently exhumed (Duretz & Gerya, 2013). Using flow laws from Ranalli (1995) for modeled crustal rheologies, Duretz & Gerya (2013) show that breakoff occurs both for intermediate-strength (wet quartz / An75) and homogeneously strong (felsic granulite) downgoing continental crust, suggesting that coupled lower crust and upper mantle lithosphere promote breakoff; however, only the case of strong crust led to coherent exhumation of deep crustal rocks during post-collisional equilibration. Petersen & Schiffer (2016) modeled extension of laterally uniform crust above a fossilized collisional suture zone within the mantle lithosphere. In addition to confirming that rifting localizes above such inherited orogenic sutures, their results show that pre-extensional crustal thickness plays a key role in establishing the dominant lithospheric flow regime and determining the amount and timing of crustal thinning and melt production. Such models highlight the important link between lithospheric strength, collisional style and post-collisional extension, but their large spatial scale (>1000 km) imposes numerical resolution limits which make it difficult to resolve and predict the finer-scale (100s of m – 10s of km) structural evolution of these post-collisional MCCs.

2.1.3. This study: high-resolution modeling of cold post-collision MCC formation

Lithosphere-scale and larger-scale (1000s of km) thermomechanical models have advanced our understanding of factors controlling MCC formation and collisional style, respectively; however, the disparate scales of these two types of models leave unresolved questions about the structural development of post-collisional extensional margins. For example, can inherited conditions control whether post-collisional margins exhume coherent exposures of mid to lower crustal rocks along localized detachments, or instead result in diffuse rifting across a zone of numerous high-angle normal faults? Do post-collisional lithospheric conditions promote

rolling-hinge style detachments or domino-style extensional arrays? How does breakoff-related removal of lithospheric mantle influence subsequent extensional style? Our study addresses these questions using high-resolution numerical models that employ post-collisional lithospheric initial conditions. Specifically, we test how the strength and geometry of inherited collisional shear zones and the strength of the lower crust affect subsequent extensional deformation of a cold continental collision margin that may have undergone slab breakoff. We identify three distinct extensional styles predicted by these models before discussing what we believe to be an exemplary case study of the large-slip detachment end-member: the Dayman-Suckling MCC (DSM) in SE Papua New Guinea.

2.2. GENERAL MODEL OF POST-COLLISIONAL EXTENSION

2.2.1. Numerical methods

For all simulations in this study we use the thermomechanical finite-element code SULEC (Ellis et al., 2011; Buitert & Ellis, 2012; Tetreault & Buitert, 2012), which solves the incompressible momentum equation for slow, creeping power-law flows in conjunction with the two-dimensional equation for unsteady thermal conduction with isotropic thermal conductivity (details in Appendix A.1). Modeled rheologies are viscoelastoplastic. Plastic failure is incorporated with a Mohr-Coulomb yield criterion:

$$\sigma_{eff} = P_{eff} \sin(\theta) + C \cos(\theta) \quad (2.1)$$

where σ_{eff} is the differential stress, P_{eff} is the effective pressure, C is the cohesion and θ is the angle of internal friction. Linear strain-softening (e.g., Lavier & Buck, 2000) is applied to the angle of internal friction (e.g., Wu et al., 2015):

$$\theta = \theta' + (\theta_0 - \theta') \left(1 - \frac{\epsilon_{ps}}{\epsilon_f}\right) \quad (2.2)$$

where θ_0 is the unstrained angle of internal friction, θ' is the fully strain-softened angle of internal friction, ϵ_{ps} is plastic strain, and ϵ_f is the cutoff strain at which full strain-softening has occurred.

A temperature-dependent effective viscosity η_{eff} is calculated for power-law flow as:

$$\eta_{eff} = \frac{1}{2} A^{-1/n} d^{m/n} \dot{\epsilon}_{eff}^{1/n-1} e^{\frac{E_a+PV}{nRT}} \quad (2.3)$$

where A is the pre-exponential constant, n is the flow law exponent, $\dot{\epsilon}_{eff}$ is the effective strain rate, d is the grain size, m is the grain-size exponent, E_a is the activation energy, V is the activation volume, R is the gas constant and T is the temperature. For materials with both dislocation creep and diffusion creep parameters, the viscous yield stress is equal to the minimum of the two flow stresses. Elastic effects are approximated by modifying (2.3) to include an effective viscoelastic viscosity based on the elastic time-stepping method of Moresi et al. (2003, equations 28 and 29) with an elastic timestep 100 times the advection timestep. We use an advection timestep of 10 kyr and a non-uniform structured mesh with grid-spacing as low as 100 x 100 m in the rapidly deforming region. Erosion is modeled as a simple diffusion function of local slope where erosion rate is given by

$$\frac{dh}{dt} = -k_e \left| \frac{dh}{dx} \right| \quad (2.4)$$

where h is the height above base level, t is time, x is the horizontal coordinate and k_e is the erosion coefficient. In all models k_e is 0.85 mm yr⁻¹. Similarly, sedimentation is applied as a simple function of surface height according to

$$\frac{dh_s}{dt} = k_s h_s \quad (2.5)$$

where h_s is the elevation below base level and k_s is the sedimentation coefficient. In all models k_s is 4.75 x 10⁻²¹ yr⁻¹ and base level is 1 km below sea-level, assuming that most sedimentation occurs offshore.

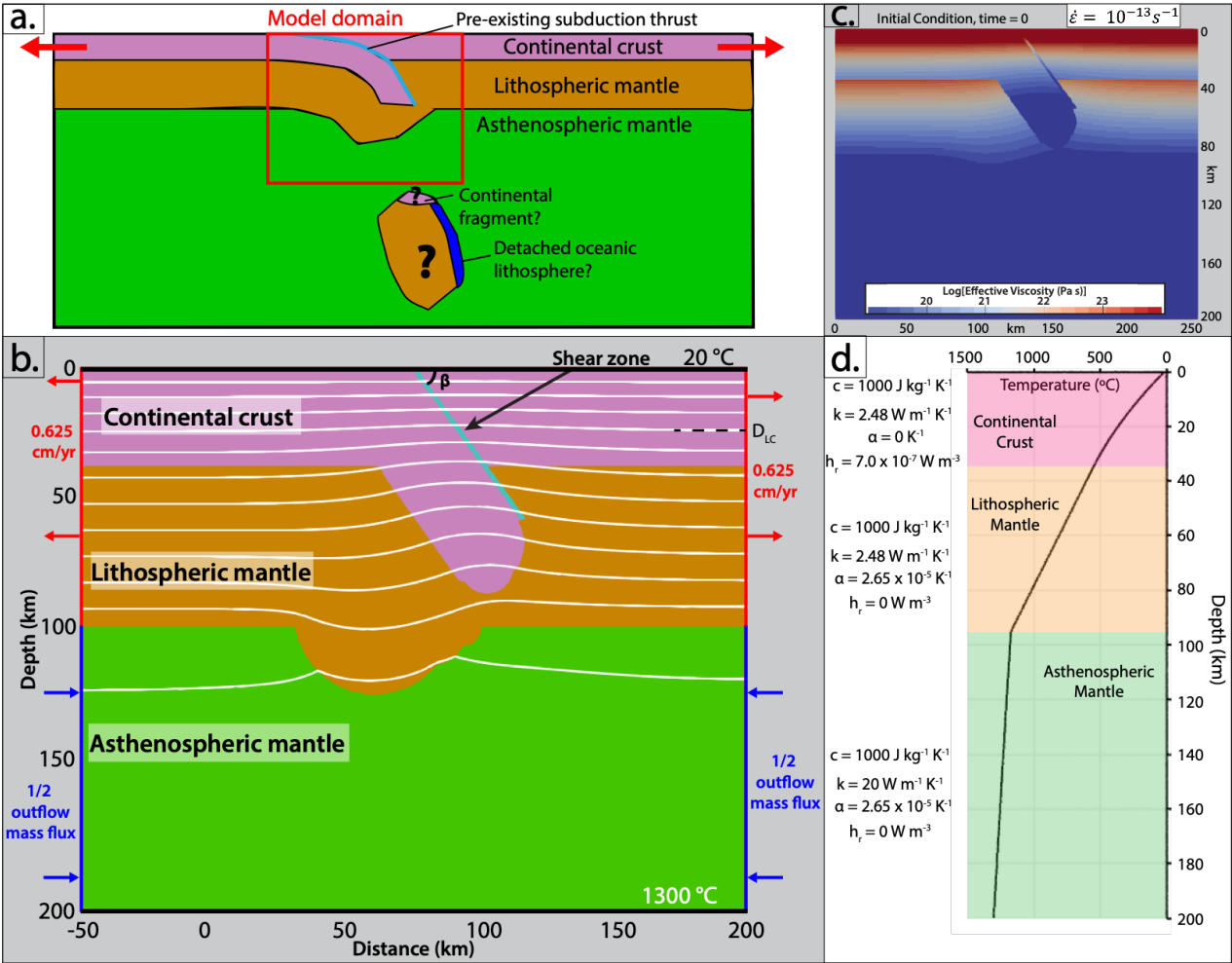


Figure 2.1. a. Conceptual model of failed continental subduction margin undergoing extension, with numerical model domain outlined in red. b. Typical numerical model geometry, boundary conditions, and initial thermal structure. White lines show isotherms in 100 °C increments. Black dashed line and DLC indicate depth below which lower crust is weakened, which is 20 km in the models shown in Figure A.5 (Appendix A). c. Initial mechanical strength contrasts for the model shown in Figure 2.2. Colored shading shows Log10 of the effective dynamic viscosity η_{eff} , defined as: $\eta_{eff} = \frac{\tau}{2\dot{\epsilon}}$, where τ is the principal in-plane shear stress and $\dot{\epsilon}$ is the principal in-plane shear strain rate (Ranalli, 1995). This value quantifies how easily deformed an area is, and is useful for tracking relative strength in both the brittle and ductile deformation regimes. d. Initial geothermal structure from a vertical profile taken near the left edge of the model in b, with thermal properties for each layer listed; c is specific heat capacity; k is thermal conductivity; α is thermal expansivity coefficient; and h_r is radiogenic heat productivity (see Appendix A.1 for details).

2.2.2. Model setup

We model a simplified failed continental subduction or collision margin that features a low-cohesion and viscously weak zone along a pre-existing subduction thrust or collisional suture (Figures 2.1a, 2.1b). Hereafter we refer to this zone as the inherited ‘shear zone’ based on the assumption that it experienced localized shear deformation during collision. The term ‘shear zone’ here does not imply specific deformation mechanisms nor does it imply that the inherited weak zone localizes extensional strain. The geometry of the inherited shear zone is simplified to dip at a constant angle in order to more clearly test the effect of different initial dips. Although other faults and mechanical weaknesses will certainly be inherited from previous phases of deformation, their mechanical role is assumed to be minor relative to that of the larger-scale inherited collisional shear zone and for simplicity they are not considered in this study. A cold subduction-style thermal structure is approximated by the steady-state solution to the heat equation with boundary temperatures of 20 °C at the surface and 1300 °C at 200 km depth with zero heat flow on the sides. Moderate extension rates of 1.25 cm/yr are applied to the lithosphere (0.625 cm/yr to each side) and distributed inflow of mantle asthenosphere replaces mass lost from lithospheric extension (Figure 2.1b). Rheological and frictional parameters closely follow those used in Wu & Lavier (2016) to allow more direct comparison of our models with previous models of crustal extension in the presence of a major weak zone. Crustal rheology is a combination of pressure-sensitive Coulomb frictional yield and temperature- and strain-rate dependent dislocation creep based on the flow law for plagioclase from Shelton & Tullis (1981) as given in Ranalli (1995), except in the tests of lower crustal strength (Appendix Figure A.5) where the activation energy is decreased for the lower 15 km of crust. Shear zone strength is varied by changing the cohesion or the activation energy of material within the 2 km thick shear zone. Pore-fluid pressure is approximated as hydrostatic in the brittle crust. Although fluid inclusions in some exhumed normal fault zones record short-term transient periods of elevated pore fluid pressure (Parry & Bruhn, 1990; Bruhn et al., 1994 and references within), these seismic-cycle timescale fluctuations are beyond the scope of this study and hence the hydrostatic approximation is most appropriate for longer-term

extensional deformation. While permeability at depth may decrease with the onset of ductility, our ductile flow law does not include a fluid pressure component. Mantle material behaves according to a Coulomb frictional yield criterion combined with a composite dislocation-creep and diffusion-creep flow law for wet olivine from Hirth & Kohlstedt (2003) and Kirby & Kronenberg (1987). Table 2.1 lists parameter values used for model runs testing the effect of slab dip angle, shear zone cohesion, shear zone viscous strength, and lower crustal strength on the model setup shown in Figure 2.1b. More details of the numerical method, thermal structure, material properties and model parameters are in Appendix A.

The model setup is based on post-breakoff conditions of previous large-scale slab-breakoff models (Duretz et al., 2011; 2012; Duretz & Gerya, 2013; Petersen & Buck, 2015). In particular, this setup approximates immediate post-breakoff conditions of the strong felsic granulite crustal model of Duretz & Gerya (2013). If interpreted in terms of breakoff processes, our setup most closely resembles the conditions when thermomechanical thinning of the slab has fully separated the two slab segments, but before any significant isostatic rebound or extension has occurred. However, because our setup does not include an attached or detached oceanic slab, it does not test the mechanism by which collision ceased. Therefore, our models may equivalently represent extension of a jammed continental subduction margin where relatively little oceanic lithosphere was subducted before the continent entered the trench, a tectonic configuration more similar to that recently proposed for (U)HP eclogite exhumation along the Austroalpine-Pennine boundary in the central Alps (Price et al., 2018).

a. Values for physical parameters used in thermomechanical modeling						
Description		Symbol	Value			
Continental crust						
Density		ρ	2700 kg m ⁻³			
Upper limit of strain-softening		ϵ_f	0.1			
Initial angle of internal friction		θ_0	30°			
Final angle of internal friction		θ'	15°			
Cohesion		C	40 MPa			
Shear modulus		μ	25 GPa			
Pre-exponential constant		A	0.125 MPa ⁻ⁿ s ⁻¹			
Flow-law exponent		n	3.05			
Activation energy		E_a	276 kJ mol ⁻¹			
Activation volume		V	0 m ³ mol ⁻¹			
Grain-size exponent		m	0			
Ultramafics- all values of continental crust, except:						
Density		ρ	3100 kg m ⁻³			
Shear zone- all values of continental crust, except:						
Cohesion		C	4 MPa			
Activation energy		E_a	236 kJ mol ⁻¹			
Sediments- all values of continental crust, except:						
Cohesion		C	1 MPa			
Mantle lithosphere- all values of continental crust, except:						
Reference density at 273 K		ρ_0	3330 kg m ⁻³			
Pre-exponential constant		A	7.0 x 10 ⁴ MPa ⁻ⁿ s ⁻¹			
Flow-law exponent		n	3.0			
Activation energy		E_a	520 kJ mol ⁻¹			
Mantle asthenosphere- values of mantle lithosphere, except:						
Reference density at 273 K		ρ_0	3300 kg m ⁻³			
<i>Mantle asthenosphere, dislocation creep parameters:</i>						
Pre-exponential constant		A	1.5 x 10 ⁻²⁴ MPa ⁻ⁿ s ⁻¹			
Flow-law exponent		n	1.0			
Activation energy		E_a	335 kJ mol ⁻¹			
Grain size		d	10 μ m			
Grain size exponent		m	3.0			
Activation volume		V	4 x 10 ⁻⁶ m ³ mol ⁻¹			
<i>Mantle asthenosphere, diffusion creep parameters:</i>						
Pre-exponential constant		A	5.33 x 10 ⁻⁴⁰ MPa ⁻ⁿ s ⁻¹			
Flow-law exponent		n	3.5			
Activation energy		E_a	480 kJ mol ⁻¹			
Activation Volume		V	11 x 10 ⁻⁶ m ³ mol ⁻¹			
b. Parameters varied in sensitivity tests (see figures in Appendix B)						
Figure Number:	Slab dip (°)	Shear zone cohesion (MPa)	Shear zone activation energy (kJ mol ⁻¹)	Lower crust activation energy (kJ mol ⁻¹)	Extension rate (cm yr ⁻¹)	Mode
B.1	30, 45, 60	4	236	276	1.25	2, 2, 1
B.2	60	4, 20, 40	236	276	1.25	1, 1, 3
B.3	60	4	176, 236, 276	276	1.25	1, 1, 3
B.4	60	4	226, 276, 305	176	1.25	1, 3, 3
B.5	60	20	276	176, 226, 276	1.25	3, 3, 3

Table 2.1. a.) Mechanical parameter values used in thermomechanical models shown in sections 2.2 and 2.3. Thermal parameters are shown in Figure 2.1. b.) List of model experiments discussed in Section 2.2. The final column lists the predicted extensional mode for each of the three model variants described in each row, respectively.

2.2.3. Results: three extensional modes

The range of parameters in Table 2.1 produce models that fall into three distinct modes of crustal extension. Weak steeply-dipping inherited shear zones develop into sustained rolling-hinge LANF systems (Mode 1) while strong shallowly-dipping contacts lead to shear zone abandonment and rifting through the hanging wall of the inherited shear zone (Mode 3). Weak or intermediate-strength shallowly dipping shear zones lead to ‘domino’-style faulting (Mode 2) where high-angle hanging-wall faults form above the active detachment as the footwall isostatically bows upward with continued extension. In this section we first describe the general features of each mode and which inherited mechanical conditions lead to which mode. The following three sections provide a detailed look at a representative example model of each mode.

In Mode 1 (Figure 2.2), deformation localizes on the pre-existing subduction thrust, which rebounds with progressive displacement to dip at lower angles in the upper 5 km and higher angles through the rest of the crust. As mantle compensation beneath the shear zone restores the originally deflected Moho to subhorizontal with continued extension, the footwall exhumes along the shear zone by a rolling-hinge mechanism until either a self-sustaining rolling-hinge detachment develops or upwelling asthenosphere focused along the ductile shear zone reaches the surface, marking full rift initiation (not shown in Figure 2.2). In Mode 2 (Figure 2.3), extension initially activates the inherited low-angle subduction thrust, but the rate of vertical upwelling of lower crust outpaces the accommodation of horizontal extension by fault slip, rotating the fault to subhorizontal above the brittle-ductile transition, misaligning it for subsequent slip, and activating new high-angle faults in the hanging wall (Figure 2.3a). The original shear zone in the upper crust is abandoned, however slip is still localized along it at depths below the brittle-ductile transition (Figure 2.3b). Mode 3 (Figure 2.4) represents the case where high-angle normal faults immediately cross cut the hanging wall and eventually develop a near-symmetric rift with focused upwelling beneath the rift axis. In Mode 3 the inherited subduction thrust shear zone never accommodates significant offset.

Sensitivity tests (Table 2.1; Appendix Figures A.1 – A.5) reveal three prominent controls on these extensional modes: 1) shear zone brittle strength, 2) shear zone viscous strength, and 3)

initial slab dip angle. An inherited shear zone with identical material properties to the surrounding crust yields immediate Mode 3 rifting, whereas a steeply dipping low-cohesion shear zone facilitates Mode 1 rolling-hinge development. Mode 2 is an intermediate style which arises when the pre-existing shear zone is not so strong or steeply-dipping as to lock up immediately, but is not so weak or steeply-dipping as to fully accommodate all crustal strain over millions of years (Figure 2). In models where the brittle portion of the shear zone is eventually abandoned, subsequent narrow rift faulting may include some continued localized offset on the inherited shear zone or may fully transition to newly developed extensional arrays, depending on the shear zone viscous strength. A shear zone with identical viscous rheological properties to the surrounding crust promotes new rifting through the footwall, while continued offset on a viscously weakened pre-existing shear zone focuses asthenospheric upwelling beneath that shear zone until a rift is initiated that is bounded on one side by the original shear zone (Appendix Figure A.4).

Initial slab dip affects the longevity of slip on the inherited shear zone vs. initiation of new high-angle normal faults, and determines whether upwelling mantle asthenosphere focuses directly beneath the exhuming footwall or migrates towards the hanging wall (Appendix Figure A.1). Steep initial dips promote Mode 1 rolling-hinge development because localized upwelling directly beneath the footwall helps exhume the brittle upper portion of the footwall as a coherent block, and because the steeper attitude of the fault at depth remains mechanically well oriented for continued slip on the inherited structure (Appendix Figure A.1). By contrast, shallowly-dipping initial faults tend to focus upwelling away from the trace of the original fault, beneath the hanging wall, causing a transition to Mode 2 or Mode 3 rifting as new high-angle fault arrays cut above the upwelling material (Figures 2.4a, 2.4b and Appendix Figure A.1).

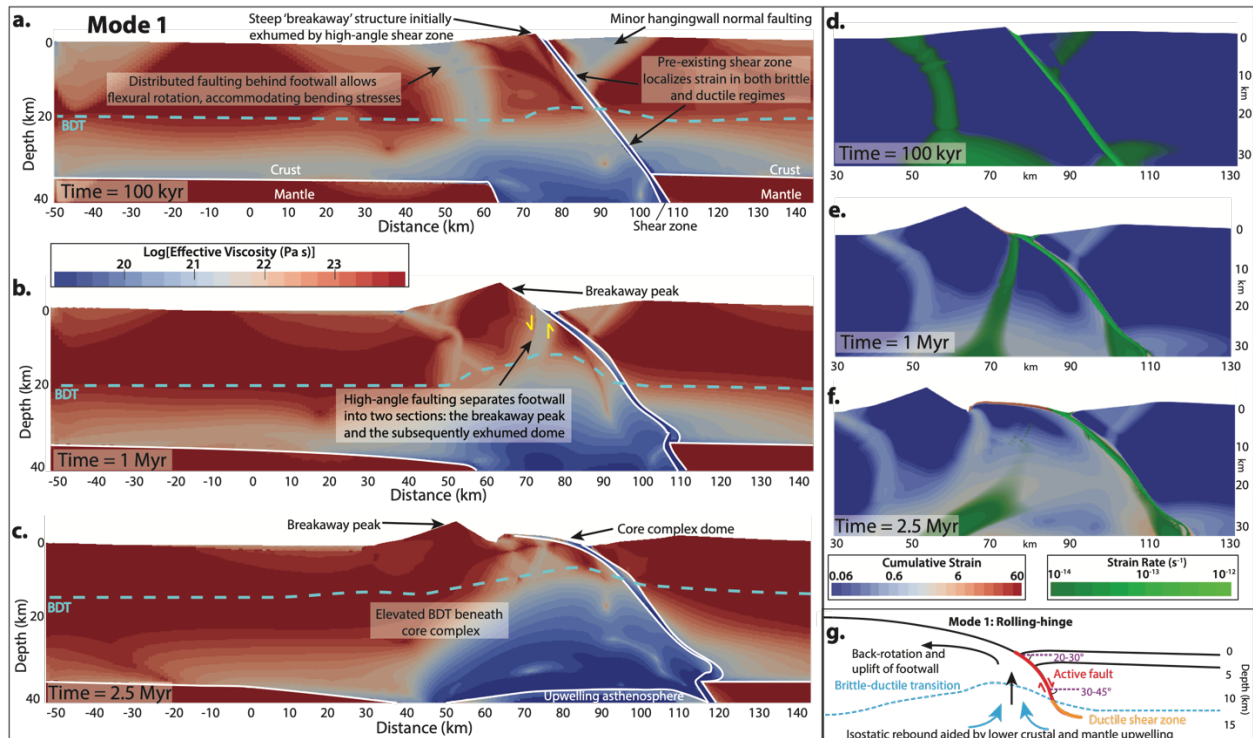


Figure 2.2. Mode 1 extension with initial shear zone dip of 60° . Crustal rheology follows a dislocation creep plagioclase flow law from Ranalli (1995) and initial brittle strength is given by cohesion of 40 MPa and internal friction angle of 30° , softening linearly to 15° over strains of 0.1. The pre-existing shear zone's activation energy is lowered by 15% and its cohesion is lowered to 4 MPa. Other material properties are in Table 1. Log10 of effective viscosity is plotted after a. 100 kyr; b. 1 Myr; c. 2.5 Myr. White lines outline regions of different material properties. Dashed blue line shows position of the brittle-ductile transition (BDT), estimated by the depth at which the minimum yield stress transitions from plastic failure to dislocation or diffusion creep. Yellow arrows show sense of offset on faults between dome and breakaway. d,e,f) Cumulative strain overlain by strain rate (for strain rate $> 10^{-14}$) at 100 kyr, 1 Myr, and 2.5 Myr. e) Interpretative schematic cartoon of Mode 1 style deformation.

2.2.3.1. Mode 1: High-angle inherited shear zone develops a rolling-hinge

A representative Mode 1 model with initial slab and fault dip of 60° is presented in Figures 2.2a-f. During early stages of extension, the exhumed footwall morphology is strongly controlled by the initial fault geometry (Figure 2.2a,d). For the steeply-dipping fault case shown here, a sharp 'breakaway peak' forms, bounding an uplifted part of the footwall that continues to exhume along the fault after 1 Myr (Figure 2.2b,e). Rapid exhumation along the originally steep fault is

concurrent with flexural back-rotation of the footwall. In our model, this rotation is partially accommodated by slip on a short-lived high-angle crustal fault that is located between the breakaway and the main normal fault, and that has a sense of dip-slip antithetic to the main normal fault. Flexural rotation occurs only in the uppermost brittle crust, while the weaker (ductile) lower crust flows beneath the footwall in response to upper crustal extension, helping decouple upper crustal deformation from the underlying mantle lithosphere. The shear zone itself begins to bend to a convex-up geometry by gradual shallowing of the near-surface portion (Figure 2.2b,e). Minor normal faulting in the hanging wall above the upper 15 km of the fault initially accommodates some extension (Figure 2.2a,d); however, these faults lock up after about 2 Myr once brittle strain fully localizes onto the original (now normal-sense) shear zone.

From 1-2.5 Myr, the shear zone warps further, and the growing offset along the shear zone begins to exhume footwall crust at a much lower angle to the surface, exhuming less topography than that created by the initial fault offset. Displacement on the curved shear zone facilitates a back-rotation of the coherent footwall block, which by 2.5 Myr exhumes a smooth dome (Figure 2.2c,f). Exhumed fault material on top of the dome is subhorizontal while earlier exposed fault material farther up the dip of the exhumed fault plane has back-rotated to achieve a dip direction counter to that of the initial shear zone. From 1-2.5 Myr a series of near-vertical faults initiated near the fault trace detach the breakaway peak from the more recently exhumed domal footwall block, decreasing the elevation difference between these two sections of the footwall (Figure 2.2b,e). Distributed normal faulting in the upper half of the brittle, upper crustal “beam” of the footwall kinematically detaches the steep breakaway from the newly exhumed domal footwall section which continues to bend coherently (Figure 2.2c,f). This faulting is consistent with the ‘snapping’ mode of accommodation of footwall bending stresses predicted by Buck (1997). By 2.5 Myr (Figure 2.2c,f) the upper 10 km resembles the classic rolling-hinge system predicted by lithosphere-scale numerical models (e.g., Lavier et al., 1999, 2000). Asthenospheric mantle upwells beneath the footwall to depths of 35 km, separating stronger mantle lithosphere on the

footwall and hanging-wall sides and supporting the elevated topography of the extended crustal region and exhumed dome.

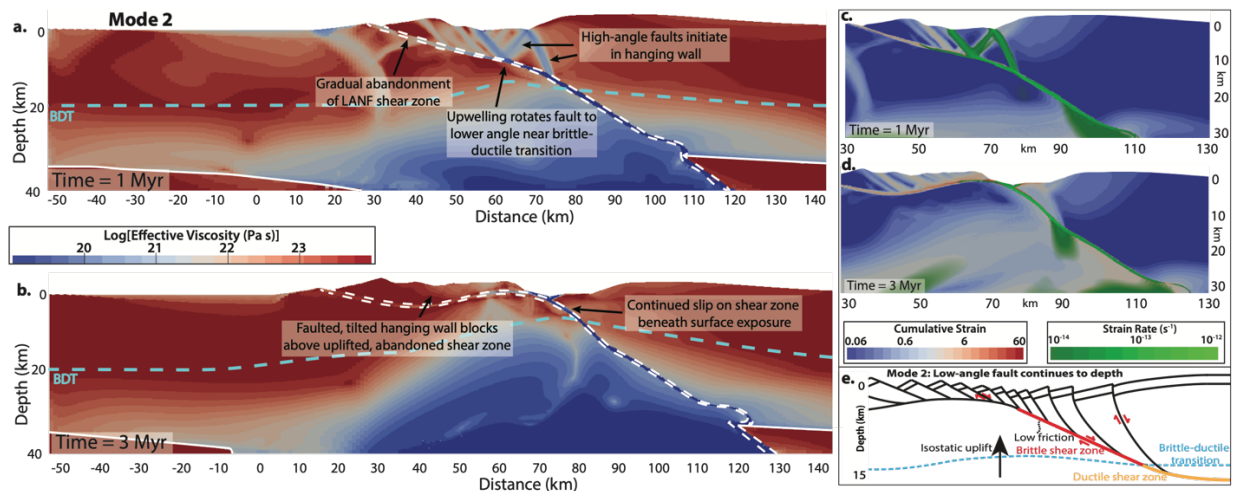


Figure 2.3. a,b) Representative Mode 2 example after 1 and 3 Myr of extension, respectively, showing log₁₀ of effective viscosity. White lines outline regions of different material properties and dashed white lines outline material originally in the inherited shear zone. Dashed blue line shows position of the brittle-ductile transition (BDT). The shear zone initially dips 30° with an internal friction angle of 25°, cohesion of 4 MPa, and viscous activation energy 25% lower than that of the surrounding crust. c,d) Cumulative strain overlain by strain rate (for strain rate > 10⁻¹⁴) at 1 and 3 Myr e) Interpretative schematic cartoon of Mode 2 style deformation.

2.2.3.2. Mode 2: Low-angle inherited shear zone leads to ‘domino’-style faulting

Mode 2 deformation arises from an inherited shear zone with low initial dip and low-to-intermediate strength. Strain localizes on the shear zone both above and below the brittle-ductile transition; however, new high-angle faults eventually cut through the hanging wall from about 10 km depth to the surface. This splay faulting accommodates much of the extension in the upper 10 km, cutting the upper 10 km of the near-fault hanging wall into a series of progressively rotated blocks (Figure 2.3) consistent with the classical assumption that the LANF continues to depth during MCC exhumation (Figure 2.3e) (e.g., Lister & Davis, 1989; Colletini, 2011; Whitney et

al., 2013). Shallow extension remains localized above the viscously deforming lower portion of the initial shear zone via serially initiated and abandoned high-angle hanging-wall faults. These faults cut a series of ‘domino’-style hanging-wall blocks which become back-tilted with continued offset and footwall warping. Beneath 10 km, strain remains localized on the original low-viscosity shear zone, and offset along this weak zone causes lower crust from the initially thickened crustal region to flow upwards into the footwall. This upwelling accompanies isostatic footwall uplift, which bends the initial shear zone to be convex-up beneath the active hanging-wall faults and concave-up beneath the abandoned back-tilted hanging-wall blocks by 1 Myr (Figure 2.3a,c).

From 1-3 Myr, the convex-up portion of the fault zone ascends as tectonic unroofing focuses vertical upwelling of lower crust beneath the footwall. The ascent of lower crustal material beneath the active convex-up shear zone portion accommodates back-rotation of the abandoned up-dip initial shear zone. This rotation leads to shallow and locally antithetic dip angles beneath the tilted hanging-wall block, and eventually to full abandonment of that segment. This warped detachment fault geometry (Figure 2.3b,d) has been predicted by previous models of detachment faults that penetrate to depth at a through-going low angle (e.g., Lister & Davis, 1989). Shallow deformation then fully localizes on the shear zone segment that has been bowed upward to dip at a slightly higher angle than the initial dip. Where sedimentation rates are low, this part of the fault is exposed at the surface by 3 Myr (Figure 2.3b,d). The shear zone remains active at a low dip angle below 20 km.

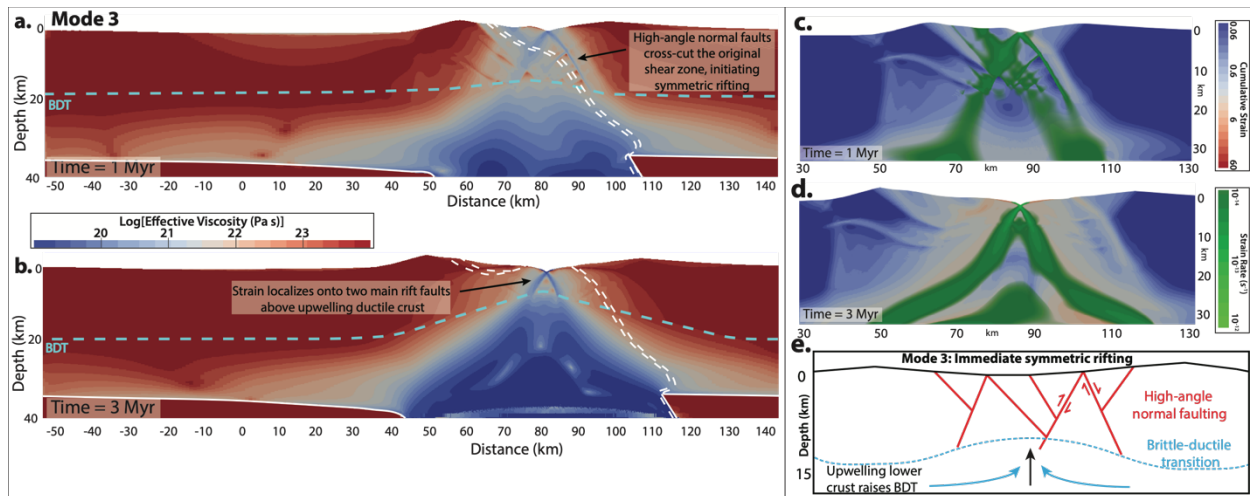


Figure 2.4. a,b) Representative Mode 3 example after 1 and 3 Myr of extension, respectively, showing log₁₀ of effective viscosity. White lines outline regions of different material properties and dashed white lines outline material originally in the inherited shear zone. Dashed blue line shows position of the brittle-ductile transition (BDT). The outlined ‘shear zone’ in this example dips 60° but has identical frictional and rheological properties to the surrounding crust. All other material properties and model parameters are as described in Table 2.1. c,d) Cumulative strain overlain by strain rate (for strain rate > 10⁻¹⁴) at 1 and 3 Myr. e) Interpretative schematic cartoon of Mode 3 style deformation.

2.2.3.3. Mode 3: Near-symmetric rifting of thickened crust

Strong initial shear zones lead to Mode 3 near-symmetric rift development initiated by high-angle normal faults penetrating through the brittle and ductile crust and cutting across the initial shear zone. The end-member Mode 3 scenario where the shear zone initially has identical frictional and rheological properties to the rest of the crust is presented in Figure 4. This setup may correspond to a margin where time-dependent fault-healing processes have removed any inherited weaknesses.

Mode 3 extension proceeds similarly to previously modeled extension of thick homogenous lithosphere, where numerous high-angle crustal faults initiate before strain-softening processes and progressive offset localize deformation onto two main high-angle rift faults dipping

opposite directions (e.g., Lavier & Buck, 2002; Huismans & Beaumont, 2007). Despite the absence of a weak initial shear zone, the weakest and most easily rifted part of the lithosphere in this Mode 3 example setup remains the thickened (i.e., partially subducted) crustal region. A series of high-angle faults above the thickened crustal margin, well-oriented for shear failure relative to the extension direction, accommodates extension above the brittle-ductile transition (Figure 2.4a,c), while flow of ductile lower crust and asthenospheric mantle into and beneath the nascent rift accommodates extension below 20 km depth. By 3 Myr, deformation localizes onto two main high-angle rift-bounding normal faults (Figure 2.4b,d). These faults focus upwelling of the lower crust beneath the emergent rift axis. Upwelling mantle asthenosphere flows into the region evacuated by the upwelling crustal material sourced from the original subducted continental slab. This mantle accommodation restores the originally deflected Moho to near-horizontal and reduces the magnitude of lateral crustal thickness variations relative to the initial configuration (Figure 4b,d).

2.2.4. Discussion of general model results

2.2.4.1. Shear zone strength and geometry

The strength and dip of the inherited shear zone strongly controls the modeled extension mode. This result suggests that the nature and geometry of inherited strength contrasts from preceding convergent phases are a major control on whether extension of jammed continental subduction margins exhumes MCCs along low-angle detachments or simply initiates a nearly-symmetrical continental rift via a series of newly formed high-angle normal faults. Wu & Lavier (2016) reached a similar conclusion regarding shear zone strength and extensional style in orogenically altered lithosphere; however, their modeled shear zones were imposed subhorizontally through the middle crust in all cases, allowing efficient decoupling between the upper and lower crust. Our results show that the geometries of weak faults or shear zones inherited

from preceding convergent phases also exert a strong control on the subsequent style of extension and rift development.

In our models, symmetric rifting by high-angle normal faulting occurs when the pre-existing shear zone is too shallow-dipping and/or too strong to allow extensional reactivation as a normal-sense detachment. Hence, if extension initiates soon after subduction ceases at a jammed collisional margin, the original subduction angle may partially control whether a long-lived detachment system develops during subsequent extension. A weak, well-oriented steeply-dipping inherited collisional thrust may be reactivated as a detachment shear zone and allow MCC formation in crust that may otherwise be too cold or strong to develop a large-offset detachment fault system. Additionally, because progressive fault healing may increase the strength of the shear zone, the time interval between convergent and extensional phases may also affect subsequent extension style (e.g., Salerno et al., 2016).

Perhaps counterintuitively, there is a range of brittle and viscous strengths for which an initial high-angle ($>45^\circ$) shear zone is more likely to develop into a sustained LANF system than an initial low-angle shear zone with identical material properties. The low-angle fault to depth is energetically unfavorable to the extent that new synthetic and antithetic high-angle faults initiate through the hanging wall, connecting to the low-angle portion near the brittle-ductile transition. Low-angle faults are less efficient at extensionally accommodating the rapid upward trajectories of lower crustal rocks from beneath the collision margin associated with the increased buoyant and isostatic stresses of the rapid transition from subduction to extension.

2.2.4.2. Removal of mantle lithosphere allows localization of extension

In addition to inherited faults, the thickened continental crust and thinned mantle lithosphere of the failed subduction margin also influence the thermomechanical evolution of the rift. The deeper subducted continental margin is the weakest part of the modeled lithosphere apart from the shear zone, due to the strong temperature-dependence of diffusion and dislocation creep.

Hence, when extension reactivates the weak shear zone, the upper crustal material removed above the thickened crust is replaced by upwelling ductile lower crust from the previously subducted margin. The mantle lithosphere beneath this region is too thin to prevent underlying mantle asthenosphere from upwelling towards the region of upwelling crust. These conditions progressively focus upwelling mantle asthenosphere through the steep ductile channel created by the remnant slab. In the Mode 1 models, these combined effects allow deep crustal footwall rocks to exhume along near-vertical trajectories until they reach the upper ~5 km of the crust, at which point their exhumation trajectories rotate to near-horizontal, following the curvature of the LANF. In some models, buoyant upwelling asthenosphere provides the underlying support of elevated MCC dome topographies in the early stages of continental rifting, as has been proposed for the D'Entrecasteaux Islands in Papua New Guinea (Abers et al., 2002).

Our models suggest that significant removal or thinning of mantle lithosphere beneath a collisional margin encourages focused, narrow extension and allows increased mechanical interaction between the asthenospheric mantle and the brittle crust. This result agrees with Manatschal et al. (2015) who showed that the most important factor controlling localization of extensional necking is the strength and structure of the strongest brittle layer, which is the upper mantle lithosphere in the case of a cold regional geothermal gradient. In addition to slab breakoff, other processes that alter or remove mantle lithosphere such as convective lithospheric delamination (e.g., Hales et al., 2005; Levander et al., 2011) or mantle erosion (e.g., Crow et al., 2011) may significantly influence the location of subsequent continental rifting. Additionally, recent modeling by Petersen & Schiffer (2016) and Balazs et al. (2017) has shown that penetrative weak zones in the mantle lithosphere can efficiently localize extensional strain without significant variations in mantle lithospheric thickness.

2.2.4.3. Rift width and mechanical decoupling in cold, strong lithosphere

One important feature of the initial model setup is the cold, subduction-style geotherm, representative of a rapid transition from convergence to extension (e.g., Duretz et al., 2011; 2012). Outside of the locally thickened collision zone, the crust remains too cold and strong to allow regional decoupling of the upper and lower crust from each other or from the mantle lithosphere. This coupled, cold crust is much stronger than that in the collision zone, so deformation focuses in a relatively narrow region. One implication of this behavior is that regions transitioning rapidly from subduction to extension may favor narrow rifting, whereas laterally broad thickened orogenic crust slowly transitioning to extension may be more likely to develop wide rift systems where lateral lower crustal flow and channelization are important processes facilitating crustal extension. This result agrees with that of Buck et al. (1999) who showed that wide rifts preferentially develop in wide regions of thickened crust with high heat-flow, where crustal thickness greatly exceeds brittle layer thickness.

For core complexes formed in hot, thick crust, the necessary mechanical decoupling between the upper and lower crust develops naturally due to the sharp strength contrast between the strong brittle upper crust and the weak, ductile lower crust (e.g., Rosenbaum et al., 2005; Whitney et al., 2013; Labrousse et al., 2016; Brun et al., 2018). These conditions are common in wide, thick orogenic systems which develop laterally pervasive layers of weak ductile lower crust with thickness of km to 10's of km (e.g., Wu et al., 2015; Wu & Lavier, 2016). Our model shows that an inherited shear zone can provide the necessary intracrustal strength contrast to decouple the upper and lower plates and allow core complex formation in lithosphere that would otherwise be too strong and cold for regional intracrustal mechanical decoupling. Wu & Lavier (2016) showed that mid-crustal shear zones could decouple the upper and lower crust in wide, hot orogenic margins, but our results expand upon theirs by showing that localized, short-lived core complex detachment systems are mechanically viable even in the absence of sustained lateral inflow of weak, ductile lower crust. In regions where preceding collisional lithospheric alteration has thinned the mantle lithosphere, buoyant upwelling mantle asthenosphere can fill the supporting

role typically played by weak lower crust in hotter MCC systems. In turn, mechanical decoupling of the crust need not be as laterally pervasive as previous models have implied; instead, locally inherited lithospheric structure can allow for short-lived core complex formation as a temporary phase of cold, narrow continental rifting. As predicted by models, a notable distinction between MCCs formed in strongly coupled, post-subduction lithosphere and those formed during broad orogenic collapse is that the former are expected to be more topographically conspicuous than the latter due to 1.) limited lateral evacuation of lower crust from beneath the exhumed footwall and 2.) buoyant mantle support associated with mantle-compensated, rather than crustally compensated, lithospheric thinning. Increased mechanical interaction between crustal detachments and mantle structure under cold conditions has also been predicted by models from Weinberg et al. (2007) that showed that mantle doming and crustal detachment faulting can occur spontaneously during extension of cold, laterally homogeneous continental lithosphere. Further work identifying inherited structures in ancient core complex systems and quantifying their mechanical strength may illuminate whether short-lived, rapidly exhumed core complexes are a common stage of lithospheric extension even in relatively cold and narrow continental rifts.

2.2.4.4. Elastic thickness, isostatic rebound and initial topography

One notable feature of the Mode 1 models is the large (up to 6 km tall) ‘breakaway’ peak exhumed during the first 1 Myr. This structure forms when the shear zone is weak and steep enough to direct most of the initial vertical isostatic adjustment into normal-sense offset along the shear zone. Large-scale topographically conspicuous breakaway peaks are not commonly observed near exhumed MCCs, because the lower plate crust is typically hot and weak enough to flow out from beneath the initially thickened breakaway section of the footwall towards the actively deforming detachment (e.g., Whitney et al., 2013). In cold lithosphere the lower crust is too strong to flow in compensation for this increased topographic load, and the breakaway structure is instead supported by the strong elastic strength of the cold lithosphere away from the actively rifting area (Appendix

Figure A.10). Although this effect explains why breakaway topography in cold detachment systems might be expected to exceed that of hot detachments, we note that the extreme breakaway topography predicted in our Mode 1 models may be exaggerated due to aspects of our initial conditions. As would be expected immediately following slab breakoff, the initial model configuration is out of isostatic equilibrium. Therefore, although applied extension modulates deformation rates in these models, much of the driving force behind the deformation stems from the buoyant force and isostatic rebound of the deeply subducted low-density continental crust. However, by not imposing any initial topography, our models likely exaggerate the magnitude of the vertical isostatic adjustment following slab breakoff. The simplified planar initial fault geometry may enhance this effect by directing a larger component of this isostatic adjustment into vertical fault offset than a more realistic curved subduction fault would. In section 2.3 we show that adjusting the initial model topography and using a curved initial fault geometry reduces the elevation of footwall exhumed in the first 1 Myr. Nonetheless, slab breakoff beneath relatively cold surrounding lithosphere is expected to form higher and more localized topography than breakoff beneath a wide region of hot, thick orogenic lithosphere.

2.3. NATURAL CASE STUDY: DAYMAN-SUCKLING METAMORPHIC CORE COMPLEX

The models in section 2.2 explored general controls on post-collisional extension style. We now examine a specific well-studied example of a post-collisional MCC: the Dayman-Suckling MCC (DSM) in SE Papua New Guinea, to evaluate whether collisional inheritance can explain the structural and thermomechanical history of a uniquely well-preserved MCC.

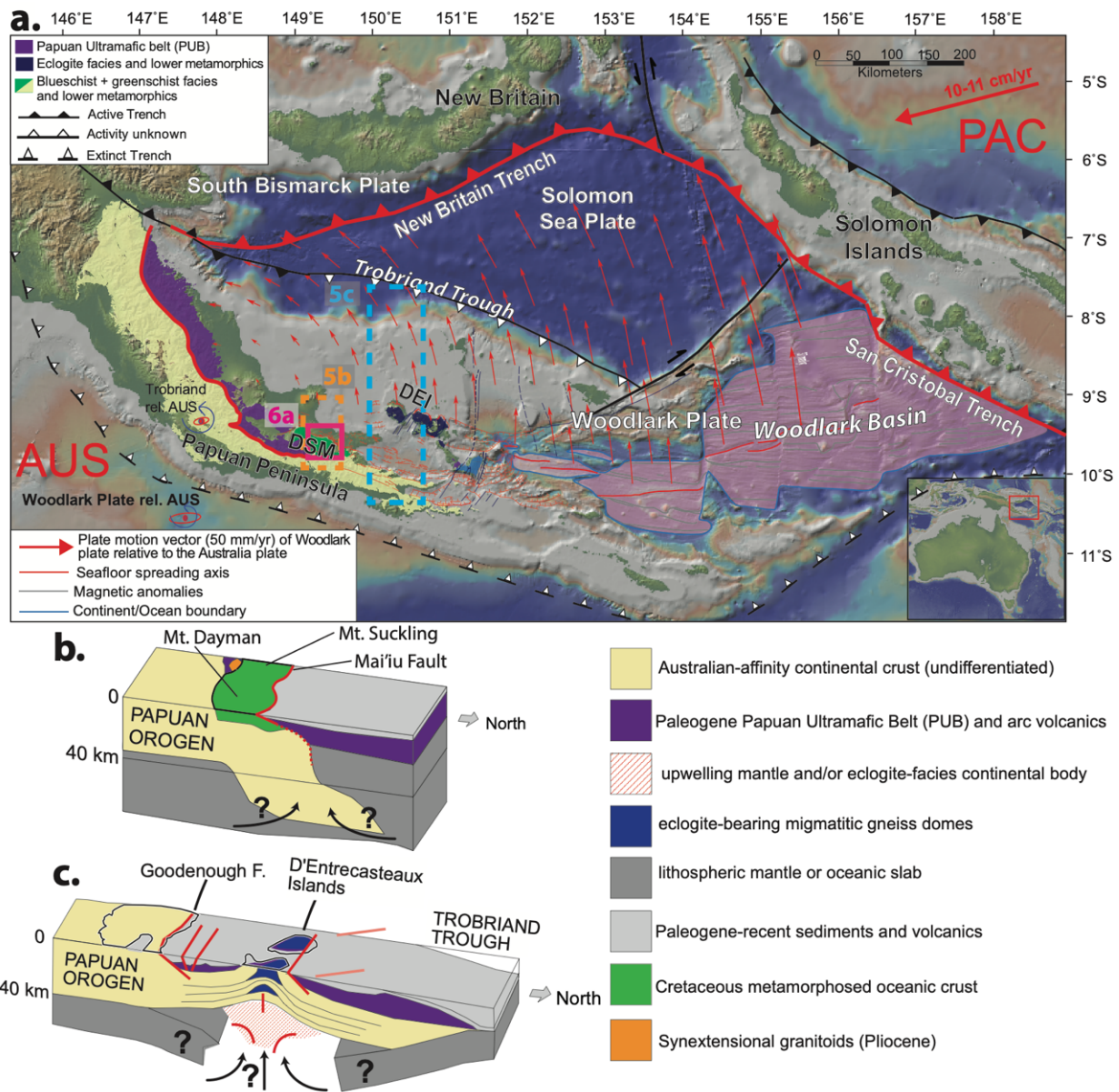


Figure 2.5. a. Regional tectonic map showing active and extinct subduction zones and spreading centers, microplate poles of rotation and Woodlark Plate velocities relative to a fixed Australian Plate (Wallace et al., 2014). Dashed orange and blue boxes show regions of Figure 5b and 5c, respectively. AUS = Australian Plate; PAC = Pacific Plate; DSM = Dayman-Suckling MCC; DEI = D'Entrecasteaux Islands; b. Interpretive cross-section through the DSM, drawn after Little et al. (2019); c. Interpretive cross-section through DEI drawn after Ellis et al. (2011). Black arrows show possible upwelling and flow patterns of upper mantle or lower crust.

2.3.1. Tectonic & geologic setting

Present-day northward subduction of the Solomon Sea plate at the New Britain and San Cristobal trenches drives active microplate rotation and local extension in the Woodlark Rift within an overall zone of convergence between the Pacific and Australian plates (Wallace et al., 2014). The Woodlark Rift is a young, active rift accommodating extension of 10-15 mm/yr in its western continental portion in the Papuan Peninsula and 20-40 mm/yr in its offshore eastern oceanic portion in the Woodlark spreading center (Wallace et al., 2014). Rifting was preceded by multiple phases of Cenozoic subduction, obduction, and orogenesis (e.g., Davies, 1980; Cloos et al., 2005; Baldwin et al., 2012; Holm et al., 2016; Little et al., 2019). Although seafloor spreading in the Woodlark basin began by 6 Ma, the timing of the initiation of onshore continental extension farther west, in the region of the DSM, is still under debate (e.g., Baldwin et al., 2012; Holm et al., 2016; Little et al., 2019). Extension has rapidly exhumed two distinct types of MCCs along this plate boundary: the D'Entrecasteaux Islands gneiss domes offshore the easternmost portion of the Papuan Peninsula, and the DSM further west within the peninsula (e.g., Baldwin et al., 2012).

The DSM includes three high peaks in the Owen-Stanley Ranges: Mt. Dayman, Mt. Suckling, and Mt. Masasoru (Figure 6). The exposed culminations range from 1700 to 3576 m elevation and vary in their degree of erosion (Mizera et al., 2019). The actively uplifting DSM (Ollier & Pain, 1980; Miller et al., 2012) is bounded to the North by the Mai'iu fault, an active LANF that dips NNE on average $\sim 21^\circ$ to the surface (Mizera et al., 2019) and accommodates 7-9 mm/yr of horizontal extension (Wallace et al., 2014) with long-term along-dip slip rates (1000 year timescales) of 8.2-15.2 mm/yr (Webber et al., 2018). Near the 2950 m tall Mt. Dayman, exhumed remnants of the Mai'iu fault are found 30 km up-dip from the fault trace in the slip direction, recording accumulated slip of similar magnitude (Mizera et al., 2019). Normal slip initiated by at least 3.3 Mya as evidenced by the age of the synextensionally intruded Suckling Granite (Daczko et al., 2011). Rapid exhumation of footwall rocks from original depths of ~ 25 km along the Mai'iu fault from circa 3 Mya is inferred to have occurred by the rolling-hinge mechanism based on a host of tectonically tilted geomorphic features, progressive back-arching of

foliation in the footwall, the convex-up shape of the exposed Mai'iu fault surface, the 30-40° alignment of microseismicity down-dip of the Mai'iu fault trace, and bedding-fault cutoff angles of up to 40-50° in former hanging-wall sediments that have been uplifted and eroded as part of an abandoned rider block (Spencer, 2010; Abers et al., 2016; Webber, 2017; Mizera et al., 2019; Little et al., 2019).

The footwall is composed of the Kutu Volcanics and Goropu Metabasalt (Davies, 1980; Daczko et al., 2011; Little et al., 2019), a 4-5 km-thick sequence of marginal basaltic oceanic rocks emplaced southward over the felsic crust of the Australian continental margin in Post-Middle Eocene to possibly Late Miocene time (Davies and Jacques, 1984; Little et al., 2019). Late Neogene, greenschist-facies extensional mylonitic fabrics in the Goropu Metabasalt formed at depths of 20-25 km and temperatures of ~425°C (Daczko et al., 2009). The hanging wall consists of oceanic-affinity lithosphere (Papuan Ultramafic Belt) capped by an eastward thickening, >2 km thick sequence of fluvial to shallow marine sedimentary rocks (Davies & Smith, 1971; Webber, 2017). DSM formation has been attributed to reversal and extensional reactivation of the main thrust of the preceding subduction episode (the Owen-Stanley fault of Davies, 1980). The transition from subduction to extension is inferred to have occurred rapidly and with little to no intervening lag time, based on observations that DSM metamorphics did not reach higher-temperature facies expected for equilibrated post-subduction geothermal gradients (Davies, 1980) and based on low exhumational geothermal gradients (~8°C/km) required by P-T-t measurements from coesite-eclogites from the nearby D'Entrecasteaux Islands (Monteleone et al., 2007; Baldwin et al., 2008; Webb et al., 2008), as well as low geothermal gradient (~18°C/km) in much of the current Woodlark rift, as measured in drill holes and from seafloor heat flow data (Martinez et al., 2001).

Geophysical and geological observations provide valuable constraints on past and present lithosphere conditions beneath these actively exhuming MCCs. Scattered offshore microseismicity 20-50 km NNE of the Mai'iu fault trace between 12-25 km depth have been inferred to delineate an active part of the Mai'iu fault dipping north at 30-40° (Abers et al., 2016). Seismic tomography

shows removal of most or all mantle lithosphere beneath the continental rift (Eilon et al., 2015; 2016), and receiver function analysis reveals varying crustal thickness from ~20 km beneath the D'Entrecasteaux Islands to ~35 km beneath the DSM (Abers et al., 2016). Overall, these observations illustrate a rapidly deforming, narrow, young, and mostly cold continental rift.

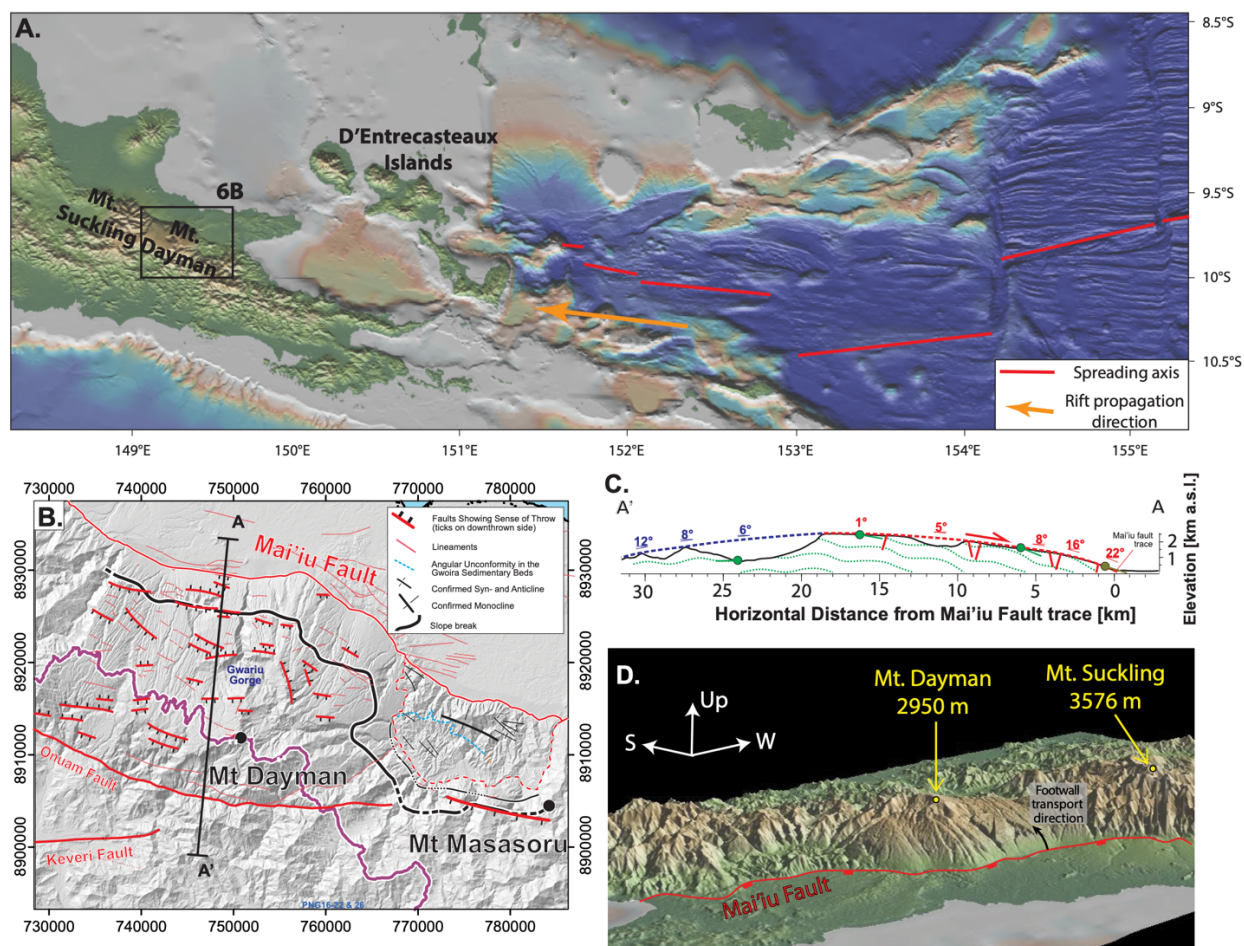


Figure 2.6: a. Simplified map showing spatial relationship between Woodlark spreading centers and the DSM. b. Hillshade DTM of Mt. Dayman area from Figure 2.6a showing mapped antithetic and locally synthetic faults cutting the footwall of the DSM, adapted from Mizera et al. (2018); c. Elevation profile of transect A'-A from Figure 2.6b with representative mapped footwall faults and back-warped footwall foliations; d. Oblique view of the DSM and Mai'iu fault, from 90m SRTM data and GeoMappApp (<http://www.geomappapp.org>).

2.3.2. Application of our model to the Dayman-Suckling MCC

The Mode 1 model (Figure 2.2) matches many key features of the DSM and Mai'iu fault, including exhumation of rocks from 25 km depth by a rolling-hinge process under extension rates of ~ 1 cm/yr. Observations from the DSM do not agree well with the structural style and surface morphology predicted by Mode 2 or 3 models. Mode 2 systems develop a series of domino-style abandoned, back-rotated hanging-wall rider blocks stranded atop the convex-up footwall, but Mt. Dayman exposes a smooth domal surface unadorned by rider blocks. Mode 3 models predict nearly symmetric high-angle normal faulting as the main mechanism of brittle crustal strain accommodation, whereas the Mai'iu fault is a single, shallowly dipping normal fault that appears to accommodate most of the extension that has exhumed the DSM. Of the modeled deformation modes, Mode 1 most closely matches the style of extension and exhumation in the DSM. Therefore, we use the Mode 1 example (Figure 2.3) as the base model setup for the DSM, which we now tune with region-specific features to more accurately represent lithospheric conditions around the DSM. The goal of constructing a model specific to the DSM is to test whether the inheritance models (Section 2.2) can be refined to approximate the observed features of a specific MCC, and thus inform our understanding of its evolution. Thus, we do not attempt to fully explore the parameter space with further sensitivity tests. The highly unique model presented below offers one explanation for the formation of the DSM, but it certainly does not rule out other formative mechanisms.

2.3.2.1. DSM-specific model

Simple modifications (Figures 2.7a and 2.7b) are applied to the Mode 1 example model setup (Figure 2.2a) in an attempt to more accurately incorporate inferred pre-extension lithospheric conditions around the Papuan Peninsula. First, the inherited weak zone in the upper 10 km is curved to reflect a more realistic subduction-phase geometry, steepening to 45° below 10 km. Initial topography is calculated for each column of elements to approximate isostatic balance using

a reference density of 3200 kg/m^3 . The upper 7 km of the lower plate is metabasaltic to simulate the Kutu-Goropu basaltic slab that was obducted onto the Australian continent during the convergent phase. This metabasaltic slab extends to 30 km depth in the collision zone, as required by 30 km slip-parallel exposures of basaltic footwall rocks on the DSM; however, the exact maximum depth to which Kutu Volcanics were subducted is not well-constrained. The contact between the basaltic slab and the underlying Australian-derived continental crust is represented by a 1 km thick interface with intermediate brittle and viscous strengths between those of intact crust and those of the main inherited shear zone. Additionally, the modeled hanging wall is of oceanic affinity, represented by a 7 km layer of basaltic oceanic crust atop a 15 km thick collisional assemblage of ultramafic crust and mantle lithosphere (the Papuan Ultramafic Body, PUB). This assemblage follows the wet olivine dislocation creep flow law of Hirth & Kohlstedt (2003) used for mantle lithosphere, but has a density of 3100 kg/m^3 . This upper plate composition is supported by the observation that the D'Entrecasteaux Islands (U)HP core rocks exhumed through a carapace of PUB rocks, indicating that the upper plate is at least partially composed of dense ultramafics (e.g., Little et al., 2007; 2011). However, the presence and abundance of PUB rocks north of the Mai'iu fault trace and the overall composition of the upper plate there is uncertain, as shear-wave velocities from teleseismic experiments are inconsistent with throughgoing ultramafics in the upper 20 km (Abers et al., 2016). Therefore, we also tested models where the upper plate consisted of more felsic, continental-affinity rocks (Appendix Figure A.12), which showed little difference in the structural evolution of the exhumed footwall dome. Figures 2.7a and 2.7b show the preferred model setup.

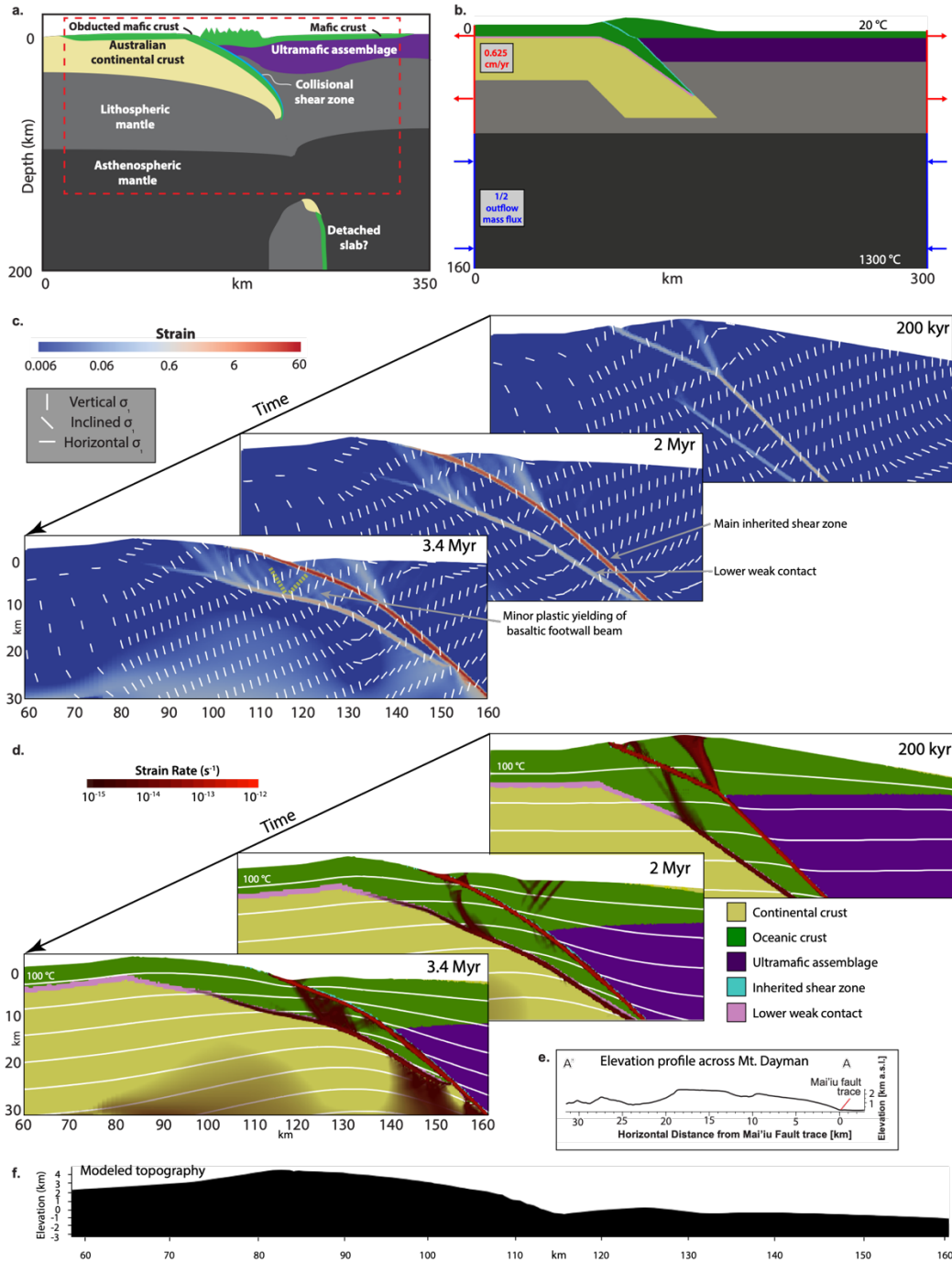


Figure 2.7. a.) Cartoon of inferred pre-extensional configuration for SE Papua. b.) Numerical model setup of a. c) and d): Plots of (c) modeled strain (colors) and maximum compressive principal stress (σ_1) directions (white lines) and (d) material properties overlain by strain rate (for strain rate $> 10^{-15}$) at 200 kyr, 2 Myr, and 3.4 Myr. White lines show isotherms in 100 °C increments. Inferred shear band orientations shown by yellow dashed lines in c. e. Slip-parallel topographic profile of Mt. Dayman, location shown in 2.6b. f.) Modeled topography at 3.4 Myr extracted from 2.7c.

2.3.2.2. *DSM model results*

Crustal strain initially localizes onto the inherited shear zone. A steep normal fault initiates through the upper 7 km of the upper plate down to the steeper portion of the inherited shear zone. Although this type of faulting is similar to that which forms a rider block, this fault is mostly abandoned by 1 Myr as strain localizes onto the inherited shear zone and the rider block candidate subsequently subsides with the rest of the hanging wall. Minor conjugate shear bands form in the upper 10 km of the metabasaltic footwall unit (Figure 2.7c, third panel; Appendix Figure A.9). Near-vertical orientations of the maximum in-plane principal stresses (σ_1) suggest that these structures reflect extensional failure. These small structures fully cut the metabasaltic slab, but do not penetrate into the underlying continental crust, instead terminating at the lower weak contact between the emplaced basaltic slab and the underlying continent. Although strain rates on this lower contact nominally exceed those of the surrounding crust, they are minimal compared to those on the main fault. Hence, we use ‘footwall’ to refer to the Goropu mafic layer (green in Figure 2.7d) plus the underlying felsic continental crust (yellow); and ‘hanging wall’ to refer to the upper plate assemblage of oceanic lithosphere (purple) and accumulated sediments.

Initial footwall exhumation follows the shallowly dipping upper segment of the inherited shear zone, so no distinct breakaway structure forms (see Section 2.2.3). With progressive offset, the shear zone bends to a more consistent curvature, dipping $\sim 22^\circ$ at the surface and flattening to $\sim 38^\circ$ below 15 km by 3.4 Myr. Near-vertical ductile flow of the deeply subducted continental crust accompanies continued fault offset, while the lower continental crust away from the shear zone remains too cold and strong to flow freely. After 3.4 Myr of extension, a smooth 4 km tall dome has exhumed, spanning a 30 km width in the extension direction. The maximum in-plane principal stresses (σ_1) in the fault-adjacent footwall rocks are subvertical or at a high angle to the fault plane, but in the subaerially exposed footwall up-dip they rotate anticlockwise to plunge only $\sim 20\text{-}30^\circ$ from the horizontal.

2.3.3. Comparison of DSM model to geological and geophysical observations

Our model results at 3.4 Mya agree well with exhumation of greenschist-facies rocks at the base of the DSM from ~20-25 km depth and ~425°C (Daczko et al., 2009). Modeled exhumation is mainly due to continued fault offset; however, isostatic footwall uplift aids the rapid vertical exhumation. Rocks at the main divide of the modeled dome structure at 3.4 Myr were originally adjacent to the trace of the inherited shear zone, as is consistent with exhumed remnants of the Mai'iu fault surface being found 30 km up-dip of the fault trace (Mizera et al., 2019). The modeled footwall exhumes through a rolling-hinge process as indicated by the progressively increasing upward convexity of the detachment, as suggested by topographic and geological field observations (Spencer, 2010; Webber, 2017; Mizera et al., 2019; Little et al., 2019).

Mappable structures on Mt. Dayman record a syn-extensional footwall stress history that features distinctive transitions in principal stress orientation during exhumation (Mizera et al., 2019). Brittle and ductile structures that are observed geologically on the DSM record both: 1) fault slip-parallel σ_1 (slip-parallel compression); and 2) a strongly compressive σ_2 that is sub-parallel to fault strike (i.e., with $\sigma_2 \sim \sigma_1$, Mizera et al., 2019). The exhumed footwall foliation in the dome is overprinted by a late-stage, sub-vertical crenulation foliation that strikes sub-parallel to the Mai'iu fault. This foliation records a late increment of post-exhumation, subhorizontal slip-parallel shortening (1). In addition, strike-parallel compression (2) occurs both at depth and near the surface, as evidenced by brittle and ductile deformation structures that deform the mylonitic fabric, and by post-exhumationally amplified, fold-like megacorrugations that are active in the landscape; these have hinges trending subparallel to slip (Webber, 2017; Little et al., 2019). The implied stress states corresponding to 1) and 2) might at first seem perplexing, but are consistent with stresses created in the model. In the model, there is a shift from a steep σ_1 in the subsurface footwall of the fault, to a sub-horizontal σ_1 in the upper exhumed part of the footwall (Figure 2.7c). This transition from slip-parallel extension in the footwall at depth to slip-parallel contraction in the near-surface, exhumed part of the footwall has been presaged by previous kinematic models

of flexural deformation accumulating near a rolling hinge (e.g., Manning & Bartley, 1994; Axen & Bartley, 1997).

Overall, the modeled development of a curved fault which dips $\sim 45^\circ$ at depth and $\sim 20^\circ$ at the surface generally agrees with geological and geophysical observations of the Mai'iu fault and the domal shape of the DSM. Offshore microseismicity from 12-25 km depth has been inferred to delineate the Mai'iu fault steepening to a dip of $30\text{-}40^\circ$ from 20-25 km depth (Abers et al., 2016; Little et al., 2019). At 3.4 Myr the modeled fault dips $\sim 38^\circ$ below 15 km, in agreement with this interpretation. Rotation to a shallower dip by progressive fault bending in our model accords with sedimentary cutoff angles of up to $45\text{-}50^\circ$ in the Gwoira rider block which record the original dip of the Mai'iu fault (Webber, 2017; Little et al., 2019).

2.3.4. Implications for Woodlark Rift development

Continental MCCs typically form in broad regions of hot, thick crust, and are exhumed along long-lived detachments which remain active with the assistance of ongoing replacement of extensionally removed upper crust by lateral inflow of weak ductile lower crust (e.g., Whitney et al., 2013 and references therein). By contrast, receiver function analysis reveals that areas south and east of the DSM have crustal thickness < 35 km (Abers et al., 2016), and a variety of geological and geophysical evidence (see section 2.3.2) implies a low geothermal gradient outside of the rift axis (Martinez et al., 2001; Ruprecht et al., 2013; Eilon et al., 2015; 2016; Abers et al., 2016). Therefore, it is unlikely that a broad region of thick, hot continental crust existed prior to the onset of Woodlark extension; rather, a laterally local (~ 50 km wide) area of thickened crust formed during subduction of the Goropu metabasalt and subsequent attempted subduction of Australian continental crust. Hence, the Mai'iu fault may not be a 'perennial' detachment maintained by lateral lower crustal flow. Instead it may represent the relatively short-lived crustal response to post-collisional equilibration of locally thickened continental crust and thinned mantle lithosphere concurrent with a change to extensional boundary conditions associated with the incipient arrival

of a fast-propagating narrow rift tip. As modeled, this process would be accompanied by upwelling of buoyant mantle asthenosphere beneath the thinning MCC footwall. Although isostatic adjustment involving near-vertical lower crustal flow may have assisted initial subaerial exhumation of the DSM, its current ~2-3.5 km topographic relief may instead or in part be supported by buoyant upwelling asthenosphere, as has been suggested for the DEI (Abers et al., 2002). Whether differences in structural style and exhumation history between the DSM and DEI reflect different self-similar stages of the westward propagating Woodlark Rift or have resulted from different pre-extension lithospheric conditions is a compelling question which remains to be tested by high-resolution 3D models or another 3 Myr of observation.

2.4. CONCLUSION

Numerical models simulating a rapid transition from continental subduction to extension predict three distinct extensional styles which strongly depend on the strength and geometry of the shear zone inherited from the subduction phase. Notably, one style involves exhumation of a domal metamorphic core complex along a rolling-hinge trajectory, suggesting that inherited intracrustal zones of weakness can facilitate core complex formation in lithosphere that would otherwise be too cold and strong to sustain a detachment fault system and allow core complex formation. A regionally specific variant of this model matches key geophysical and geological observations from the Dayman-Suckling metamorphic core complex in Papua New Guinea, suggesting that inheritance of a weakened collisional shear zone may explain the formation of these core complexes within a relatively narrow and cold incipient continental rift.

Chapter 3: Earthquake supercycles as part of a spectrum of normal fault slip styles

Copyright statement: An edited version of this paper was published by AGU. Copyright 2017 American Geophysical Union.

Biemiller, J., & Lavier, L. (2017). Earthquake supercycles as part of a spectrum of normal fault slip styles. *Journal of Geophysical Research: Solid Earth*, 122(4), 3221–3240.
<https://doi.org/10.1002/2016JB013666>

ABSTRACT

Like thrust boundaries in subduction zones, some normal faults show evidence of temporally transient slip patterns, such as temporally clustered earthquakes or periods of elevated creep-rate. We create rate-and-state friction numerical models to assess whether typical distributions of frictional parameters can explain transient slip on normal faults. We constrain our models with geometry from the Wasatch Fault Zone, where 5-10 kyr timescale earthquake clusters are recorded on fault scarps. We use numerical models to test whether these earthquake clusters could be the geologic representation of ‘supercycles’ which we define as long-period stress cycles containing multiple seismic cycles. Field observations, laboratory data and analogue experiments suggest that the ratio of velocity-weakening to velocity-strengthening material varies with the ratio of brittle to ductile material in the shear zone. We therefore employ a linear transition of frictional parameters with depth to simulate bulk frictional properties of the shear zone. We find that for generalized normal faults, rate-and-state friction predicts a spectrum of slip behaviors including steady aseismic creep, aseismic transients, clustered earthquakes, and regular seismic cycle earthquakes. The dominant control on slip behavior is the degree of weakening material in the potentially seismogenic fault patch. Earthquake clusters occur with higher proportions of velocity-weakening material which correspond to more-competent, less-ductile shear zone assemblages. We find that rate-and-state friction predicts a wider spectrum of slip behavior on active normal faults than has been previously recognized, potentially due to geologic preservation and identification issues.

3.1. INTRODUCTION

3.1.1 Background

Fault slip by earthquakes represents the sudden accumulation of permanent inelastic strain (duration in seconds) that accompanies the release of elastic strain built up over a variable period of loading (100s to 1000s of years) (e.g., Scholz, 2002). When averaged over long time scales, fault slip rate deviates very little from the far field tectonic rate as predicted by rigid plate tectonics (e.g., Bennett et al., 2003; Thatcher, 2009; Wernicke et al., 2000; Gold & Cowgill, 2011). However, seismological and paleoseismological observations have challenged these two paradigms: (1) A new class of slip phenomena occurring over minutes (very low frequency earthquakes) to years (silent earthquakes) has been discovered. It includes deep episodic tremor (e.g., Obara, 2002), low or very low-frequency earthquakes (e.g., Ito et al., 2007), slow slip events (e.g., Hirose and Obara, 2005) and silent earthquakes (e.g., Kostoglodov et al., 2003) and can be grouped under the common appellation of slow-slip events (Ide et al., 2007; Vidale & Houston, 2012). (2) In some active tectonic regions fault slip rate deviates significantly from the tectonic rate when averaged over secular time scales (hundreds to thousands of years). Examples of such areas include some sections of the San Andreas fault (Weldon et al., 2004), the East California Shear Zone and the Los Angeles Basin (Dolan et al., 2007), the Wasatch front and the Basin and Range Province (Friedrich et al., 2003; Wallace, 1987), the Awatere fault in New Zealand (Gold & Cowgill, 2011) and the Solomon subduction interface near Newbare (Thirumalai et al., 2015). It therefore appears that faults that were previously thought to exhibit brittle, stick-slip behavior now show a new class of transient slip behavior occurring over a wide range of time scales (Lavier et al., 2013).

Slip transients are widely accepted to play an important role in deformation at many subduction zones. Peng & Gomberg (2010) outline a spectrum of subduction zone slip behaviors ranging from tremor and low-frequency earthquakes to slow-slip events and great earthquakes.

The periodicity and interactions between these mechanisms are not fully understood, though it is thought that elevated pore fluid pressures (Liu & Rice, 2007; Saffer & Wallace, 2015; Skarbek & Rempel, 2016) and frictional heterogeneity (Wallace et al., 2012; Skarbek et al., 2012) play a key role in allowing multiple slip mechanisms with different periodicities to occur at individual subduction zones. In addition to typical subduction zone seismic cycles, recent observations from Sumatra suggest that 200-year timescale supercycles control the number and timing of subduction zone earthquakes between the largest earthquakes and may explain the variability of earthquake magnitude during different events at one subduction zone (Sieh et al., 2008). Whether slip transients and supercycles occur on normal faults and by similar mechanisms as those in subduction zones remains poorly understood.

Temporal variations in slip-rate on normal faults have been recognized in Hawaii, Italy and the Basin and Range. The recurrence intervals of these slip transients range from ~2 years on the flanks of Kilauea, Hawaii (Montgomery-Brown et al., 2009) to 1-kyr-timescale earthquake clusters on the Fucino Fault in Italy (Benedetti et al., 2013) and 10-kyr-timescale earthquake supercycles on the Wasatch Fault in the eastern Basin and Range (Friedrich et al., 2003). In addition to individual seismic cycles within these supercycles, recent GPS results show periods of increased aseismic creep with durations of 2-4 years across the Basin and Range (Chamoli et al., 2014). These patterns suggest that some normal fault systems are dominated by transient slip behaviors that span multiple timescales and fall between the end-members of steady aseismic creep and regular seismic-cycle behavior whereby a locked fault accumulates elastic strain over the interseismic period before releasing it in rapid seismic slip.

Rate-and-state friction describes the friction between two surfaces as a function of the velocity at which they are moving past each other (the 'rate') and the time the surfaces have been in contact with each other (the 'state') (e.g., Dieterich, 1979, 1981; Ruina, 1983). Modeling efforts in the last decade have focused on explaining earthquakes, slow-slip events, slip transients and slip periodicity in subduction zones using different model setups within a rate-and-state frictional framework (e.g., Liu & Rice, 2007; Yang et al., 2012, 2013; Segall & Bradley, 2012; Skarbek et

al., 2012; Li & Liu, 2016). Fully dynamic and quasi-dynamic simulations based on rate-and-state friction have also reproduced the spectrum of seismic and aseismic slip behaviors observed over multiple seismic cycles on strike-slip faults (e.g., Lapusta & Liu, 2009; Barbot et al., 2012; Veedu & Barbot, 2016). As numerical models progress towards the integration of seismic-cycle deformation into long-term tectonic models (e.g., Herrendörfer et al., 2015; Lambert & Barbot, 2016), we introduce novel numerical procedures that allow for simulation of rate-and-state frictional earthquake cycles within an established long-term tectonic modeling framework. In this study we apply these rate-and-state friction modeling methods to investigate necessary conditions for transient slip cycles and earthquake clustering in active normal fault systems.

3.1.2. Examples of slip transients on normal fault systems

The Fucino Fault System (FFS) in central Italy is a segmented network of normal faults that strike NW and dip SE. The FFS shows distinct earthquake clustering and seismic supercycles through the Holocene as recorded by ^{36}Cl concentrations in fault scarp exposures analyzed and reported by Benedetti et al. (2013). Data from over 800 samples collected from seven distinct segments of the FFS show concentrated periods of elevated slip rate each lasting 500 years to 3 kyr. Benedetti et al. (2013) report that 3 to 10 clustered earthquakes ruptured most of the fault system during three distinct periods from 12 – 9 kya, 5 – 3 kya, and 1.5 – 1 kya (see Figure 5d. from Benedetti et al., (2013)). These 1 kyr-timescale earthquake clusters suggest that seismicity and slip on an active normal fault may be controlled by supercycles that span multiple seismic cycles and cause transient periods of large, clustered earthquakes. Faults slipping within these cycles experience long periods of strain accumulation separated by shorter periods of elevated strain release. The seismic hazard implications of periods of increased large-magnitude earthquakes warrant further work on normal fault earthquake supercycles.

The Wasatch Fault Zone (WFZ) is a segmented system of west dipping normal faults that bounds the eastern edge of the Northern Basin and Range province in the Western United States,

separating it from the Colorado Plateau to the east. Faults in the WFZ dip from 30-70° at the surface (Friedrich et al., 2003) but may flatten to subhorizontal at depths as shallow as 4 km as inferred from seismic reflection profiles (Smith & Bruhn, 1984) or as deep as 7-10 km as inferred from continuous GPS and seismic reflection profiles (Velasco et al., 2010). The dip variations along strike may be due to fault zone segmentation and may reflect modern or historical strain differences between individual segments (Machette et al., 1991).

Modern seismicity in the Northern Basin and Range is observed in three distinct belts, one of which traces the WFZ (Friedrich et al., 2003). Compiled paleoseismological studies show unique earthquake histories for the five central segments of the WFZ, though it is possible that multiple segments ruptured contemporaneously during some earthquakes (McCalpin & Nishenko, 1996). Both composite and individual-segment paleoearthquake records show notable clustering of events. The composite record of all WFZ segments includes clusters of earthquakes with average recurrence time of <160 years, though the Holocene average recurrence interval is ~395 years (Machette et al., 1991). The Holocene record includes seismic gaps of up to 3 kyr on some segments. These data suggest that mechanisms causing temporally transient seismic strain release may be the dominant controls on recent deformation in the WFZ.

3.1.3. Frictional properties of normal fault zones

The Altotiberina Fault (ATF) dips at about 15-20° beneath the Northern Apennines and is part of an active low-angle normal fault (LANF) system. We constrain our model with frictional data from an inactive exposed analogue fault East of the well-studied ATF for numerous reasons. First, the subsurface structure and geometry of the ATF are well-constrained by previous geological and seismic-reflection studies (Chiaraluce et al., 2007). Second, experimental rate-and-state friction parameters of rocks within the intact fault core of an inactive exposed low-angle normal fault - the Zuccale Fault - in the Northern Apennines are available (Smith & Faulkner, 2010; Niemeijer & Collettini, 2014). Finally, the ATF is of great interest because of the unresolved

mechanical paradox of active low-angle normal faults. Andersonian theory predicts that normal faults should initiate and slip at high dips ($>45^\circ$) and frictionally lock up at dips $<30^\circ$ (Axen, 1992; Wernicke, 1995; Collettini & Barchi, 2004). However, slip along low-angle normal faults is common in the rock record (Platt et al., 2015) and is currently observed at multiple locations globally (e.g., Wernicke, 1995; Collettini, 2011; Platt et al., 2015). It is likely that low angle slip is made possible by the combination of the presence of preexisting shear zones, high shear flow in the lower crust and variable strength with depth (Wu & Lavier, 2016). In this study we focus on generalized normal fault systems characterized by experimental frictional properties from the ATF system, which outline a spectrum of possible slip behaviors for active LANFs. Future work modeling detailed LANFs using rate-and-state friction will provide more precise insight into how temporal variations in slip rate relate to the initiation and evolution of LANF systems.

3.1.4. General slip behaviors of normal faults

Active normal fault rift systems accommodate extension rates ranging from less than one mm/yr up to 25-40 mm/yr (Abers, 2001). This extension is accommodated by a variety of slip styles observed on normal faults around the world. Some normal faults, such as those in the Gulf of Corinth and the Apennines, experience frequent earthquakes on steeply dipping near-surface fault sections (McKenzie & Jackson, 1983; Jackson, 1987; Abers, 2009). However, some normal faults within these same systems have been inferred and observed geodetically to deform by aseismic creep (Hreinsdóttir & Bennett, 2009; Abers, 2009). Many normal faults consist of a near-surface high-angle ($40-70^\circ$) portion that slips seismically, and a deeper low-angle ($<30^\circ$) to sub-horizontal detachments that may creep aseismically (Wernicke, 1995; Abers, 2009). Little modern seismicity has been observed on active low-angle normal faults, leading to the proposal that these faults slip primarily by aseismic creep (Collettini & Sibson, 2001; Abers, 2009). A variety of mechanisms have been proposed for aseismic creep on active low-angle normal faults, including fault weakening due to elevated pore-fluid pressures (Axen, 1992; Collettini & Barchi, 2004),

rotated principal stress orientations (Axen, 1992), and creep on networks of low-friction minerals such as talc (Collettini et al., 2009) or serpentinite (Floyd et al., 2001).

The variety of slip mechanisms observed within a single normal fault system raise compelling questions about how different deformation mechanisms interact along a fault and how this deformation is expressed at the Earth's surface over multiple timescales. In their study of the WFZ, Friedrich et al. (2003) describe three orders of strain accumulation and release defined by the timescales over which they act to explain discrepancies between geologic and geodetic slip-rate estimates, assuming relatively uniform long-term strain accumulation (Figure 3.1, redrawn from Friedrich et al. (2003)). First-order slip represents long-term tectonic strain rates on the order of 1-10 Myr. Second-order slip describes 10 kyr timescale fault dynamics and includes the previously discussed supercycles of earthquake clusters. Proposed explanations for these second-order slip-rate variations on the WFZ include variable glacial-interglacial surface loading (Hetzl & Hampel, 2005) and time-variable fault loading by downdip creep transients at the brittle-ductile transition (Lavie et al., 2013). Third-order slip includes local strain-rate transients and individual seismic cycle strain accumulation and release on the order of 100 yr – 1 kyr. Friedrich et al. (2003) argue that only first- and second-order displacement is recorded in the geologic record, while modern GPS measures the system at some period of time within a third-order cycle (Figure 3.1). Hence, normal faults may experience short-period aseismic slip transients (i.e. creep events) that are not recorded in the geologic record. We investigate how third-order slip patterns relate to second-order slip cycles for generalized normal fault systems obeying rate-and-state frictional laws.

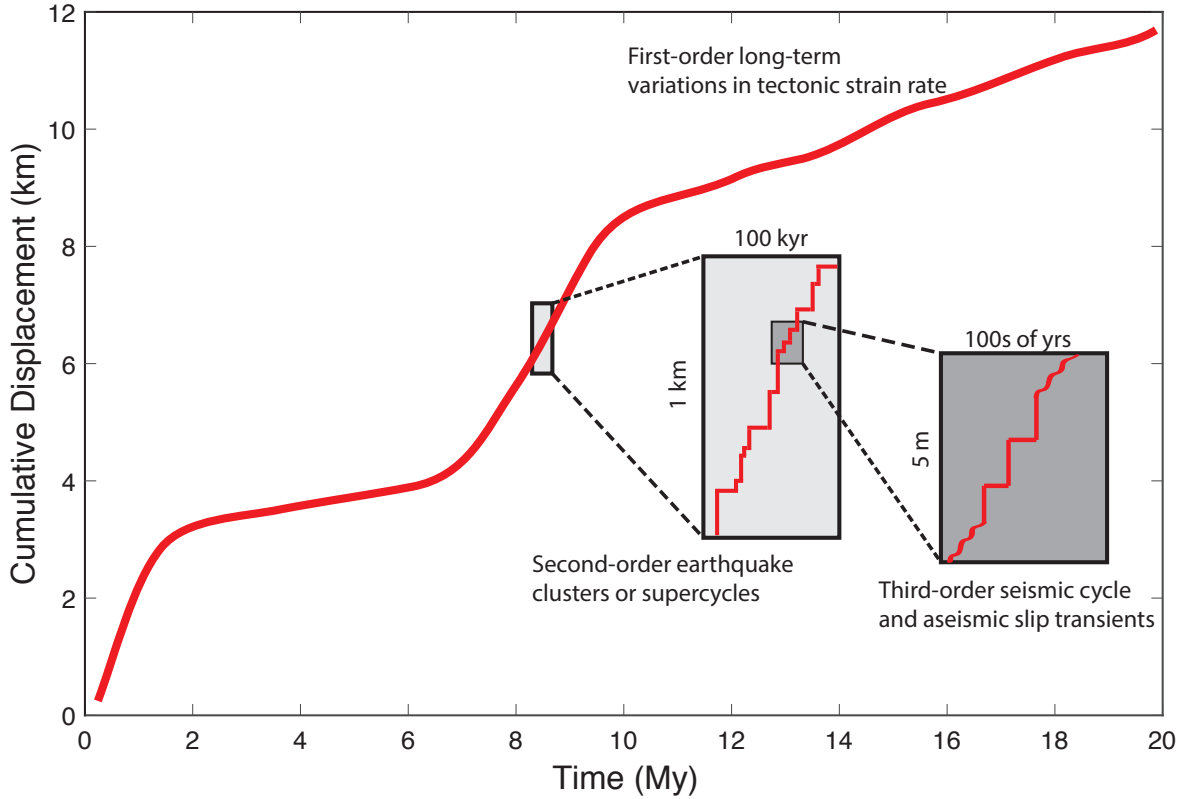


Figure 3.1. Representative displacement vs. time plot showing three orders of slip behavior distinguished by their timescales. Drawn after Friedrich et al. (2003).

3.2. METHODS

3.2.1. Rate-and-State Constitutive Equations

The single-state-variable rate-and-state friction ‘aging’ formulation of Dieterich (1979, 1981) and Ruina (1983) shows that friction on a given fault patch is determined by the frictional properties of the materials in contact, the time over which the surfaces have been in contact with each other, and the velocity at which they are moving past each other. In this formulation the shear stress on a fault patch under constant normal stress is given by:

$$\tau = \sigma_n \left(f_0 + a \ln \frac{V}{V_0} + b \ln \frac{V_0 \theta}{L_C} \right) \quad (3.1)$$

where σ_n is the normal stress on the surface, a and b are positive parameters describing the friction due to slip velocity V and state variable θ , f_0 is the reference coefficient of friction, V_0 is the reference slip velocity, and L_C is the characteristic slip length. The state variable is interpreted as

the time over which the surfaces have been in contact and the rate of change of θ is a function of both the current state and velocity as given by:

$$\dot{\theta} = 1 - \frac{v\theta}{L_c} \quad (3.2)$$

The physical implications of a and b are readily understood by considering the quantity $a-b$, which determines whether friction increases or decreases due to an increase in slip velocity. If $a-b < 0$ the interface is rate-weakening, whereby an increase in slip velocity decreases the friction. If $a-b > 0$ the interface is rate-strengthening, such that an increase in slip velocity increases the friction. Velocity-strengthening materials are associated with stable sliding because any increase in velocity is countered by an increase in friction. Velocity-weakening materials can give rise to unstable seismic slip, though for an earthquake to nucleate the velocity-weakening patch must exceed a critical nucleation size (e.g., Rice & Ruina, 1983; Rice, 1993; Lapusta & Liu, 2009).

3.2.2. General numerical procedure

In order to simulate long-term tectonic deformation over thousands to million of years with short periods of fast slip representing earthquakes, we develop a new numerical technique to truncate inertial frequencies of vibration above the velocity threshold predicted by the “aging” law for rate-and-state slip behavior. This approach allows us to simulate long periods of slow tectonic deformation punctuated by seismic slip without wave generation caused by earthquakes. The fault is represented in the x direction as a surface over a finite domain $[0, L]$ discretized with N elements of variable width Δx_i where i is the node number. The fault surface is loaded in shear by the motion of an elastic plate of length L and thickness H driven at the tectonic plate velocity V_p . The elastic tractions are balanced at the fault interface by the aging law for the rate-and-state shear tractions (Rice, 1993; Lapusta et al., 2000). We solve the force balance by using the Fast Lagrangian Analysis of Continua (FLAC) algorithm (Cundall, 1989). This approach calculates the quasistatic solution of the equation of motion through damping of a pseudo-inertial term. The equation of motion is:

$$\rho \dot{\mathbf{u}} = \nabla \cdot \boldsymbol{\sigma} + \rho \mathbf{g} \quad (3.3)$$

where ρ is the density, $\dot{\mathbf{u}}$ is the velocity vector, $\boldsymbol{\sigma}$ is the Cauchy stress tensor, \mathbf{g} is the acceleration due to gravity and $\nabla \cdot$ is the divergence operator. FLAC calculates stress in the elements. Forces and velocities are evaluated at the nodes using a finite difference discretization (Cundall, 1989). For a two-dimensional planar fault we evaluate shear stress in the downdip direction as in previous R&S studies (e.g., Liu & Rice, 2007; Yang et al., 2012). The shear stress over time at the fault surface is given similarly to Lapusta & Liu (2009) as:

$$\tau = \tau_0 + \Delta\tau_e - V \frac{G}{2C_S} \quad (3.4)$$

where τ is the shear stress at time $t + \Delta t$, τ_0 is the shear stress at time t , $\Delta\tau_e$ is the change in shear stress over the adapted time-step Δt , V is the slip velocity in the down-dip direction, G is the shear modulus and C_S is the shear-wave velocity. The last term is the radial damping term, which completes the quasi-static solution by applying a viscous force during earthquakes to account for energy lost by seismic wave propagation (e.g., Rice, 1993; Lapusta & Liu, 2009). The rate-and-state shear stress on the fault interface is balanced by the tectonic loading of an elastic plate of thickness H . The corresponding elemental shear stress increment for the elastic loading is:

$$\Delta\tau_e = \frac{1}{2} G_p \frac{(V_p - V_e)}{H} \Delta t \quad (3.5)$$

where the elemental velocity of element i is $V_e = (u_i + u_{i+1})/2$, \dot{u}_i and \dot{u}_{i+1} are the nodal down-dip velocities at nodes i and $i+1$ respectively, and G_p is the shear modulus of the elastic plate. The rate-and-state shear stress at the interface is expressed as (Lapusta & Liu, 2009):

$$\tau_{rs} = a \sigma_n \sinh^{-1} \left(\frac{V}{2V_0} \exp \left(\frac{f_0 + b\phi}{a} \right) \right) \quad (3.6)$$

where a and b are rate and state variables, f_0 the static friction coefficient, ϕ the state quantity, σ_n the loading stress normal to the fault interface and V_0 a characteristic velocity. The state quantity ϕ is expressed as:

$$\phi = \log \left(\frac{V_0 \theta}{L_C} \right) \quad (3.7)$$

where θ is the state variable and L_C the characteristic slip length. Instantaneously, the equation of motion at the fault interface is:

$$\rho \dot{u}_x = \frac{\partial(\tau_{rs} - \Delta\tau_e)}{\partial x} \quad (3.8)$$

where the right-hand side is the nodal force, f_i . The effect of loading from gravity is implicitly taken into account through σ_n . To achieve equilibrium, the nodal force, f_i is damped according to the direction of velocity:

$$ma_i = (f_{damped})_i = f_i - 0.8 \text{sgn}(\dot{u}_i) |f_i| \quad (3.9)$$

where m is the nodal mass, a_i is the nodal acceleration in the x coordinate, $(f_{damped})_i$ is the damped nodal force, \dot{u}_i is the nodal velocity in the x coordinate and sgn is the signum function. In all cases we attempt to reach critical damping (as defined for an oscillator) to reach equilibrium consistent with the mass, m of the oscillator defined by equation 9. The motivation for the choice of damping or amplification is based on the observation that in an under-damped oscillator, the direction of force is always opposite to the velocity direction, while in an over-damped system, the direction of the force is parallel to the velocity direction. The integration of the nodal forces provides an estimate of the nodal velocities \dot{u}_i as:

$$\dot{u}_i = \frac{f_i}{m} \Delta t \quad (3.10)$$

Δt is calculated using the adaptive time stepping algorithm described in Lapusta and Liu (2009). In our model we modify the nodal density to damp the high frequency oscillations corresponding to a fictitious nodal density, ρ_f , scaled with the slip velocity as:

$$\rho_f = \frac{G}{\dot{u}_{max}^2 (\Delta x_{min}/L_C)^2} \quad (3.11)$$

where G is the shear modulus, Δx_{min} is the minimum grid space and \dot{u}_{max} the maximum slip velocity over $[0, L]$. To assure stability the time-step is scaled with slip-velocity to be $\Delta t = 0.2L_C/\dot{u}_{max}$ such that when \dot{u}_{max} reaches the shear velocity C_s , then $\Delta t = 0.2L_C/C_s$, giving:

$$\rho_f = \frac{G}{C_s^2} \quad (3.12)$$

When $\dot{u}_{max} < 10^{-12} \text{ ms}^{-1}$ then the time-step is set to $\Delta t = 0.5\Delta x_{min}/\rho_f$, where ρ_f is a fictitious density used to simulate long term tectonic slip.

We use the estimate of nodal velocity, \dot{u}_i as a first guess to balance elastic loading over time with the rate and state shear stress to get an estimate of slip velocity, V^* :

$$\tau_0 + \Delta\tau - V^* \frac{G}{2c_s} = a\sigma_n \sinh^{-1}\left(\frac{V^*}{2V_0} \exp\left(\frac{f_0 + b\phi}{a}\right)\right) \quad (3.13)$$

We follow the numerical approach of Lapusta et al. (2000) and Lapusta & Liu (2009) to update the state quantity ϕ . This choice leads to the time-dependent ϕ equation (Lapusta et al., 2000; Lapusta & Liu, 2009):

$$\dot{\phi} = \frac{V_0}{L_C} e^{-\phi} - \frac{V}{L_C} \quad (3.14)$$

which is used to solve for ϕ^* , a first ‘guess’ of ϕ after time-step Δt , using the resultant slip velocity estimate. Refer to Lapusta & Liu (2009) for full details of this calculation. We use ϕ^* to calculate a first guess of velocity V^* by equating the traction on the fault to its rate-and-state strength given in equation (3.13). We solve equation (3.13) using an adapted Newton-Raphson and Halley method, where the Newton-Raphson method is implemented only when the Halley method fails to converge quickly. We note that solving equation (3.13) is the most time-intensive computational step in our procedure and that the implementation of fourth- or fifth-order Runge-Kutta solvers (as in Lambert & Barbot, 2016; Qiu et al., 2016) or alternative formulations of this equation (as in Lambert & Barbot, 2016) may improve the efficiency of our numerical procedures; however this analysis is beyond the scope of this paper. We use V^* to recalculate predicted slip along the fault, which we then use to calculate ϕ^{**} , a more accurate prediction of ϕ . We plug ϕ^{**} into equation (3.13) to calculate a second order approximation of velocity V^{**} which we take to be the slip velocity during the time-step Δt . We then interpolate this velocity as \dot{u}_x on $[0, L]$ to evaluate the shear stress along the fault after time-step Δt and to determine the appropriate size of the subsequent time-step. We present benchmark comparisons of our model to results of Liu & Rice (2007) in Appendix B.

3.2.3. Model Geometry & Parameters

3.2.3.1. Typical Model Parameters & Spatial Discretization

Some parameters are held constant over all model runs, which we briefly discuss here. The reference slip-velocity V_0 and reference coefficient of friction f_0 are inherently reference values

and by nature should remain constant between model runs. We take $V_0 = 10^{-6}$ m/s and $f_0 = 0.6$ as in Lapusta et al. (2000). We take the shear modulus $G = 25$ GPa and shear-wave speed $C_S = 3$ km/s. A summary of typical values in rate-and-state friction numerical models is presented in Lapusta & Barbot (2012). Normal stress and a - b distributions are described in Section 3.2.3.2 and we vary the plate velocity V_p to simulate different rates of extension on normal faults. We use rates of $V_p = 3, 6, 9$ mm/yr which correspond to modern extension rates in the Wasatch Fault Zone (Friedrich et al., 2003), the central East African Rift (Stamps et al., 2008), and the Mai'iu Fault Zone in SE Papua New Guinea (Wallace et al., 2014), respectively.

Rice (1993) defines a critical nucleation cell-size h^* which must be much larger than a modeled cell size dx within any velocity-weakening patches in order to capture seismic slip while retaining a stiff mesh that can be treated as a continuum. This critical cell-size as presented by Hillers et al. (2006) is:

$$h^* = \frac{2GL_C}{\pi\sigma_n(b-a)_{max}} \quad (3.15)$$

Rice (1993) estimates that $dx/h^* < 0.25$ is sufficient for slow slip velocities. Hillers et al. (2006) use a maximum $dx/h^* = 0.4$ while Lapusta et al. (2000) select $dx/h^* = 0.025$. We take the characteristic slip distance L_C to be constant along the fault and choose a realistic value of 8 mm, as in Lapusta & Liu (2009). We use $dx = 100$ m. Our choices of L_C and dx lead to maximum dx/h^* ranging from 0.0984 to 0.1567 in the velocity-weakening portion of our model, which are on the order suggested as sufficiently small by previous authors. Note that most of the velocity-weakening patch has much lower dx/h^* than these maximum values. Finer grid-spacing would be required for a fully dynamic model (e.g., Lapusta & Liu, 2009); however, the grid-spacing used appears appropriate for our model in which inertial frequencies are damped. We tested $dx = 50$ m and $dx = 25$ m and saw no significant difference or instability in our results, leading to our confidence that $dx = 100$ m is an appropriate grid-spacing.

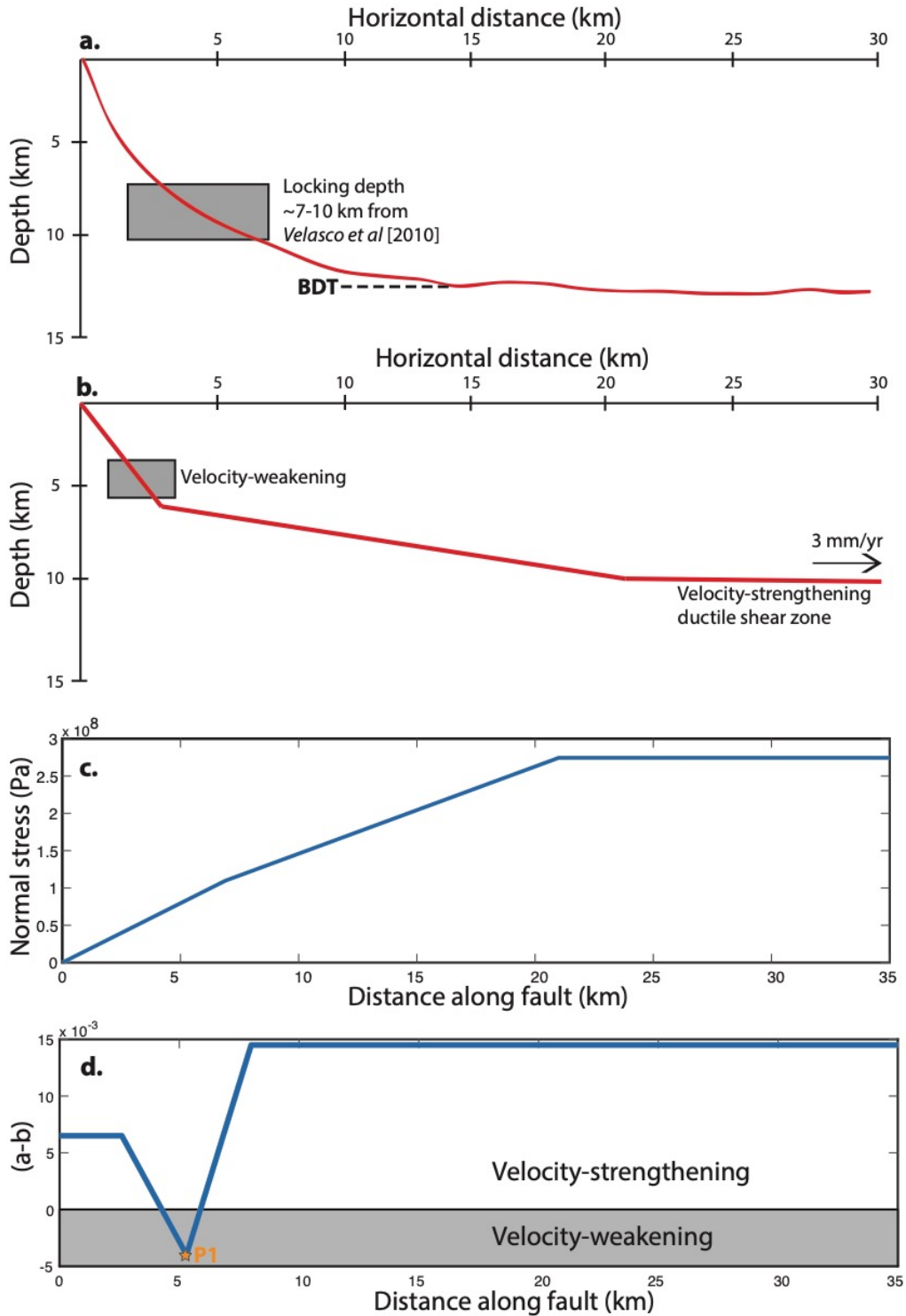


Figure 3.2. a. Realistic geometry of a Wasatch Fault Zone segment at depth. b. Modeled fault geometry. c. Associated model normal stress distribution. d. Associated a-b profile showing location of velocity-weakening zone along the fault. The orange star 5.3 km downdip on the fault denotes the location of point P1 where velocities and cumulative displacements are tracked in Figures 3.4, 3.6, and 3.8.

3.2.3.2. Normal Fault Model Setup

Since constraints on the structure and rheology of normal faults at depth are limited, we simulate a generalized active normal fault system with geometric constraints from the Wasatch Fault Zone and frictional constraints from the Zuccale Fault in the Northern Apennines Fault Zone. Subsurface geometries of different segments of the WFZ are unique, but generally consist of steeply dipping (40-70°) portions near the surface that shallow out to low-angle and subhorizontal detachments at depths of 4-10 km (e.g., Zoback, 1983; Smith & Bruhn, 1984; Velasco et al., 2010). We model a fault dipping at 60° down to 6 km depth where it shallows to a 20-degree detachment to 10 km depth, where it becomes subhorizontal and extends 14 km further. The total modeled fault length is 35 km. Figure 3.2a shows a realistic fault geometry, while Figure 3.2b shows the geometry used in the model. The lithostatic normal stress profile used is shown in Figure 3.2c and reaches a maximum of 274 MPa on the subhorizontal detachment at 10 km depth. Fluid inclusions from the WFZ suggest that effective stresses alternate between lithostatic and hydrostatic down to 11 km depth (e.g., Parry & Bruhn, 1986; Parry & Bruhn, 1987; Sibson, 2000). Model tests of normal stress distributions downdip of the imposed velocity-weakening zone show that there is little difference in slip behavior of the weakening patch under lithostatic or hydrostatic states of stress at depth. It is thought that fluid pressures within normal faults at depth may be high enough to induce fault-weakening mechanisms (e.g., Evans, 1990; Axen, 1992; Sibson, 2000; Collettini & Barchi, 2004), though fracture networks around the fault zone at shallow depths are likely to relieve fluid pressures in the updip portion of the fault (Collettini & Barchi, 2004).

We use rate-and-state *a-b* values and distributions derived from high-pressure high-temperature velocity-stepping rock deformation experiments on fault gouge from exposures of the Zuccale Fault, an abandoned low-angle normal fault on the western edge of the ATF system. Smith & Faulkner (2010) report preliminary *a-b* values for different rock units within one outcrop of exposed fault core. Their results show mostly velocity-strengthening behavior at room-temperature, though one sample of talc-phylonnite shows velocity-weakening behavior at an effective normal stress of 50 MPa. Den Hartog & Spiers (2013) show that increasing the

temperature of phyllosilicate rocks at constant confining pressures decreases their experimental values of $a-b$ up to temperatures of at least 350° C. Niemeijer & Collettini (2014) performed further velocity-stepping experiments on Zuccale Fault gouge at effective normal stresses of 20 – 150 MPa and temperatures ranging from room temperature to 300 °C. Their results reflect a clear dependence of frictional properties on temperature. Most samples still exhibited velocity-strengthening behavior, but two samples at 150° C and numerous samples at 300 °C exhibit velocity-weakening behavior, with reported $a-b$ values as low as -0.015 at 150 °C. These data suggest that while the fault zone may contain mainly velocity-strengthening rocks, portions of the fault may accommodate slip in unstable velocity-weakening layers.

We map $a-b$ values from these studies to approximate depths based on experimental temperatures and pressures, assuming a typical crustal lithostatic pressure gradient of 27 MPa/km and geothermal gradient of 30 °C/km. The total model fault length is 35 km and consists of an updip velocity-strengthening portion ($a-b = .0065$) down to 2.5 km depth, transitioning into a velocity-weakening patch ($a-b = -.004$) from 4 to 6 km depth, which soles into a velocity-strengthening ($a-b = .0145$) sub-horizontal detachment at 10 km depth (Figure 3.2b & 3.2d). The downdip velocity-strengthening section extends 14 km to simulate loading by deep creep near the brittle-ductile transition (e.g., Lavier et al., 2013).

In contrast to many previous rate-and-state numerical studies (e.g., Rice, 1993; Liu & Rice, 2005, 2007; Yang et al., 2012) we do not prescribe a frictionally homogeneous velocity-weakening seismogenic slip patch. Instead, we model a fault zone with shallow velocity-strengthening properties associated with low normal stresses and unconsolidated fault gouge (Scholz, 2002) transitioning gradually into velocity-weakening material at 4-5 km depth which transitions gradually back to velocity-strengthening material at greater depths to represent a predominantly ductile shear zone as temperatures reach those necessary to allow quartz and feldspar plasticity near the brittle-ductile transition (Scholz, 2002; Jammes et al., 2015). This $a-b$ profile (Figure 2d) resembles that used to model strike-slip faults in California by Wei et al. (2013), who conclude

that frictional heterogeneities within the traditionally velocity-strengthening near-surface region are necessary to recreate observed creep events.

For most model runs, the a-b distribution is smoothed to simulate gradual transitions in material properties with gradually increasing temperature and pressure. We choose a minimum $a-b = -0.004$ from within the 150°C experimental range of Niemeijer & Collettini (2014) to represent our most velocity-weakening scenario, but our models with smoothed a-b profiles may more accurately reflect the bulk frictional properties of an active fault core because slip may occur through a complex network of different fault rocks as discussed above. After explicitly defining the a-b profile shown in Figure 2d we apply a five-point moving average filter to the a-b values along the entire fault. The main effect of the filter is to smooth the transition points between segments of the a-b profile and to smooth and reduce the amplitude of the a-b peak at the weakening patch (Figure 3d). The motivation for the smoothing experiment is to compare slip patterns on faults with a slip patch composed of velocity-weakening material (Figure 3b) with those of faults with slip on a heterogeneous mixture of velocity-weakening and velocity-strengthening layers, represented in our model as a smoothed a-b profile (Figure 3d). We find that the number of times the filter is applied serves as a useful parameter for testing the response of the fault to less-negative minimum a-b values and smoother a-b distributions. We define the smoothing factor κ as the number of times the smoothing filter is applied.

Consider the simplified theoretical model with only two types of fault rock shown in Figure 3.3a and 3.3c where clasts of brittle, competent, velocity-weakening material are surrounded by a matrix of low-viscosity, incompetent, velocity-strengthening material (e.g., Fagereng & Sibson, 2010). In relation to this conceptual model, a higher κ represents an increased proportion of incompetent velocity-strengthening matrix to competent velocity-weakening clasts (Figure 3.3c). In our model framework a higher κ could also represent an increased degree of preferential alignment of clasts allowing for the formation of interconnected fracture networks filled with velocity-strengthening material. Our physical interpretation of κ is further discussed in section 3.4.3. Our smoothing technique aims to best represent the bulk frictional properties at depth within

the limitations of a two-dimensional planar fault model and with the understanding that a single a - b value may not fully capture the complexity of slip through a heterogeneous fault zone.

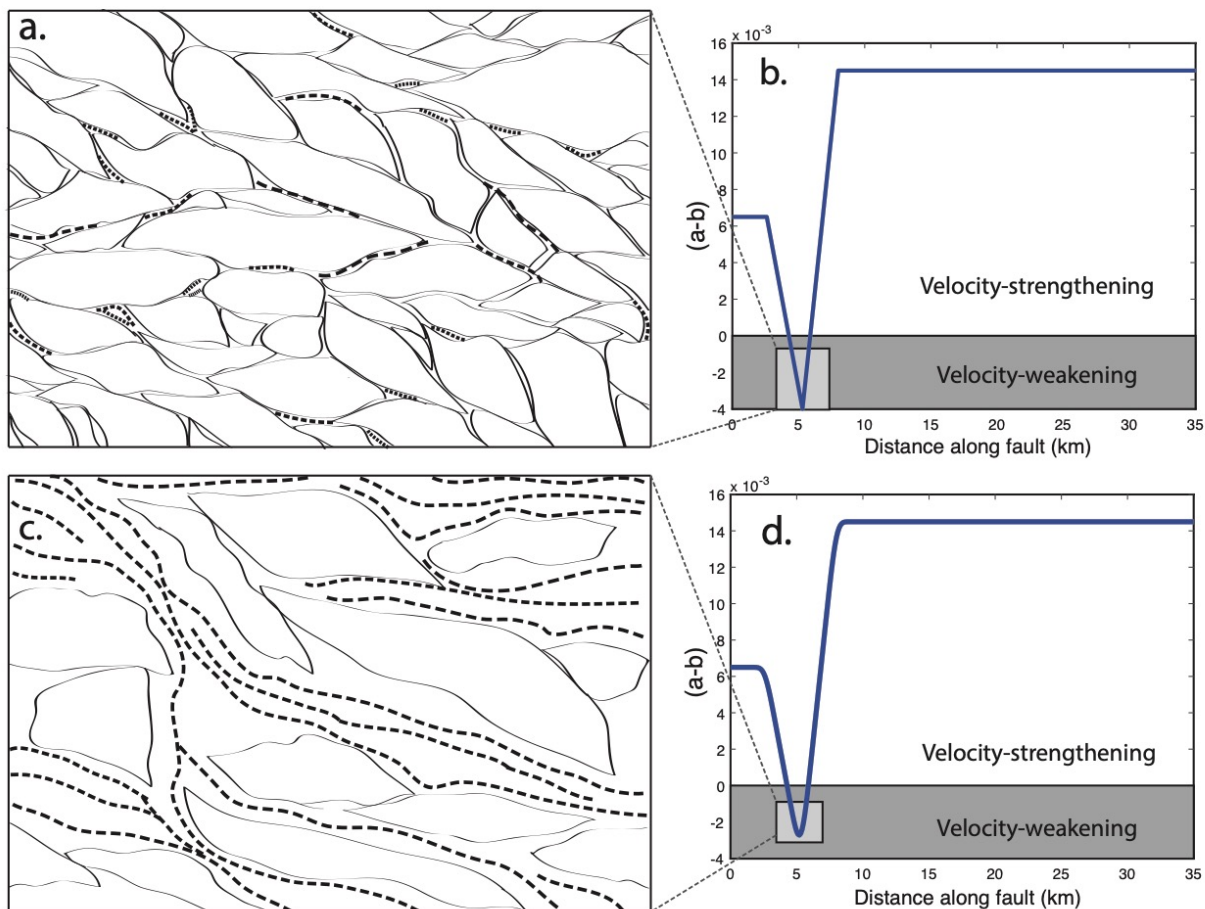


Figure 3.3. a. Schematic of two-member theoretical fault zone model with $\sim 95\%$ brittle velocity-weakening clasts and $\sim 5\%$ low-viscosity velocity-strengthening matrix (dashed lines). b. Corresponding a - b profile along the fault; $\kappa = 0$. c. Schematic of fault zone model with $\sim 50\%$ brittle velocity-weakening phacoids and $\sim 50\%$ low-viscosity velocity-strengthening matrix. d. Corresponding a - b profile along the fault; $\kappa = 5$. Shear direction from bottom-right to top-left. The higher proportion of ductile matrix to brittle clasts in c allows for aligned fracture networks to form, facilitating aseismic creep. In our models, scenario a is represented by a small κ and scenario c by a large κ or bulk velocity-strengthening a - b . Drawn after Fagereng & Sibson (2010).

3.3. RESULTS

3.3.1. Parameter Tests

We ran multiple models with the conditions described in section 3.2.2 while varying plate velocity (Appendix Figure B.2) and κ to determine their influence on the slip behavior of the weakening patch. For κ of zero to six, we find four main characteristic response regimes: pure seismic (Figure 3.4a), mostly seismic (Figure 3.4b), seismic clustering (Figure 3.4c), and aseismic periodic (Figure 3.4d). We do not include results for κ greater than six as they tend towards the decaying periodic response of section 3.3.1, which is expressed as steady creep (Figure 3.5). We focus on conditions leading to slip transients and the properties of those transients.

The control of κ on the response phase diagram (Figure 3.5) is intuitive, given that a higher κ implies a less-negative minimum a-b value. Smoother a-b profiles in the weakening patch can be interpreted as fault cores with less prominently velocity-weakening material or a heterogeneous mix of velocity-weakening and velocity-strengthening material. A κ value of zero leads to pure seismic-cycle slip for all plate velocities tested, implying that a threshold minimum a-b value of -0.004 is sufficient to cause purely seismic-cycle slip within the velocity-weakening patch. As κ increases, the response changes to mostly seismic slip with periods of aseismic slip transients lasting from 40 – 150 years. Some periods of over 1 kyr are still dominated by pure seismic cycle slip within this regime. The third regime shows clear earthquake clustering, where groups of earthquakes are separated temporally by 100 yr – 5 kyr periods of aseismic slip transients. These aseismic periods separate clusters of two to ten events, though a few model runs exhibit solitary earthquakes. The final regime is aseismic periodic, similar to the complex periodic regime of Liu & Rice (2007). These models are dominated by slow-slip events with periodicity and magnitude controlled by κ and the plate velocity. Maximum slip rates during the slow-slip events reach up to an order of magnitude greater than V_p . The phase diagram in Figure 3.5 reflects similar stability regimes to experimentally-derived slip stability phase diagrams of Leeman et al. (2016), who parameterize laboratory-based slip stability based on a critical system stiffness that depends on a-

b , σ_n , and L_C . In this study we do not vary σ_n or L_C distributions so stability appears dependent on a - b distributions alone; however, it is possible that varying σ_n or L_C in future models may reveal more complex stability dependencies similar to those observed experimentally. Figure 3.6 shows representative plots of cumulative displacement over time for the different regimes. Cumulative displacements in the ‘creep event’ regime of Figure 3.6c resemble surface-displacement plots of Wei et al. (2013) who impose a small near-surface velocity-weakening patch updip of the traditional velocity-weakening fault region in order to match observed postseismic creep-events observed on strike-slip faults in California.

A commonly reported parameter thought to influence the response of rate-and-state numerical models is W/h^* , where W is the width of the velocity-weakening patch and h^* is the critical nucleation length defined in equation 3.15 (e.g., Liu & Rice, 2007). Liu & Rice (2007) present the slip response phase diagram of their model in terms of W/h^* and find that higher W/h^* correspond to seismic slip while lower W/h^* correspond to aseismic creep. Liu et al. (2012) show that the ratio of total plate-loading moment released by earthquakes at oceanic transform faults is dependent on W/h^* , with higher values leading to higher seismic moment release. Previous studies have employed constant a - b and σ_n values within the velocity-weakening patch, leading to straightforward calculations of W/h^* . Our bulk a - b interpretation and lithostatic σ_n profile do not lend themselves to calculation of one W/h^* value to describe the entire velocity-weakening fault patch, because h^* varies through the patch. However, to allow comparison with previous models it is important to report similarly parameterized results, so we choose to present our slip regimes in terms of $(W/h^*)_{\max}$, the maximum value of W/h^* in the velocity-weakening patch. Figure 3.7a correlates $(W/h^*)_{\max}$ with the slip regimes and minimum a - b values from Figure 3.5. We interpret the physical meaning of $(W/h^*)_{\max}$ in our models in terms of the ratio of competent to incompetent material within the shear zone in the potentially velocity-weakening portion of the fault zone, similar to our interpretation of κ and a - b distribution. Figure 3.7b-d show representative shear zone schematics with different ratios of brittle competent clasts to ductile incompetent matrix and their

corresponding slip regimes, as delineated by $(W/h^*)_{\max}$. We further discuss this interpretation in section 3.4.3.

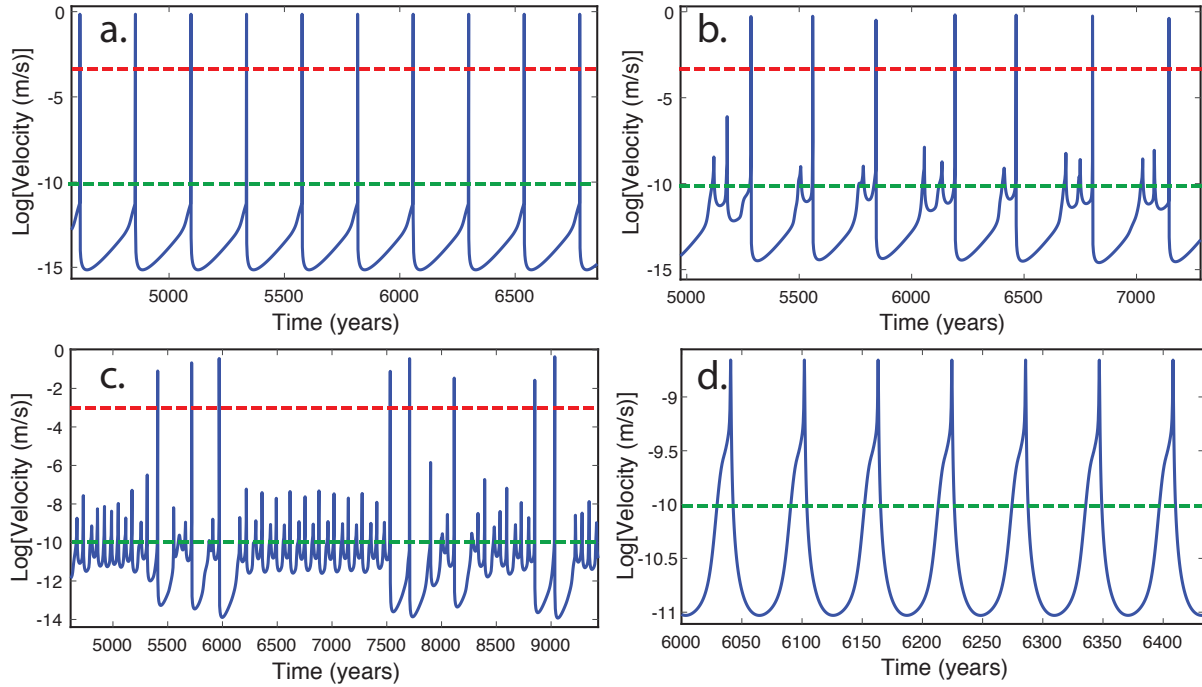


Figure 3.4. Representative characteristic slip responses of point P1 (see Figure 3.1 for its location) shown by slip-velocity vs. time plots. Red dashed lines denote 1 mm s⁻¹ slip rates for reference. Green dashed lines denote the loading plate-velocity of $V_p = 3 \text{ mm yr}^{-1}$. a. No smoothing, pure seismic cycle slip. b. $\kappa = 3$, mostly seismic slip separated by few aseismic slip transients. c. $\kappa = 5$, earthquake clusters separated by periods of aseismic slip transients lasting up to 1 kyr. d. $\kappa = 6$, aseismic periodic slip transients.

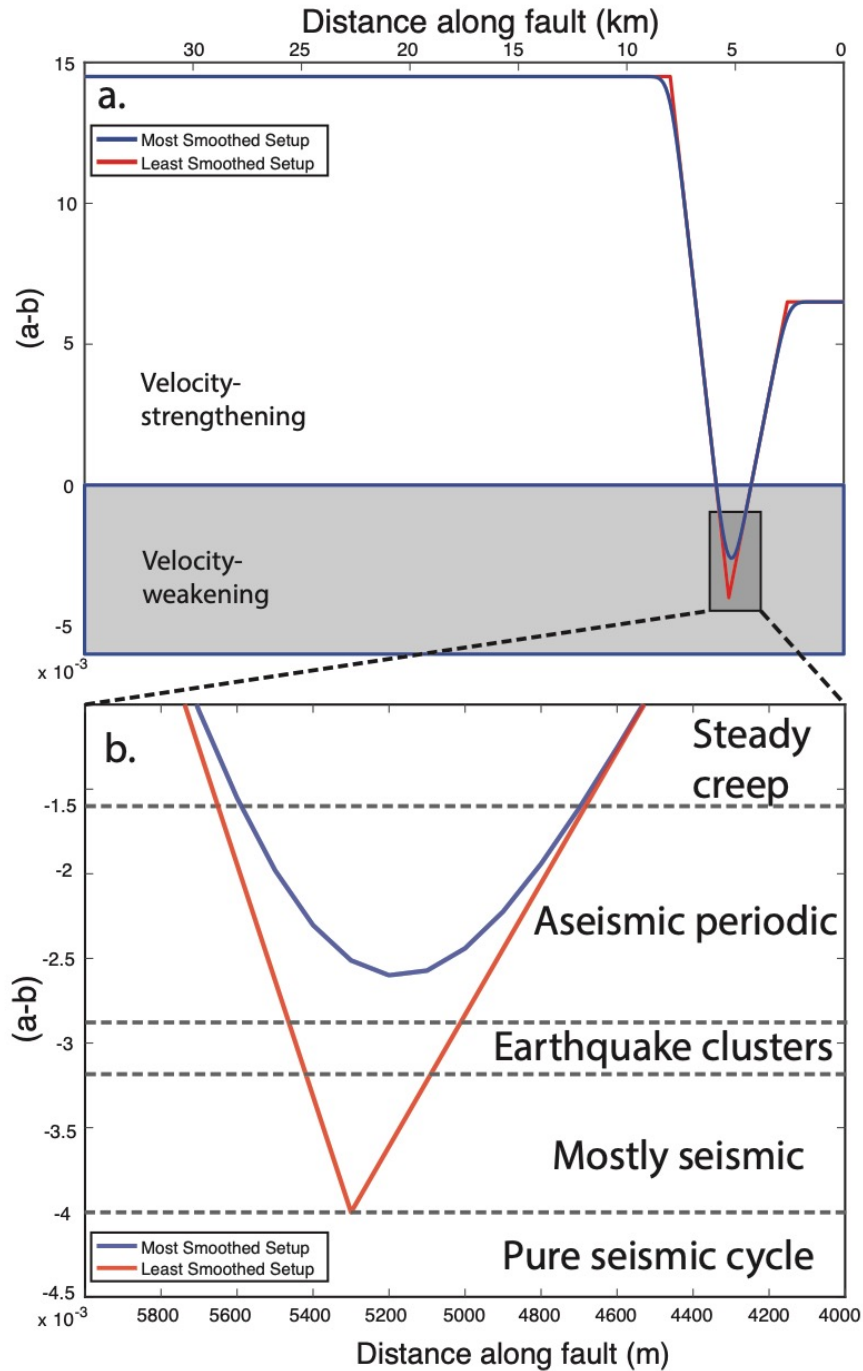


Figure 3.5. a. Schematic diagram to provide context for where the velocity-weakening patch is along the fault. b. Slip behavior phase diagram showing thresholds of minimum $a-b$ in the weakening patch for each slip regime. The blue profile represents higher $\kappa = 5$, corresponding to a shear zone with more ductile velocity-strengthening material. The red profile represents lower $\kappa = 0$, corresponding to a shear zone with more brittle velocity-weakening material.

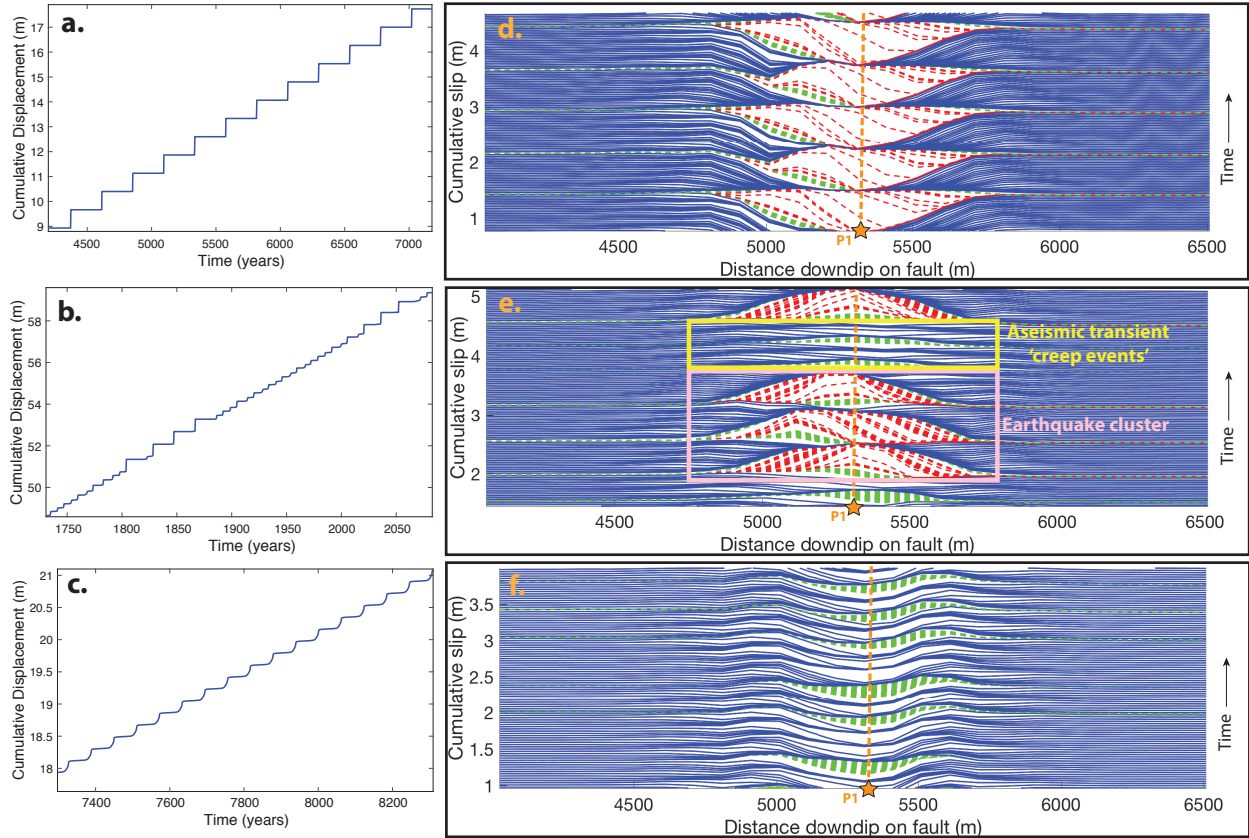


Figure 3.6. a-c. Modeled cumulative slip over time plots at point P1 for three characteristic regimes: a. pure seismic cycle, b. earthquake clustering, and c. aseismic slip transients (creep events). d-f. Cumulative slip vs. time plots for a section of the fault extending from 3.5 to 6.5 km downdip, which includes the velocity-weakening patch. Note that the total fault domain extends 3.5 km updip and 28.5 km downdip from the section plotted. When the maximum velocity of any point on the fault is greater than 1 mm/s slip is contoured every 1 second with a dashed red line. When the maximum velocity is less than 1 mm/s but greater than $100V_p$, slip is contoured every 15 minutes with a dashed green line. When the maximum velocity is less than $100V_p$, slip is contoured every 20 years with a solid blue line. Orange stars and lines indicated the location of the point P1, for which cumulative slip is tracked in a-c. Colored boxes and labels indicate the occurrence of an earthquake cluster and aseismic slip transients in e. These plots correspond to the three characteristic regimes: d. pure seismic cycle, e. earthquake clustering, and f. aseismic slip transients.

3.3.2. Earthquake Clustering & Aseismic Slip Transients

To investigate the properties of the modeled earthquake clustering, we further analyze the representative model scenario with $\kappa = 5$, $L_C = 8$ mm, $h = 100$ m, and $V_p = 3$ mm/yr, corresponding to extension rates on the Wasatch Fault or Fucino Fault. Following the initial loading period, slip on the fault is characterized by steady creep in the velocity-strengthening sections updip and downdip of a conditionally stable region which slips in clusters of earthquakes separated by 500 yr – 5 kyr interseismic periods of aseismic complex periodic slip transients (Figure 3.8a). The recurrence intervals of events within each earthquake cluster range from 200 to 400 years. Some clusters include 100-300 year periods of aseismic slow-slip transients within the cluster, though most clusters exhibit purely seismic slip separated by locked periods of little to no slip. The interseismic periods within the clusters exhibit a pre-rupture rise-time of about 50 years over which the locked patch transitions from purely locked until it approaches sub-creeping velocities at which point it ruptures seismically. Although clustered earthquakes dominate the slip of the weakening patch, a few earthquakes in the 50 kyr model occur singularly. Each cluster contains 2-6 events. The irregularity of the number of events per cluster and the duration of aseismic intervals between clusters are consistent responses to an inherently complex system like a fault zone governed by nonlinear rate-and-state friction. We find that slightly varying the a-b values of the weakening zone shifts the temporal distribution of earthquake cluster implying a complex relationship between the distribution of different rock units in a fault zone and the resulting slip patterns despite constant loading conditions.

The down-dip velocity-strengthening zone creeps steadily in our model, effectively constantly loading the variably locked velocity-weakening patch updip of it. The updip velocity-strengthening zone also generally creeps steadily, though fault patches within the transition into the velocity-weakening zone experience small slip-transients as well, and can rupture seismically if earthquakes from the weakening zone propagate far enough updip or downdip into the transition zones. Some earthquakes originate from the downdip end of the weakening patch and rupture updip, but most events rupture the center of the weakening patch and propagate both updip and

downdip. Some events are fully stopped downdip by the strengthening portion of the fault, while others propagate downdip a few km into the strengthening portion as slow-slip events. The fully strengthening portions accommodate most of the far-field loading by aseismic creep, but we note that the fully weakening patch and some patches within the transition zones from strengthening to weakening accommodate significant slip both by both seismic rupture during earthquakes and aseismic creep during slow-slip events.

Slow-slip events within the weakening patch are not purely simple periodic, but rather exhibit a complex oscillatory behavior between faster and slower slow-slip events (Figure 3.8b). During the slower events the fault reaches maximum velocities one order of magnitude higher than V_p and during faster events it reaches maximum velocities two to three orders of magnitude higher than V_p . The recurrence time after a faster slow-slip event before the next event occurs is longer than the recurrence time after slower events. After faster events the recurrence time ranges from 80 – 100 years, while after slower events it ranges from 40 – 60 years. Transient slip lasts for 5 – 25 years within each event, though the maximum velocity is typically sustained for less than 1 year. Within the slow-slip dominated periods the slip velocity of the weakening patch resembles the ‘complex periodic’ stability regime of Liu & Rice (2007).

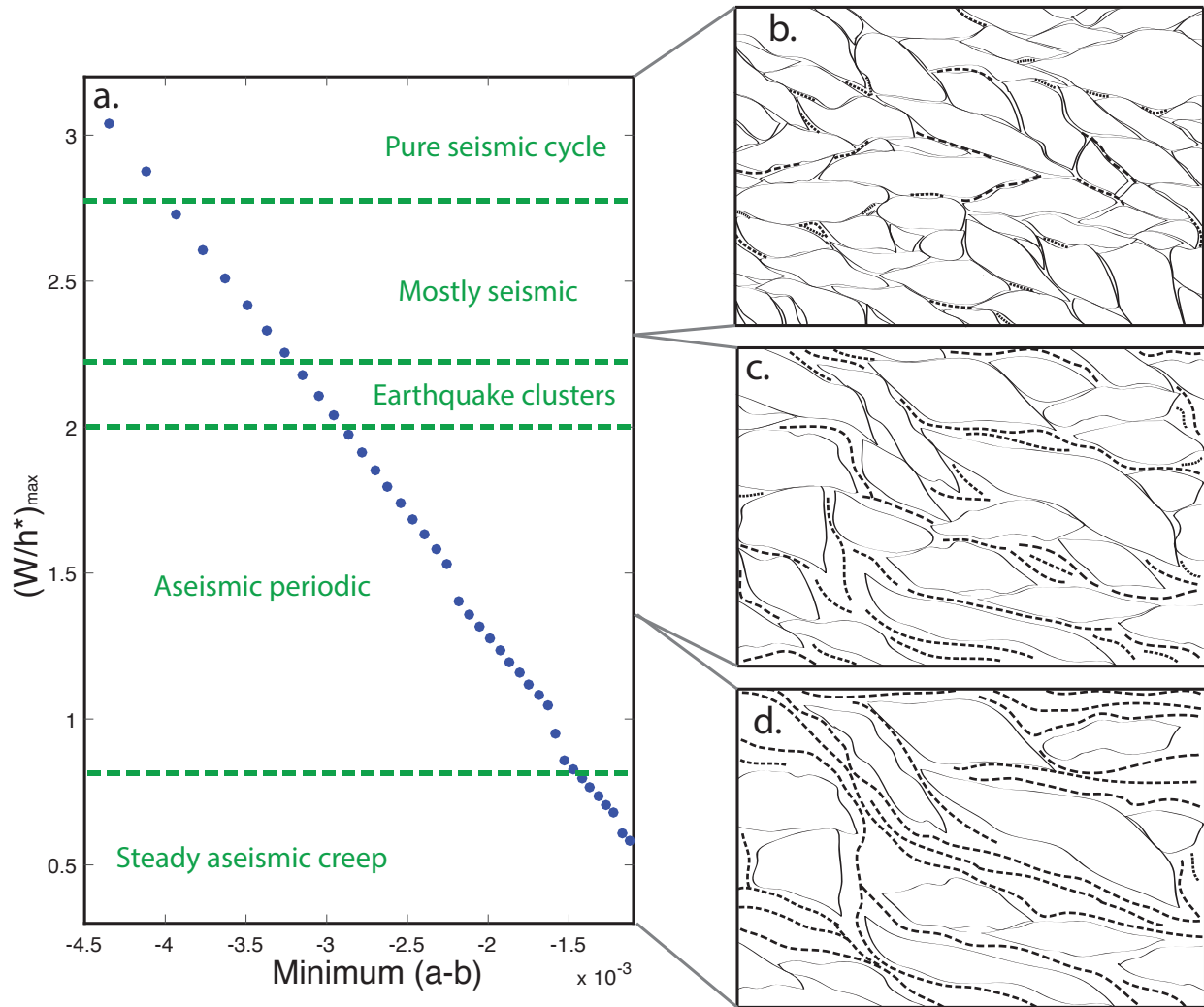


Figure 3.7. a. $(W/h^*)_{\max}$ vs. minimum a-b for a typical normal fault model, each blue dot represents one model run with a different κ . Green dashed lines show the slip response regimes from Figure 3.5. b. Predominantly tightly-packed brittle competent shear zone, corresponding to seismic cycle slip. c. Shear zone with a higher proportion of incompetent ductile matrix, allowing some small interconnected matrix-filled fracture networks to form, facilitating a combination of seismic and aseismic slip. d. Shear zone with a sufficient proportion of ductile incompetent matrix to form large interconnected fracture networks, facilitating predominantly aseismic creep processes.

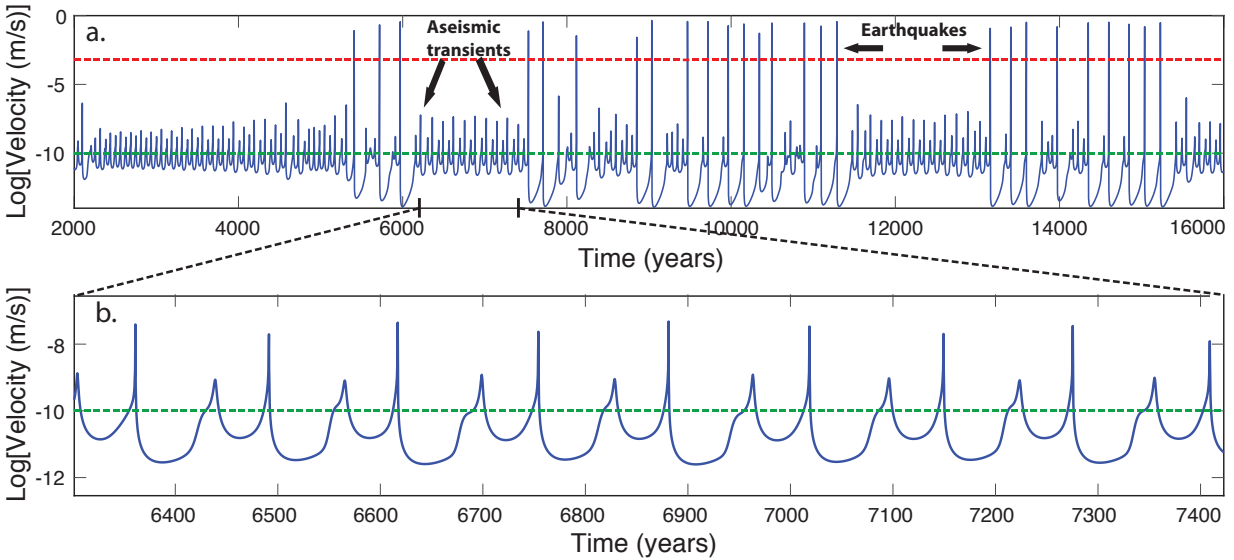


Figure 3.8. a. Slip velocity over time for the weakening patch (at point P1; see Figure 3.1 for its location) in the model setup described in section 3.3.2. Note the clustered seismic events separated by 1 kyr – timescale periods of aseismic slow-slip transients. b. Zoomed-in velocity vs. time plot showing complex periodic aseismic creep events occurring between earthquake clusters. Note the oscillation between slower and faster creep events. Red dashed line denotes 1 mm/s slip rates for reference. Green dashed lines denote the loading plate-velocity of $V_p = 3$ mm/yr.

3.4. DISCUSSION

3.4.1. Earthquake clusters and creep events

The clustered earthquakes in our model (Figure 3.8a) suggest that a fault under constant tectonic loading can slip in irregular high strain-rate periods separated by quiet periods of plate-velocity-scale strain-rate and few to no earthquakes. We refer to these 1-10 kyr cycles as supercycles because they include numerous seismic cycles and span much longer periods of time than traditional seismic cycles. Our results agree with Friedrich et al. (2003) who note that to explain the high Holocene slip-rate recorded on the WFZ as earthquake clusters in the geologic record under traditional time-predictable or slip-predictable earthquake models would require a highly variable loading rate on the 10-kyr timescale, for which there is no evident or compelling geophysical mechanism. We propose that the observed earthquake clusters and variable slip-rate

periods observed on normal faults such as the Wasatch Fault Zone can be explained by rate-and-state constitutive friction laws. We note that the number of earthquakes in our 25-kyr model exceeds the number recorded and identified on the Wasatch Fault segment in a similar time period, however this discrepancy may be explained by a lack of preservation of WFZ events, assumptions in our model, or the fact that far-field tectonic loading may be partially accommodated by neighboring fault segments or splay faults. Our models show that heterogeneously distributed realistic rate-and-state friction values across a normal fault zone under constant tectonic loading can produce earthquake clusters and slip-transients on 10 kyr timescales.

The slip-transients we have described as slow-slip events constitute a significant portion of the long-term slip on our modeled fault. It is important to distinguish these transients from traditional slow-slip events seen globally in subduction zones. The events in our model have recurrence intervals of 40-60 years, while slow-slip event recurrence intervals in subduction zones range from months to a few years (Schwartz & Rokosky, 2007). The modeled normal fault slip transients accommodate 15-20 cm of slip per event, but this slip occurs over 5 – 25 years, suggesting that these transients are recurring periods of high creep-rate, rather than distinct short-duration ‘events,’ such as those seen in subduction zones. Nonetheless, the bimodal populations of fast and slow creep events (Figure 3.8b) in our model correlate well with slow-slip events observed on the Hikurangi subduction interface off of New Zealand, where both short-term (a few weeks) and long-term (1-1.5 years) events have been recorded (Wallace et al., 2012). In addition, Veedu & Barbot (2016) report bimodal ‘bursts’ of slip in a three-dimensional rate-and-state model of the Parkfield segment of the San Andreas Fault which correspond to the observed low-frequency earthquake ‘period-doubling’ recurrence intervals of both three and six days. As in our study, they report lower slip in events following the longer inter-event periods (see Extended Data Figure 1b in Veedu & Barbot (2016) for comparison to Figure 3.8b of this study). While our results cannot resolve whether the deformation mechanism in subduction zone slow-slip events, strike-slip periodic tremor events and normal fault slow-slip transients are the same, it is plausible that the processes are mechanistically similar and that the difference in duration, total slip magnitude, and

recurrence interval are caused by the order-of-magnitude difference in tectonic loading and plate velocity.

3.4.2. Control on slip response by shear zone composition

The model parameter that most directly affects which slip mode the fault deforms by is the smoothing factor κ , which reduces the amplitude of the velocity-weakening peak on the a-b profile along the fault. Our physical interpretation is that κ represents the bulk ratio of incompetent ductile matrix to competent brittle clasts in the shear zone near the brittle-ductile transition (e.g., Fagereng & Sibson, 2010; Lavier et al., 2013; Jammes et al., 2015; Reber et al., 2015). Normal faults with shear zones composed mostly of well-packed competent clasts are more likely to slip in a periodic seismic cycle, while those with shear zones composed of a mix of competent and incompetent material are more likely to give rise to earthquake clusters like those seen on the WFZ and the FFS. Shear zones composed of mostly incompetent matrix may deform in slow-slip or creep transients, while completely ductile shear zones promote steady aseismic creep, possibly along networks of very low-friction minerals (e.g., Collettini et al., 2009). Higher smoothing also increases the total length of velocity-strengthening patches surrounding the velocity-weakening patch, which may buffer some of the stress-perturbations that would otherwise lead to rupture in the velocity-weakening patch by relieving stress as creep updip and downdip of it. The increased length of velocity-strengthening patches may arrest seismic rupture from the velocity-weakening patch more efficiently than in the unsmoothed case. These effects represent a scenario with a smaller velocity-weakening patch, which could be due to different shear zone rock compositions and rheologies or a higher geothermal gradient.

Our modeled fault differs from previous studies in our treatment of the geometrical and frictional heterogeneity within the velocity-weakening section of a fault. The velocity-weakening patch is frictionally heterogeneous, transitioning from the velocity-neutral stability transition around 4 km depth to a velocity-weakening peak around 4.5 km depth back to a velocity-neutral

lower stability transition around 5 km depth (Figure 3.2). Experimental data (Den Hartog & Spiers, 2013; Niemeijer & Collettini, 2014) show that $a-b$ is a function of temperature, which implies that $a-b$ is also a function of depth in a fault zone. In addition, the polymineralic nature of fault zones (quartzofeldspathic rocks for example) and the variability in rheological behavior of the different mineral phases as functions of temperature, pressure, and fluid content (Lavier et al., 2013; Reber et al., 2015; Jammes et al., 2015) suggest that the ratio of brittle (dominantly weakening) versus ductile (dominantly strengthening) material decreases with depth. We therefore argue that gradual friction transitions through the velocity-weakening patch better reflect the temperature-dependence seen in experiments and the polymineralic nature of fault rheology than abrupt frictional transitions at specific depths between homogeneous velocity-strengthening and velocity-weakening segments do.

Another motivation for using gradual friction transitions is the complexity of stress and slip interactions between different rock layers. Experimental data represent friction within individual fault rock units under specific temperature and pressure conditions, but fault cores are composed of multiple rock layers of different strengths, competencies, and rate-and-state parameters. Smith & Faulkner (2010) and Niemeijer & Collettini (2014) show that the Zuccale Fault core is composed of five unique rock units of different mineralogies, coefficients of friction, and rate-and-state parameters. Active slip surfaces are not necessarily planes within one particular rock unit, hence the interactions between stick-slip on velocity-weakening surfaces and creep along velocity-strengthening surfaces suggests bulk stability complexity that is not fully understood. Therefore, we prescribe gradual transitions in $a-b$ through the velocity-weakening patch to represent the bulk stability of a given section of a shear zone, understanding that our bulk-stability interpretation diverges slightly from the traditional description of rate-and-state friction as a property of a particular predefined planar interface between two surfaces.

We interpret $a-b$ values on a 2D fault model as a function of the frictional properties of individual fault rock units, the proportions of the fault core made of each unit, and of the geometry of fractures, clasts, and matrix within the shear zone. Lavier et al. (2013) suggest that the

development of interconnected fracture networks through a shear zone may promote creep via ductile deformation of low-viscosity material within the fracture network. Similar networks of talc have been proposed to facilitate aseismic creep on LANFs (Collettini et al., 2009). A shear zone with a sufficient proportion of interconnected low-viscosity velocity-strengthening material oriented favorably to creep may yield a positive bulk value of $a-b$ for that fault patch, even in the presence of abundant clasts of velocity-weakening rocks. Fagereng & Sibson (2010) and Niemeijer & Collettini (2014) propose that shear zones composed of a mixture of velocity-strengthening and velocity-weakening rocks can deform seismically, but that ruptures between competent velocity-weakening clasts may be impeded and arrested by attempted propagation into neighboring velocity-strengthening material.

We propose that gradual transitions better represent shear-zone $a-b$ values as a function of increasing temperature and depth as seen in experiments (Den Hartog & Spiers, 2013; Niemeijer & Collettini, 2014). We briefly discuss physical deformation mechanisms that may be active and necessitate a bulk $a-b$ estimation. Niemeijer & Collettini (2014) interpret the lack of influence of effective normal stress on recorded $a-b$ values as an indication that grain-size reduction processes are not important after an initial shear is completed. Our models do not account for the creation of new fractures or grain-size reduction processes. We model earthquakes as an outcome of rate-and-state friction between clasts within the shear zone of velocity-weakening patches and model aseismic creep as localized shear on velocity-strengthening networks. Our bulk $a-b$ representation for mixed velocity-strengthening and velocity-weakening materials simulates the competition between cataclastic flow and slip on thermally weakened surfaces described in Niemeijer & Collettini (2014). Another deformation mechanism they propose to explain the temperature-dependence of $a-b$ in mixed shear zones is frictional-viscous flow, described as the movement of competent rock across a network of weak, interconnected minerals such as talc. This mechanism involves dissolution, diffusion, and precipitation of minor geometric asperities on the competent unit and is highly dependent on temperature and the chemistry of the competent and incompetent units (Niemeijer & Collettini, 2014). We model the wide array of active shear-zone deformation

mechanisms and the complexity of their interactions using a simplified bulk rate-and-state parameter setup.

3.4.3. Shear zone composition and W/h^*

The parameter W/h^* is commonly presented in rate-and-state numerical models as the controlling variable on slip behavior of a fault, however a physical interpretation of W/h^* is not typically discussed further than identifying that the fault length between rate-and-state stability transitions and the critical nucleation length affect the slip behavior (e.g., Liu & Rice, 2007, 2009; Rubin, 2008; Skarbek et al., 2012; Liu et al., 2012; Li & Liu, 2016). We propose a physical interpretation of W/h^* related to the geometry and composition of the shear zone at potentially seismogenic depths. In our model $(W/h^*)_{\max}$ is comparable to the smoothing factor κ and corresponds to the previously discussed slip regimes (Figure 3.7a), which we interpret in terms of the ratio of brittle to ductile material in the shear zone. The width W describes the width of the velocity-weakening portion of the fault, which is determined by the depth at which the bulk rate-and-state stability transitions from velocity-strengthening to velocity-weakening. In terms of shear zone composition, these transitions occur where the fault transitions from a shear zone containing sufficient proportions of velocity-strengthening, ductile, incompetent material to facilitate aseismic creep processes to a shear zone composed of a higher proportion of velocity-weakening, brittle, competent clasts susceptible to seismic rupture following accumulation of elastic strain energy between clast faces. The rheology and frictional parameters of the individual fault rock units are also important in determining the bulk a - b values for a given fault patch, but for a given assortment of shear-zone rock units, we suggest that the depths of bulk frictional transitions, the width W of the potentially seismogenic zone, and the critical slip length h^* are primarily controlled by the temperature, pressure, and proportion of competent to incompetent material of the shear zone.

3.4.4. Future work

An important assumption in our two-dimensional model is that the normal fault is planar and hence is not affected by along-strike variations in geometry or stress. Many normal fault systems, including the WFZ and the FFS, are divided into segments along-strike with unique geometries and stress histories (e.g., McCalpin & Nishenko, 1996; Cowie & Roberts, 2001; Friedrich et al., 2003; Velasco et al., 2010; Benedetti et al., 2013). Some earthquakes rupture all connected segments in these systems, while other rupture through only one or a few (e.g., McCalpin & Nishenko, 1996; Friedrich et al., 2003; Benedetti et al., 2013). Along-strike linkage geometries and stress interactions between individual fault segments have been proposed to explain variable loading and slip-rate along-strike (e.g., Bürgmann et al., 1994; Cowie & Roberts, 2001) and Coulomb stress-shadows are thought to limit along-strike earthquake rupture between fault segments (Harris & Simpson, 1998). Qiu et al. (2016) find that slip complexity and earthquakes of varying magnitudes and rupture characteristics arise spontaneously from a three-dimensional rate-and-state model with uniform velocity-weakening $a-b$ to 20 km depth overlying a downdip region with uniform velocity-strengthening $a-b$ values when applied to a realistic three-dimensional geometry of the main Himalayan thrust. Our model does not account for along-strike heterogeneity and we expect that future work applying rate-and-state friction to a three-dimensional system of segmented normal faults will reveal more details about stress and strain accumulation and release over multiple seismic cycles. We recognize the limitations in applying our two-dimensional model results to explain the full slip and stress history of any particular fault system, but we believe there is merit in exploring the range of potential slip behaviors on normal faults in relatively isolated systems in order to better understand the frictional conditions that may give rise to geologically and geodetically observed fault slip. We hope this paper stimulates discussion of slip complexity on normal faults and prompts more rigorous three-dimensional modeling studies of more complete normal fault systems.

Collecting data to test our hypothesis that long-period aseismic complex-periodic creep events can occur on constantly loaded normal faults is difficult due to preservation and resolution

issues in the geologic record. Friedrich et al. (2003) assert that third-order slip transients, such as our modeled creep events, are unlikely to be recorded in the geologic record. These events would likely be indistinguishable from steady-creep deformation or may be erroneously associated with the slip of a preceding or succeeding earthquake. Nonetheless, testing models with data is crucial and we suggest two methods for testing our results.

First, maintaining campaign or continuous GPS networks across normal faults, such as BARGEN in the Basin & Range (e.g., Niemi et al., 2004), over 50-100 years should be able to resolve potential changes in annual slip-rate due to entering or exiting a creep event. More immediately, coral paleogeodesy of uplifted coral terraces on active normal fault hanging walls, such as those in SE Papua New Guinea, may be able to resolve 1-5 kyr slip histories of both earthquakes (from dating terraces) and creep events (from dating growth stagnation periods in individual coral microatolls). Coral paleogeodesy on near-trench terraces has proved useful in revealing detailed deformation histories in subduction zones with variable slip-rates on similar timescales (e.g., Taylor et al., 1985, 2005; Thirumalai et al., 2015) and may be a fruitful path for future work testing variable slip-rates on normal faults with appropriate coral assemblages.

3.5. CONCLUSIONS

We show that rate-and-state friction can explain earthquake clustering and 10-kyr timescale slip-rate transients on normal faults with realistic physical and frictional properties, such as those recorded in the geologic record in the Wasatch Front of the Basin and Range and in the Fucino Fault System in central Italy. Our models suggest that slip transients occur on normal faults and may play an important role in the long-term deformation of a normal fault zone. Our results show that slow-slip transients can occur on fault patches that also slip seismically at times, suggesting that multiple slip modes can be active on the same normal fault patch over 10-kyr timescales. We propose that the ratio of competent to incompetent material in the shear zone near the brittle-ductile

transition may control the slip regime of an active normal fault, and may be the most appropriate physical interpretation of the commonly reported controlling parameter W/h^* .

Recognizing transient slip patterns on normal faults in GPS data or the geologic record will advance our understanding of the spectrum of fault slip behaviors and allow for detailed comparison of normal fault slip styles with slip patterns in other tectonic settings. A spectrum of transient slip styles is known to play an important role in the net slip of some subduction zone thrust faults in the form of slow-slip events, low- and very-low-frequency earthquakes, and tremor tremor. Further geologic, geophysical and modeling studies examining the mechanisms that cause slip transients in normal faults and subduction zone faults will provide insight on a potential relationship between the two phenomena.

Chapter 4: Emerged Coral Reefs Record Holocene Low-angle Normal Fault Earthquakes

Copyright statement: An edited version of this paper was published by AGU. Copyright 2020 American Geophysical Union.

Biemiller, J., Taylor, F., Lavier, L., Yu, T. L., Wallace, L., & Shen, C. C. (2020). Emerged Coral Reefs Record Holocene Low-Angle Normal Fault Earthquakes. *Geophysical Research Letters*, 47(20), 1–12. <https://doi.org/10.1029/2020GL089301>

ABSTRACT

Low-angle normal faults (LANFs; dip $<30^\circ$) accommodate kilometers of crustal extension, yet it remains unclear whether these faults can host large earthquakes or if they predominantly creep aseismically. Most active LANFs typically slip at rates of <3 mm/yr. Here, we report U-Th ages from a series of distinct levels of formerly shallow-living corals killed by uplift-induced emergence of the footwall of one of the world's fastest-slipping LANFs, the Mai'iu fault in Papua New Guinea, which slips at rates of 8-12 mm/yr. Coral ages and coastal morphology indicate punctuated episodic uplift events consistent with seismic slip on the Mai'iu fault. Maximum episodic uplift increments of 0.5-1.8 m imply earthquakes of $M_w >7$. We present the first coral paleoseismological record of normal fault earthquakes, which constrain the timing and surface uplift patterns of multiple LANF seismic cycles and confirm that LANFs can slip in large ($M_w >7$) earthquakes.

PLAIN LANGUAGE SUMMARY

The Earth's crust breaks along fractures and faults, including 'normal faults,' where tectonic plates pull apart. Subsequent slip on these faults enables plates to move away from each other and can occur via slow fault creep or infrequent fast earthquakes. Although normal faults typically intersect the surface of the Earth at a steep angle, some low-angle normal faults intersect

the Earth's surface at a shallower angle. It remains unclear whether these faults typically creep gradually or slip in large earthquakes because active low-angle normal faults are uncommon and slip at low long-term slip rates. This study uses uplifted fossilized coral reefs to reconstruct the timing and style of fault slip near one of the world's fastest-slipping low-angle normal faults, the Mai'iu fault in Papua New Guinea. Isotopic and geomorphological evidence from corals killed by fault-related coastal uplift show that the Mai'iu fault slips infrequently and episodically, revealing a history of large earthquakes in this region.

4.1. INTRODUCTION

Under typical Andersonian stress regimes with static friction coefficients of 0.6-0.85 (Byerlee's friction), normal faults tend to form and slip at dips of 45-60° and should frictionally lock up at dips <30° (e.g., Collettini & Sibson, 2001, and references within). Despite their enigmatic frictional origins, normal-sense detachment faults dipping <30° commonly record km-scale geologic offsets (e.g., Axen, 2004; Lister & Davis, 1989). Detachment-style low-angle normal fault (LANF; dip <30°) systems typically consist of a main shallowly-dipping detachment underlying a series of more steeply-dipping normal 'splay' faults that dissect the hangingwall (e.g., Axen, 2004; Lister & Davis, 1989; Wernicke, 1995). These splays may cut rider blocks, sections of hangingwall material that move with the footwall following abandonment of the shallowest portion of the LANF (e.g., Choi et al., 2013; Webber et al., 2020). Active LANFs are rare and typically slip at dip-slip rates of ≤ 5 mm/yr (e.g., Webber et al., 2018), and it remains unclear whether LANFs can slip in large ($M_w \geq 7.0$) earthquakes (e.g., Abers, 2009).

Dipping 16-24° at the surface and slipping at dip-slip rates of 8-12 mm/yr, the Mai'iu fault in Papua New Guinea is one of the world's fastest-slipping LANFs (Biemiller et al., 2020b; Wallace et al., 2014; Webber et al., 2018). These high slip rates raise important questions about the seismic style of active LANF systems. Do LANFs creep aseismically or slip in large episodic earthquakes? Does seismic slip rupture both the underlying low-angle detachment and the steeper

splay faults? The Mai'iu fault provides an ideal natural laboratory to investigate the seismic style of active LANFs. Here, we use coral paleogeodesy to construct a record of Holocene slip in Goodenough Bay, where the uplifting Mai'iu fault footwall forms a coral-fringed coastline (Figure 4.1).

4.1.1. LANF seismicity

The longstanding question of whether LANFs host large earthquakes remains unresolved due to somewhat conflicting observations from geology, geodesy and seismology. Despite km-scale extensional offsets on LANFs (e.g., Axen, 2004; Lister & Davis, 1989), ancient seismically generated LANF pseudotachylites (e.g., Little et al., 2019; Prante et al., 2014), modern evidence of complex transtensional ruptures involving slip on an underlying low-angle detachment (Fletcher et al., 2014, 2016), and evidence for active LANF slip (Webber et al., 2018, references within), few large earthquakes with low-angle normal-sense rupture planes have been recorded (Abers, 2001, 2009; Collettini, 2011; Jackson & White, 1989). The largest LANF earthquakes with well-resolved rupture planes were M_w 5.9-6.2 events with dips of 30-33° (Jackson & White, 1989; Collettini, 2011), but the larger 1985 M_w 6.8 Woodlark Basin earthquake is inferred to have occurred on a seismically imaged LANF (Abers et al., 1997; Abers, 2001). Based on limited GPS data and historical accounts, Cummins et al. (2020) proposed that the ~12°-dipping Banda detachment beneath the Banda Sea slips in large ($M_w > 7.5$) earthquakes at rates of 5-6 cm/yr. GPS velocities across the 15-20°-dipping Altotiberina fault in the Apennines have been used to infer that the fault is primarily creeping aseismically (Hreinsdóttir & Bennett, 2009), while subsequent modeling prefers spatially heterogeneous creep and locking on both the Altotiberina and its hangingwall splays (Anderlini et al., 2016). Microseismicity on its creeping segments shows that some seismic slip accompanies creep, but only ~30% of slip appears to be accommodated seismically (Valoroso et al., 2017). Structural geology, seismic reflection imaging, microseismicity and geodetic modeling support the emerging view that the Altotiberina fault

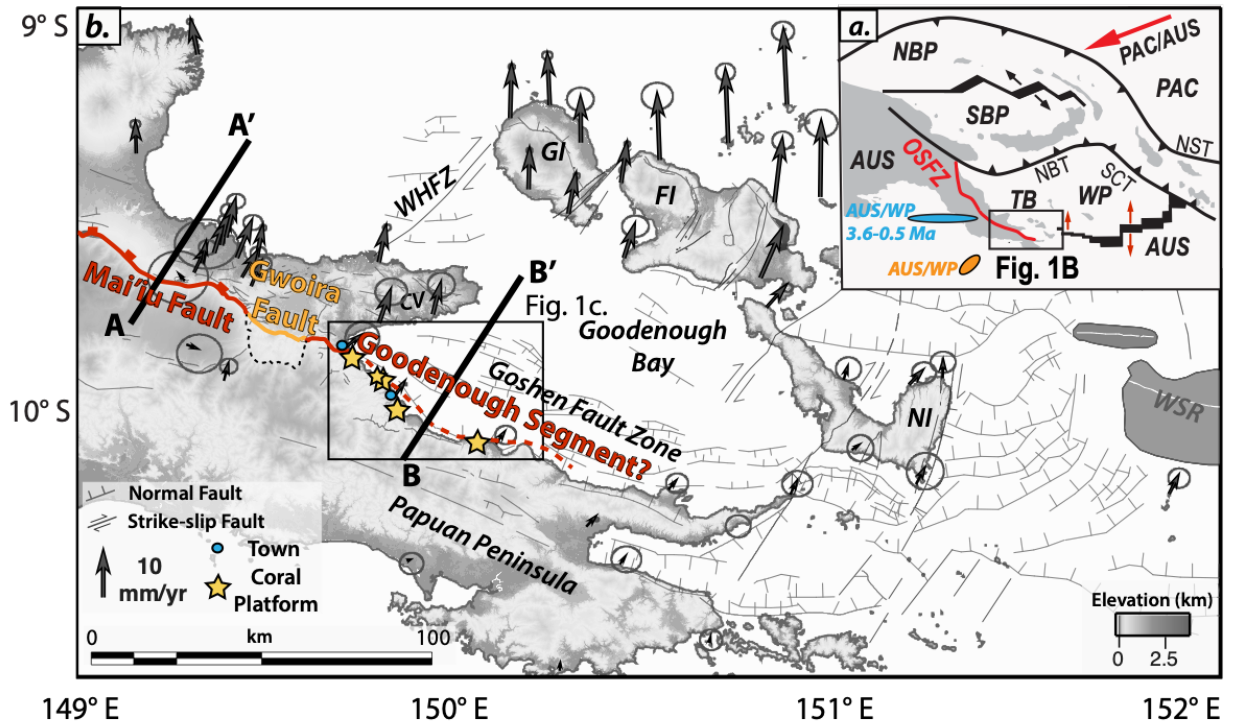
consists of both predominantly creeping (Umbria-Marche) and predominantly locked (Citta-di-Castello) segments (Anderlini et al., 2016; Brozetti et al., 2009; Hreinsdóttir & Bennett, 2009; Valoroso et al., 2017). However, friction experiments on exhumed LANF rocks and gouges show primarily velocity-strengthening behavior (Niemeijer & Collettini, 2014; Numelin et al., 2007; Smith & Faulkner, 2010) which should promote aseismic creep and inhibit seismic slip, although some protoliths of LANF gouges show velocity-weakening behavior (Biemiller et al., 2020b). Disparate observations indicate that LANFs are mechanically and frictionally heterogeneous structures that deform by a spatiotemporally complex mixture of seismic and aseismic processes.

4.1.2. Tectonic setting

Strike-perpendicular horizontal extension of 8-11 mm/yr across the ESE-WNW-striking Mai'iu fault is driven by rapid counter-clockwise rotation of the Woodlark microplate (Wallace et al., 2014) in response to northward subduction of oceanic crust underlying the Solomon Sea at the New Britain and San Cristobal trenches (e.g., Baldwin et al., 2012; Wallace et al., 2004; Figure 4.1). Where the Mai'iu fault dips 16-24° at the surface, it exhumes the Dayman-Suckling metamorphic core complex in its western end via a rolling-hinge process along a convex-up fault that steepens to 30-40° from ~5-10 km depth (Figure 4.1e; Abers et al., 2016; Little et al., 2019; Mizera et al., 2019; Webber et al., 2020). East of the shallowly dipping surface trace, the uppermost ~1 km-deep portion of the Mai'iu fault has been abandoned and its hanging wall is cut by the active and more steeply-dipping Gwoira fault, which outlines the actively back-tilting Gwoira rider block (Webber et al., 2020). East of the Gwoira fault, extension is distributed across the D'Entrecasteaux Islands, faults within Goodenough Bay including the Goshen fault zone, and the Mai'iu-Gwoira-Goodenough (MGG) fault system (Figure 4.1b), as evidenced by GPS velocities, microseismicity, and seismic reflection imaging (Abers et al., 2016; Biemiller et al., 2020b; Fitz, 2011; Fitz & Mann, 2013a, 2013b; Wallace et al., 2014). Here, the MGG system steps offshore and appears to follow the southern Goodenough Bay shoreline, as reflected in the young fault-

bounded faceted morphology of the steep ($\sim 45^\circ$ -dipping) northernmost slopes there (Figure 4.1d) and inferred from seismic reflection profiles (Fitz & Mann, 2013a). Fault surface modeling of structural measurements and microseismicity suggests that the Mai'iu fault dips $20\text{-}30^\circ$ below Siri Siri (Webber et al., 2020), at the western edge of Goodenough Bay near the coral sampling locations in our study (Figure 4.1c). Schematic crustal cross-sections drawn after Fitz & Mann (2013a) compare the inferred MGG fault geometries along the Dayman and Goodenough segments in Figures 4.1e-f. East of Normanby Island, continental breakup is complete and extension proceeds via seafloor spreading at the Woodlark Spreading Ridge (Figure 4.1).

The southern Goodenough Bay coastline is characterized by rounded headlands where coral reefs armor the coast, alternating with embayments in which sediment accumulates and suppresses reef development (Figure 4.1c-d). The coastal morphology, fossil coral reefs subaerially exposed to elevations >300 m, and previously reported late Holocene coastal uplift rates of >3 mm/yr (Mann & Taylor, 2002; Mann et al., 2004, 2009) reflect rapid late Quaternary coastal uplift and confirm that the Goodenough segment of the MGG fault is an ideal location to study active LANF slip. We surveyed, sampled, and dated these emerged coral reefs at five locations (Figure 4.1c) to reconstruct the uplift and slip history of the active MGG LANF system.



PAC = Pacific Plate; AUS = Australian Plate; WP = Woodlark Plate; NBP = North Bismarck Plate; SBP = South Bismarck Plate; NBT = New Britain Trench; SCT = San Cristobal Trench; OSFZ = Owen-Stanley Fault Zone; MGG = Mai'iu-Gwoira-Goodenough; WHFZ = Ward Hunt Fault Zone; CV = Cape Vogel; WSR = Woodlark Spreading Ridge; D'Entrecasteaux Islands: GI = Goodenough Island; FI = Fergusson Island; NI = Normanby Island.

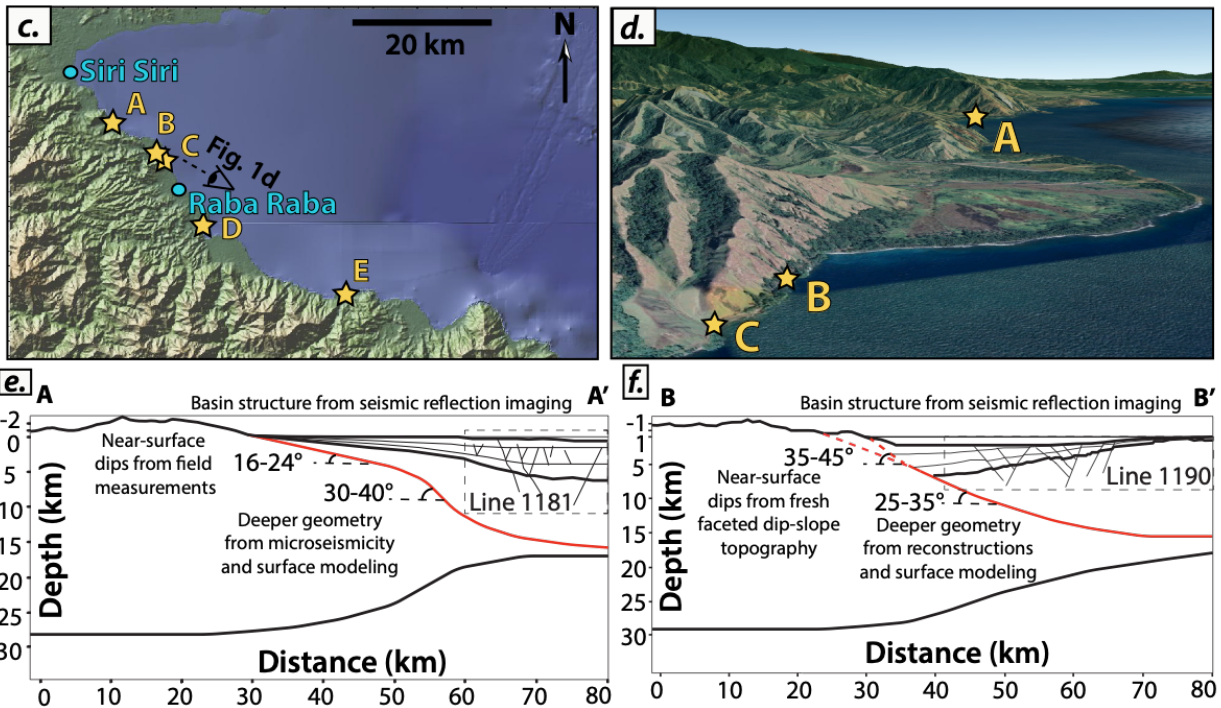


Figure 4.1. a.) Tectonic map with present (orange; Wallace et al., 2014) and 3.6—0.5 Ma (blue; Taylor et al., 1999) poles of rotation of the Woodlark Plate relative to the Australian Plate. b.) Local tectonic map with faults from Little et al. (2019). The MGG fault system is mapped in three segments: the 16-24° dipping Mai’iu fault (red), the more steeply dipping Gwoira fault (yellow) and the inferred offshore continuation through Goodenough Bay (dashed red). GPS velocity vectors from Wallace et al. (2014) and Biemiller et al. (2020b). c.) Emerged Holocene corals dated in this study; d.) Along-strike view of fault-bounded topography along the southern Goodenough Bay coastline; e-f.) Schematic crustal-scale cross-sections across the Dayman (e; A-A’) and Goodenough segments (f; B-B’) based on interpreted seismic lines (Fitz & Mann, 2013a; Fitz, 2011). Representative geometry of the Mai’iu fault (solid red) and potentially active synthetic splay faults (dashed red) are inferred from surface geology, seismic reflection, and microseismicity (Abers et al., 2016; Fitz & Mann, 2013a; Little et al., 2019; Mizera et al., 2019; Webber et al., 2020). Topography from 90-m SRTM data and GeoMapApp (<http://www.geomapapp.org>).

4.2. METHODS

4.2.1. General approach

Corals die if they emerge above some highest level of survival (HLS) that for many corals is near mean low low water (MLLW) (e.g., Goodwin & Harvey, 2008). This simple mechanism of subaerial coral death is a fundamental principle of coral paleosea-level and paleogeodesy: when relative sea-level drops such that a coral is no longer sufficiently submerged, that coral dies (e.g., Sieh et al., 2008; Taylor et al., 1980, 1987, 1990; Thirumalai et al., 2015; Zachariassen et al., 1999, 2000). The radiometric clock (U-Th) begins ticking when the coral dies and ceases to fix radioactive isotopes into its carbonate skeleton. By sampling, surveying, and dating the youngest parts of corals from surfaces that emerged due to relative sea-level fall, it is possible to reconstruct the timing and magnitude of coastal emergence. It is crucial to sample the youngest corals in growth position across the emerged reef to ensure that measured maximum ages reflect the timing of coastal emergence. For example, corals below the reef surface may return ages older than that of subaerial emergence, whereas the youngest, surficial corals should return ages similar or identical to that of emergence.

Using these approaches, we identified, sampled and dated emerged coral shorelines from five locations along the Goodenough Bay coastline (Figure 4.1c-d; Appendix Figure C.1), labeled A-E from west to east. Our basic observations are that corals have emerged; additional evidence for meter-scale emergence events (>10 m total late Holocene emergence) in the absence of large non-tectonic sea-level changes leads us to conclude that the vast majority of emergence occurred by tectonic uplift in abrupt events (section 4.4.1).

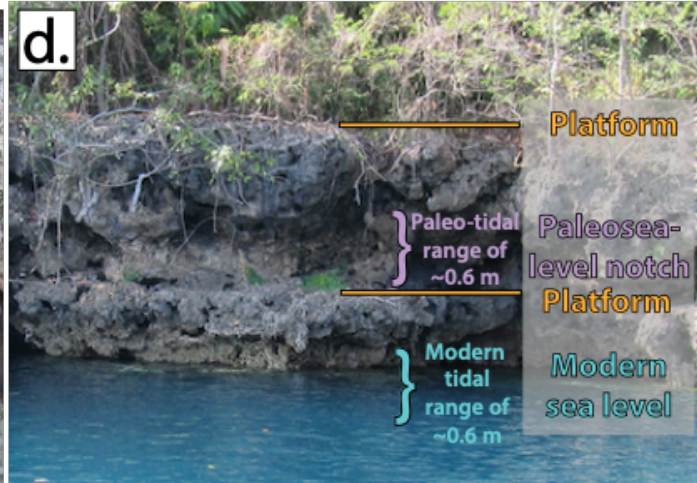
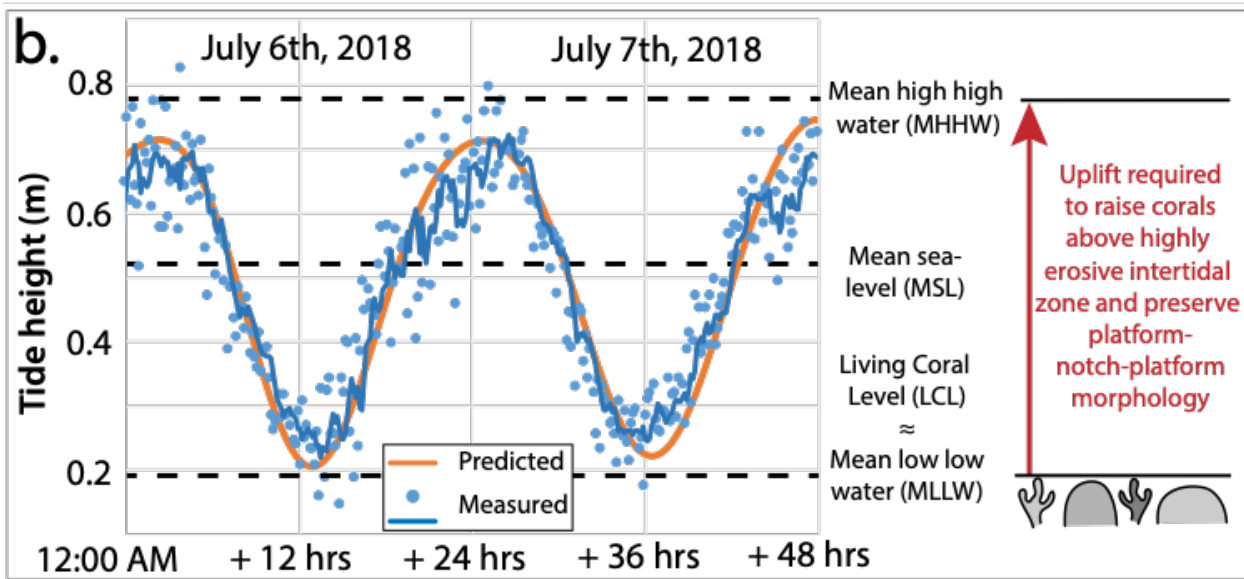
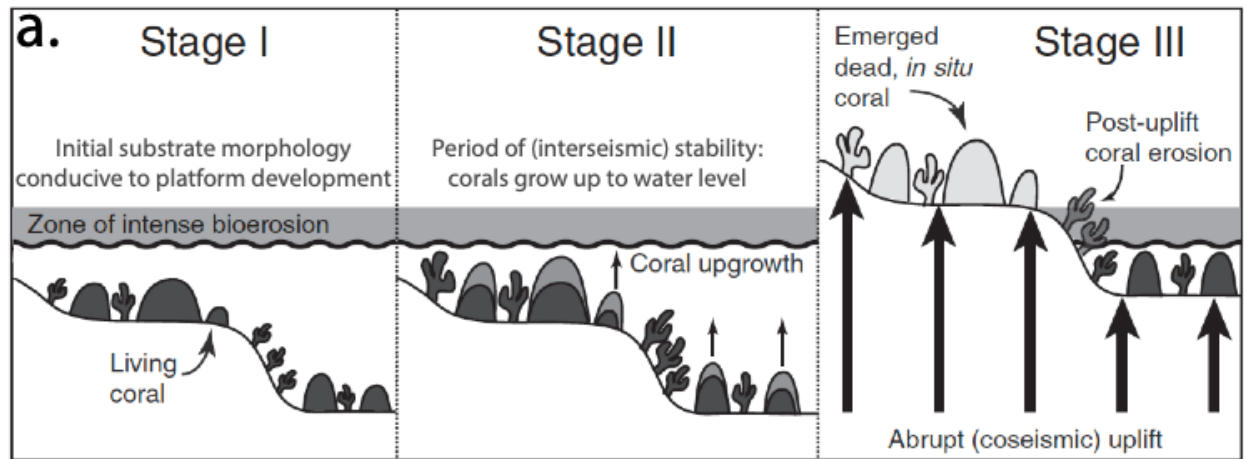


Figure 4.2. a.) Schematic modified from Thirumalai et al. (2015) showing growth and rapid emergence of a coral platform. b.) Predicted and measured tidal range over two days, showing estimated emergence required to preserve distinct platforms (section 4.4.1). c.) Sampled encrusting *Favia* sp. coral. d.) Emerged platform-notch-platform sequence with labeled mean tidal range.

4.2.2. Surveying and sampling

The best-preserved emerged corals were found encrusting distinct uneroded reef platforms (Figure 4.2d). To ensure that sampled corals closely represent those living just prior to emergence, we sampled only corals in growth position that appeared *in situ* on the uppermost and outermost surfaces of these platforms wherever possible. Corals from the two highest platforms at D were not sampled from its surface due to poor preservation; instead, they were sampled from 1-2 m beneath the surface in cliffs. We avoided corals with off-white interiors, as these were likely infiltrated by terrestrial sediment that could bias U-Th ages by introducing additional ^{230}Th . Certain coral genera (e.g., *Porites* and *Diploastrea*) with open skeletal architectures are more prone to sedimentary contamination. Others, like some *Favia* sp., *Platygyra* spp. and *Goniastrea* spp., are more commonly pristine and uncontaminated (Figure 4.2c). Nonetheless, we sampled a variety of coral species and morphologies common in shallow water. Wherever possible, we collected two or more samples of each platform, although some sites contained more pristine *in situ* corals than others. We leveled and measured sample elevations above living coral level (ALC) where possible. Where living coral level was inaccessible, elevations were measured above current water level (ACW). Tidal adjustments from ACW to ALC from a pressure tide gauge offshore Raba Raba (Figure 4.1c, 4.2b; Appendix Table C.1) are minimal (≤ 5 cm) due to sampling primarily within two hours of low tide amidst dominantly diurnal tidal cycles (Figure 4.2b; Appendix Figure C.5) – i.e. sampling while current water level was approximately equal to MLLW.

4.2.3. U-Th dating

We determined the ages of coral samples with U-Th dating methods using multicollector-inductively coupled plasma mass spectrometry (MC-ICP-MS) (Shen et al., 2012, Cheng et al., 2013). Isotopic determinations are given in Appendix Table C.2. Ages standardized to 1950 CE are given in units of yr BP (where BP = before 1950). For most dates, corrections of only 0.1-5 yr is required using a $^{230}\text{Th}/^{232}\text{Th}$ initial atomic ratio of $4 (\pm 2) \times 10^{-6}$. High ^{232}Th contents of 7814 and 1476 ppt for mid-Holocene samples 18-NADE-W and 18-NADE-Z, respectively, indicate detrital contamination requiring significant corrections of >10 yrs. These coral ages are $3,800 \pm 50$ and $5,337 \pm 22$ yrs, and their age uncertainties are not large enough to alter the interpretation of their emergence ages.

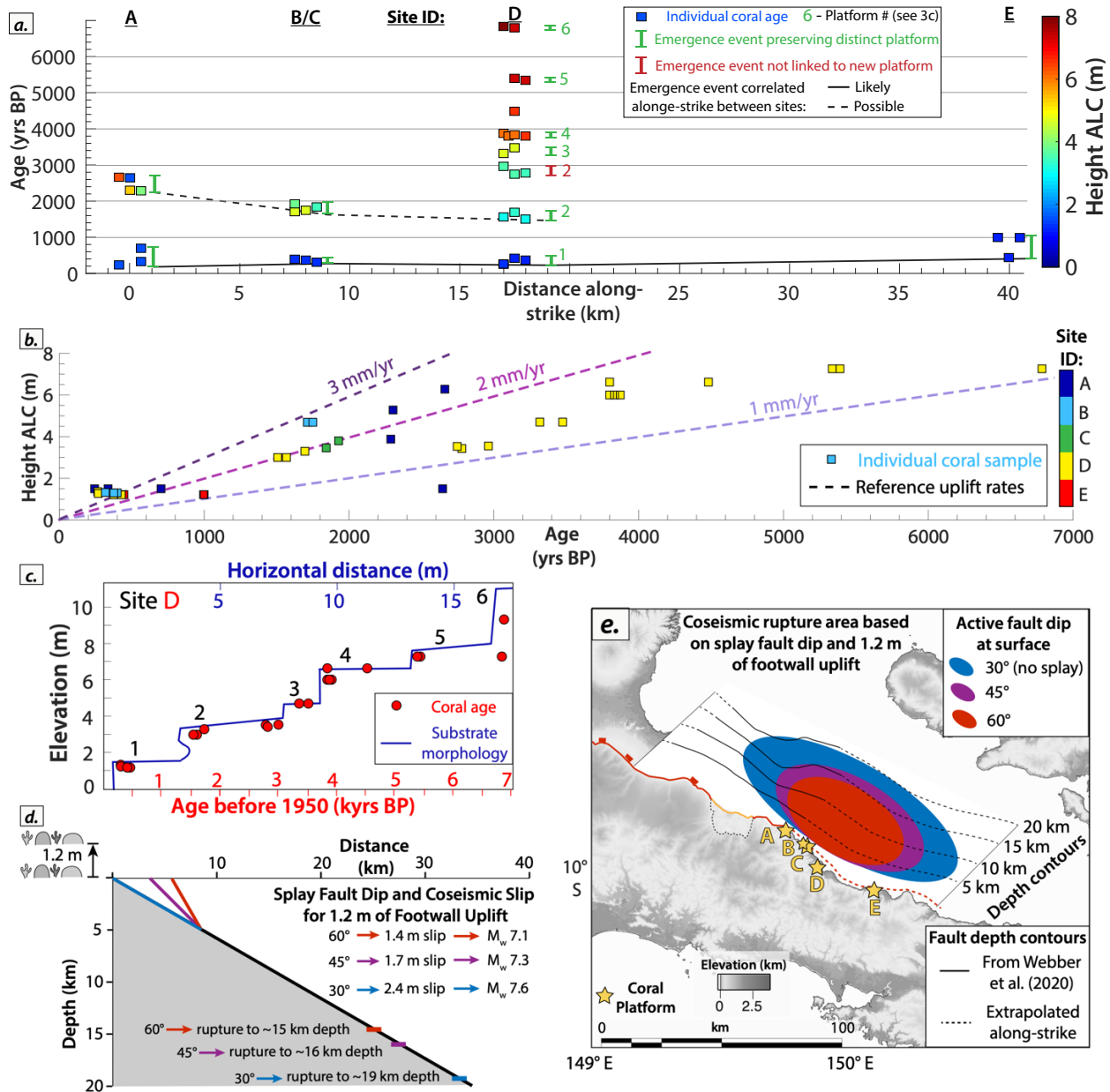


Figure 4.3. a.) Coral ages and along-strike sample locations colored by elevation ALC with lines showing along-strike correlations between emergence events. Plotted ages are offset laterally up to 500 m to show all samples in each cluster. b. All coral ages and elevations ALC colored by site. Dashed lines show reference uplift rates. c.) Coral ages and elevations with schematic topographic profile of individually numbered platform sequence at site D. d.) Inferred coseismic slip characteristics on the MGG detachment for near-surface splay fault dips of 60°, 45°, and 30° (no splay fault) based on 1.2 m of coseismic uplift, a splay-detachment intersection depth of 5 km, and the scaling relationships of Leonard (2010). e.) Mapview of representative rupture areas associated with slip distributions from d. Mai'iu fault depth contours (solid) drawn from Webber et al. (2020) and inferred (dashed) along-strike.

4.3. RESULTS

4.3.1. Coral ages

At each site, we sampled corals from one or more well-preserved emerged shoreline platforms (Figures 4.2d, 4.3a-c; Appendix Figure C.3; Appendix Table C.1). Individual U-Th ages range from 243.2 ± 1.9 to $6,822 \pm 15$ yrs BP (Appendix Table C.2) and show a general trend of higher elevation samples returning older ages, confirming that these ages reflect emergence-related coral death (Figure 4.3a-c). Ages from each platform tend to cluster, most notably at D, which sourced the largest number of dated samples across all sites. Conditions enabling platform formation above the lower two levels (Figure 4.3a) occurred only at D, where four distinct higher-elevation platforms (Figure 4.3c, platforms 3-6) record progressively older emergence ages. Because corals from the highest platforms were sampled from below the platforms' upper surfaces, the ages of platforms 5 and 6 at D indicate maximum emergence ages for these platforms ($\sim 5,337$ and $\sim 6,785$ yrs BP, respectively), which may have emerged several hundred years after these corals died, but certainly emerged prior to emergence of the subsequent lower platform (platform 4; $\sim 3,800$ yrs). Progressively higher and older coral platforms reflect the spatiotemporal history of coastal emergence at D over the last 5,000 years.

4.4. DISCUSSION

4.4.1. Coral ages and coastal morphology record episodic tectonic uplift

In this section, we discuss the evidence and possible mechanisms for episodic emergence. We find that the emerged coral platforms reflect dominantly episodic tectonic emergence of this coast and are the result of several enabling conditions combined with the processes of rapid coral growth just below MLLW and intense bioerosion focused near mean sea-level. These conditions include: 1. A suitably wide, shallow substrate 1-2m below the highest living corals prior to: 2. A period of at least a few hundred years (likely the interseismic period) of relative sea-level stability for corals to build the platform up to MLLW and for erosion above MLLW to create cliffs and

bioerosion/solution notches; and 3. Emergence events > 0.6 m that raise the platform and its corals sufficiently above mean high tide level such that they are protected from intense bioerosion.

Because the most intense erosion (primarily bioerosion) of an emerged reef occurs while it is located in the intertidal zone, the emerged coastal morphology reflects the rate and temporal pattern of coastal emergence. Gradual emergence would expose the entire emerging reef surface to severe intertidal bioerosion, as each coral would spend several hundred years in the intertidal zone as it progressed from MLLW HLS to above high tide levels (Figure 4.2b). This bioerosion would erase distinguishing morphological features of the emerged reef, such as individual coral heads, and may replace them with fossilized bioerosion features such as echinoid burrows (Appendix Figure C.2). For example, at a location with 1 m tidal cycles, a mean steady emergence rate of 2 mm/yr would expose emerging corals to intense intertidal bioerosion for at least 500 years. In contrast, punctuated episodic meter-scale coastal emergence events can rapidly raise previously submerged corals above the intertidal zone and preserve their morphology in a series of well-preserved emerged coral shorelines separated by incised sea-level notches (where there is a cliff) or by eroded surfaces where corals have been partially removed (e.g., Taylor et al., 1980, 1987, 1990, 2008; Thirumalai et al., 2015). However, episodic emergence events do not always correlate one-to-one with emerged platforms, because pre-emergence reef morphology also controls whether distinct platforms form (Taylor et al., 1990; Thirumalai et al., 2015).

Along the southern Goodenough Bay coastline, we found distinct well-preserved platforms hosting intact, minimally eroded branching and head corals (Figure 4.2c,d). At D, we identified six morphological platforms corresponding to seven clusters of Th ages (Figure 4.3c). To preserve each of these platforms, the coastline must have rapidly emerged by an increment $\geq \sim 0.6$ m (the intertidal range: Figure 4.2b). This lower limit of emergence for platform preservation explains why the corals with clustered ages corresponding to ~ 0.5 m of emergence are not preserved within a distinct platform (older cluster of platform 2, Figure 4.3c), while all other corals with clustered ages associated with ≥ 1.2 m of emergence were found within discrete uneroded platforms. Creating and preserving this platform morphology requires both sufficient time for platform

development and sufficient emergence to surpass the intertidal zone. The lowermost platform levels are separated by distinct concave-out sea-level notches containing preserved echinoid burrows at their seaward bases (Appendix Figure C.2). The preservation of these platform-notch-platform sequences indicates episodic meter-scale rapid emergence events preceded by negligible emergence for several hundred years, the time needed to build a platform and erode an intertidal notch (e.g., Berdin et al., 2004; Pirazzoli, 1986).

The platform-notch-platform morphology is indicative of episodic relative sea-level changes, which the U-Th ages confirm (Figure 4.3a). Regional sea-level changes during emergence of these corals have contributed to net emergence, but this component is minor relative to net emergence. In southeastern Papua New Guinea, the relatively well-documented Holocene sea-level record shows only gradual (<0.5 mm/yr) regional sea-level regression since 6 kyrs BP (e.g., Chappell & Polach, 1976; Dickinson, 2009; Grossman et al., 1998; Tamisea & Mitrovica, 2011). Mean global sea-level rise was minimal from ~ 3 to 0.17 kyrs BP, with most occurring after ~ 1860 CE with a global mean of ~ 30 cm (e.g., Church & White, 2011; Kopp et al., 2016). In the absence of meter-scale rapid ocean-volume-driven sea-level regressions, episodic active tectonic uplift is the most likely mechanism causing the emergence of the southern shoreline of Goodenough Bay, consistent with the pristine fault-bounded triangular-faceted scarp morphology of the coastal ranges (Figure 4.1c-d) and previously reported Holocene tectonic uplift (Mann & Taylor, 2002). Based on the distinct morphology of the platform-notch-platform sequences, tectonic uplift must have occurred episodically and abruptly, implying seismic slip on one or more active faults.

4.4.2. Uncertainties

Site D hosts the most individual episodic uplifts recorded by coral paleoshorelines atop morphological platforms, revealing seven uplifts on six distinct terraces with tightly clustered ages (Figure 4.3a). Additionally, sites A, B, D and E all record a shared uplift event around 300 yrs BP.

Nonetheless, a few outliers at A, D, and E are older than the clustered coral emergence ages from their respective platforms, suggesting that the outlier corals died prior to full emergence of their platforms (Figure 4.3b, 4.3d). Although we do not believe these anomalous dates obscure the uplift history, we briefly discuss a few explanations for these outliers. Some corals inevitably died for various reasons prior to full emergence, possibly during previous uplifts too small to emerge the entire platform. Additionally, healthy corals living 1.5 m below sea-level may not thrive when uplifted to 0.3 m below sea-level and could die before emerging subaerially. These corals may be incorporated into a subsequently uplifted platform but would reflect ages from the previous uplift rather than the final uplift that raised them above sea-level. Brief climatically induced sea-level lows, such as the 1982-1983 ENSO events (e.g., Widlansky et al., 2015), may kill some shallow corals without long-term emergence. These processes could explain how a few platforms record ages similar to those at other sites, while also recording some older ages (e.g., the platform at E; platform 5 at D; Figure 4.3). Despite uncertainties and outliers, the clear platform-notch morphology, consistency of the youngest ages of the lowermost platform across all sites and the strong punctuated age-elevation trend at D imply that most emergence occurs episodically during punctuated Holocene seismic slip and consequent meter-scale uplifts.

4.4.3. Maximum recurrence intervals and coseismic uplifts

Inter-uplift-event times at D give recurrence interval estimates for the largest earthquakes, while the height between subsequent platforms gives the maximum vertical throw associated with each earthquake. Smaller earthquakes likely occur more frequently on these faults but do not cause large enough vertical displacements to be recorded by individual preserved platforms. Hence, recurrence intervals and coseismic uplifts calculated here are both maxima, recognizing that smaller uplifts would be incorporated into the elevation and time gaps between uplifts large enough to raise coral platforms above the erosive intertidal zone (Figure 4.2). Stochastic modeling of Gutenberg-Richter-distributed earthquakes of magnitude $2 < M < 7$ on a single fault predicts that

80% of total slip occurs during M 6-7 events while only 20% occurs during M 2-6 events (Nicol et al., 2005), suggesting that the larger earthquakes uplifting platforms above the intertidal zone represent a majority of cumulative fault slip.

Estimated using the heights and youngest coral ages of each platform, recurrence intervals at D are irregular, ranging from 440–1520 years (Appendix Figure C.4). Although platform-preserving maximum coseismic uplifts range from 1.2–1.8 m, three of the four uplifts are between 1.2–1.3 m. Although the regularity of older uplift increments suggests some degree of slip-predictability, the outliers point to a more complicated relationship between time and earthquake slip (Appendix Figure C.4). This variability is similar to that of well-documented active normal fault systems like the Fucino (Benedetti et al., 2013) and Wasatch faults (Machette et al., 1991; McCalpin & Nishenko, 1996).

4.4.4. Low-angle normal fault earthquakes

The coral paleogeodetic record reveals punctuated, episodic uplifts of the southern Goodenough Bay coastline consistent with footwall uplift during seismic slip on the MGG LANF system. Dip-slopes dipping $\sim 45^\circ$ above site B suggest that rupture of that segment propagates to the surface along more steeply-dipping near-surface splay faults that sole into the shallowly-dipping detachment, similar to the active fault geometry beneath the nearby Gwoira rider block (Figure 4.1d, 4.1f; Webber et al., 2020). To determine whether these earthquakes are isolated on the near-surface splay faults or include slip on the low-angle detachment below, we consider earthquake scaling relationships and the slip increments required to produce the observed uplifts. For a near-surface fault dip of 45° , mean coseismic uplifts of 1.2 m at D require up to 1.7 m of coseismic slip. Using self-consistent empirical earthquake width-length-slip scaling laws for interplate dip-slip faults (Leonard, 2010), 1.7 m of slip corresponds to a M_w 7.3 earthquake with 29 km (downdip) rupture width and 67 km (along-strike) rupture length. For a splay-detachment intersection depth of 3 km and detachment dip of 30° , this rupture width implies rupture to 15 km

depth and includes slip on the detachment from 3 – 15 km depth. More shallowly-dipping near-surface fault geometries and larger uplift increments imply larger earthquakes up to M_w 7.6 (Figure 4.3d,e). Although there is some uncertainty in this intersection depth because previous seismic reflection images do not reach the coast, the large increment of coseismic surface uplift strongly implies that part of the underlying low-angle detachment fault has slipped seismically in moderately large earthquakes in the past 6 kyr. Additionally, the inferred along-strike rupture length of 67 km (assuming 1.7 m of slip and scaling relationships from Leonard, 2010) suggests the possibility that the largest earthquakes may rupture both the Goodenough Bay segment and the nearby (<50 km away) shallowly-dipping Dayman segment.

Figure 4.3d-e illustrates the rupture implications of the uncertainty in near-surface detachment and splay fault geometries: more steeply-dipping splay faults require less coseismic slip and smaller rupture areas to generate the episodic uplift increments recorded by the emerged coral reefs. Onshore and offshore splay faults are abundant; however, their dips are not well-constrained. Nonetheless, >1 m uplifts imply coseismic slip to $>\sim 15$ km depth during $M_w > 7$ earthquakes even with a splay-detachment intersection as deep as 5 km (Figures 4.3d,e), suggesting that rupture involves coseismic slip on a significant portion of the detachment.

The coral platforms are not laterally continuously preserved and single platforms can only be definitively tracked along-strike between sites B and C. This lateral variability in platform preservation is due in part to intense erosion and the lack of suitable substrates for platform development along certain stretches of the coast (section 4.4.1); however, some variability may also stem from spatiotemporally complex coseismic rupture patterns, particularly because different sets of splay faults may slip during each earthquake. If rupture occasionally propagates to the surface along some of the inboard onshore splay faults, portions of the coastline may periodically behave as hangingwall blocks, coseismically subsiding rather than uplifting. The spatiotemporal variability of near-surface rupture patterns may also explain the widely variable recurrence intervals and uplift increments in the coral record (section 4.4.3).

Our results show that LANFs can slip in large earthquakes, and that rupture may propagate to the surface along one or more of the many near-surface high-angle splay faults. This style of LANF seismic slip agrees with evidence from the Altotiberina fault, particularly the Citta di Castello region, where surface geology, seismicity, seismic reflection and GPS velocities indicate frictional locking and seismic slip on the 25-30°-dipping detachment to depths of 7-10 km, with ongoing seismic slip and aseismic creep on multiple hangingwall faults (Brozetti et al., 2009; Anderlini et al., 2016). Brozetti et al. (2009) interpret the downdip limit of rupture as the depth at which the LANF flattens into a subhorizontal (dip<10°) midcrustal detachment. For continental LANFs, this geometric transition likely reflects the mechanical transition with depth from predominantly brittle frictional slip in the upper crustal fault zone to predominantly ductile (diffusion or dislocation) creep in a deeper subhorizontal mylonitic shear zone (e.g., Lavier & Manatschal, 2006). There is no direct image showing the Mai'iu fault flattening at depth, but Fitz & Mann (2013a) inferred a flattening depth of ~15 km in structural reconstructions based on seismic reflection data and basin analysis of the Western Goodenough Bay, which aligns with the downdip rupture limit inferred from coral paleo-uplifts. In contrast, microseismicity onshore and offshore western Cape Vogel outlines a 30-40°-dipping planar structure from ~15-25 km depth that appears to delineate the deeper extent of the western Mai'iu fault (Abers et al., 2016), implying that the fault may not flatten above 25 km. Nonetheless, the stark transition from the microseismically quiet upper 15 km to more abundant microseismicity at 15-25 km depth in this region suggests a strong contrast in mechanical behavior (e.g., Harris, 2017; Bürgmann, 2018; references within), consistent with a transition from a frictionally locked fault updip to a ductilely creeping mylonitic shear zone downdip (Biemiller et al., 2020b; Little et al., 2019; Mizera et al., 2020). In summary, evidence for meter-scale uplift events (reflecting >1.5 m of seismic slip on the LANF), combined with likely rupture widths inferred from earthquake scaling relationships suggest that LANF earthquakes can involve the entire seismogenic layer, with rupture from the brittle-ductile transition zone to the surface.

4.5. CONCLUSIONS

U-Th ages from emerged corals confirm active Holocene tectonic uplift of the southern Goodenough Bay coastline and provide paleoseismological evidence of large ($M_w > 7$) earthquakes on a low-angle normal fault. Episodic uplifts of 0.5-1.8 m of the Mai'iu fault footwall suggest that earthquakes can rupture the upper 15 km of the fault, with seismic slip propagating to the surface along higher-angle splay faults. Uplift age-elevation patterns indicate spatiotemporally variable fault slip rates, coseismic uplift increments, and earthquake recurrence intervals. Our results demonstrate that seismic hazard models must consider active LANFs, in contrast with previous studies that suggest they may primarily slip aseismically (e.g., Chiaraluce et al., 2007; Collettini et al., 2009; Hreinsdóttir & Bennett, 2009; Wernicke, 1995).

Chapter 5: Mechanical Implications of Creep and Partial Coupling on the World's Fastest Slipping Low-angle Normal Fault in Southeastern Papua New Guinea

Copyright statement: An edited version of this paper was published by AGU. Copyright 2020 American Geophysical Union.

Biemiller, J., Boulton, C., Wallace, L., Ellis, S., Little, T., Mizera, M., Niemeijer, A., Lavier, L. (2020). Mechanical Implications of Creep and Partial Coupling on the World's Fastest Slipping Low-Angle Normal Fault in Southeastern Papua New Guinea. *Journal of Geophysical Research: Solid Earth*, 125(10), 1–24. <https://doi.org/10.1029/2020JB020117>

ABSTRACT

We use densely spaced campaign GPS observations and laboratory friction experiments on fault rocks from one of the world's most rapidly slipping low-angle normal faults, the Mai'iu fault in Papua New Guinea, to investigate the nature of interseismic deformation on active low-angle normal faults. GPS velocities reveal 8.3 ± 1.2 mm/yr of horizontal extension across the Mai'iu fault, and are fit well by dislocation models with shallow fault locking (above 2 km depth), or by deeper locking (from ~5-16 km depth) together with shallower creep. Laboratory friction experiments show that gouges from the shallowest portion of the fault zone are predominantly weak and velocity-strengthening, while fault rocks deformed at greater depths are stronger and velocity-weakening. Evaluating the geodetic and friction results together with geophysical and microstructural evidence for mixed-mode seismic and aseismic slip at depth, we find that the Mai'iu fault is most likely strongly locked at depths of ~5-16 km and creeping updip and downdip of this region. Our results suggest that the Mai'iu fault and other active low-angle normal faults can slip in large ($M_w > 7$) earthquakes despite near-surface interseismic creep on frictionally stable clay-rich gouges.

PLAIN LANGUAGE SUMMARY

In regions of extension, where tectonic plates pull apart, the Earth's crust breaks along fractures, or 'normal faults,' that allow parts of the crust to slip past each other. Many of these faults intersect the Earth's surface at a steep angle, but some anomalously low-angle normal faults are oriented at a shallower angle to the surface. Faults can slip during infrequent fast earthquakes or through slower gradual fault creep. Because active low-angle normal faults are rare and typically have low long-term slip-rates, it is not clear whether they cause large earthquakes or creep gradually. Using two approaches, this study addresses whether earthquakes occur on one of the fastest-slipping of these types of faults, the Mai'iu fault in Papua New Guinea. One approach uses GPS measurements to track patterns of displacement of the Earth's surface near the Mai'iu fault over three years. Surface displacements confirm that the Mai'iu fault slips actively and are used to constrain models of fault slip at depth. The second approach uses laboratory experiments on rocks from the Mai'iu fault zone to test whether these rocks tend to slip unstably in earthquakes, or creep stably under conditions similar to those in the fault zone. Laboratory results show that rocks from the shallowest parts of the fault tend to creep stably, while deeper fault rocks tend to slip unstably. Combining laboratory, geological and GPS results to map slip behaviors to different fault zone depths, we find that the Mai'iu fault most likely creeps near the Earth's surface but can generate larger earthquakes at greater depths.

5.1. BACKGROUND & INTRODUCTION

5.1.1. Introduction

Active continental rift systems accommodate extension at rates ranging from <1 mm/yr to a few cm/yr (Abers, 2001; Ruppel, 1995). This extension is facilitated by a variety of seismic and aseismic deformation processes on normal faults, including slip in devastating M_w 6+ earthquakes such as the 6 April 2009 L'Aquila event in Italy that killed over 300 people (Anzidei et al., 2009). Some extending regions, such as the Gulf of Corinth and the Apennines, experience frequent

earthquakes on steeply dipping ($>40^\circ$) near-surface fault sections (Abers, 2009; Jackson, 1987; Jackson & McKenzie, 1983). In these same systems, there is also evidence for aseismic creep on other, less steeply-dipping normal faults (Abers, 2009; Hreinsdóttir & Bennett, 2009; Valoroso et al., 2017). Extensional systems commonly consist of a series of near-surface high-angle (dipping $40-70^\circ$) normal faults that are at least in part seismogenic, and that sole into a deeper low-angle ($<30^\circ$) to sub-horizontal detachment fault, which may creep aseismically (Abers, 2009; Colletini, 2011; Wernicke, 1995).

The mechanics of initiation and subsequent slip of detachment faults dipping at low angles ($<30^\circ$) near the Earth's surface are not fully understood. These 'low-angle normal faults' (LANFs) appear to defy Mohr-Coulomb friction theory. This theory posits that under a vertical maximum principal stress, normal faults formed in the brittle crust with Byerlee values of friction should initiate at dips of $60-70^\circ$ and should frictionally lock up and stop slipping at dips $<30^\circ$ (e.g., Axen, 1992, 2004; Wernicke, 1995). However, geologic offsets of ~ 10 km or more on shallowly dipping detachments are commonly observed globally (e.g., Wernicke, 1995; Colletini, 2011; Platt et al., 2015), and a variety of seismological, geodetic and geologic observations indicate that some LANFs are active today (e.g., Abers, 2001, 2009; Anderlini et al., 2016; Chiaraluce et al., 2007, 2014; Colletini, 2011; Hreinsdóttir & Bennett, 2009; Numelin et al., 2007a; Valoroso et al., 2017; Wallace et al., 2014; Webber et al., 2018). Dip slip rates of active and inactive LANFs range from <1 to 10s of mm/yr (Webber et al., 2018). The mechanical paradox of slip on LANFs is most apparent at or near the Earth's surface, where the maximum principal stress is likely to be near-vertical and deformation is assumed to occur predominantly by brittle, frictional failure (e.g., Abers, 2009).

A longstanding and societally important question is whether LANFs can generate large earthquakes and, if so, how frequently (e.g., Wernicke, 1995). The instrumental record of $M_w > 5.5$ normal-fault earthquakes with unambiguously discriminated rupture planes is sparse (Colletini et al., 2019; Jackson & White, 1989), but it includes two events in the Gulf of Corinth with reported dips as low as 30° and 33° , and with magnitudes of 5.9 and 6.2, respectively. Other

earthquakes with indiscriminate nodal planes are inferred to reflect LANF slip based on their seismological and geological context (Collettini, 2011), including the notable 29 October 1985 M_w 6.8 Woodlark Basin earthquake. This event occurred around a seismologically imaged LANF, aligned parallel to one of the focal planes, and may be the largest LANF earthquake documented globally (Abers, 2001; Abers et al., 1997).

Due to the rarity and typically low slip rates (a few mm/yr or less) of active LANFs (Webber et al., 2018), geodetic observations across them are scarce and can be difficult to interpret. However, available results indicate some degree of aseismic creep on the active Altotiberina LANF in the Northern Apennines, Italy (Anderlini et al., 2016; Chiaraluce et al., 2014; Hreinsdóttir & Bennett, 2009; Valoroso et al., 2017). GPS velocities have been used to infer that this fault actively slips at 1.5 mm/yr (Anderlini et al., 2016) to 2.4 mm/yr (Hreinsdóttir & Bennett, 2009). Hreinsdóttir & Bennett (2009) used dislocation modeling of GPS velocities to infer that slip on the Altotiberina fault occurs predominantly by aseismic creep below a locking depth of 4 km; however, Anderlini et al. (2016) showed that these velocities are better fit by models with heterogeneous coupling and partial creep on the Altotiberina fault and splay faults in its hanging wall.

A variety of mechanisms have been proposed for aseismic creep on LANFs. These include: 1) an enhanced tendency for stable slip resulting from elevated pore-fluid pressures (Axen, 1992; Collettini & Barchi, 2004; Ikari et al., 2009; Abers, 2009); 2) rotated principal stress orientations favoring slip on low-angle faults (Axen, 1992, 2020); and/or 3) creep on interconnected networks of frictionally stable minerals (e.g., Collettini, 2011; Collettini et al., 2019) such as talc (Collettini et al., 2009a), clays (Ikari et al., 2009; Ikari & Kopf, 2017) or serpentine (antigorite/lizardite) (Floyd et al., 2001). It remains unclear whether fault rocks composed of these frictionally stable mineralogies are abundant on active LANFs; and, in particular, whether they are present (or thermodynamically stable) at the depths where LANFs are inferred to be creeping. One promising approach to understanding mechanisms of LANF slip involves the integration of friction experiments and microstructural analyses of rocks exhumed along an active LANF with

corresponding geodetic observations of surface deformation around the same fault. Such an integrated approach has the potential to illuminate the mechanics and spatial extent of active LANF slip. Evaluating these disparate datasets in tandem can help connect geodetic signals of LANF slip to geologically and experimentally constrained deformation mechanisms.

Here, we address the question of whether LANFs creep aseismically or slip in earthquakes following periods of locking and interseismic elastic strain accumulation by presenting and modeling data from a dense campaign GPS network spanning the world's most rapidly slipping active LANF, the Mai'iu fault in southeast Papua New Guinea (PNG; Webber et al., 2018). To strengthen our interpretation of the geodetic data, we perform hydrothermal velocity-stepping friction experiments on exhumed samples from different parts of the Mai'iu fault rock sequence under a range of relevant crustal conditions. Our results complement new microstructural observations of deformation mechanisms within the Mai'iu fault rocks in Mizera et al. (2020). Geological and geodetic evidence suggests that the Mai'iu fault slips at dip-slip rates of ~ 10 mm/yr (Wallace et al., 2014; Webber et al., 2018). The Mai'iu fault is therefore an ideal natural laboratory in which to use both geology and geodesy to study the nature of interseismic deformation on an active crustal-scale, misoriented fault. We employ detailed geodetic surveys, elastic dislocation modelling techniques, and laboratory friction experiments on rocks from the Mai'iu fault to address the mechanics and seismic behavior of a rapidly slipping, active LANF.

5.1.2. Tectonic and geological setting of the Mai'iu fault

The Woodlark Rift in southeast PNG is a young, actively propagating rift located within a region of microplates between the converging Pacific and Australian plates (Figure 5.1a; Baldwin et al., 2012 and references within) and is well-known for hosting active low-angle normal faults near its westward transition from oceanic spreading to continental rifting (Abers, 1991, 2001; Abers et al., 1997, 2016; Little et al., 2007). Northward subduction of Solomon Sea oceanic lithosphere at the San Cristobal and New Britain trenches drives rapid counterclockwise rotation

of the Woodlark and Trobriand microplates at $2\text{--}2.7^\circ/\text{Myr}$ relative to Australia about nearby Euler poles to the SW (Figure 5.1a), yielding primarily N-S extension in the Woodlark Rift. Extension rates range from $20\text{--}35$ mm/yr in the eastern Woodlark spreading center to $5\text{--}15$ mm/yr in the onshore continental portion of the rift in the Papuan Peninsula and D'Entrecasteaux Islands (Wallace et al., 2014). Recent seismicity is focused just west of the oceanic-continental rift transition, following the Woodlark Rise westward through the D'Entrecasteaux Islands (Figure 5.1d; Abers et al., 1997, 2016). This seismicity commonly aligns with geologically mapped and/or geodetically inferred active normal faults or strike-slip transfer faults (Little et al., 2007, 2011; Wallace et al., 2014). From Goodenough Island west to Cape Vogel, microseismicity focused in the upper 15 km along a WSW-trending corridor termed the Ward Hunt Strait fault zone delineates a possible actively deforming transfer zone in continental crust near the Papuan Peninsula (Abers et al., 2016; Figure 5.1b, 5.1d). Few shallow (<12 km) earthquakes have been observed to the west of the Ward Hunt Strait fault zone, where most extension appears to collapse onto a single fault—the low-angle Mai'iu fault. Offshore to the northeast of the Mai'iu fault trace, aligned microseismicity from 12-25 km depth outlines a $30\text{--}40^\circ$ -dipping planar zone inferred to be the downdip extent of the Mai'iu fault (Figure 5.1d; Abers et al., 2016).

Dipping $\sim 21^\circ$ where it intersects the Earth's surface, the Mai'iu fault is the dominant mapped fault in the continental Woodlark rift between $149.0\text{--}149.6^\circ\text{E}$ (Figure 5.1; Abers et al., 2016; Mizera et al., 2019; Little et al., 2019; Wallace et al., 2014). The footwall of the Mai'iu fault hosts the actively exhuming Dayman-Suckling metamorphic core complex, a smoothly corrugated domal structure exposing very low-grade (pumpellyite-actinolite-facies) rocks near its ~ 3 km-high crest and higher-temperature (greenschist-facies) rocks along its northern margin near sea level (Daczko et al., 2009; Little et al., 2019). The Mai'iu fault juxtaposes metabasaltic rocks—the Goropu Metabasalt—in its footwall against ultramafic rocks of the Papuan Ultramafic Belt, and structurally above, unmetamorphosed conglomeratic rocks in its hanging wall (e.g., Little et al., 2019; Mizera et al., 2020). Over the past few Myr, the Mai'iu fault is inferred to have slipped at ~ 12 mm/yr, based on the slip-parallel width (at least 30 km) of exhumed fault remnants atop the

Dayman-Suckling metamorphic core complex and the exposure at >2 km elevation of 2–3 Ma syn-extensional granites in the footwall that were originally buried at depths of 4–10 km (Little et al., 2019; Mizera et al., 2019; Österle et al., 2020). In addition, accumulation of cosmogenic nuclides in quartz veins on the exhumed fault scarp of the Mai'iu fault indicate Holocene to present-day dip-slip rates of 11.7 ± 3.5 mm/yr (Webber et al., 2018). For a 21° dip, modern dip-slip rates of 7.5–9.6 mm/yr across the Mai'iu fault have been estimated from a regional-scale network of GPS velocities (Wallace et al., 2014) and agree well with geologic slip rates.

Minor synthetic and antithetic splay faults in the hanging wall of the Mai'iu fault are presumed to intersect the active fault at depths of up to a few km (Figure 5.1; Little et al., 2019; Mizera et al., 2019). The most prominent of these, the Gwoira fault, cuts the upper ~ 1 km of the Mai'iu fault hanging wall east of Mt. Dayman (Webber et al., 2020). Inception of this splay fault led to abandonment of the shallowest portion of the Mai'iu fault farther south. East of the Gwoira fault, the Mai'iu fault system steps offshore and remains active along the southern Goodenough Bay coastline, as evidenced by Holocene uplift of coral reef terraces at rates of up to 4.3 mm/yr (Biemiller et al., 2020a; Mann & Taylor, 2002; Mann et al., 2004, 2009). The well-preserved platform-notch-platform morphology and clustered $^{230}\text{Th}/^{234}\text{U}$ ages of these emerged reefs reflect episodic and presumably coseismic meter-scale uplift events, suggesting that the Goodenough Bay segment of the Mai'iu fault system slips in moderately large ($M_w > 7$) earthquakes (Biemiller et al., 2020a).

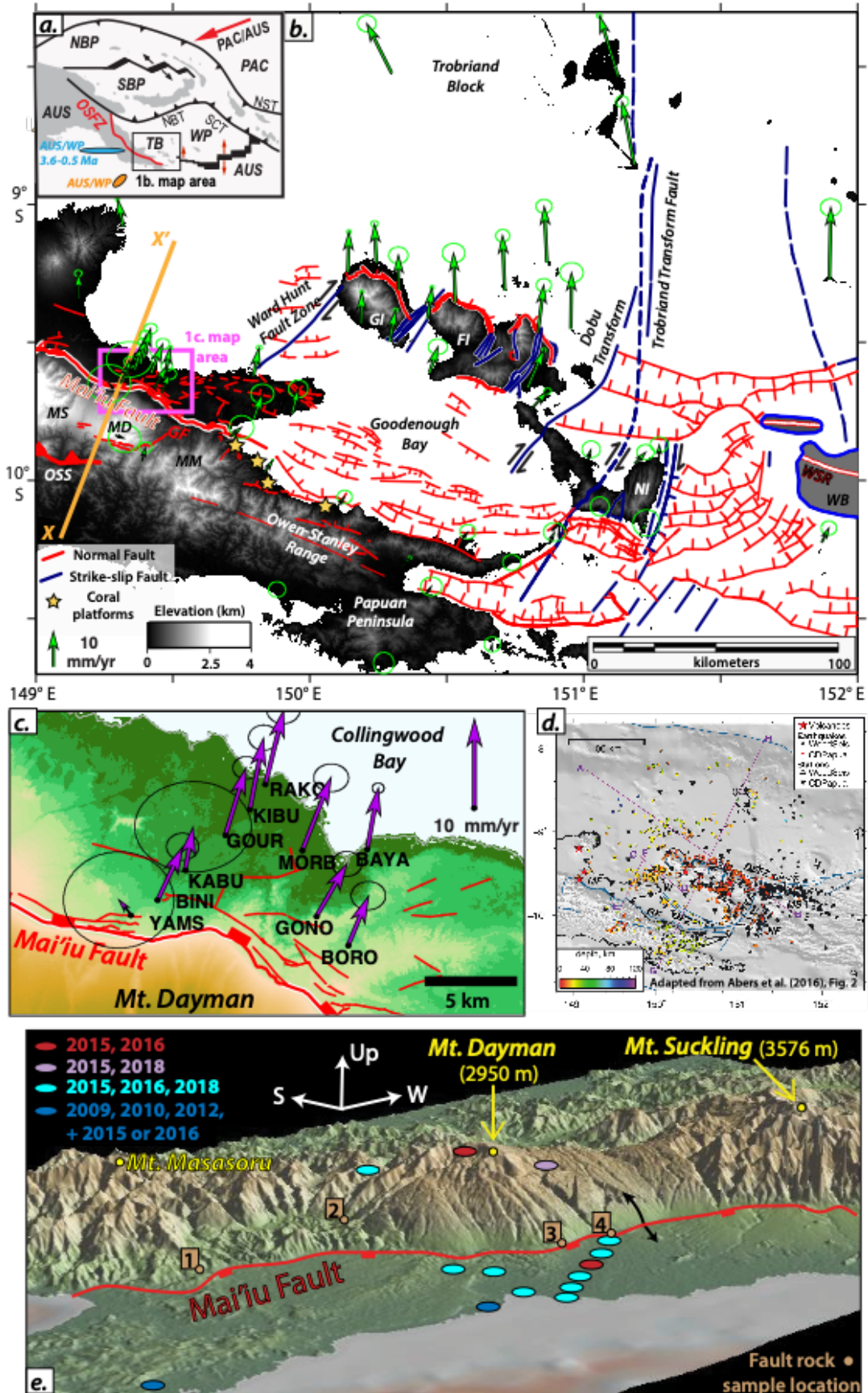


Figure 5.1. a.) Regional tectonic map of PNG with main map area outlined, showing overall Australia-Pacific Plate convergence and Woodlark spreading (vectors). Ellipses show modern (orange; Wallace et al., 2014) and 3.6–0.5 Ma (cyan; Taylor et al., 1999) poles of rotation of the Woodlark Plate relative to the Australian Plate. b.) Topographic map with faults from Little et al. (2007, 2011, 2019) and GPS velocities relative to the Australian Plate (section 5.2; Wallace et al., 2014). Ellipses show 95% confidence intervals based on formal uncertainties. Stars indicate uplifted Holocene coral platforms. Dashed box shows area of 1c. c.) Enlarged map of dense GPS velocity field on the Mai’iu fault hanging wall. d.) Regional map showing seismicity and seismometer locations from Abers et al. (2016). e.) Oblique view of the Mai’iu fault and Dayman-Suckling Metamorphic Core Complex (Mt. Masasoru, Mt. Dayman, and Mt. Suckling). Black arrows show sense of motion across the fault. Ellipse colors show observation years at GPS sites near the fault (see key), and brown circles show fault rock sample locations. Samples from each site include: 1.) PNG-15-70; 2.) PNG-14-19E, PNG-14-19F, and PNG-16-17D2H; 3.) PNG-14-33A and PNG-14-33B; 4.) PNG-15-50B and PNG-16-151e from adjacent sites; see Appendix Figure D.7 for details. Topography from 90-m SRTM (Shuttle Radar Topography Mission) data and GeoMapApp (<http://www.geomapapp.org>). AUS = Australian Plate; PAC = Pacific Plate; NBP = North Bismarck Plate; SBP = South Bismarck Plate; WP = Woodlark Plate; NBT = New Britain Trench; SCT = San Cristobal Trench. MF = Mai’iu fault; GF = Gwoira fault; MS = Mt. Suckling; MD = Mt. Dayman; MM = Mt. Masasoru; OSS = Owen-Stanley Suture zone; GI = Goodenough Island; FI = Fergusson Island; NI = Normanby Island; TB = Trobriand Block; WSR = Woodlark Spreading Ridge; WB = Woodlark Basin.

5.1.3. Mai’iu fault rock sequence and deformation mechanisms

Little et al. (2019) details the exhumed Mai’iu fault rock sequence. Working structurally upwards and towards the most recently formed part of the sequence, this includes: a mafic mylonite zone (1 to several 10s of metres thick), a layer of foliated cataclasite-breccia (<2 m thick), an ultracataclasite layer (~40 cm thick), and mineralogically variable fault gouges immediately below the principal displacement surface of the fault (<20 cm thick; see section 5.3.1 for more details of this sequence). The arrangement of progressively lower-temperature fault rocks narrowing upward (normal to the fault surface) is interpreted as a time sequence of strain localization, where the higher units are more shallowly-derived and have cannibalized those underlying them (Little et al., 2019).

The mylonitic rocks are LS-tectonites that have a strong NNE-trending stretching lineation and normal-sense shear fabrics (Little et al., 2019). Pseudosection modelling of the greenschist-facies mineral assemblage (epidote, actinolite, chlorite, albite, titanite, \pm quartz, \pm calcite) in the mafic mylonites indicates peak metamorphic conditions of $\sim 425 \pm 50^\circ\text{C}$ and 5.9–7.2 kbar. The mafic mylonites rocks are inferred to have been exhumed from $\sim 25 \pm 5$ km depth, yielding a depth-averaged geothermal gradient of $\sim 17^\circ\text{C}/\text{km}$ (Daczko et al., 2009). Microstructural analyses indicate that Neogene and younger shearing in the polyphase mafic mineral assemblage comprising the mylonite zone was accomplished by diffusion-accommodated grain-boundary sliding (along epidote, actinolite, chlorite, and albite grains; see Mizera et al., 2020) together with syn-tectonic chlorite precipitation at temperatures $> 270^\circ\text{C}$ (Little et al., 2019; Mizera et al., 2020). The mylonite zone was overprinted and brittlely reworked into the structurally overlying foliated cataclasites.

The foliated cataclasites host abundant pseudotachylite veins that indicate prior seismic slip on the Mai'iu fault. $^{40}\text{Ar}/^{39}\text{Ar}$ ages for two pseudotachylite veins are ~ 2.2 Ma (Little et al., 2019). Given the dip-slip rate of ~ 10 mm/yr, these ages suggest pseudotachylite formation (i.e., seismic slip) at depths of ~ 10 -12 km (Webber et al., 2018; Little et al., 2019). Geothermometry measurements obtained from syntectonic chlorite in the foliated cataclasites reveal an average temperature of $273 \pm 46^\circ\text{C}$ (1σ), yielding a mean geothermal gradient of $\sim 22 \pm 4^\circ\text{C}/\text{km}$ if they were active at 10-12 km depth, where the mutually cross-cutting pseudotachylite veins formed (Mizera et al., 2020).

Cross-cutting relationships between pseudotachylite veins, ultramylonite bands, and ductilely sheared calcite extension veins in the foliated cataclasite layer imply mixed-mode seismic and aseismic slip, and have been used to infer a peak in fault strength near the brittle-ductile transition (Little et al., 2019, Mizera et al., 2020). Such a strength peak at ~ 10 -12 km depth approximately coincides with the up-dip end of the corridor of microseismicity that Abers et al. (2016) attribute to the Mai'iu fault at depths of 12-25 km (Figure 5.1d). Gouges comprise the principal slip zone in outcrops. The gouges are not cut by veins or folded by any of the foliations

present in the underlying units, suggesting that these gouges formed and slipped during latest stages of deformation in the uppermost few km of the fault zone. Overall, microstructural analyses of the Mai'iu fault rock sequence reveal that the fault zone accommodates shear strain in both seismic slip and aseismic creep via a complex synexhumational series of frictional-viscous deformation mechanisms.

5.2. CAMPAIGN GPS EXPERIMENT

5.2.1. GPS data and velocities

In 2015, a network of 12 new campaign GPS monuments was installed near Mt. Dayman, ranging from the domal footwall of the Mai'iu fault northward across the fault trace into the lowlands of the hanging wall and the coast of Collingwood Bay (Figure 5.1e). The network was designed with densest station spacing in the lowlands to resolve any signal of elastic strain accumulation in the hanging wall of the Mai'iu fault. Stations were installed with station spacings of 3–5 km sub-parallel to fault slip direction (NNE, Figure 5.1e). We measured all these sites in 2015 and remeasured most of them in 2016 and 2018 using Zephyr geodetic antennas with Trimble 5700 and R7 receivers. Due to the absence of road access in the area, all of the lowland sites were visited on foot and the high mountain footwall sites were accessed via helicopter and on foot. All observations lasted at least two days, with most lasting three or more. A few of the sites were destroyed over the course of the study: UR1A was destroyed between 2015–2016 (after the first measurement: no velocities were derived from this site and it is not included in any velocity plots), and KABU and DD01 were destroyed between 2016–2018 (after the second measurement). Additionally, we remeasured seven previously established sites (Wallace et al., 2014), extending the time series of these original sites and helping tie the new sites into the pre-existing regional campaign GPS network. We incorporated campaign GPS data collected at 40 sites between 2009–2012 by Wallace et al. (2014), as well as data from a few sites measured by Australian National

University prior to 2009. The sites and years of all campaign data are listed in Appendix Table D.1.

Data were processed and aligned with the global reference frame ITRF14 using the GAMIT and GLOBK software packages (Herring et al., 2015, 2018). We used GAMIT to estimate orbital and rotational parameters, neutral atmospheric delays, and phase ambiguities to solve for the relative positions and covariance matrices of sites in our network. We also accounted for ocean tidal loading (from Onsala Space Observatory, <http://holt.oso.chalmers.se/loading/>) in the processing. These relative solutions were combined with solutions generated by the MIT processing center (Herring et al., 2016) from IGS global continuous GPS stations using a global Kalman filter, GLOBK, placing tight constraints on the positions of a subset of well-established global IGS network sites in order to tie our site positions into the ITRF14 reference frame. Site velocities were estimated from time series of daily position solutions. Formal uncertainties were augmented to account for random-walk noise (e.g., following approaches used by Beavan et al., 2016; Koulali et al., 2015; Williams et al., 2004; Zhang et al., 1997; see Appendix D.1).

To correct for static coseismic displacements at our sites due to regional large earthquakes (e.g., Banerjee et al., 2005; Tregoning et al., 2013), we used STATIC1D (Pollitz, 1996) to calculate the surface displacement at each site due to static elastic interactions from planar dislocations in a spherical layered half-space with PREM elastic stratification (Dziewonski & Anderson, 1981), representing fault slip in the 2007 M_w 8.1 Solomon Islands earthquake and all M_w 6.9+ earthquakes from 2009 to July 2018 (Hayes, 2017; Lay et al., 2017; Lee et al., 2018; Strasser et al., 2010; Taylor et al., 2008; U.S. Geological Survey, 2019; Wallace et al., 2015). These regional earthquakes were between 350 and 825 km away from our local network spanning the Mai'iu fault. See Appendix D.2 for details.

Relative to a fixed Australian Plate, horizontal velocities for sites on the hanging wall of the Mai'iu fault trend NNE, approximately perpendicular to the fault trace. These velocities generally align with previously reported velocities showing southeast PNG rotating counterclockwise relative to the Australian Plate around a nearby Euler pole (Figures 5.1, 5.2;

Wallace et al., 2014). Hanging wall velocities gradually increase with strike-perpendicular distance northwards from the fault trace and show 8.3 ± 1.2 mm/yr of NNE-SSW horizontal extension across the fault, measured from the elastic block models (section 5.2.2) as the horizontal extension rate perpendicular to the strike of the modeled Mai'iu fault in Figure 2a. This extension rate corresponds to 7.6-10.2 mm/yr dip-slip rates for a 21° -dipping fault. One outlier is the hanging wall site nearest to the fault trace, YAMS, which shows subtle NNW motion, but this velocity is based on only two years of observation and therefore has higher uncertainty than most other sites in the network.

5.2.3. Elastic block and dislocation modeling approaches

We undertake two different approaches to modeling the GPS velocity data to investigate the degree of interseismic coupling and slip rates on the Mai'iu fault. To tie our velocities into a regionally kinematically consistent reference frame, we first use an elastic block modeling approach (similar to Wallace et al., 2014). After establishing a fixed-footwall reference frame using the elastic block model, we use simpler two-dimensional elastic dislocation models to determine the Mai'iu fault properties that best explained the observed surface velocity data (similar to Hreinsdóttir & Bennett, 2009).

In the elastic block models, we represent the tectonic deformation responsible for GPS velocities in southeast PNG as the interactions between adjacent elastic crustal blocks, with each rotating about an independent Euler pole of rotation. Although we are most interested in near-field deformation associated with the Mai'iu fault, our wider dataset spans the broader southeast PNG region where crustal deformation can be described by the rotations and interactions between numerous microplates and crustal blocks (Wallace et al., 2014; Figures 5.1, 5.2a). Therefore, we model multiple crustal blocks (Figure 5.2a) and invert the GPS velocities for poles of rotation for each block relative to the Australian Plate (our velocities are in an Australia-fixed reference frame).

In these crustal block models, elastic strains accumulated along block boundaries are modeled as backslip on block-bounding faults and parameterized by the kinematic fault coupling ratio, Φ , which describes the fraction of predicted relative plate motion that is accrued as a slip deficit rate. For example, if $\Phi = 0$, the fault is creeping at full plate motion rate, while if $\Phi = 1$, there is no creep in the interseismic period of our GPS measurements and the fault is fully locked. The slip deficit rate is simply the coupling ratio multiplied by the long-term slip rate on the fault from the crustal block motions. We use TDEFNODE (McCaffrey, 2009) to jointly invert for the block poles of rotation and the spatial distribution of Φ on block-bounding faults. The model is constrained by kinematic data including GPS velocities, earthquake slip vectors, and transform fault orientations from throughout the southeast PNG region.

Block boundaries and fault geometries are defined on the basis of regional tectonics, field mapping studies, and geophysical constraints such as seismicity. For this model, block and fault geometries are based largely on those of Wallace et al. (2014), although some geometries such as the position and dips of the Mai'iu fault have been updated based on recent field mapping (Little et al., 2019; Mizera et al., 2019; Webber et al., 2018, 2020) and seismological observations (Abers et al., 2016). The statistical significance of various block configurations is tested with an F -test for block independence (Figures 5.2a; Appendix Figure D.3; Appendix Table D.5). We utilize our preferred configuration for subsequent models testing fault coupling (Figure 5.2a).

Joint inversion of diverse local and regional kinematic datasets within a block model framework helps to ensure that modeled block rotations and fault coupling are consistent with both regional tectonic motions and local observations. In addition, simple 2-D planar dislocation fault models can provide focused insight into the tradeoffs between slip rate, locking depth, and fault geometry, especially for dense GPS networks that span major active faults. For this reason, we also perform a simple inversion of strike-perpendicular GPS velocities across the Mai'iu fault for fault dip, locking depth, and dip-slip rate using the solutions for planar dislocations in an elastic half-space from Okada (1985). This simplified 2-D approach has been used to model GPS velocities related to slip on other LANFs (Hreinsdóttir & Bennett, 2009) and reverse and strike-

slip faults (Beavan et al., 1999). In such models, a single fault is represented as a two-dimensional planar dislocation that extends infinitely in the third dimension. In our case, predicted elastic contributions to surface displacement due to interseismic backslip on the locked dislocations are added to the long-term fault-strike-perpendicular plate motion rate and compared with observed surface velocities to calculate the misfit between the model and the data. By minimizing the data misfit as expressed by the reduced χ^2 , these models highlight the range of fault properties and locking most likely responsible for observed surface displacements. The calculated χ^2 is minimized through an extensive grid search of the three fault parameters (dip, slip rate, and locking distribution), as discussed in Section 5.3.2.

5.2.3. Elastic block model results

Our preferred elastic block model treats Fergusson/Goodenough Islands, Normanby Island, Goodenough Bay, and the Papuan Peninsula as discrete independent crustal blocks, similar to that of Wallace et al. (2014). More complex configurations (with additional blocks) do not produce a statistically significant improvement in fit to the data (see *F*-tests and results in Figure 5.2a; Appendix Figure D.3; Appendix Table D.5). The best-fitting model of jointly inverted block poles of rotation and fault locking are shown in Figure 5.2a, indicating 8.3 ± 1.2 mm/yr of horizontal extension across the Mai'iu fault. This model predicts locking of the western segment of the Mai'iu fault down to only 2 km depth, below which the fault creeps. Deeper locking occurs on the eastern segment through Goodenough Bay and the faults immediately north of Goodenough Island, although this is not well-constrained due to a relative lack of GPS sites on the largely submarine hanging wall east of our study area.

Inversions producing the model in Figure 5.2 allow fault coupling ratios to vary from 0 – 1, but they impose a constraint that coupling decreases with increasing depth. To test how such assumptions affect the preferred locking model, additional inversions were performed with different constraints on locking, such as allowing coupling to vary freely with depth or assuming

a discrete and uniform locking depth (Appendix D.3; Appendix Figure D.4). The large misfit of models with prescribed locking depths from the surface to $>\sim 2$ km confirm that campaign GPS velocities are inconsistent with Mai'iu fault locking from the surface to more than a few kms depth. Inversions with fewer imposed locking constraints, including those in which no downdip decrease in coupling is prescribed (i.e., no assumption that the fault is locked at the surface), all converge on best-fitting models with shallow locking to <2 km depth (Appendix Figure D.4), compatible with a LANF creeping at most depths. To test how the higher uncertainty in velocity at site YAMS affects these inversion results, we also performed inversions that excluded YAMS and found that they yield similar results: the Mai'iu fault predominantly creeps below a shallow locking depth (~ 2 km) in the best-fitting model with $\chi^2 = 1.70$ (Appendix Figure D.4i).

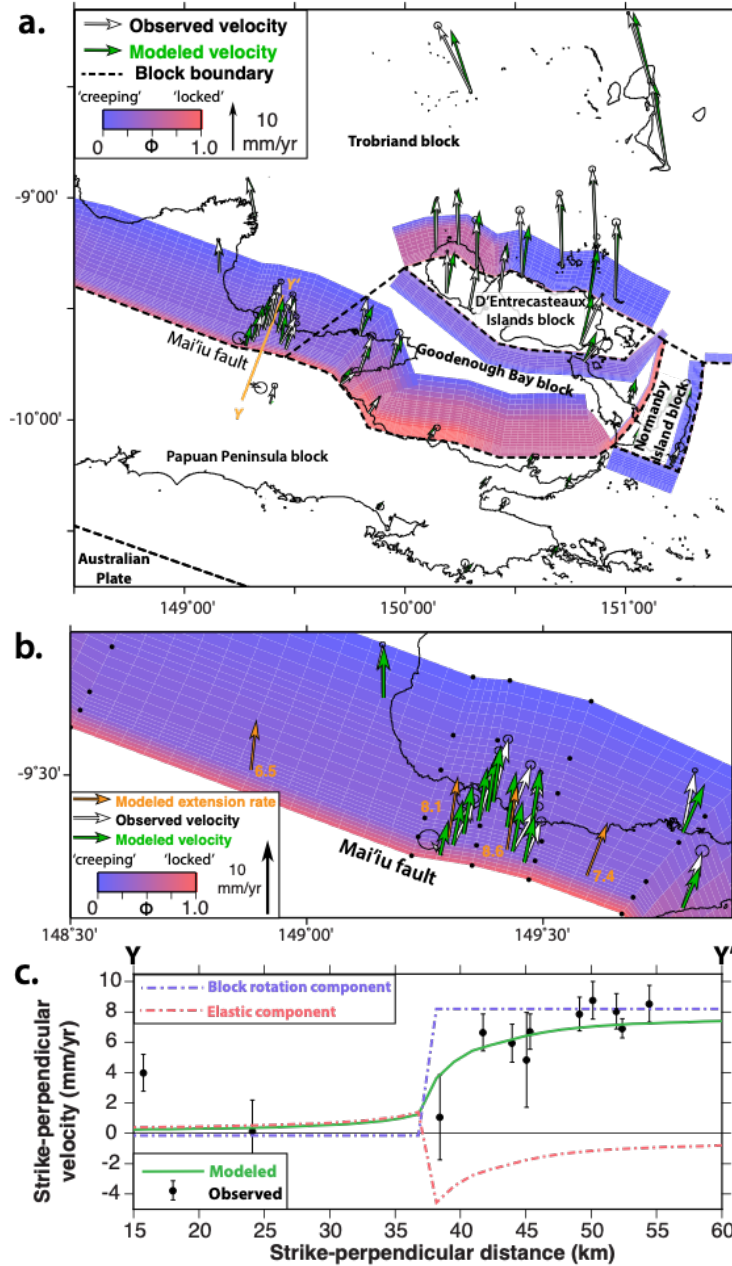


Figure 5.2. Best-fitting elastic block fault locking model results colored by kinematic fault coupling ratio Φ . Vectors indicate observed (white) and predicted (green) GPS velocities. a.) Preferred locking model. Dashed lines show preferred block boundaries (Appendix Figure D.3; Appendix Table D.3). b.) Enlarged view of GPS velocities near the modeled Mai'iu fault, which is predominantly uncoupled below 2 km depth. Labeled orange vectors show modeled rates and directions of relative motion between adjacent blocks across the fault. c.) Strike-perpendicular horizontal velocities relative to the Papuan Peninsula footwall block for sites in the Mai'iu fault network (Profile Y – Y' in 5.2a). Observed velocities (black), modeled velocities (green), and the modeled velocity contribution of elastic strain (pink) and block rotations (purple) are shown.

5.2.4. 2-D Dislocation modeling

5.2.4.1. Model 1: Locked-to-surface models

Modeled crustal block rotations help to establish a footwall-fixed reference frame in which explore Mai'iu fault locking in more detail using 2D dislocation models. We compare the predicted horizontal surface velocities (now in a footwall-fixed reference frame) from 128,000 two-dimensional elastic half-space planar dislocation models to the strike-perpendicular GPS velocities from sites within a 65 km strike-perpendicular distance of the Mai'iu fault trace along profile X-X' (Figure 5.1b). This approach offers a focused look at how modeled fault properties affect the fit to GPS velocities, but does not account for three-dimensional factors such as along-strike variations in fault geometry or locking. We first test the slip rate, dip angle, and locking depth of a single fault locked to the Earth's surface, as in previous GPS studies of LANF locking (Hreinsdóttir & Bennett, 2009). Although the shallow ($\leq 24^\circ$) dip of the Mai'iu fault along its trace is well-constrained (Little et al., 2019; Mizera et al., 2019), the fault surface exhumed on the Dayman-Suckling metamorphic core complex steepens northward (Webber et al., 2020), and fault-related microseismicity implies a similar northward steepening dip (Figure 5.1d; Abers et al., 2016). We therefore allow the modeled fault dip to vary in order to more fully explore the parameter space. We test fault dip angles ranging from 1 - 80° in 1° increments, dip-slip rates of 0.5 – 20 mm/yr in 0.5 mm/yr increments, and locking depths of 0.5 – 20 km in 0.5 km increments (Figure 5.4a; Appendix Figure D.6). For the strike-perpendicular horizontal velocities, the best-fitting (minimum $\chi^2 = 0.94$) modeled fault dips 26° , is locked down to 2 km depth, and slips at 10 mm/yr below this depth (model 1; Figure 5.3a-c). This result indicates that the observed GPS horizontal velocities can be explained by active aseismic creep below a shallow locking depth on a gently dipping normal fault. The close match between the best-fit model's fault dip and the geologically inferred fault dip supports this result. Vertical velocities (which have high uncertainties) are modeled (Figure 5.3b,e) but not used to constrain the grid search. Joint modeling

of vertical and horizontal components (e.g., Beavan et al., 2010; Bennett et al., 2007; Segall, 2010; Serpelloni et al., 2013) yields similar locking results (Appendix D.4). Note that the best-fit $\chi^2 < 1.0$ suggests that the random-walk noise model may slightly overestimate the velocity uncertainty corrections, particularly for campaign sites with only two or three years of observations.

5.2.4.2. Model 2: Consideration of shallow creep and splay fault activity

The setup of model 1 is inherently limited by the assumptions that the fault is locked at the surface and that only one planar structure is active, which may not be appropriate for this and other LANF systems. The hanging walls of major detachment faults are commonly cut by minor splay faults that may variably slip or creep (e.g., Anderlini et al., 2016). In the case of the Mai'iu fault, discontinuous splay faults have been mapped in parts of the hanging wall (Figure 5.1b; Little et al., 2019, Webber et al., 2020). Additionally, the shallow portions of many LANFs, including the Mai'iu fault (section 5.3.2-5.3.3), contain gouges of weak, frictionally stable mineralogies that may promote near-surface aseismic creep (Collettini, 2011, and references within; Little et al., 2019). To test whether these mechanisms allow aseismic creep in the near-surface portions of the Mai'iu fault and/or its splay faults, we develop buried dislocation models that do not require full fault locking at the Earth's surface and that allow for slip on adjacent splay faults (model 2).

Our buried dislocation models allow for creep both updip and downdip of a locked patch or “asperity” (e.g., Collettini et al., 2019). Because the velocity at YAMS is more consistent with footwall motion, we treat it as a footwall site in these models: essentially, this treatment considers the possibility that, in the shallowest subsurface, creep may transfer from the main Mai'iu fault to one of the many active splay faults in the hanging wall, some of which are <1 km from the main fault trace (Little et al., 2019). The modeled fault trace is hence projected between sites YAMS and BINI in order to incorporate YAMS into the footwall. Note that in all buried dislocation scenarios, the data-fit improves significantly by treating site YAMS as part of the footwall: for models based on the horizontal velocities, χ^2 decreases from 0.95 with YAMS in the hanging wall

to 0.89 with YAMS in the footwall. The best-fit buried dislocation model (model 2; $\chi^2 = 0.89$; Figure 5.3d-f) fits the horizontal velocities better than the best-fit model with locking imposed at the surface (model 1; $\chi^2 = 0.94$; Figure 5.3a-c). The best-fit model with a buried locked zone involves a 35°-dipping fault, locked from 5 to 16 km depth and slipping at 10.5 mm/yr updip and downdip of the locked zone (Figure 5.3d-f), consistent with microseismic, structural, and surface modeling evidence that the Mai'iu fault steepens to dip 30-40° between ~5-12 km depth (Abers et al., 2016; Little et al., 2019; Webber et al., 2020). Fixing fault dip to a geologically and geodetically reasonable average crustal dip of 35°, Figure 5.4b shows tradeoffs between the total depth range of locking (depth range D, Figure 5.3f), the depth of the updip limit of locking (depth P, Figure 5.3f), and slip rate. We note that in future work the uncertainty in shallow fault slip behavior could be reduced by remeasuring the hanging wall site nearest to the fault trace, YAMS, in order to derive a more meaningful secular velocity above the shallowest fault zone; nonetheless, despite its high uncertainty, the velocity of YAMS still helps constrain the range of possible secular velocities near the fault trace and is used in the preferred kinematic model inversions. To determine the effects of this velocity on the kinematic model results, inversions were performed using all velocities except YAMS (Appendix Figures D.9, D.10). These inversions yield less of a distinction between the two preferred locking scenarios of Models 1 & 2: shallow near-surface locking with deeper creep or stronger locking at depth with creep updip and downdip of the strongly locked region (Appendix Figure D.10c). Although the specific fault parameters of the best-fitting models vary slightly when YAMS is excluded, the two preferred models are strikingly similar to the best-fitting Models 1 & 2 based on inversions that included YAMS (Figure 5.3). Geologic, experimental, and seismological evidence help distinguish between these two families of kinematic models (section 5.4.2).

Model 2 assumes that interseismic fault creep updip of a more strongly locked region is mechanically feasible. Shallow interseismic fault creep occurs above locked seismogenic patches on a variety of faults (Harris, 2017), including the strike-slip Hayward fault in California (Harris, 2017 and references within) and the Nankai subduction megathrust, where periodic slow-slip

events near the trench occur updip of the locked portion of the megathrust (Araki et al., 2017). However, recent analytical models predict a strong stress-shadow effect updip of the locked portion of subduction megathrusts that should prevent significant creep on the unlocked updip portion of the fault regardless of its frictional stability (Almeida et al., 2018). In other words, even an unlocked, frictionally stable shallow portion of a megathrust may not feel high enough driving stresses to creep interseismically when located updip of a strongly locked patch. By analogy, this type of model may predict that significant shallow creep updip of a more strongly locked portion of a LANF should not occur, either.

Because the downdip width (~19 km) of the locked LANF patch inferred by model 2 is much smaller than that of a locked megathrust, and because along-strike locking patterns may be heterogeneous and patchy, the efficacy of this stress shadow effect may be limited. Additionally, the stress shadow models (Almeida et al., 2018) assume homogeneous elastic properties at all depths, whereas the shallow portions of many normal fault hanging walls consist of unconsolidated, fractured sedimentary units. High shear stresses associated with deep creep between strong metabasaltic and plutonic rocks could be expected to drive more internal deformation and/or fault creep in weak hanging wall sediments at shallow levels than in the strong hanging wall of the homogeneous model. Heterogeneous locking and elastic properties along with frictionally weak, velocity-strengthening shallow fault gouges (section 5.3) help explain how shallow interseismic creep coeval with deeper locking (model 2) is a mechanically feasible model for interseismic LANF slip.

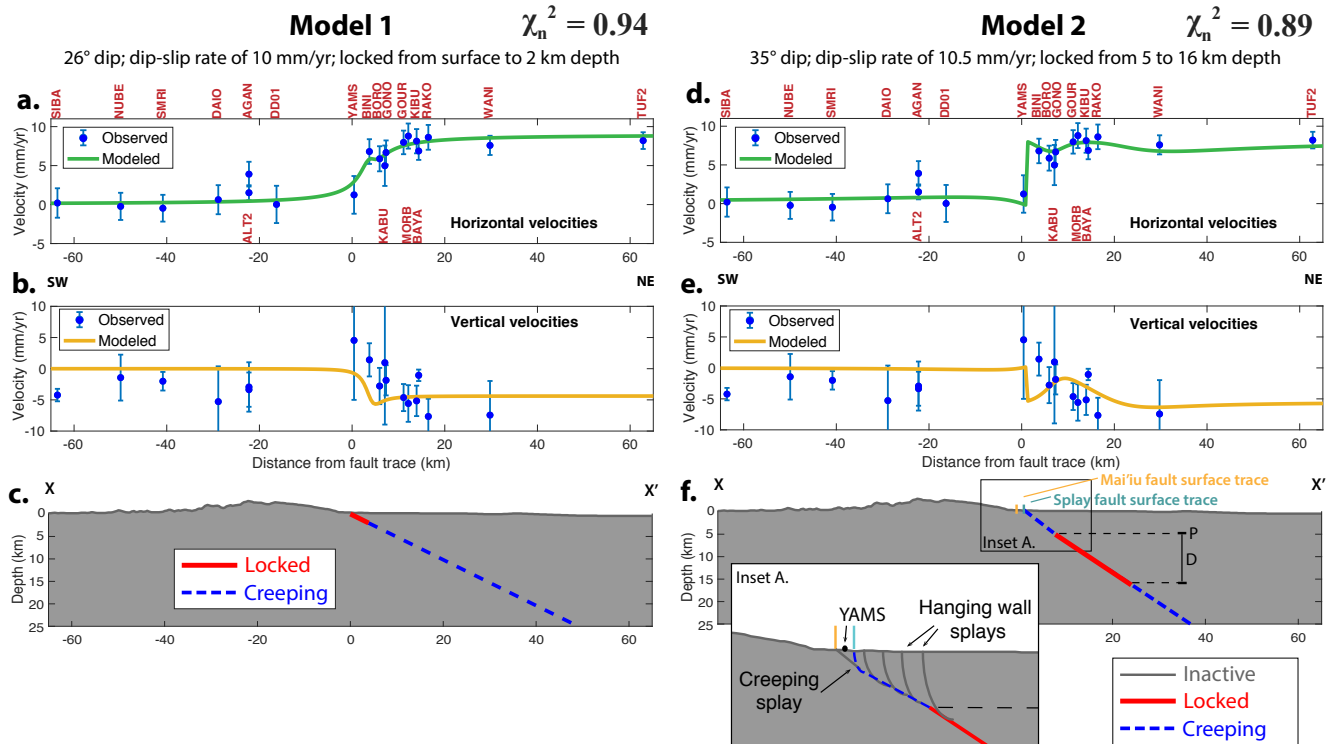


Figure 5.3. Best-fitting two-dimensional planar elastic half-space dislocation locking models based on strike-perpendicular horizontal velocities projected onto profile X-X' of Figure 5.1b. Red labels show GPS site names. a-c.) Model 1; locked to 2 km depth. d-f.) Model 2; locked from 5 to 16 km depth, with creep and splay fault slip above 5 km depth. a,d): Observed (blue) and modeled strike-perpendicular velocities. b,e): Observed and modeled vertical velocities. c,f): Schematic of fault locking models. Profile topography from 90-m SRTM data and GeoMapApp (<http://www.geomapapp.org>).

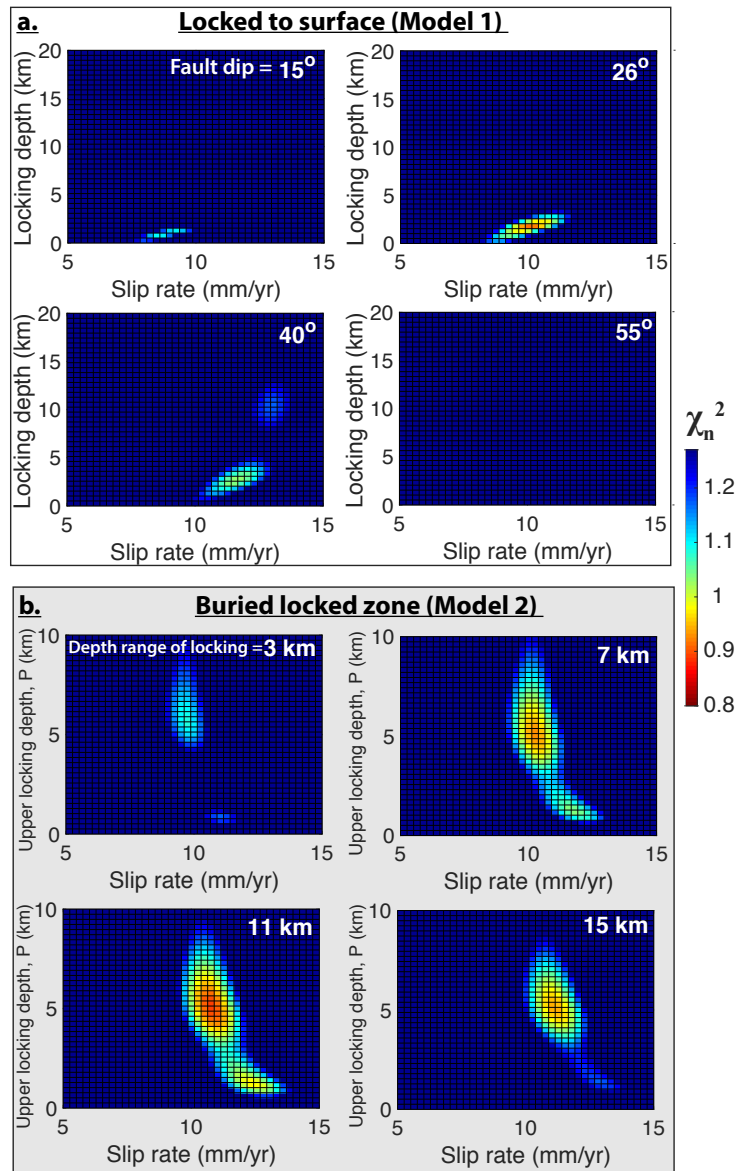


Figure 5.4. Example of misfit (χ^2) tradeoffs for 2D dislocation models capped at $\chi^2=1.27$ (equivalent to 75% confidence interval for model 2 calculated with F -tests for statistical significance) to highlight those models that fit the data reasonably well. a.) Tradeoffs between locking depth and slip rate for locked from surface to depth models with different dip angles. Locked-at-surface models prefer shallow locking (<4 km depth) on a shallowly dipping ($\sim 26^\circ$) fault slipping ~ 9 -12 mm/yr, while steeply dipping faults ($\geq 40^\circ$) do not fit the data well ($\chi^2 > 1.0$). b.) Buried-dislocation models show tradeoffs between the updip depth of locking (depth P , Figure 5.3f) and slip rate with different depth ranges of locking (depth D , Figure 5.3f). Fault dip shown here is fixed to the best-fitting value of 35° ; however, P , D , slip rate, and dip were all varied in grid searches. These models prefer a more strongly locked zone from ~ 5 -16 km depth on a shallowly dipping ($\sim 35^\circ$) fault slipping ~ 10 -12 mm/yr.

5.3. MAI'IU FAULT FRICTIONAL STRENGTH AND STABILITY FROM ROCK DEFORMATION EXPERIMENTS

5.3.1. Fault rock sample descriptions

Over three field seasons, spectacular exposures of the Mai'iu fault were observed and sampled. Structural results show that fault slip has occurred primarily within fault rocks comprising a narrow (< 3 m), high strain fault core (Little et al., 2019) (Figure 5.5). The frictional properties of these fault rocks likely govern the mode of frictional fault slip at different levels on the fault. Figure 5.5b shows a schematic section of the Mai'iu fault rock sequence that is partially eroded on exhumed parts of the active fault, but fully preserved in outcrops along the inactive segment of the Mai'iu fault. Eight Mai'iu fault rock samples were studied in detail to determine their mineralogy and frictional properties: two types of footwall foliated cataclasite (Figure 5.5c); a footwall ultracataclasite (Figure 5.5d); four types of footwall fault gouge (Figures 5.5e and 5.5f); and a sliver of hanging wall serpentine schist entrained within the footwall (Figure 5.5c, inset).

The mylonitic rocks (not sampled for friction experiments) were overprinted and reworked into the structurally overlying, ~2 m-thick foliated cataclasites. The latter contains veins of friction melt (pseudotachylite), brittle faults, and multiple generations of calcite veins (Figure 5.5c). The foliated cataclasites investigated in this study (PNG16-17-D2H and PNG16-151E) have a cm-to-mm-spaced, differentiated, and pervasively folded foliation defined by light-coloured albite and quartz±calcite-rich domains and darker phyllosilicate (predominantly chlorite)-rich folia. This microstructure indicates fluid-assisted diffusive mass transfer during the dissolution of mafic minerals (epidote and actinolite) (Mizera et al., 2020). Shear-induced creep by diffusive mass transfer and/or frictional viscous flow likely accompanied the formation and folding of the pervasive foliation (Little et al., 2019; Mizera et al., 2020).

In all outcrops, the foliated cataclasites are overlain sharply by a 5-to-40 cm-thick ultracataclasite (PNG15-50B) formed through cataclastic grain-size reduction and authigenic

precipitation of calcite, corrensite, and potassium feldspar (Figure 5.5d). Massive green-gray and red mafic gouges (PNG14-33A and PNG14-33B) or light (PNG14-19E) to medium grey (PNG14-19F) corrensite-saponite gouges sharply overly the ultracataclasite layer and form the <20 cm-thick principal slip zone in surface outcrops (Figures 5.5a, 5.5b, 5.5e and 5.5f).



Figure 5.5. Summary of fault rocks analyzed. Sample locations are shown in Figure 5.1e and Appendix Figure D.7 and listed in Appendix Table D.6. (a) Exposure of the inactive Mai'iu fault showing the footwall fault rock sequence sharply overlain by unmetamorphosed hanging wall sedimentary rocks. (b) A schematic cross section through the fault core, including the structural position of the fault rocks sampled (after Little et al., 2019; Mizera et al., 2020). (c) Fault-exhumed exposure of the foliated cataclasite unit and a pseudotachylite vein. Inset: foliated serpentinite schist (>10 m thick) entrained between the footwall and hanging wall of the Mai'iu fault, stranded atop the footwall north of Mt. Masasoru. (d) Outcrop of cohesive ultracataclasite unit structurally overlying foliated cataclasites. (e) Mafic fault gouges, and (f) corrensite-saponite fault gouge comprising the principal slip zone.

5.3.2. Experimental methods and materials

We performed hydrothermal friction experiments on powdered gouges derived from eight of these Mai'iu fault rock types (Figure 5.6; Table 5.1; Appendix Table D.6) using the rotary shear apparatus in the High Pressure and Temperature Laboratory at Utrecht University (Niemeijer et al, 2008, 2016). In these experiments, a thin layer (~1.5 mm) of gouge is placed between two ring-shaped Ni-alloy pistons (22/28 mm inside/outside diameter) and confined by Ni-alloy rings with a low friction (Molykote) coating. The piston assembly is mounted inside a water-filled pressure vessel that houses an internal furnace. The vessel is located within a 100 kN capacity Instron loading frame which is used to apply the normal force. Rotation of the vessel creating shear within the layer is achieved using an electromotor attached to two 1:100 gear boxes. For more details, refer to Niemeijer et al (2008, 2016). To create a powdered gouge, samples were crushed and sieved to a grain size fraction < 150 μm . In all experiments, we applied stepwise increases in effective normal stress (15 MPa/km), fluid pressure (10 MPa/km) and temperature (25 $^{\circ}\text{C}/\text{km}$) to simulate slip in progressively deeper parts of the fault (Table 5.1). The temperature gradient imposed was informed by geophysical and geological evidence for a 17-26 $^{\circ}\text{C}/\text{km}$ geothermal gradient on the Mai'iu fault (Tjhin, 1976; Martinez et al., 2001; Daczko et al., 2009; Little et al., 2019; Mizera et al., 2020). The thermal structure of the Mai'iu fault is summarized in Little et al. (2019), who document that two exploration wells and shipboard heat flow measurements indicate a present day geothermal gradient of only ~20 $^{\circ}\text{C}/\text{km}$ assuming thermal equilibrium of the temperature measurements and a tropical seafloor temperature of 20 $^{\circ}\text{C}$ at ~30 m depth (Tjhin, 1976). In Goodenough Bay, topography and sediment-corrected heat flow data average 73 mW/m^2 . Assuming a linear geotherm and lithospheric conductivity of 3.2 $\text{W}/\text{m}^{\circ}\text{C}$, this translates into a geothermal gradient of ~23 $^{\circ}\text{C}/\text{km}$ (cf. Martinez et al., 2001). Mizera et al. (2020) present a geologically constrained thermal profile of the Mai'iu fault. Temperature in the mylonites is pinned by the pseudosection thermobarometry of Daczko et al (2009), which revealed a

temperature of 425 °C at 25 km depth, which is less than 17 °C/km. Additional temperature constraints are provided by the chemistry of syntectonic chlorite in the foliated cataclasites (our samples PNG-16-17-D2H and PNG-16-151e), which yields a temperature range of 158 °C to 356 °C with an average of 273 ± 46 °C (1σ) (Mizera et al., 2020). Based on known slip rates and Ar-Ar psuedotachylyte ages, the foliated cataclasites were exhumed from 10-12 km, yielding a mean geothermal gradient of $\sim 22 \pm 4$ °C/km (Little et al., 2019). Clay mineralogy (corrensite and saponite) indicate lower temperatures in fault gouges formed at depths <10 km, and mylonite chlorite geothermometry indicates higher temperatures at depths >12 km (Mizera et al., 2020).

Once the desired pressure (P) and temperature (T) conditions were reached, we allowed the system to equilibrate for at least 30 minutes before shearing began at 1 $\mu\text{m/s}$. Initial shearing at 1 $\mu\text{m/s}$ occurred for 5 mm to establish a steady state friction level and a mature microstructure. The velocity dependence of friction was investigated by subsequently applying a velocity-stepping scheme of 0.3-1-3-10-30 $\mu\text{m/s}$. Following these velocity steps, the motor driving displacement was stopped, and PT conditions were changed. Under the new PT-conditions, the 1 $\mu\text{m/s}$ run-in displacement was reduced to 2.5 mm, but otherwise the procedure remained the same. The frictional properties of each fault rock were measured over a range of temperatures and pressures corresponding to an active, extensional fault zone (Table 5.1); a more detailed analysis of the pressure and temperature conditions at depth in the Mai'iu fault zone can be found in Mizera et al. (2020). Data were acquired at a rate of 900 Hz and averaged to rates of 1-100 Hz, depending on the sliding velocity. Raw data were processed to obtain shear stress as a function of sliding distance, which was further analyzed in terms of rate-and-state frictional (RSF) properties using a Dieterich state evolution law (Dieterich 1979, 1981; Marone, 1998) and the inversion scheme detailed in Reinen & Weeks (1993) and Ikari et al. (2009) (Appendix D.6).

Although increasing temperature, normal stress and fluid pressure in tandem makes it difficult to isolate the effects of each individual condition, this step-wise simulated-depth approach allowed for finer sampling of the suite of depth-dependent crustal conditions under which each sampled fault rock unit is inferred to have deformed in the natural fault zone. We note that future

experiments on the exhumed Mai'iu fault rock sequence testing a range of each individual experimental condition (e.g., experiments at different temperatures under identical fluid pressures and effective normal stresses) could be used to isolate and quantify the individual effects of temperature, fluid pressure, and normal stress and allow these results to be more broadly applied to other mature mafic fault zones with different geothermal gradients or fluid pressure distributions. Nonetheless, the range of depths simulated by the experimental conditions here (Table 5.1) provide a detailed account of the depth-dependent mechanical behavior of the Mai'iu fault (Figures 5.6, 5.7, 5.8).

<i>Exp.</i>	<i>Sample #</i>	<i>Fault rock</i>	σ_n^{eff} (MPa)	P_f (MPa)	T (°C)	μ_{ss}
u368*	PNG-14-19F	Lower gouge	30-60-90-120	20-40-60-80	50-100-150-200	0.24-0.18-0.19-0.26
u369*	PNG-14-19E	Upper gouge	30-60-90-120	20-40-60-80	50-100-150-200	0.14-0.11-0.13-0.13
u370	PNG-14-19F	Lower gouge	30-60-90-120	20-40-60-80	50-100-150-200	0.23-0.21-0.20-0.28
u371	PNG-14-19E	Upper gouge	30-60-90-120	20-40-60-80	50-100-150-200	0.15-0.13-0.11-0.14
u487	PNG-15-50B [^]	Ultracataclasite	120-150	80-100	200-250	0.63-0.74
u493	PNG-15-50B	Ultracataclasite	90-120-150-180	90-120-150-180	150-200-250-300	0.59-0.59-0.66-0.72
u495	PNG-15-70	Serpentinite	90-120-150-180	90-120-150-180	150-200-250-300	0.37-0.41-0.48-0.57
u496	PNG-15-70	Serpentinite	120-150-180-210	80-100-120-140	300-350-400-450	0.50-0.60-0.62-0.63
u497	PNG-15-50B	Ultracataclasite	120-150-180-210	80-100-120-140	300-350-400-450	0.75 [#] -0.80-0.80-0.73
u545	PNG-14-33B	Upper mafic gouge	30-60-90-120	20-40-60-80	50-100-150-200	0.22-0.26-0.28-0.35
u546	PNG-14-33A	Lower mafic gouge	30-60-90-120	20-40-60-80	50-100-150-200	0.41-0.46-0.50-0.56
u547	PNG-14-33A	Lower mafic gouge	30-60-90-120	20-40-60-80	50-100-150-200	0.40-0.44-0.48-0.57
u772	PNG-16-17D2H	Foliated cataclasite	90-120-150-180	60-80-100-120	150-200-250-300	0.75-0.72-0.73-0.72 [#]
u773	PNG-16-151e	Foliated cataclasite	90-120-150-180	60-80-100-120	150-200-250-300	0.66-0.60-0.59-0.57
u774	PNG-16-17D2H	Foliated cataclasite	120-150-180-210	80-100-120-140	300-350-400-450	0.57-0.60-0.47-0.44
u775	PNG-16-151e	Foliated cataclasite	120-150-180-210	80-100-120-140	300-350-400-450	0.67-0.67-0.66 [#] -0.61

Table 5.1. List of sampled fault rocks and experiments performed with experimental conditions (effective normal stress, pore fluid pressure, and temperature) and values of friction (=shear stress / effective normal stress, ignoring cohesion) at the end of each run-in (at 1 mm/s). The sliding velocity was 1 mm/s initially and then stepped to 0.3-1-3-10-30 mm/s with 0.5-1.5-1.5-1.5 mm of displacement. Steady state friction (mss) is determined at the end of the run-in at 1 mm/s at each sneff-T-Pf condition. * Run-in at 10 mm/s, step from 0.3 to 1 mm/s omitted, step from 30-100 mm/s included, ^ experiment terminated prematurely due to pore fluid leak, # indicates peak value of stick-slip.

5.3.3. Frictional strength results

We report the results of all experiments in Figure 5.6, which shows the coefficient of friction (defined as shear stress / effective normal stress, ignoring cohesion) as a function of load-point displacement. All samples tested show changes in friction with PT conditions, but the largest differences in friction are between samples. The measured frictional strength covers the range of $\mu=0.1$ to $\mu=0.8$ (see also Table 5.1 and Appendix D.5). The uppermost, light gray saponite gouge sample is the weakest with $\mu=0.11-0.15$, followed by the underlying, medium gray saponite gouge ($\mu=0.18-0.28$), the red mafic gouge ($\mu=0.22-0.35$), the serpentinite schist ($\mu=0.37-0.63$), the green-grey mafic gouge ($\mu=0.40-0.57$), the “inactive” foliated cataclasite ($0.44-0.75$), the “active” foliated cataclasite ($\mu=0.57-0.67$) and finally the ultracataclasite ($\mu=0.59-0.80$). The abundance of the weak clay mineral saponite is a good indicator of the weakness of the sample (e.g. Lockner et al., 2011; Sone et al., 2012), whereas the sample derived from the serpentinite schists show friction values in the range of pure lizardite (e.g. Moore et al., 1997; Moore & Lockner, 2013). Friction of the foliated cataclasites and the ultracataclasite is comparable to results from friction studies on gouges of granitic composition (e.g. Niemeijer et al., 2016), of quartz (e.g. Chester & Higgs, 1992; Niemeijer et al., 2008), and of plagioclase (e.g. He et al., 2013). In general, the friction coefficients of most fault gouges increase with increasing simulated depth (i.e., increasing temperature, effective normal stress, and fluid pressure) during an individual experiment. In some experiments, strengthening is the result of a long-term displacement-dependent increase in friction (e.g. Figure 5.6c), whereas in other experiments strengthening is abrupt and is the result of increased simulated depth (e.g. Figure 5.6b).

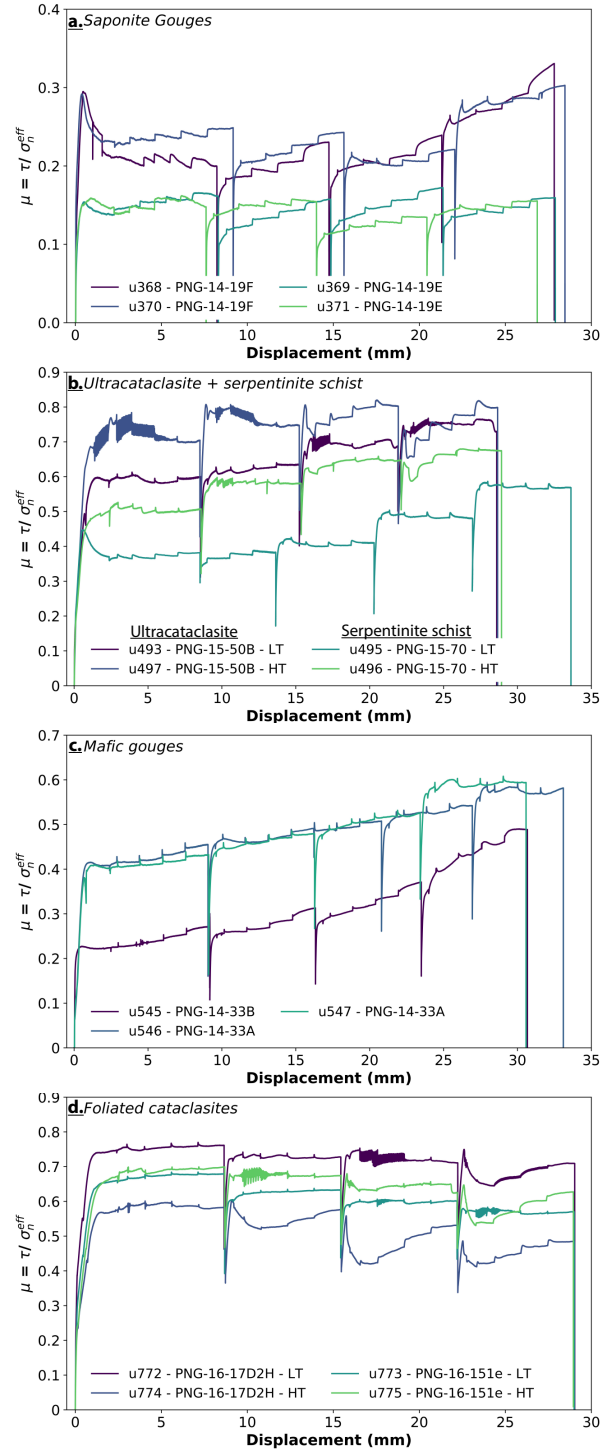


Figure 5.6. Friction measured during velocity-step experiments on Mai’iu fault rocks (Section 5.3.1; Figure 5.5; Table 5.1; Appendix Table D.6) including a.) corrensite-saponite gouges, b.) ultracataclasite and serpentinite schist; c.) mafic gouges; d.) foliated cataclasites. Colors indicate individual experiments (‘u368’) on numbered samples (‘PNG-14-19F’) under lower-temperature (LT) or higher-temperature (HT) conditions.

5.3.4. Rate-and-state frictional stability results

Although a relationship between fault strength and frictional stability has been proposed (Ikari et al., 2011), fault frictional strength alone gives little indication as to whether the fault creeps aseismically or slips in episodic earthquakes. Instead, frictional stability is described within the framework of rate-and-state friction, where the instantaneous effective friction coefficient depends on both the current slip velocity ('rate') and the time over which two fault surfaces have been in contact with each other ('state'). Experimentally derived values of rate-state parameters a , b , and critical slip distance d_c describe the frictional stability of a material: materials with $(a-b)>0$ are velocity-strengthening, whereby an increase in slip velocity causes an increase in friction promoting stable creep; materials with $(a-b)<0$ are velocity-weakening, whereby an increase in slip velocity causes a decrease in friction, promoting unstable, potentially seismic slip (e.g., Dieterich, 1979, 1981; Gu et al., 1984; Rice & Tse, 1986; Ruina, 1983).

We invert the velocity-stepping data for individual rate-state friction parameters a , b and d_c . Figure 5.7 shows $(a-b)$ values as a function of up-step sliding velocity for all samples tested. There is considerable variation in $(a-b)$ with simulated depth. All samples show some negative $(a-b)$ values under certain experimental conditions, indicating potential for unstable slip. In all fault gouge-derived samples, $(a-b)$ increases with increasing sliding velocity, regardless of the depth simulated (Figures 5.7a, 5.7c). Negative values are restricted to temperatures of 150-200 °C. Samples derived from foliated cataclasites and ultracataclasites show predominantly negative values of $(a-b)$ transitioning to positive values at temperatures of 400 and 450 °C. Interestingly, at $T=400$ and 450 °C, the cataclasites' $(a-b)$ decreases with increasing sliding velocity. Finally, $(a-b)$ values for the sample derived from serpentinite schist show three regimes of velocity dependence: lower temperature (150 °C) velocity strengthening, intermediate temperature (200-350 °C) velocity weakening and high temperature velocity strengthening (400-450 °C). As before, $(a-b)$ decreases with increasing sliding velocity in the higher-temperature regime. The serpentinite

schist's rate dependence is consistent with the behavior of lizardite, a low-temperature ($T < 300$ °C) serpentine mineral that comprises 82% of the sample (e.g., Moore et al. 1997; Moore & Lockner, 2013; Schwartz et al., 2013) (Appendix Table D.6).

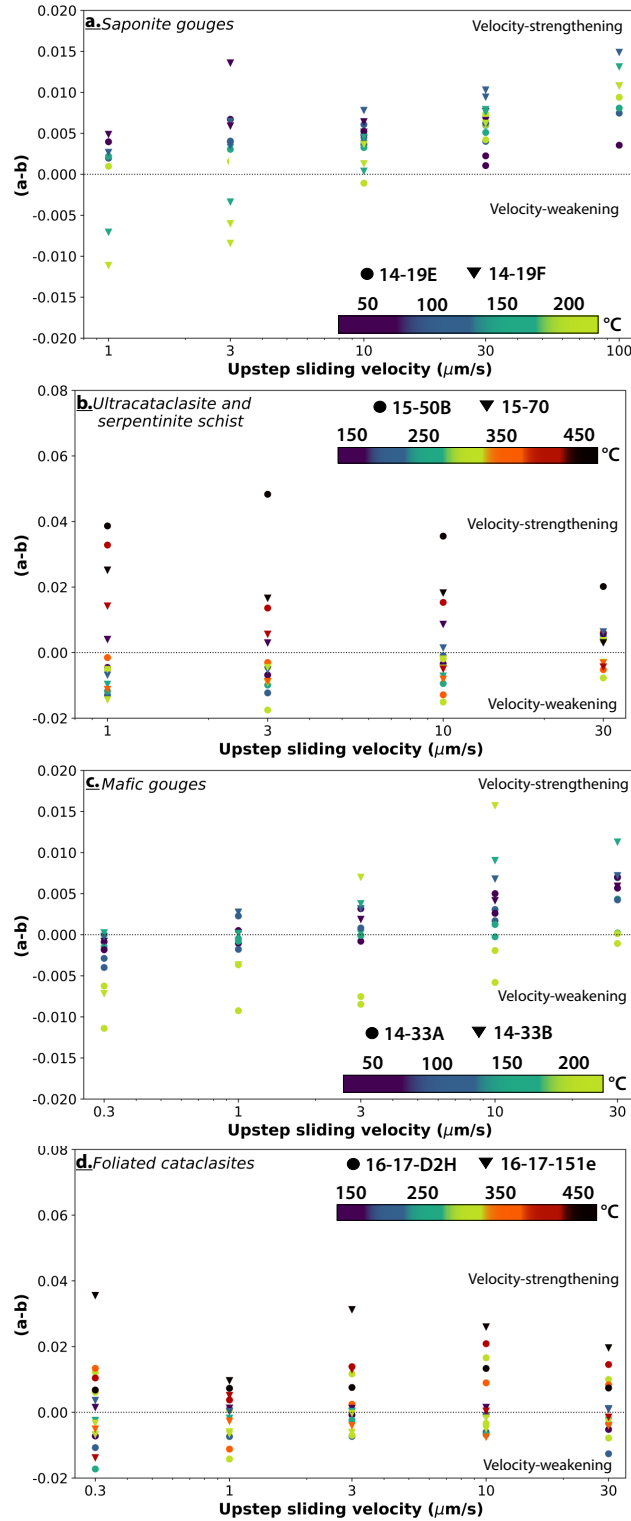


Figure 5.7. Rate-state-friction stability parameters ($a-b$) from velocity-stepping experiments on Mai'iu fault rocks (Section 5.3.1; Figure 5.5, Table 5.1; Appendix Table D.6) including a.) corrensite-saponite gouges, b.) ultracataclasite and serpentinite schist; c.) mafic gouges; d.) foliated cataclasites.

5.4. DISCUSSION

5.4.1. Experimental constraints on fault slip behavior

5.4.1.1. Evidence for frictional strain-weakening of a rolling-hinge detachment

Our experimental results show that the Mai'iu fault gouges inferred to be active at the shallowest depths are frictionally weak ($\mu = 0.11 - 0.35$), with the most phyllosilicate-rich (saponitic) gouge exhibiting the lowest static friction coefficients of 0.11 – 0.15. Saponite is thermodynamically unstable above ~ 150 °C (e.g., Boulton et al., 2018; Moore, 2014), implying that these weak gouges control the frictional strength of only the shallowest and most mechanically misaligned portions of the Mai'iu fault, down to inferred depths of ~ 6 km (Figure 5.8; Mizera et al., 2020). At greater depths and higher temperatures ($T = 150 - 225$ and $150 - 300$ °C, respectively), chlorite thermometry from syntectonic structures (e.g., veins, shear bands) indicates that slip occurred in the mafic ultracataclasite and foliated cataclasite units (Mizera et al., 2020), which are frictionally stronger ($\mu = 0.59 - 0.80$ and $\mu = 0.44 - 0.75$, respectively). This increase in frictional strength with depth coincides with the depth range over which the fault dip steepens from $15-22^\circ$ in the upper 4–5 km to $30-40^\circ$ below 5–6 km (Abers et al., 2016; Little et al., 2019; Mizera et al., 2019; Webber et al., 2020). Based on this striking correlation between fault dip at depth and the static frictional strength of the associated fault rocks deformed at those depths, we infer that the static frictional strength of the Mai'iu fault rocks partially controls the fault geometry, with slip at shallow dip angles in the near-surface facilitated by abundant weak saponitic gouges, and slip at steeper dip angles at greater depths occurring on frictionally stronger (ultra-) cataclasites. Formation of saponite (or other weak phyllosilicate minerals in other LANFs) results in a syn-exhumational reaction-weakening of the fault, consistent with classic geodynamic models of detachment faults that require plastic strain-weakening of the normal fault zone in order for it to evolve into a long-lived rolling hinge-style detachment (e.g., Lavier et al., 1999; 2000).

Although this geodynamic plastic strain-weakening is commonly modeled as a loss of cohesion (e.g., Lavier et al., 1999; 2000; Choi et al., 2013; Choi & Buck, 2012), our experimental results show that the effective strain-weakening of an active rolling-hinge detachment fault (Mizera et al., 2019; Little et al., 2019) can be at least partially accomplished by the reduction of the static coefficient of friction as a result of fluid-assisted mineral transformation reactions that form weak phyllosilicate minerals such as saponite.

The static frictional strength of active LANFs is thought to influence both fault geometry according to classical Mohr-Coulomb-type fault mechanics (e.g., Axen, 2004; Choi & Buck, 2012; Choi et al., 2013; Collettini et al., 2009b; Collettini & Sibson, 2001; Yuan et al., 2020) and wedge geometry according to critical wedge theory and limit analysis (e.g., Yuan et al., 2020). The low frictional strength ($\mu \sim 0.2$) of clay-rich and/or hydrated gouge minerals such as talc and smectite should allow normal faults filled with these minerals to remain active at shallower dips (e.g., Collettini, 2011) and may resolve the apparent mechanical paradox of these anomalously low-angle structures. Although prior experimental friction studies of LANF zone rocks show some evidence of friction coefficients of 0.2 – 0.3 in the most phyllosilicate-rich or heavily foliated samples, many previously tested gouges show friction coefficients >0.4 (Collettini et al., 2009b; Haines et al., 2014; Smith & Faulkner, 2010; Niemeijer & Collettini, 2014; Numelin et al., 2007b). Our results confirm that shallow LANF gouges can be extremely frictionally weak, but suggest that LANF strength at greater depths depends on the frictional strength of the deeper fault rock protoliths of these gouges.

5.4.1.2. Depth-dependent frictional stability

One explanation for the paucity of recorded earthquakes on some LANFs is that they primarily creep aseismically (e.g., Abers, 2009; Hreinsdóttir & Bennett, 2009), implying that the fault material is predominantly velocity-strengthening through the brittle crust (e.g., Collettini, 2011). Indeed, velocity-stepping experiments on exhumed LANF gouges (Niemeijer & Collettini,

2014; Numelin et al., 2007b; Smith & Faulkner, 2010) and typical LANF gouge minerals (Colletini, 2011 and references within) show predominantly velocity-strengthening behavior under upper crustal conditions, with a thermally activated transition to velocity-weakening behavior at >300 °C (Niemeijer & Colletini, 2014).

Velocity-stepping experiments on Mai'iu fault sequence rocks ranging from mylonitic protoliths to well-developed gouges were performed under a range of temperature (50 – 450 °C), effective normal stress (30 – 210 MPa), and pore-fluid pressure (20 – 140 MPa) conditions associated with a range of crustal depths (~3 – 25 km, as inferred by Mizera et al., 2019). The saponite-rich gouges exhibit strictly velocity-strengthening behavior for temperatures <150 °C, with the less-saponitic sample transitioning to velocity-weakening at $T \geq 150$ °C. In contrast, mild velocity-weakening behavior is observed for low upstep-velocities at $T=50-200$ °C in the mafic gouges, which contain less saponite ($< 22\%$) and more remnant (ultra-)mafic clasts, chlorite, actinolite and epidote. The mafic gouges transition to velocity-strengthening with increasing upstep-velocity. These results suggest that the Mai'iu fault likely creeps at $T < 150$ °C (~ 6 km depth), but that local fault stability depends on the proportion of saponite to mafic components in the gouge. The hydrological and thermochemical conditions that promote the formation and accumulation of saponite appear crucial to development of frictionally weak, velocity-strengthening behavior in the upper reaches of the fault zone.

The fault rocks active at greater depths ($> \sim 6$ km, based on temperatures >150 °C from Mizera et al., 2020) are more strongly and consistently velocity-weakening than any of the shallowly formed gouges. The cataclasites and ultracataclasite samples show predominantly negative ($a-b$) values ($-0.02 < (a-b) < 0$) at 150-350 °C, transitioning to consistently positive ($a-b$) values ($0 < (a-b) < 0.05$) at ≥ 400 °C. This transition to velocity-strengthening behavior around $T=400$ °C corresponds to the conditions under which most chlorite and chlorite-actinolite gouges have been observed to be strongly velocity-strengthening ($T \geq 400$ °C and $\sigma_n^{eff} = P_f \geq 100$ MPa, Okamoto et al., 2019, 2020). We infer that deformation at depths greater than the ~ 400 °C isotherm

(> ~20-25 km depth) occurs primarily by aseismic ductile creep in the mafic mineral assemblage (chlorite, actinolite) within the mylonitic shear zone.

Altogether, the experimental friction results outline three primary temperature-dependent stability regimes of the Mai'iu fault rock sequence: low-temperature (≤ 150 °C) velocity-strengthening, intermediate-temperature (150-350 °C) velocity-weakening, and high-temperature velocity-strengthening (400-450 °C). Because the driving velocity in our experiments (1 $\mu\text{m/s}$) is orders of magnitude faster than natural tectonic plate rates, the frictional stability transitions observed in each rock type may shift to somewhat lower temperatures at slower deformation rates, as predicted by microphysical models (e.g., Chen et al., 2017 and references therein). In addition, laboratory experiments and geological mapping cannot constrain the size and spatial distribution of frictionally locked patches, which are determined by a variety of factors including the spatial distribution of different fault rocks and gouge minerals, local thermal structure, fault roughness and architectural complexity, presence and distribution of pore fluids, and local history and heterogeneity of stress and slip on the fault, among others (e.g., Avouac, 2015; Bürgmann, 2018; Harris, 2017; Scholz, 2019; references within).

5.4.2. Contemporary slip behavior in the context of geological and experimental evidence

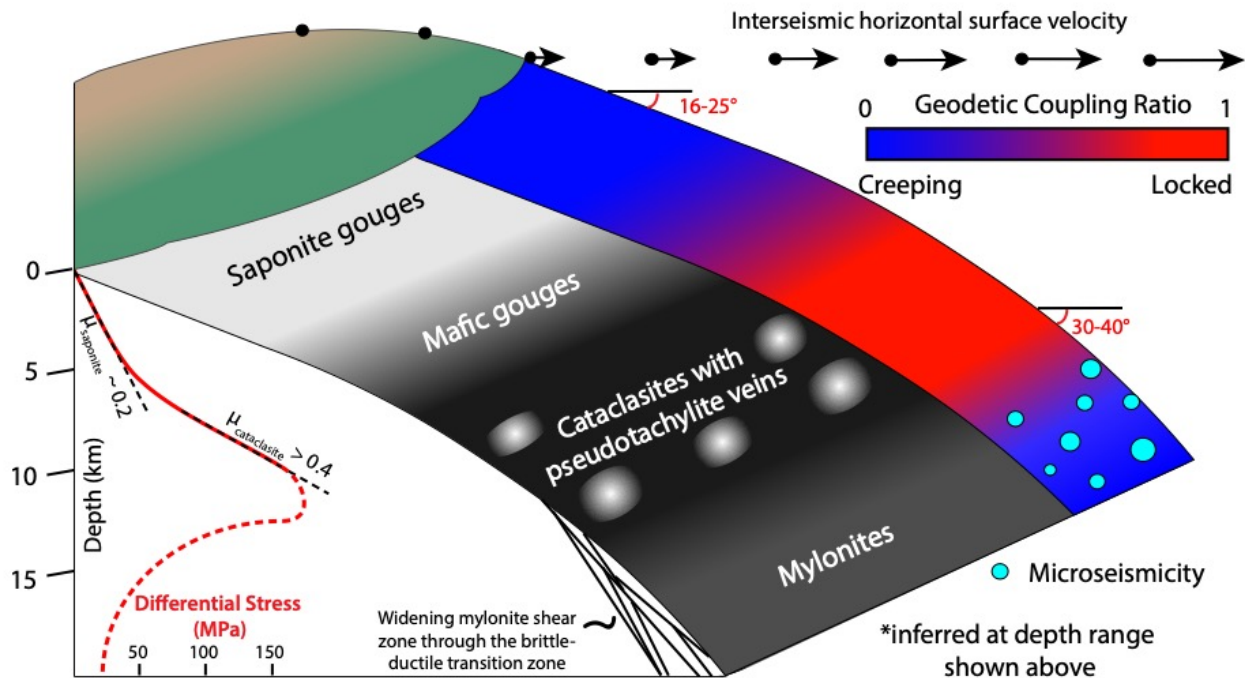
GPS velocities near the active Mai'iu LANF reveal ~8 mm/yr of horizontal extension corresponding to ~10 mm/yr dip-slip on a normal fault dipping 26-35°. Horizontal velocities are fit similarly well by ~10 mm/yr of dip-slip with distinctly different distributions of interseismic fault locking: 1) aseismic creep below a shallowly locked patch (~2 km deep) that projects to the surface at the main fault trace; or 2) aseismic creep updip and downdip of a deeper locked patch (locked from ~5-16 km depth) that projects to the surface along a splay fault within the hanging wall. We evaluate these two scenarios with respect to the experimental friction results alongside geological and geophysical evidence of Mai'iu fault slip.

The strongly velocity-strengthening behavior of the shallowest saponitic Mai'iu fault gouges (Figure 5.7a) suggests frictionally stable creep near the surface, while the predominantly velocity-weakening behavior of the cataclastic fault units deformed at greater depths (Figures 5.7b, 5.7d) points to deeper seismic slip and interseismic locking. The largely velocity-weakening behavior of the cataclasites and ultracataclasites from $T=150-350\text{ }^{\circ}\text{C}$ implies that frictional fault slip from $\sim 8-20\text{ km}$ depth likely occurs as seismic or microseismic events that release elastic strain accumulated around frictionally locked patches. Along with evidence for sufficient seismic slip to generate pseudotachylite melts at 10-12 km depth (Little et al., 2019) and cause episodic meter-scale coastal uplifts further along-strike as recorded by emerged fossilized coral reefs (section 5.1.2; Biemiller et al., 2020a), these results are most consistent with model 2 (Figure 5.3d-f), which exhibits strong locking over the $\sim 5-16\text{ km}$ depth range and would predict both earthquake nucleation and relatively uninhibited earthquake propagation through frictionally unstable velocity-weakening fault rocks (Figures 5.6-5.8). Model 1, by contrast, predicts aseismic creep below 2 km depth and negligible seismogenic potential at the depths of pseudotachylite formation and velocity weakening fault rocks. Although seismic rupture nucleated elsewhere could potentially propagate through a creeping segment to generate pseudotachylites, the depth-dependent stratification of fault slip stability illustrated by experimental friction and microstructural evidence implies deeper, stronger locking most consistent with model 2.

Frequent and localized microseismicity is common along actively creeping fault segments (e.g., Bürgmann et al., 2000; Harris, 2017; Malservisi et al., 2005; Wolfson-Schwehr & Boettcher, 2019). Strongly aligned microseismicity from $\sim 12-25\text{ km}$ depth (Figure 5.1d; Abers et al., 2016) not only outlines the deeper extent of the Mai'iu fault, but also suggests that a deeper portion of the fault zone actively creeps, generating microseismic events during frictional failure of small locked asperities within the creeping shear zone. The updip cutoff depth of this microseismicity suggests a transition from steady creep below to stronger locking above, and may be associated with a transition from frictional-viscous velocity-strengthening creep to frictional velocity-weakening behavior around 10-15 km (Figure 5.8); however, because the Mai'iu fault is near the

edge of the seismic network of Abers et al. (2016), the exact depth of this transition as defined by microseismicity is not tightly constrained (Figure 5.1d). It is also important to note that the network of permanent continuous seismometers in PNG is sparse and that dense deployments (e.g., Ferris et al., 2006; Abers et al., 2016) have thus far been temporary; hence, the detection limit for earthquakes near the Mai'iu fault is high ($M_w > 4.5$) and it is typically not possible to compute high-quality locations for these events, making it difficult to detect and identify any potential seismic indicators of slip behavior such as small ($M_w < \sim 4$) repeating earthquakes adjacent to strongly locked patches. We suggest that future work involving dense permanent or semi-permanent seismic deployments focused on the Mai'iu fault could reveal even more details of active LANF mechanics and, in particular, more tightly constrain the spatial distribution of locked, creeping, and partially coupled portions of the Mai'iu fault.

The apparent seismically delineated depth-dependent mechanical transitions on the Mai'iu fault may be explained by our experimentally observed frictional transition from velocity-weakening to velocity-strengthening behavior in the cataclastic fault rocks at around 400 °C (Figures 5.6, 5.7), as well as the microstructurally recorded mixed frictional-viscous deformation in the cataclasites and mylonites (Little et al., 2019; Mizera et al., 2020). The general depth range of this mechanical transition agrees well with model 2's predicted coupling transition from stronger locking around 5-16 km depth to creep downdip of this region; this coupling transition is not predicted by model 1 (Figures 5.3, 5.8). Combining our geodetic results with the diverse geological, experimental and seismological evidence for mixed seismic slip and aseismic creep, we infer that the Mai'iu fault is more strongly locked and potentially seismogenic from ~5-16 km depth and creeps both updip and downdip of this zone (model 2; Figure 5.8).



	Fault Rock Unit	Friction Coefficient	Frictional Stability*	Deformation Mechanism*
	Saponite gouges	0.11 - 0.28	Velocity-strengthening	Aseismic frictional creep
	Mafic gouges	0.22 - 0.57	Velocity-weakening to velocity-strengthening	Mixed diffusion creep, frictional-viscous creep & seismic slip ('partial locking')
	Cataclasites with pseudotachylite veins	0.44 - 0.80	Both velocity-weakening and velocity-strengthening	
	Mylonites	0.6 - 0.8	Both velocity-weakening and velocity-strengthening	Diffusion creep, grain-boundary sliding, small frictional failures

Figure 5.8. Inferred distribution of active Mai'iu fault rocks and deformation mechanisms, along with the resulting geodetic coupling and horizontal surface velocities. Stronger locking occurs in the velocity-weakening cataclastic units, while stable interseismic creep occurs updip and downdip of this zone in the saponite gouges and mylonites, respectively. Frictional stability and strength derived from experiments (Figures 5.6, 5.7) for all units except the mylonites, for which frictional behavior is inferred from microstructures (Little et al., 2019; Mizera et al., 2020) and microseismicity (Abers et al., 2016). The differential stress profile is based on frictional strength above the brittle-ductile transition zone (solid line) and inferred only schematically below (dashed line), but is consistent with preliminary peak differential stress estimates of ~140-185 MPa in the cataclasites from calcite twinning paleopiezometry (Mizera et al., 2020).

5.4.3. Mechanical implications for LANFs

Active aseismic LANF creep below a shallow locking depth (model 1) would agree well with previous geodetic inferences of shallow aseismic creep on another active LANF, the Altotiberina fault (Hreinsdóttir & Bennett, 2009). However, allowing for more complex structures including creep and locking of nearby splay faults, subsequent modeling of the Altotiberina fault (Anderlini et al., 2016) has shown that a spatially heterogeneous pattern of locked and creeping patches is more consistent with observed surface GPS velocities. Similarly, based on the velocity-weakening frictional behavior of exhumed fault rocks, coseismically generated pseudotachylites exhumed from ~10–12 km depth, microseismicity data highlighting fault creep below ~12 km depth, and the results of geodetic models that allow for splay fault slip and patchy locking at depth, the Mai'iu fault appears to be more strongly locked from ~5–16 km depth (model 2) and to be creeping interseismically along its shallowest portions (<~5 km depth).

We suggest that the strongly coupled depth range of ~5–16 km corresponds to the brittle strength peak for the Mai'iu fault rock sequence where interseismic elastic strain can accumulate between periods of cataclastic deformation of potentially unstable velocity-weakening mylonitic protoliths (i.e., cataclasite and ultracataclasite units, Figures 5.5–5.7). With progressive slip and exhumation, fluid-assisted chemical reactions precipitate frictionally stable velocity-strengthening phyllosilicate gouge minerals (clays such as saponite; Figure 5.7a), responsible for the apparent transition towards aseismic creep near the surface. Models with deep locking below ~15 km do not fit the GPS data well (Figure 5.4; Appendix Figures D.4, D.6); therefore, we infer that downdip of the strongly locked portion, slip occurs mostly by aseismic diffusive mass transfer creep processes, punctuated by microseismicity associated with occasional failure of small locked asperities and the fracturing of intact competent clasts within the primarily ductilely-deforming shear zone and also by the infrequent downdip propagation of large earthquake slip. While we propose that the apparent depth-dependence of Mai'iu fault slip behavior is related to depth-

aligned syn-extensional transitions in fault rock mineralogy, it is important to note that many physical conditions besides mineralogy also vary with depth. Thus, the inferred stratification of fault slip behavior likely results from intertwined transitions in temperature, fluid pressure, and mineralogy. Transitions from aseismic locked patches to microseismic creeping patches are common along strike-slip faults (e.g., Avouac, 2015; Bürgmann, 2018; Harris, 2017; references within). Along subduction megathrusts, lithology-dependent transitions in rheological and frictional properties (e.g., Behr et al., 2018) may explain the downdip transition from locked to slow-slipping/creeping regions with microseismicity and/or tremor (e.g., Schwartz & Rokosky, 2007; Lay et al., 2012; Bostock et al., 2019).

Our preferred interpretation of slip on the Mai'iu fault implies that it may be capable of hosting and even nucleating sizeable, albeit relatively infrequent, earthquakes. Assuming a typical dip-slip rupture width-length ratio of 0.668 (Leonard, 2010) and shear modulus of 25 GPa, nominal slip of 1 m on a locked patch dipping 35° from 5-16 km depth would correspond to a $\sim M_w$ 6.7 earthquake; allowing for rupture to the surface increases this estimate to $\sim M_w$ 7.0. These estimated magnitudes agree well with both the largest reported LANF earthquake globally (M_w 6.8, 29 October 1985; Abers, 1991; Abers et al., 1997) and estimations of Mai'iu fault earthquake magnitude based on the stress and slip required for coseismic melting and pseudotachylite formation (M_w 6.0+; Little et al., 2019). Taken together, these observations and calculations illustrate the potential severity of Mai'iu fault earthquakes and the importance of including the Mai'iu fault and other active LANFs in future seismic hazard assessments and risk mitigation plans.

5.5. CONCLUSIONS

New campaign GPS and experimental friction data from the Mai'iu fault in Papua New Guinea illuminate the patterns and mechanisms of creep and locking on one of the world's fastest-slipping active low-angle normal faults. Horizontal GPS velocities indicate 8.3 ± 1.2 mm/yr of

active extension across the Mai'iu fault. Friction experiments show that clay-rich gouges from the shallowest and most poorly aligned portion of the fault are both weak ($\mu = 0.11-0.35$) and predominantly velocity-strengthening, while cataclastic fault rocks deformed at greater depths on more steeply dipping parts of the fault are stronger ($\mu = 0.44-0.84$) and predominantly velocity-weakening. Two distinct fault locking models fit the GPS data equally well: one that requires aseismic creep below ~ 2 km depth and one with a locked patch from $\sim 5-16$ km depth. A range of geological, experimental, and seismological data support the geodetic model with interseismic locking from $\sim 5-16$ km depth and shallower aseismic creep on the Mai'iu fault and one or more hanging wall splay faults. This model also agrees with geological and coral paleoseismological evidence of seismic slip on the Mai'iu fault and confirms that LANFs may be capable of hosting $M_w 7.0+$ earthquakes despite the abundance of velocity-strengthening fault gouges at shallow depths which promote interseismic creep near the Earth's surface.

Chapter 6: Conclusion

The research presented in this dissertation aimed to study a uniquely active detachment fault system to advance our understanding of the tectonic, geologic, and mechanical processes that form continental metamorphic core complexes in the footwalls of low-angle detachment faults and accommodate slip on these mechanically enigmatic normal faults.

In chapter 2, geodynamic models tested the influence of tectonically inherited post-subduction or post-collisional thermomechanical conditions on the structural style and evolution of subsequent lithospheric extension. Model results showed that the dip of an inherited mechanically weak shear zone strongly controls whether this zone localizes extension as a long-lived detachment fault or is abandoned in favor of rifting on newly initiated normal faults. Counterintuitively, these models show that more steeply dipping inherited shear zones are more likely to develop into sustained detachment fault systems that dip at a low angle near the surface via a rolling-hinge mechanism, whereas shallowly dipping inherited shear zones are more easily abandoned by newly formed higher-angle normal faults. Models based on lithospheric conditions in southeast Papua New Guinea suggest that mantle buoyancy due to pre-extensional removal of mantle lithosphere may explain the conspicuous ~3 km topographic expression of the DSM.

In chapter 3, numerical models of fault slip governed by rate-and-state friction explored how fault rock frictional stability affects the seismic-cycle slip behavior of low-angle normal faults. These models predict that normal faults with certain frictional stability distributions may slip in episodic creep events or in sequences of clustered earthquakes, suggesting that a spectrum of slip behaviors between steady aseismic creep and perfectly periodic earthquake cycle slip may occur on non-subduction crustal faults. These normal fault creep events may be more difficult to detect with current instrumentation due to their longer timescales of activity (decades to hundreds of years) relative to subduction zone slow-slip events. Nonetheless, denser continuous seismological and geodetic arrays monitoring active LANFs could provide insight into ongoing sub-seismic slip cycles.

In chapter 4, emerged coral reef platforms along the southern Goodenough Bay coastline were surveyed and dated using U/Th isotopic ratios to better understand coastal emergence and tectonic uplift near the Mai'iu fault. The distinct platform-notch-platform sequence morphology of the preserved coral reefs are indicative of episodic emergence events separated by periods of

hundreds of years of vertical stability or gradual subsidence. In the absence of rapid sea level fluctuations, these emergence events are inferred to be tectonically driven and represent the surface expression of paleoearthquakes on the Mai'iu-Gwoira-Goodenough detachment system, including higher-angle near-surface splay faults. Episodic uplift increments of 0.5 – 1.8 m with recurrence intervals of 440 – 1520 years correspond to $M_w > 7.0$ earthquakes on this active fault system and imply some coseismic slip on an underlying low-angle normal detachment fault. These results show that the active normal faults in the southeastern Papuan Peninsula are seismogenic and likely pose future seismic hazard risks for coastal communities there.

In chapter 5, surface velocities measured from campaign GPS observations near the Mai'iu fault trace were modeled to determine slip rates and spatial patterns of creep and locking on the world's most rapidly slipping low-angle normal fault. Inversions of these data for preferred kinematic slip models yielded two families of equally viable non-unique interseismic locking solutions: one with near-surface locking and deeper creep and one with near-surface creep and deeper locking. Constraining these slip models with the results of geological, microstructural, and experimental friction studies of the exhumed Mai'iu fault rocks with the GPS velocities, the slip models with deeper locking and shallow aseismic creep are preferred. The integrated geophysical and geologic observations from the Mai'iu fault suggest that this fault and other active LANFs may host large ($M_w > 7.0$) earthquakes and must be considered in seismic hazard potential estimates for southeast Papua New Guinea.

An overarching conclusion of this work and the related geological and experimental studies of the Mai'iu fault zone is that the modern seismic-cycle slip behavior of an active long-lived detachment fault is inextricably linked to the fault's long-term tectonic, structural, mineralogical and slip history. For example, frictionally weak clay-rich fault gouges form from mineralogical reactions during sustained slip on one major dominant normal fault that localizes crustal strain accommodating regional extension. The formation and accumulation of these gouges further weakens the fault and serves as one mechanism of fault zone 'strain-softening' or strain-weakening that enhances strain localization and promotes subsequent slip on the main detachment. Geodynamic models of lithospheric extension show that significant strain-weakening is necessary to localize extension and develop a perennial detachment system rather than rifting via a wide array of steeper normal faults. Slip-synchronous mineralogical reactions weaken the fault and facilitate subsequent slip and strain localization in a positive feedback loop

that helps explain why detachment faults are such long-lived structures that can accommodate 10's of kms of offset. These abundant clay-rich gouges in the shallow fault zone are typically velocity-strengthening and promote shallow aseismic frictional creep. In contrast, the deeper velocity-weakening mylonitic and cataclastic fault rocks cannot sustain such high localized strain rates via aseismic diffusion or dislocation creep. Instead, this portion of the fault partially locks and the surrounding rocks accumulate some of the tectonically applied loading as elastic strains that are eventually relaxed during coseismic slip. Although many details remain to be resolved in future work, observations from the Mai'iu fault show that tectonic-timescale and seismic-cycle-timescale deformation processes on detachment fault systems strongly influence one another. Carefully integrating evidence of both seismic-cycle deformation (e.g. from geodesy, seismology, paleoseismology, frictional stability laboratory experiments) and tectonic-timescale deformation (e.g. from structural geology, tectonic geomorphology, plate reconstructions, geodynamic models) can help us better understand both the evolution and ongoing deformation of major plate boundary fault zones.

Appendices

APPENDIX A: SUPPLEMENTARY MATERIAL FOR CHAPTER 2

A.1. Numerical procedure

We use the thermomechanical geodynamic finite-element Lagrangian-Eulerian code SULEC version 5.2 (developed by Susan Ellis and Susanne Buitert) which solves the incompressible momentum equation for slow, creeping power-law flows:

$$\frac{\partial \sigma'_{ij}}{\partial x_j} - \frac{\partial P}{\partial x_i} + \rho g_i = 0 \quad (\text{A.1})$$

where σ' is the deviatoric stress tensor, P is the dynamic pressure and g is the acceleration due to gravity. Plastic failure is incorporated with a Mohr-Coulomb yield criterion:

$$\sigma'_{eff} = P_{eff} \sin(\theta) + C \cos(\theta) \quad (\text{A.2})$$

where σ'_{eff} is the differential stress, P_{eff} is the effective pressure, C is the cohesion and θ is the angle of internal friction. Linear strain-softening (e.g., Lavier & Buck, 2000) is applied to the angle of internal friction (e.g., Wu et al., 2015):

$$\theta = \theta' + (\theta_0 - \theta') \left(1 - \frac{\epsilon_{ps}}{\epsilon_f}\right) \quad (\text{A.3})$$

where θ_0 is the unstrained angle of internal friction, θ' is the fully strain-softened angle of internal friction, ϵ_{ps} is plastic strain, and ϵ_f is the cutoff strain at which full strain-softening has occurred.

A temperature-dependent effective viscosity η_{eff} is calculated for power-law flow as:

$$\eta_{eff} = \frac{1}{2} A^{-1/n} d^{m/n} \dot{\epsilon}_{eff}^{1/n-1} e^{\frac{E_a + PV}{nRT}} \quad (\text{A.4})$$

where A is the pre-exponential constant, n is the flow law exponent, $\dot{\epsilon}_{eff}$ is the effective strain rate, d is the grain size, m is the grain-size exponent, E_a is the activation energy, V is the activation volume, R is the gas constant and T is the temperature. For materials with both dislocation creep and diffusion creep parameters, the viscous yield stress is equal to the minimum of the two flow stresses. Elastic effects are approximated by modifying (A.4) to include an effective viscoelastic viscosity based on the elastic time-stepping method of Moresi et al. (2003) (equations 28 and 29) with an elastic timestep 100 times the advection timestep. Effective yield stress of each element is taken to be the minimum of the viscous and plastic yield stresses for that element, and strains are

updated at each time step according to the constitutive law associated with this minimum yield stress. Temperature is computed at each time-step using the two-dimensional equation for unsteady thermal conduction with isotropic thermal conductivity:

$$\rho c \frac{\partial T}{\partial t} = \frac{\partial}{\partial x} \left(k \frac{\partial T}{\partial x} \right) + \frac{\partial}{\partial y} \left(k \frac{\partial T}{\partial y} \right) + Q \quad (\text{A.5})$$

where c is the specific heat capacity, t is time, k is thermal conductivity and Q is heat production.

Temperature-dependent density is simulated according to the Boussinesq approximation:

$$\rho = \rho_0 (1 - \alpha (T - T_0)) \quad (\text{A.6})$$

where α is the coefficient of thermal expansivity and ρ_0 is the density at reference temperature T_0 . Details of the equations and numerical formulations of SULEC are found in Buitter & Ellis (2012) and Tetreault & Buitter (2012). As in previous modeling studies, a minimum effective viscosity of 10^{19} Pa s is imposed (e.g., Wu et al., 2015; Wu & Lavier, 2016).

Solver tolerance is set to 5%, meaning that the final solver iteration for one timestep is the first iteration where the maximum change in nodal velocity anywhere in the domain between successive iterations is less than 5%. Viscosity and density of each element are computed at each timestep for the material associated with the majority of tracer particles in that element. The minimum number of particle tracers per element is 6.

A.2. Model description

The reference model geometry is simplified with a flat slab geometry to isolate the typical behavior and controls of extensionally reactivated failed continental subduction systems. For models shown in the text, the domain consisted of a 250 km wide by 200 km deep structured grid of 586,500 elements with initial element dimensions of 100 m by 100 m in the crustal region of interest from 0 to 40 km depth and 30 to 130 km horizontal position. Some parameter-testing models shown in the Supporting Information used coarser meshes. We model 35 km-thick continental crust subducted to 70 km depth beneath equally thick continental crust. Most models include a 2 km-thick frictionally and viscously weak layer between the plates which simulates a

weakened thrust interface inherited from the subduction phase. Although the thickness of the weak zone relative to the numerical cell size is known to affect strain localization in numerical models, we fix the shear zone width in this study to 2 km, a value that allows a wide range of extensional styles and amount of strain localization for the shear zone material properties tested. Subducted continental crust penetrates the 65 km-thick mantle lithosphere which overlies 100 km of mantle asthenosphere. Extension rates of 1.25 cm/yr are applied in the lithosphere and compensated by inflow of mantle asthenosphere, as discussed in the text.

Thermal structure is given by the steady-state solution to the heat equation with boundary temperatures of 20 °C at the surface and 1300 °C at 200 km depth with no heat flow on the sides. This yields an average crustal geothermal gradient of 15 °C/km. The thermal structure matches the 600°C Moho temperature of the ‘cold’ case from Whitney et al. (2013), the 800°C isotherm at 60 km as in Wu et al. (2015), and the 1300°C isotherm at 200 km as in the initial conditions and throughout regions of unperturbed lithosphere in the slab breakoff model of Petersen & Buck (2015).

Material properties used in the models from the main text are shown in Table 2.1. Properties of the crust, shear zone, and mantle lithosphere are based on those used by Wu et al. (2015) and Wu & Lavier (2016) in their studies on the effect of crustal and shear zone strength on extensional mode in orogenic settings. These choices are motivated by their utility in comparing different core complex models, but are ultimately founded in experimental material properties from Jaoul et al. (1984), Ranalli (1995), and Kirby & Kronenberg (1987). The lithosphere-asthenosphere boundary (LAB) is located at the initial 1200 °C isotherm, however compositional differences between the mantle lithosphere and mantle asthenosphere are also imposed to simulate realistic mantle rheology and deformation mechanisms. Seismology shows that the mantle lithosphere deforms primarily by dislocation creep while the mantle asthenosphere deforms by both dislocation creep and diffusion creep (Savage, 1999). Hence, we employ a composite dislocation and diffusion creep law for wet olivine (Hirth & Kohlstedt, 2003) for mantle material beneath the LAB and a simple olivine creep law (Kirby & Kronenberg, 1987) for mantle material

above the LAB, as has been used in previous modeling studies (e.g., Tetreault & Buitter, 2012). Because the flow mechanism in the lithosphere is assumed to be dislocation creep (e.g., Savage, 1999; Tetreault & Buitter, 2012), a diffusion creep flow stress is not computed in the lithosphere and m is only nonzero for asthenospheric mantle material. Thermal expansivity is not considered for crustal lithologies in our model. Thermal conductivity of the mantle asthenosphere is $20 \text{ Wm}^{-1}\text{K}^{-1}$ to allow mantle convection and to maintain the adiabat within the mantle asthenosphere as in Tetreault & Buitter (2012).

A.3. Additional Model Results

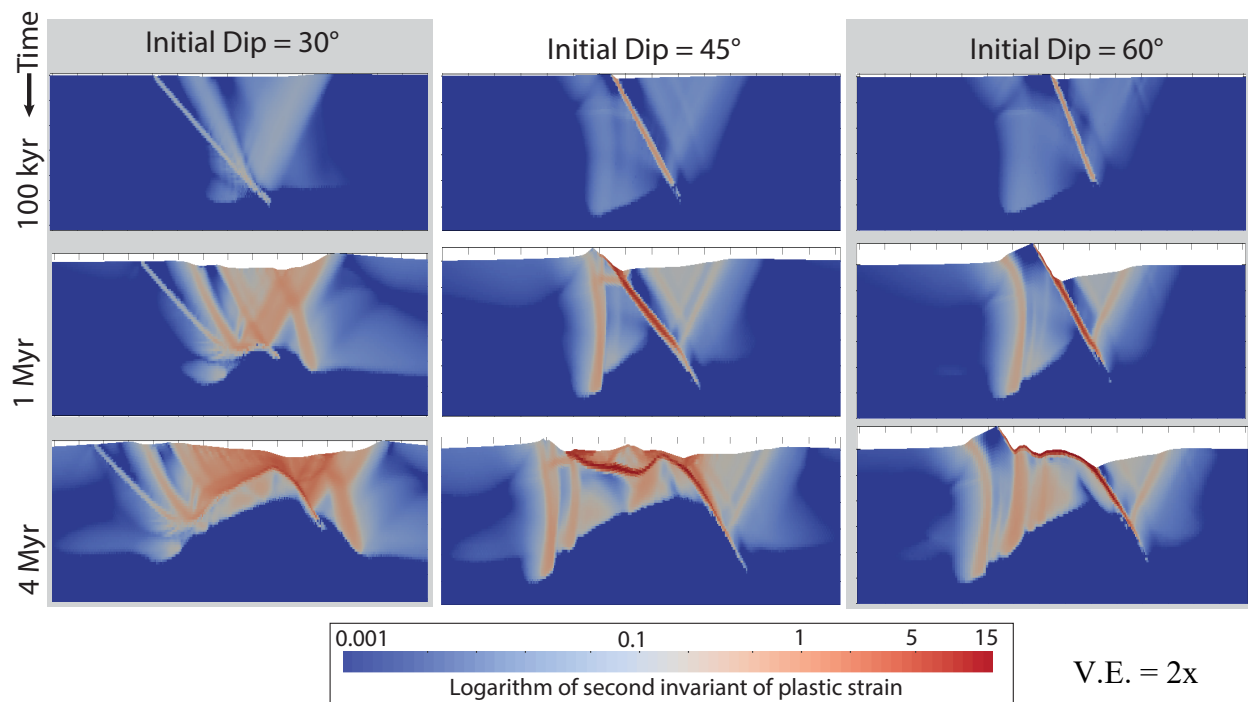


Figure A.1. Comparison of extensional style for varying slab dips of 30, 45, and 60° at times of 0.1, 1, and 4 Myr. Plots show \log_{10} of the second invariant of plastic strain in the crust. All models shown are 150 km wide and 30 km deep. Vertical exaggeration = 2. All other model properties are the same as in Table 2.1. Note that despite the low frictional and viscous strength of the initial shear zones in these models, high-angle normal faults initiate rifting above the pre-existing fault for the 30° case, while strain localizes on the pre-existing fault and exhumes a domal structure in the 60° case. In the intermediate 45° case strain localizes on the pre-existing fault, but significant activation of newly initiated high-angle fault through its footwall accommodate some extension and cut the hanging wall block that ends up stranded above the initial fault surface at 4 Myr.

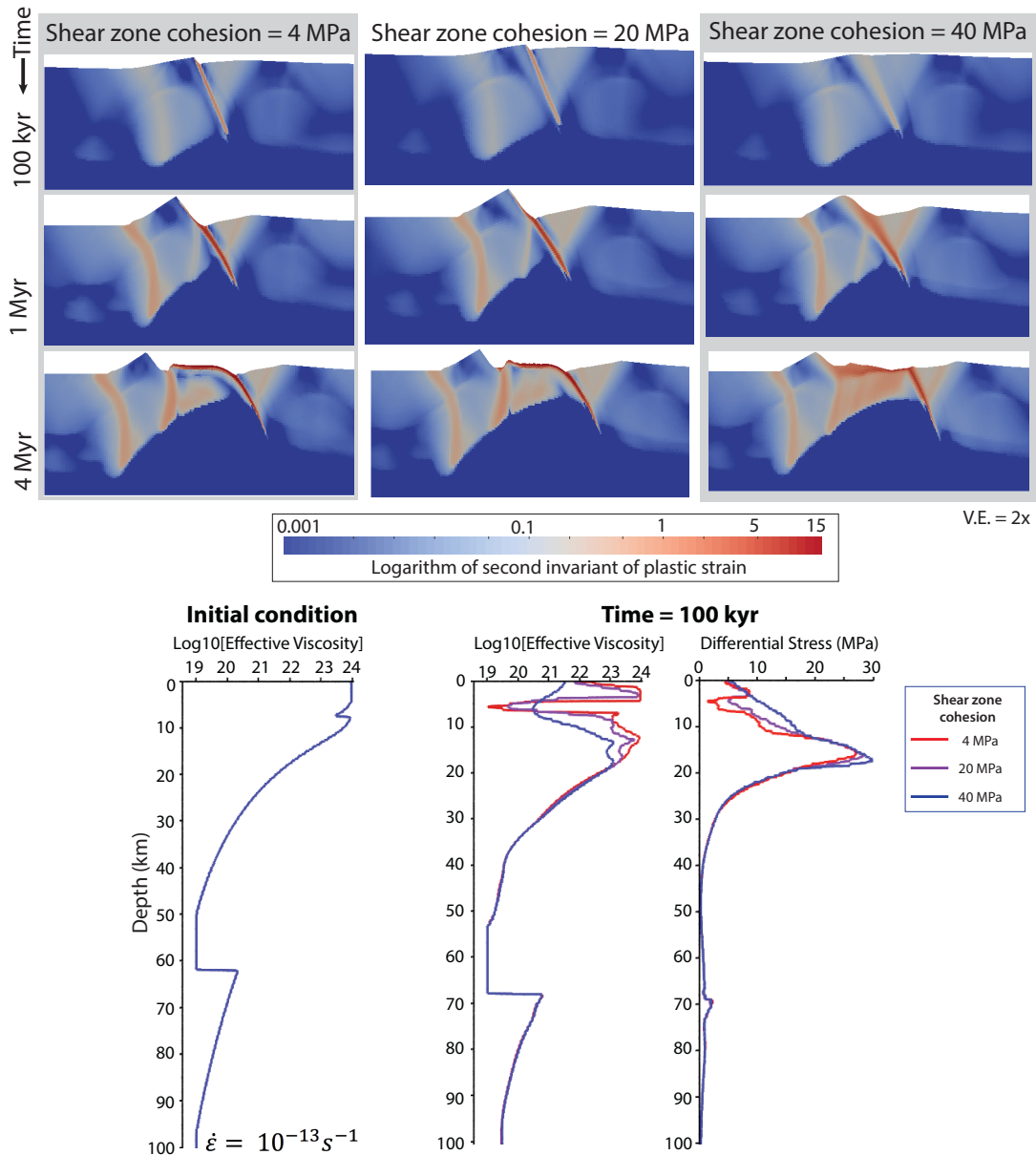


Figure A.2. Comparison of extensional style for varying shear zone cohesions of 4, 20, and 40 MPa at times of 0.1, 1, and 4 Myr, respectively. The viscous strength of the shear zone is lower than the surrounding crustal material. Initial shear zone and slab dip is 60° . Plots show \log_{10} of the second invariant of plastic strain in the crust. All models shown are 150 km wide and 30 km deep. Vertical exaggeration = 2. All other model properties are the same as in Table 2.1. Note that the shear zone with higher cohesion and frictional strength predicts more distributed faulting through the footwall and does not exhume a domal core complex. Lower panels: initial strength profile with depth (\log_{10} (effective viscosity)) from within the actively deforming shear zone region and strength profiles after 100 kyr, as strain begins to localize (differential stress, \log_{10} (effective viscosity)) for the three models shown in the upper panels.

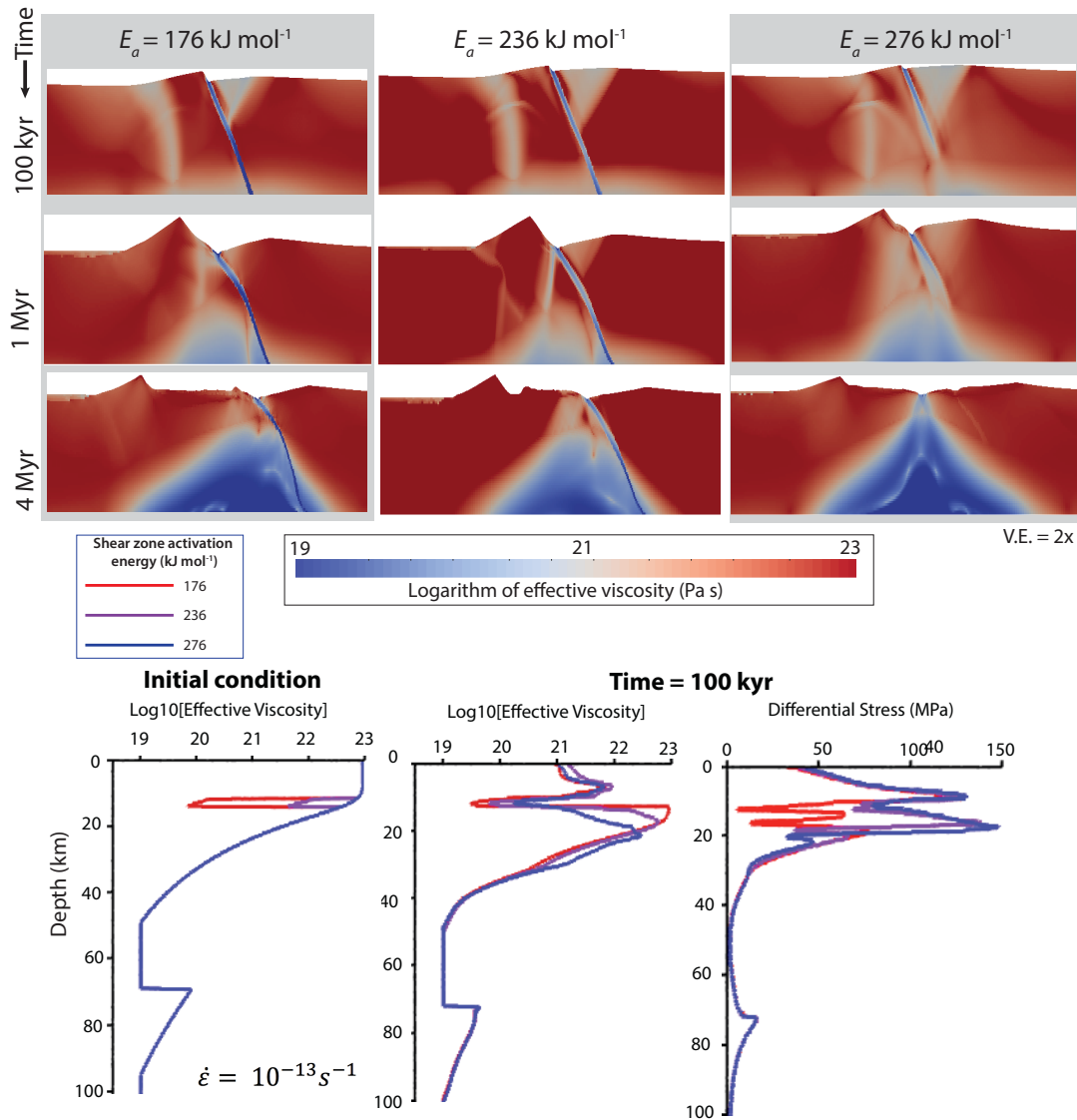


Figure A.3. Comparison of extensional style for varying shear zone viscous activation energies of 1.76×10^5 , 2.36×10^5 , and 2.76×10^5 J mol⁻¹ at times of 0.1, 1, and 4 Myr, respectively. Plots show log₁₀ of the second invariant of plastic strain in the crust. All models shown are 150 km wide and 30 km deep. Vertical exaggeration = 2. All other model properties are the same as in Table 2.1. Lower panels: initial strength profile with depth (log₁₀(effective viscosity)) from within the actively deforming shear zone region and strength profiles after 100 kyr, as strain begins to localize (differential stress, log₁₀(effective viscosity)) for the three models shown in the upper panels.

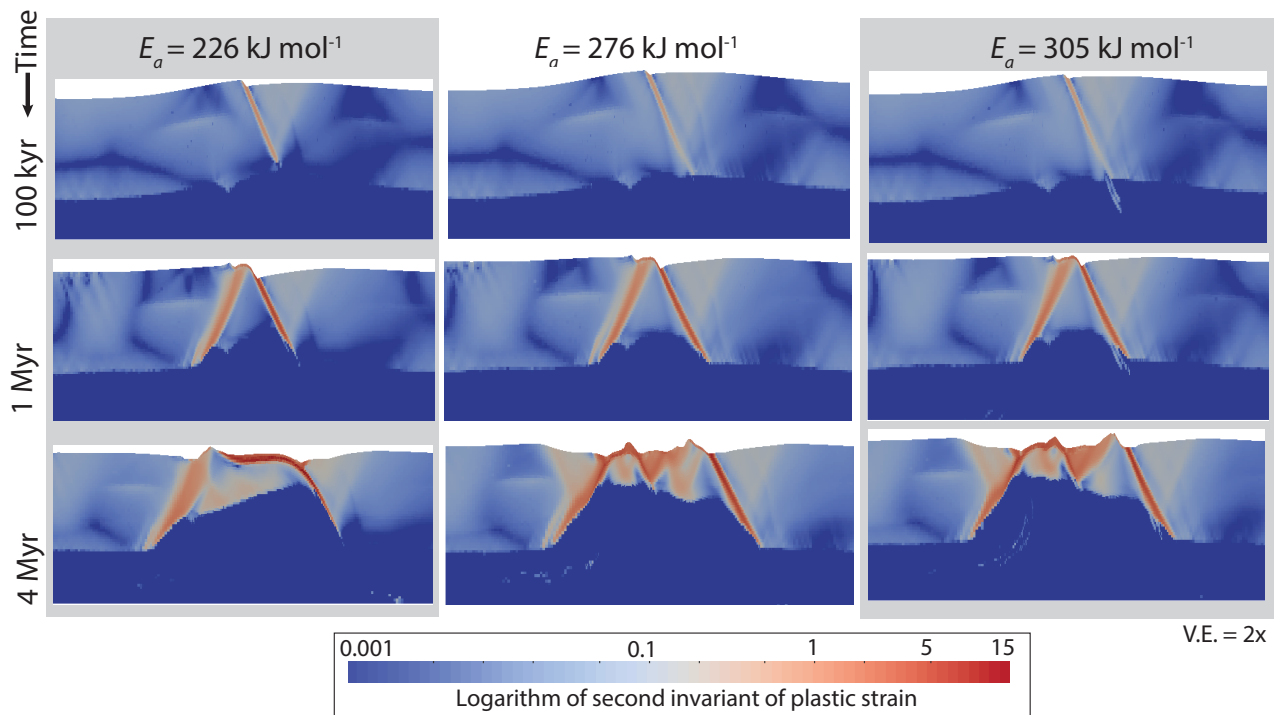


Figure A.4. Comparison of extensional style for varying shear zone viscous activation energies of 2.26×10^5 , 2.76×10^5 , and 3.05×10^5 J mol⁻¹ above weak lower crust at times of 0.1, 1, and 4 Myr. Lower crust is initially given as crustal material between 20 and 35 km depth. Plots show log₁₀ of the second invariant of plastic strain in the crust. All models shown are 150 km wide and 30 km deep. Vertical exaggeration = 2. Weak lower crust activation energy is 1.76×10^5 J mol⁻¹ below 20 km. All other model properties are the same as in Table 2.1. Note that only the low-viscosity initial shear zone case predicts a single domal core complex, while higher viscosity shear zone configurations predict double domes and bivergent high-angle rift faulting.

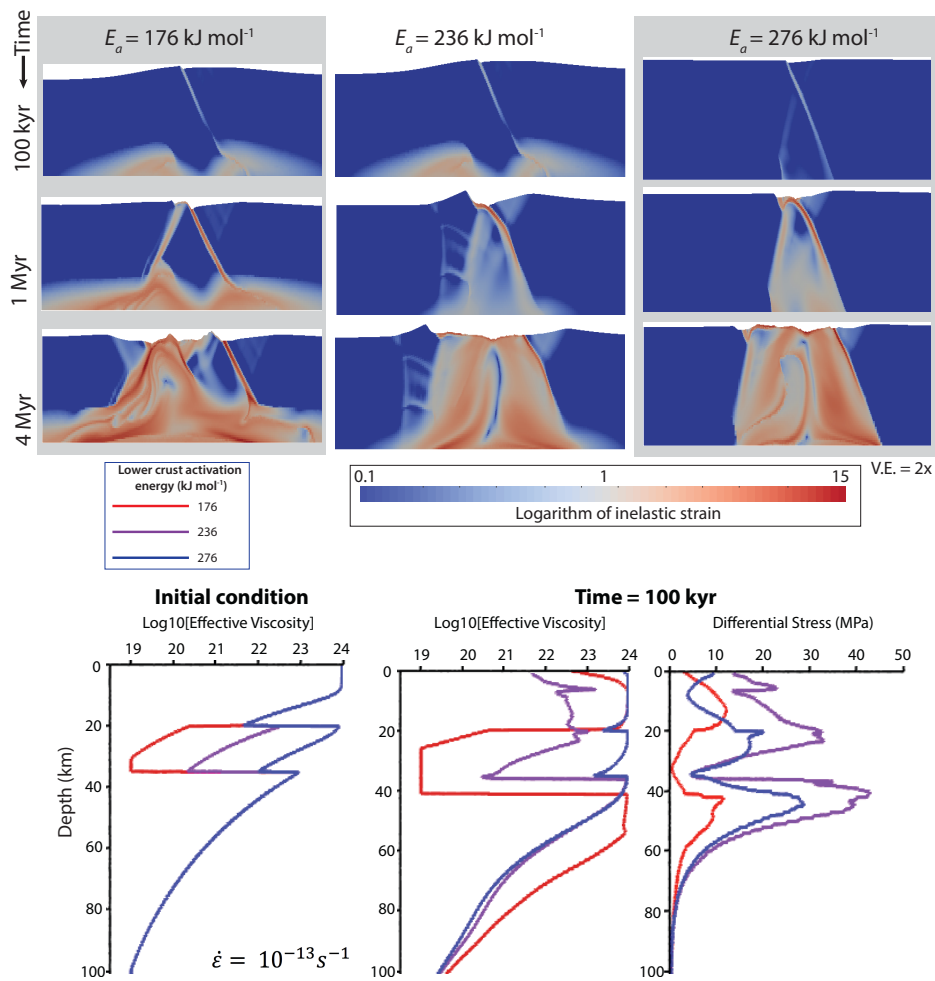


Figure A.5. Comparison of extensional style for varying lower crustal strengths with activation energies of 1.76×10^5 , 2.26×10^5 , and $2.76 \times 10^5 \text{ J mol}^{-1}$ at times of 0.1, 1, and 4 Myr. Lower crust is initially given as crustal material between 20 and 35 km depth. Shear zone viscous properties are identical to those of the upper crust. Plots show \log_{10} of the second invariant of inelastic strain in the crust. All models shown are 150 km wide and 30 km deep. Vertical exaggeration = 2. All other model properties are the same as in Table 2.1. Lower panels: initial strength profile with depth (\log_{10} (effective viscosity)) taken from left of the actively deforming region and strength profiles after 100 kyr, as strain begins to localize (differential stress, \log_{10} (effective viscosity)) for the three models shown in the upper panels, showing effect of weak lower crustal rheology.

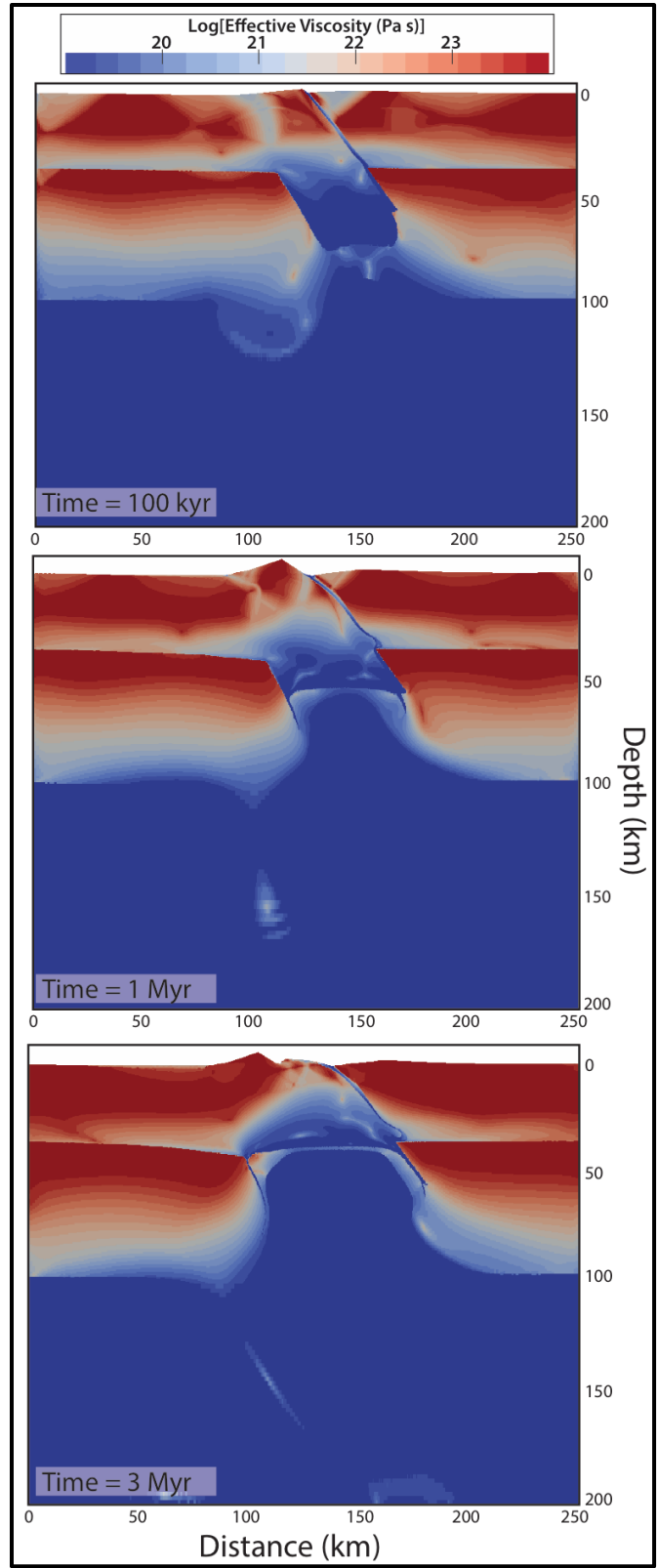


Figure A.6. Full model domain of Mode 1 example shown in Figure 2.2 of the main text at model times 0.1, 1, and 3 Myr.

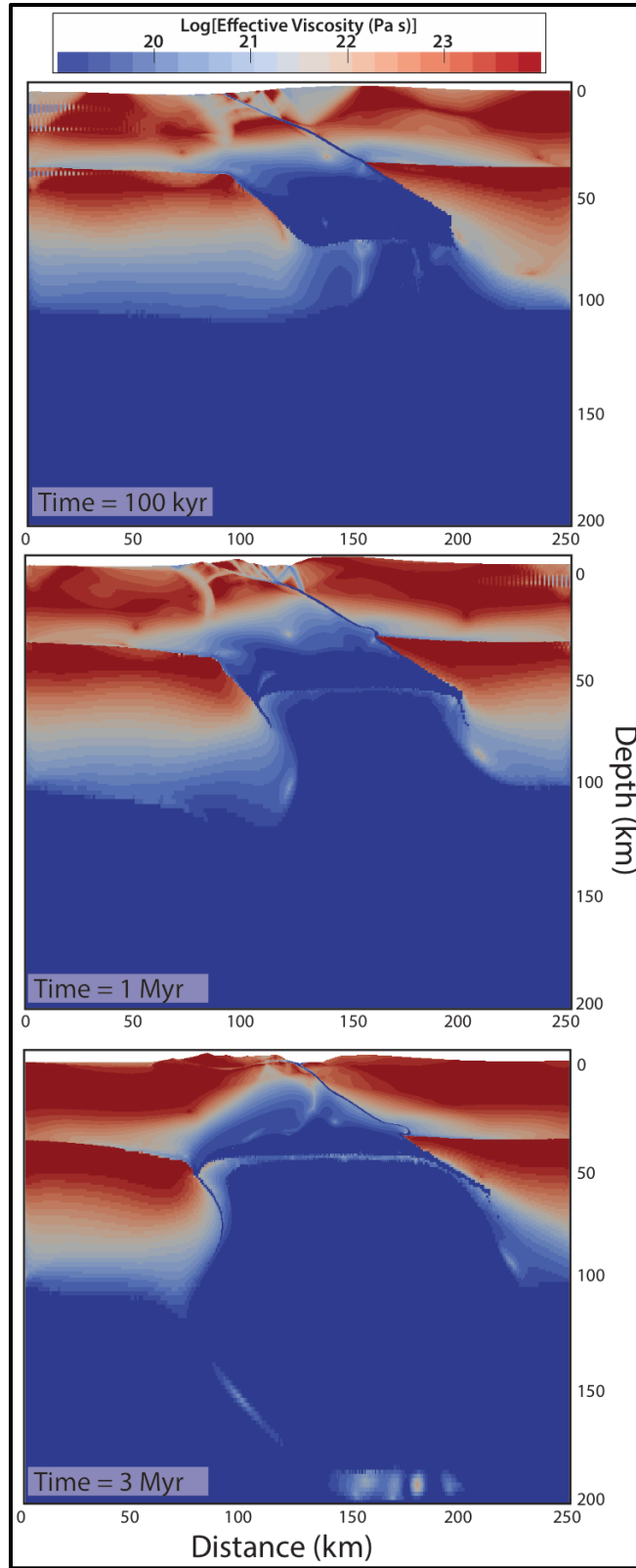


Figure A.7. Full model domain of Mode 2 example shown in Figure 2.3 of the main text at model times 0.1, 1, and 3 Myr.

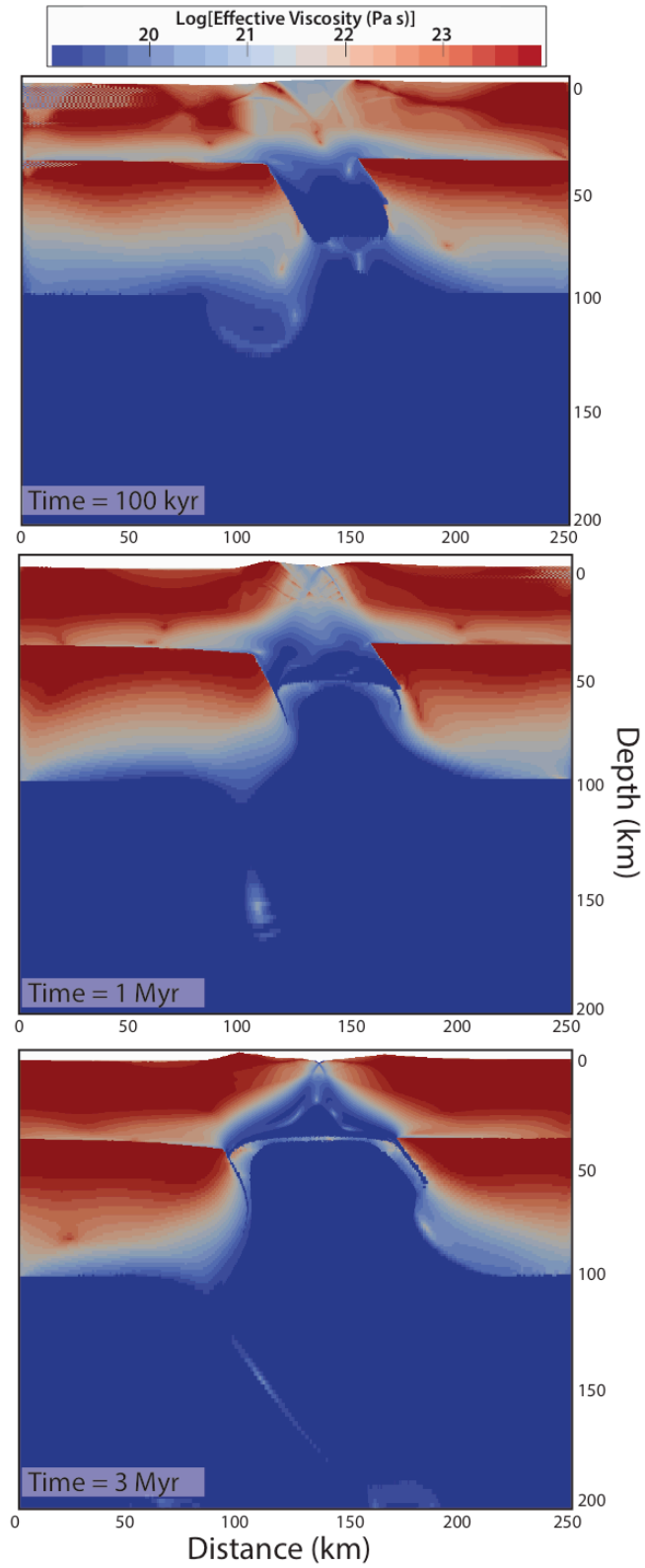


Figure A.8. Full model domain of Mode 3 example shown in Figure 2.4 at model times 0.1, 1, and 3 Myr.

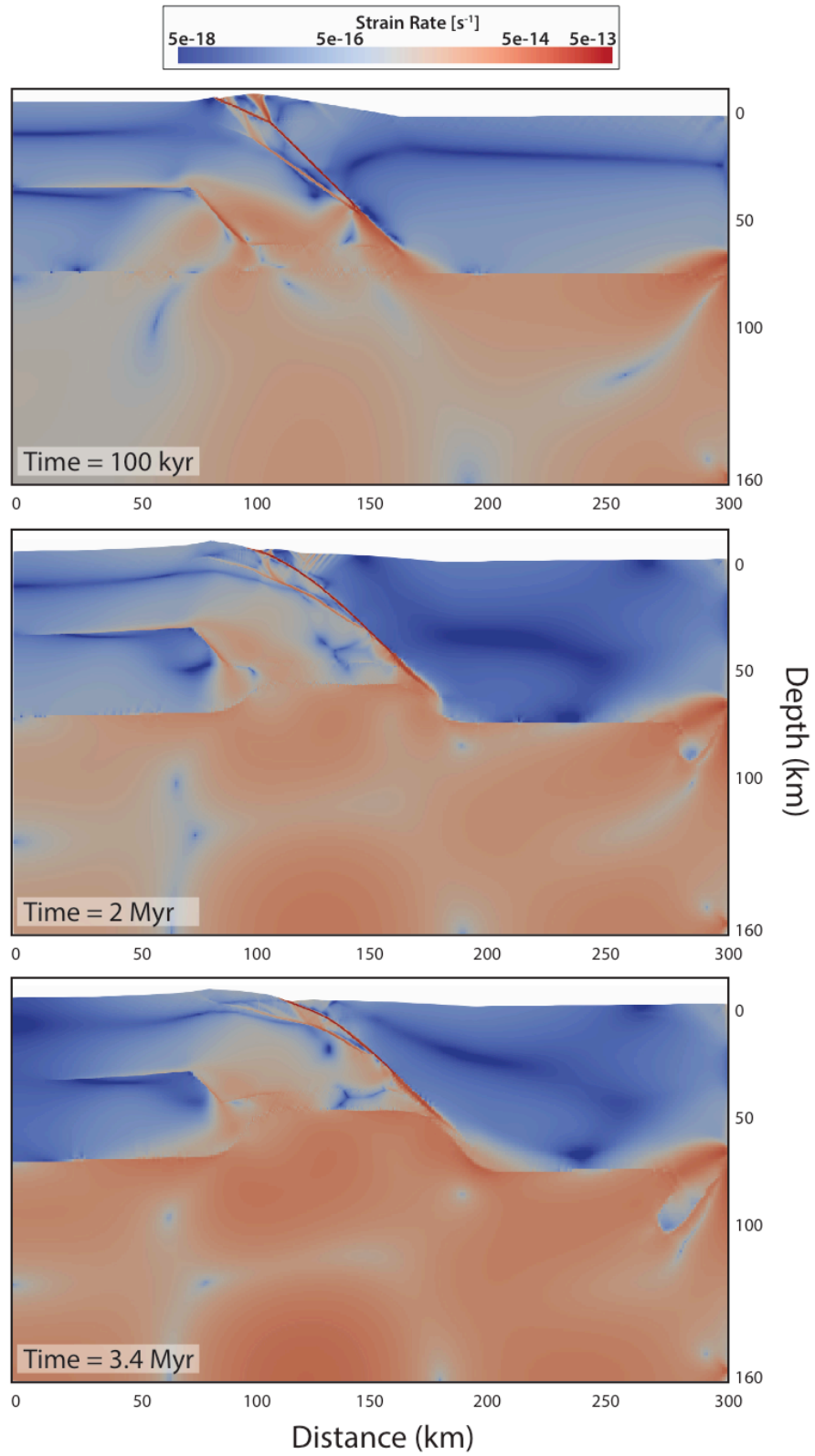


Figure A.9. Strain rate plots of full model domain for DSM-specific model (Figure 2.7) at 200 kyr, 2 Myr, and 3.4 Myr.

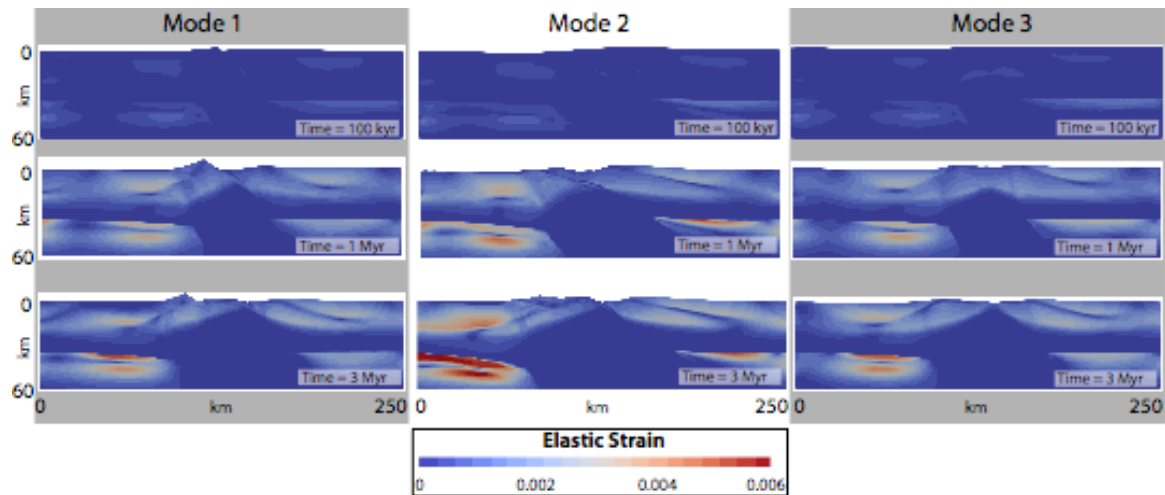


Figure A.10. Elastic strain for the three representative modal models from the text (Figures 2.2, 2.3, 2.4) at 100 kyr, 1 Myr, and 3 Myr.

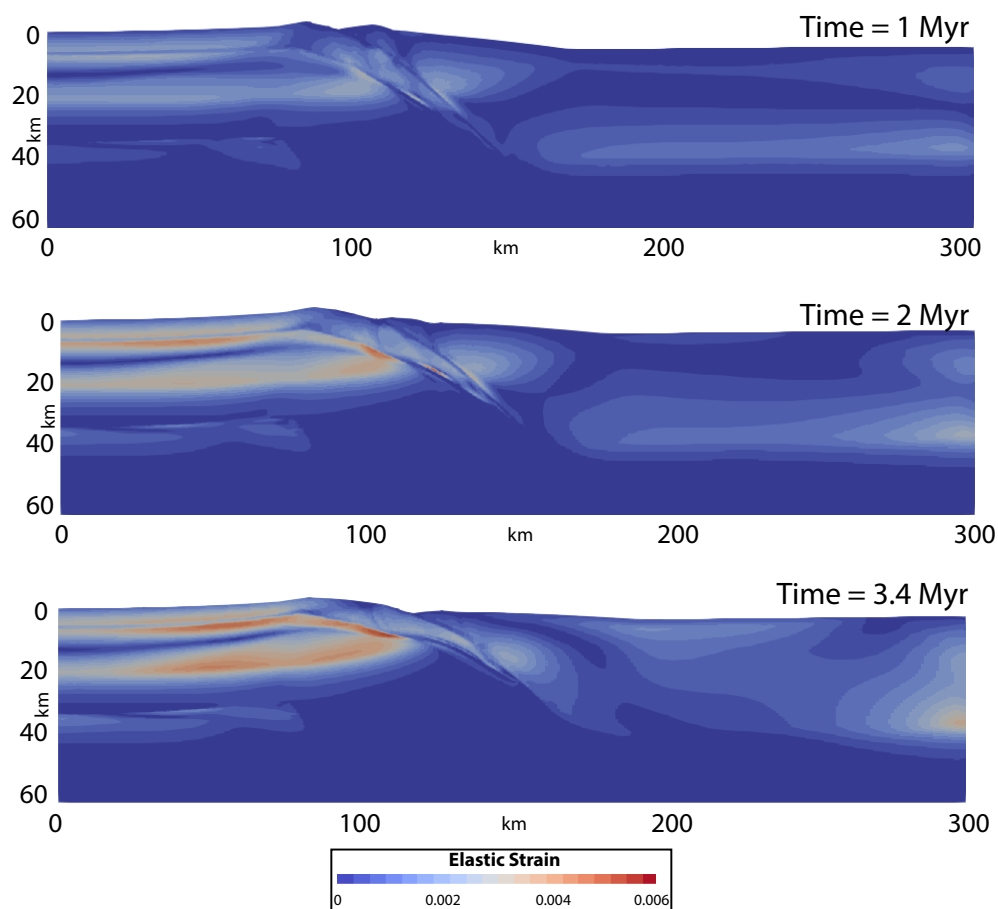


Figure A.11. Elastic strain in the preferred Dayman Dome model (Figure 2.7) at 1 Myr, 2 Myr, and 3.4 Myr, showing the distribution of bending and flexural elastic stresses in the footwall.

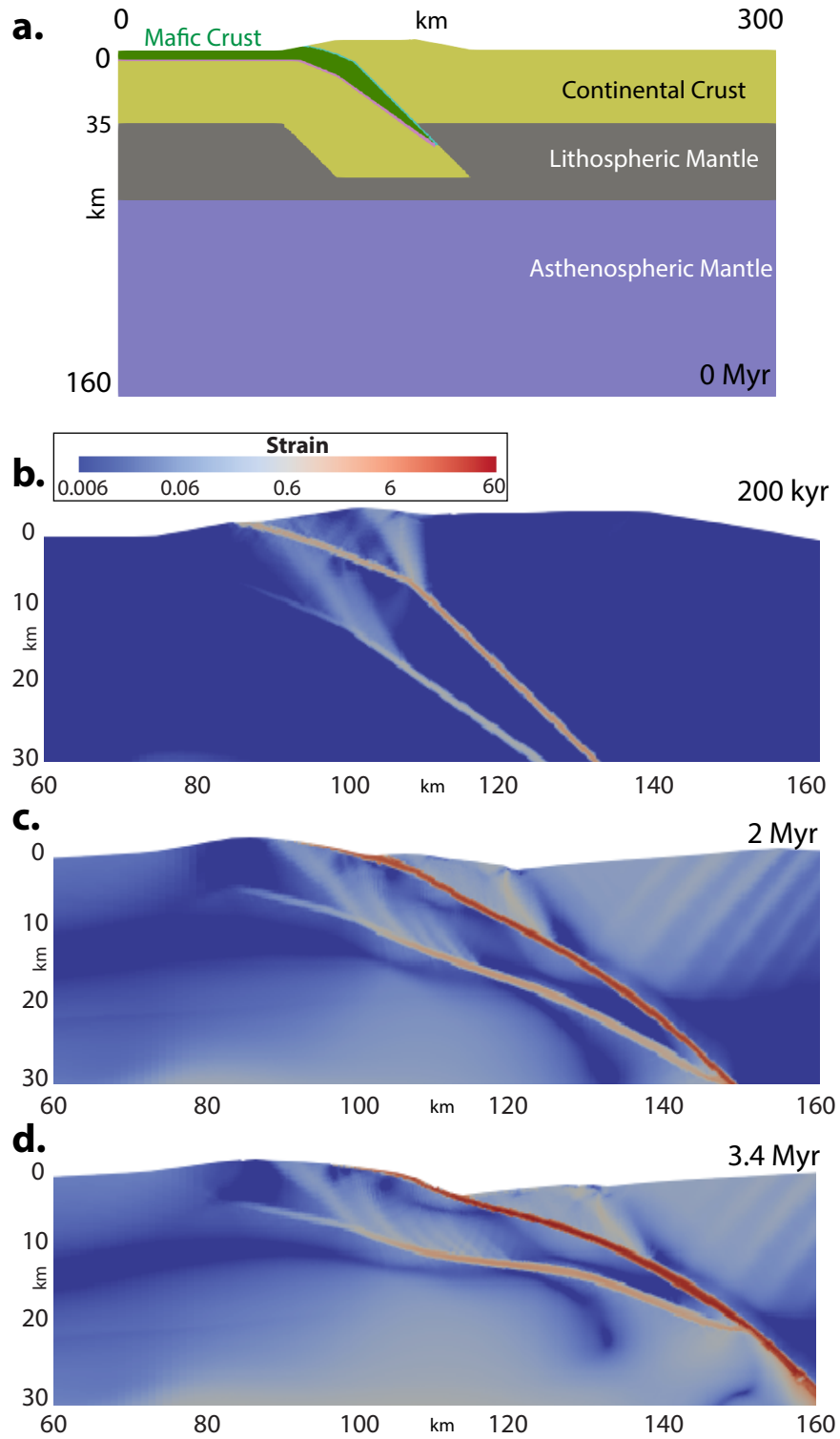


Figure A.12. Model of Dayman Dome exhumation with continental crust in the upper plate hanging wall. All other model parameters are the same as the model in Figure 2.7 of the main text. a.) Initial model geometry, with weak zones as shown in Figure 2.7. b-d.) Strain after 200 kyr, 2 Myr, and 3.4 Myr.

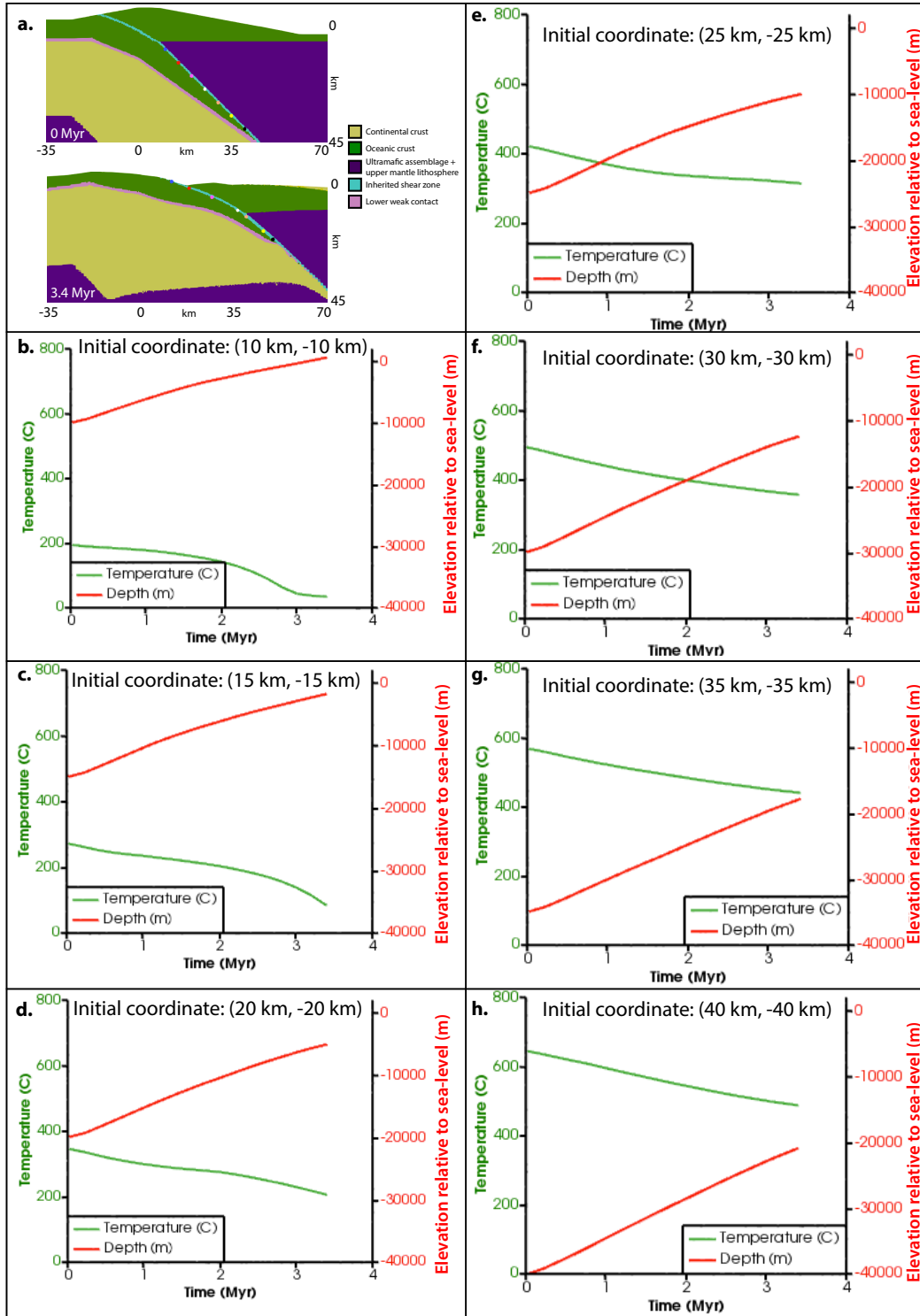


Figure A.13. Depth and temperature histories of particles shown in (a) at times 0 and 3.4 Myr for Dayman Dome model (Section 2.3). Note that depths plotted here are relative to modeled sea-level (elevation = 0) and therefore underestimate total vertical exhumational trajectory (change in depth of overlying rock column) by about 7 km due to the initial surface topography in the model setup.

APPENDIX B: SUPPLEMENTARY MATERIAL FOR CHAPTER 3

B.1. Benchmarks

Few reliable benchmark tests exist for rate-and-state friction on a planar fault due to the inherent nonlinearity of the system. In the absence of an accepted benchmark, we use the model setup and results from section 3 of Liu & Rice (2007) to test the validity of our numerical method. Liu & Rice (2007) apply rate-and-state friction to a modeled subduction zone fault interface to investigate slip behavior of a weakening patch with near-lithostatic pore-fluid pressure downdip of a fully locked shallow patch. The velocity-weakening patch transitions into a velocity-strengthening region with near-lithostatic pore-fluid pressures extending downdip and loaded constantly at 37 mm/yr. They model the Cascadia subduction interface using temperature-dependent a - b profiles. We choose Liu & Rice (2007) as our benchmark because of the clear presentation of the spectrum of slip behaviors possible for the stability transition associated with a weakening patch embedded between two strengthening patches on a 2D planar fault. Liu & Rice (2007) run numerous models varying L_C and W , the width of the unlocked portion of the fault updip of the first stability transition from velocity-strengthening to velocity weakening, finding that the variable controlling the slip behavior at the stability transition is W/h^* , where h^* is the critical cell size described in section 3.3.1. Examples of each characteristic response and the associated phase diagram are found in Liu & Rice (2007) Figures 8 and 7, respectively.

We recreate the fault geometry, a - b profile, normal stress profile, cell size, and plate velocity from Liu & Rice (2007) to test whether our rate-and-state FLAC code yields the four response phases at the stability transition for similar values of the controlling variable, W/h^* . Our model recreates all four characteristic responses, with the same phase transitions occurring as W/h^* increases. The actual values of W/h^* at these transitions differ by less than one order of magnitude from those presented in Liu & Rice (2007). We attribute these differences to our use of a non-uniform characteristic slip length L_C , whereby we decrease L_C to 0.246 mm within the velocity-weakening patch to agree with laboratory values of L_C , as Liu & Rice (2007) do in

subsequent results following their phase response model runs (i.e. Figure 10 of Liu & Rice (2007)). For computational feasibility, updip of the weakening zone L_C is set to 7.85 mm, which is larger than laboratory values. Using L_C values of this order of magnitude is common in rate-and-state numerical modeling (e.g., Hillers et al., 2006; Liu & Rice, 2007; Lapusta & Liu, 2009), the implications of which are discussed in Hillers et al. (2006). We employ the non-uniform L_C method because it more fully captures seismic responses in velocity-weakening and velocity-neutral patches. Minor differences in the timing and shape of the characteristic responses may be due to different initial conditions between our models. We allow the fault to load from an unstressed initial condition whereas Liu & Rice (2007) impose an initial state of stress close to that of failure. The overall agreement between our model and that of Liu & Rice (2007) lends confidence to the rate-and-state numerical scheme we apply to normal faults in this paper.

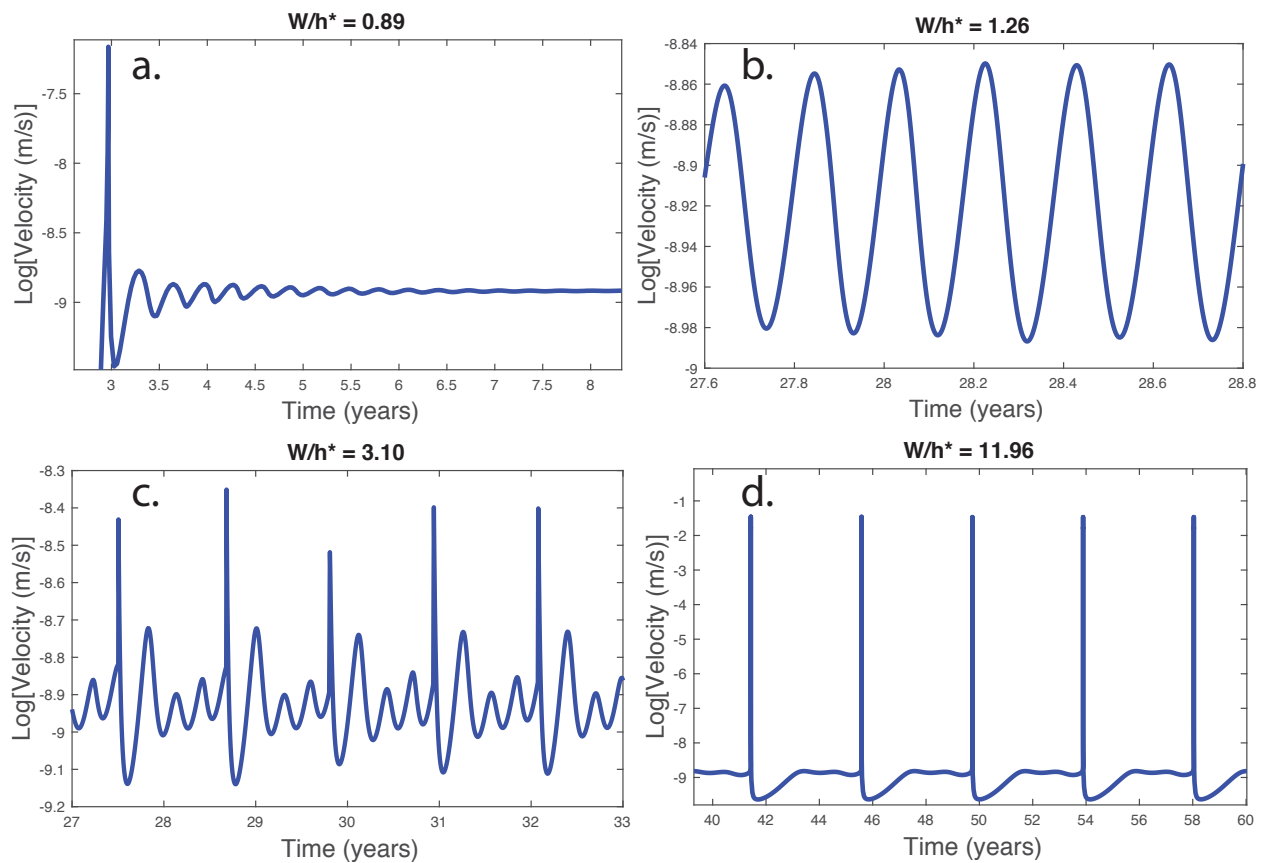


Figure B.1. Results of benchmark tests using the model setup of Liu & Rice (2007). All four characteristic responses at the slip transition are obtained: a. Decaying periodic. b. Simple periodic. c. Complex periodic. d. Seismic.

B.2. Parameter Testing

In Figure B.2 we present parameter testing of κ ranging from zero to five for plate velocities of $V_p = 3, 6, 9$ mm/yr, corresponding to modern extension rates in the Wasatch Fault Zone (Friedrich et al., 2003), the central East African Rift (Stamps et al., 2008), and the Mai'iu Fault Zone in SE Papua New Guinea (Wallace et al., 2014), respectively. We find that the controlling factor on the slip regime for each model is κ , which is a proxy for the minimum a-b value in the weakening patch (right vertical axis in Figure B.2). In our tests the driving plate velocity

determines the magnitude and recurrence interval of earthquakes within clusters, but does not affect the number of events or clusters observed over time periods associated with a set amount of extension. The characteristic slip response patterns of the weakening patch appear mostly independent of plate velocity, suggesting that earthquake clusters can occur for normal faults accommodating a range of extension rates given appropriate frictional parameters in the shear zone.

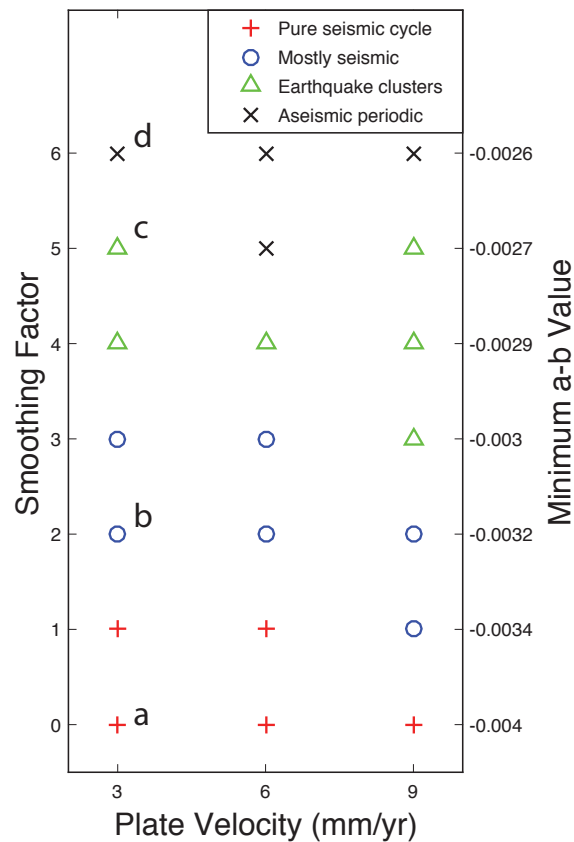


Figure B.2. Characteristic slip response phase diagram for different κ and plate velocities. The representative cases shown in Figure 3.6 are labeled with letters a – d.

APPENDIX C: SUPPLEMENTARY MATERIAL FOR CHAPTER 4

Average emergence rates (Figure C.3c) are calculated by dividing each coral age by the elevation ALC of that coral, then averaging these rates for each individual site. The maximum recurrence interval (section 4.4.3; Figure C.4) is estimated as the difference in age between the youngest coral samples from two subsequent platforms at a single site; the maximum coseismic uplift increment (section 4.3; Figure C.4) of that event is estimated as the difference in height between the lowest sample elevations of the two coral platforms (Figure C.3c). Note that emergence rates should be nearly identical to uplift rates for events in the last 3 kyr, but that emergence rates for older platforms may exceed uplift rates due to ~2 m of sea-level regression from 6-3 kyr; hence, the emergence rates for older platforms represent their maximum uplift rates.

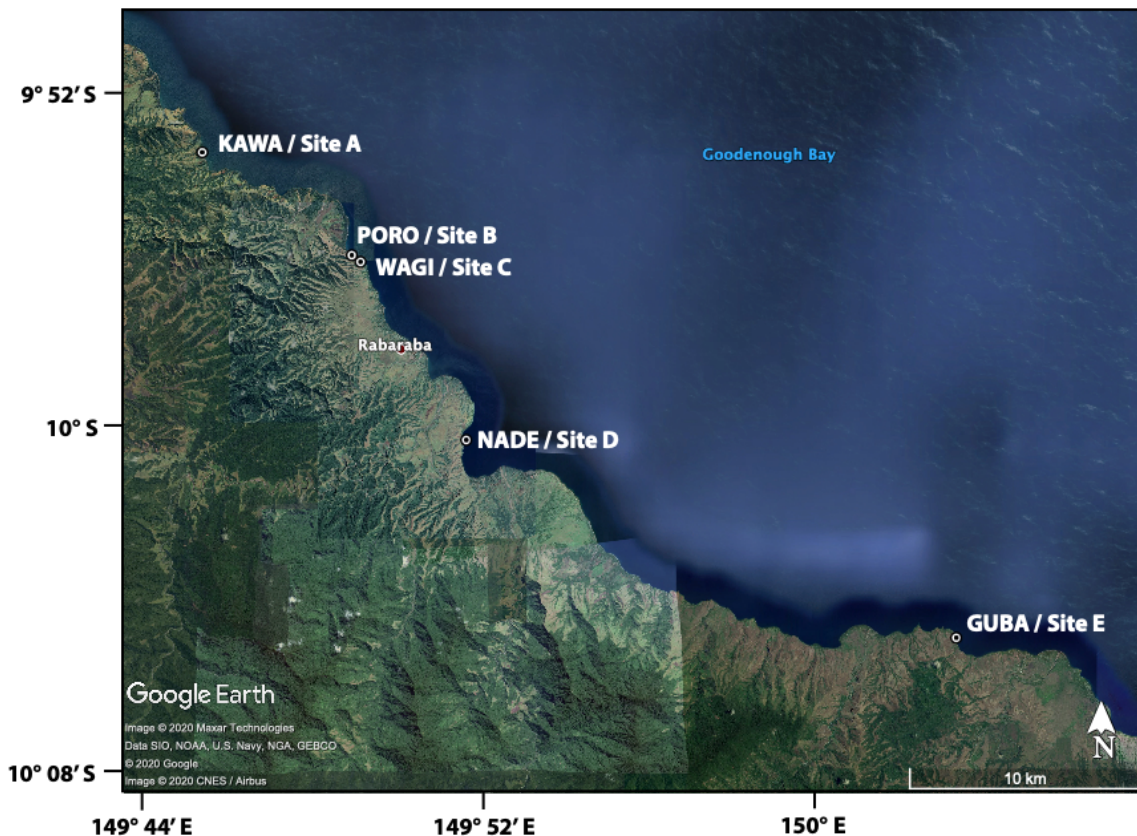


Figure C.1. Detailed map of southern Goodenough Bay coastline showing coral sample locations (white dots). The village of Rabaraba, offshore of which our tide gauge was installed, is shown in red.



Figure C.2. Photos showing field examples of the coral platform sequences (top, middle, lower right) and outcrop examples of intertidal echinoid burrows above a platform level (lower left).

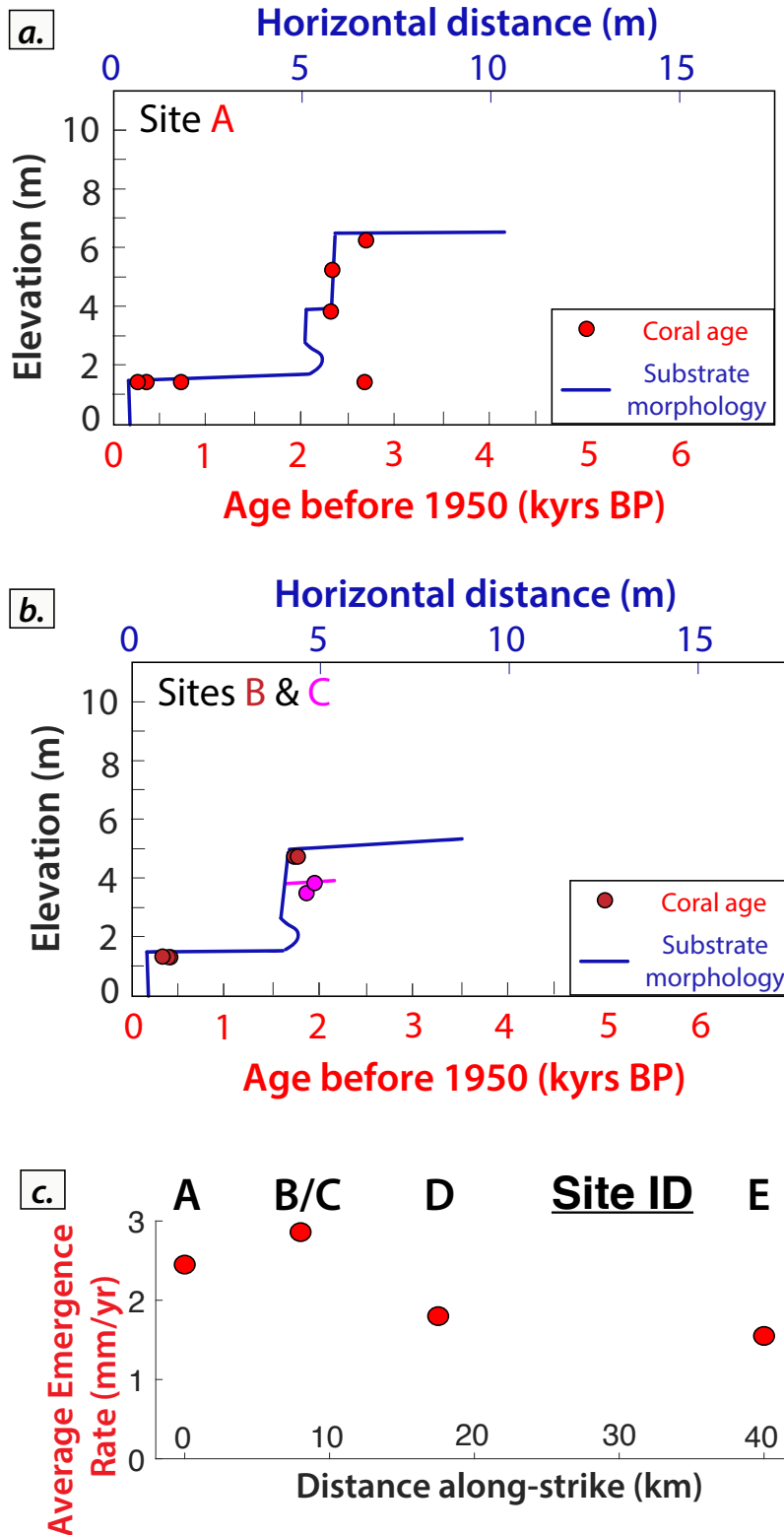


Figure C.3. Coral sample ages and elevations with schematic topographic profiles (blue) of platform sequences at sites: a.) A; b.) B & C. See Figure 4.3c for profiles at site D. c.) Average emergence rates for each site.

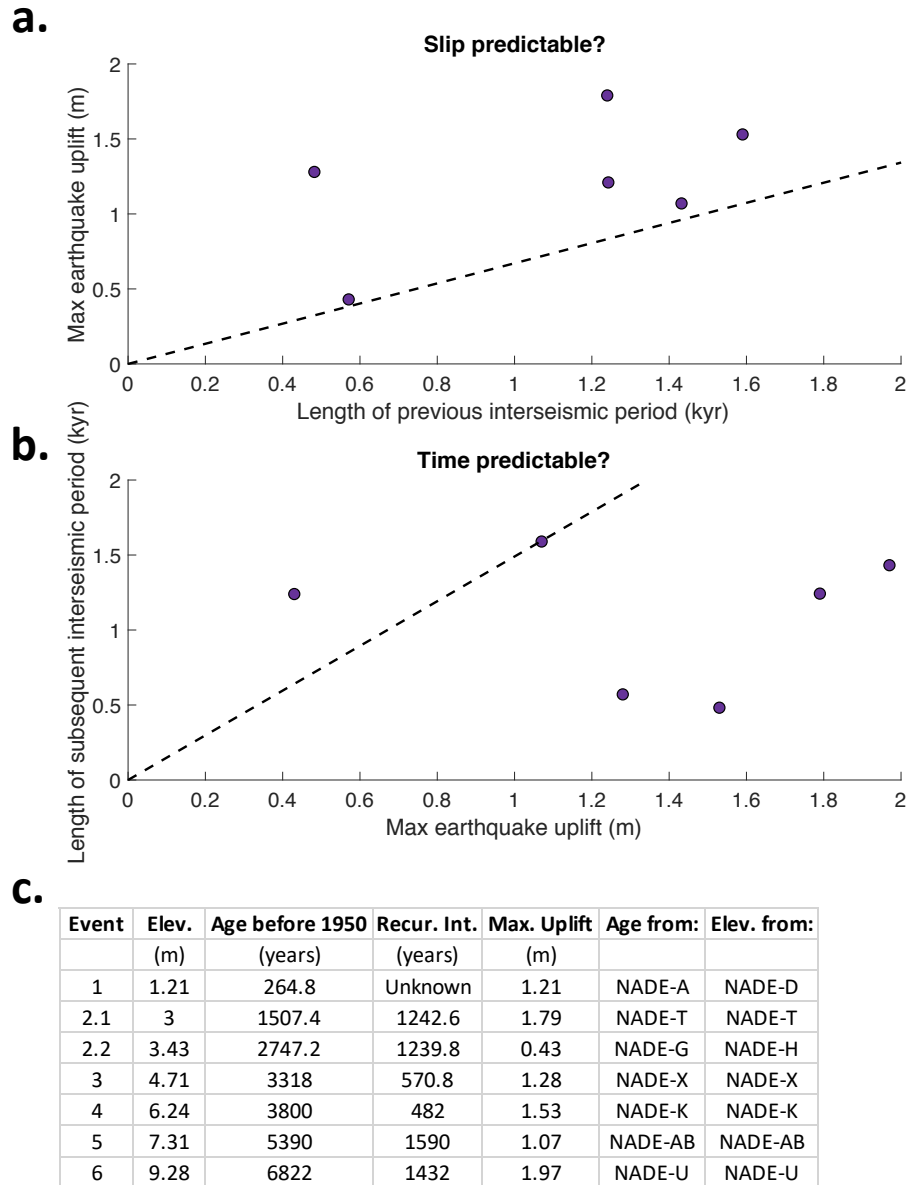


Figure C.4. Uplift-recurrence interval plots testing whether recorded earthquakes at Site D are a.) slip-predictable or b.) time-predictable. For a mean uplift rate of 1.5 mm/yr (dashed line), data should plot along the dashed line if the model holds. Earthquakes on the MGG fault system appear to be neither strictly slip-predictable nor strictly time-predictable, although the limited number of observed earthquake cycles may limit this interpretation. Additionally, removing smaller earthquakes from the maximum earthquake uplifts may shift some events towards the slip- or time-predictable lines, although this is beyond the resolution of the coral record. c.) Details of the calculated values plotted in a & b. ‘Age before 1950’ is the youngest coral age of each age cluster and ‘Age from:’ is the associated sample. ‘Elev.’ is the lowest sample elevation of each cluster and ‘Elev. from’ is the associated sample. ‘Recur. Int.’ is the time before the subsequent uplift event; ‘Max. Uplift’ is the maximum uplift of each event.

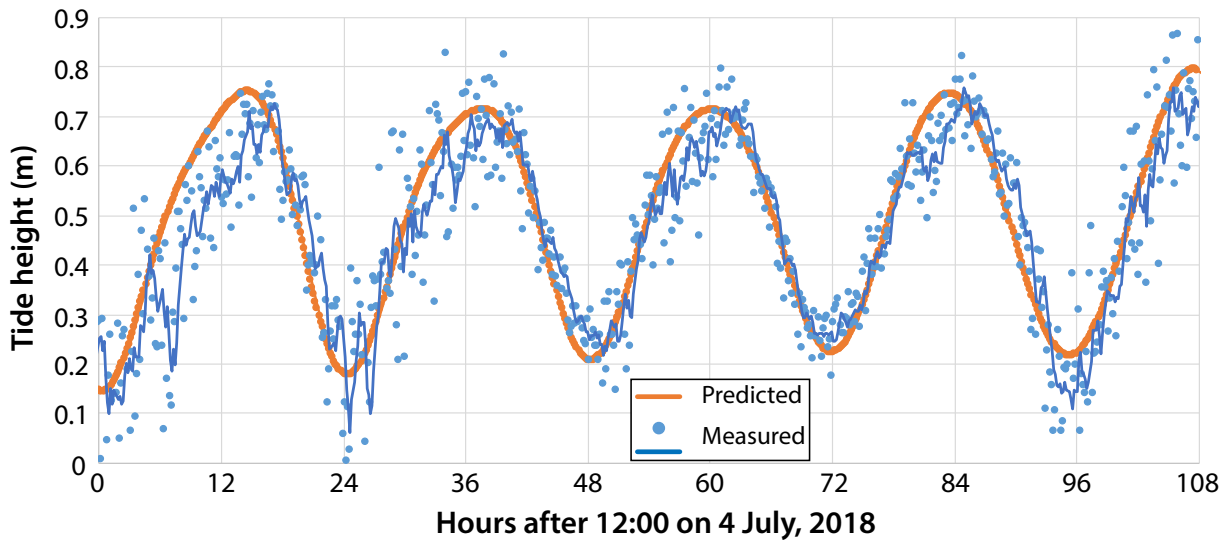


Figure C.5. Extended measured (blue) and predicted (orange) tidal range from 4 – 9 July, 2018. Times are given in local time. During the study period, local tides were primarily diurnal with relatively stable mean high high-water (MHHW), mean sea-level (MSL), and mean low low-water (MLLW) levels.

Sample ID	Latitude (°)	Longitude (°)	Elevation (m)	Datum	Tidal Adj. (m)	Adjusted Elev. (m ALC)
18 GUBA-B	-10.08130	150.05365	1.22	ALC	0	1.22
18 GUBA-C	-10.08130	150.05365	1.22	ALC	0	1.22
18 GUBA-D	-10.08130	150.05365	1.22	ALC	0	1.22
18 KAWA-A	-9.89227	149.75539	1.70	ACWL	0	1.70
18 KAWA-B	-9.89227	149.75539	1.78	ACWL	0	1.78
18 KAWA-C	-9.89227	149.75539	1.67	ACWL	0	1.67
18 KAWA-D	-9.89227	149.75539	1.26	ACWL	0	1.26
18 KAWA-F	-9.89227	149.75539	5.63	ACWL	0	5.63
18 KAWA-G	-9.89227	149.75539	4.63	ACWL	0	4.63
18 KAWA-H	-9.89227	149.75539	3.86	ACWL	0	3.86
18 NADE-A	-10.01017	149.85817	1.36	ALC	0	1.36
18 NADE-AA	-10.01017	149.85817	7.26	ACWL	0.05	7.31
18 NADE-AB	-10.01017	149.85817	7.26	ACWL	0.05	7.31
18 NADE-B	-10.01017	149.85817	1.27	ALC	0	1.27
18 NADE-D	-10.01017	149.85817	1.21	ACWL	0	1.21
18 NADE-E	-10.01017	149.85817	1.21	ACWL	0	1.21
18 NADE-F	-10.01017	149.85817	3.55	ALC	0	3.55
18 NADE-G	-10.01017	149.85817	3.53	ALC	0	3.53
18 NADE-H	-10.01017	149.85817	3.43	ALC	0	3.43
18 NADE-J	-10.01017	149.85817	6.24	ALC	0	6.24
18 NADE-K	-10.01017	149.85817	6.24	ALC	0	6.24
18 NADE-L	-10.01017	149.85817	6.24	ALC	0	6.24
18 NADE-P	-10.01017	149.85817	3.00	ALC	0	3.00
18 NADE-S	-10.01017	149.85817	3.25	ALC	0	3.25
18 NADE-T	-10.01017	149.85817	3.00	ALC	0	3.00
18 NADE-U	-10.01017	149.85817	9.28	ALC	0	9.28
18 NADE-V	-10.01017	149.85817	6.52	ALC	0.05	6.57
18 NADE-W	-10.01017	149.85817	6.52	ALC	0.05	6.57
18 NADE-X	-10.01017	149.85817	4.66	ALC	0.05	4.71
18 NADE-Y	-10.01017	149.85817	4.70	ALC	0.05	4.75
18 NADE-Z	-10.01017	149.85817	7.26	ACWL	0.05	7.31
18 PORO-A2	-9.93243	149.81462	1.32	ACWL	0.05	1.37
18 PORO-B2	-9.93243	149.81462	1.32	ACWL	0.05	1.37
18 PORO-C	-9.93243	149.81462	1.42	ACWL	0.05	1.47
18 PORO-K	-9.93243	149.81462	4.69	ACWL	0	4.69
18 PORO-L	-9.93243	149.81462	4.69	ACWL	0	4.69
18 WAGI-C	-9.93500	149.81805	3.52	ACWL	0	3.52
18 WAGI-D	-9.93500	149.81805	3.80	ACWL	0	3.80

Table C.1. List of all sampled corals with GPS coordinates, elevations, tidal adjustments and tidally corrected elevations. ALC = Above Living Coral. ACWL = Above Current Water Level.

Sample ID	Weight g	²³⁸ U ppb ^a	²³² Th ppt	⁸³⁴ U measured ^b	[²³⁰ Th/ ²³⁸ U] activity ^c	²³⁰ Th/ ²³² Th atomic (x 10 ⁶)	Age (yr ago) uncorrected	Age (yr ago) corrected ^{c,d}	Age (yr BP) rel. to 1950 AD	⁸³⁴ U _{min} corrected ^e	Adjusted Elev. (m ALC)
18 GUBA-B	0.15130	2211.0 ± 2.4	7.4 ± 3.1	143.0 ± 1.4	0.011107 ± 0.000039	54886 ± 22822	1,064.7 ± 3.9	1,064.6 ± 3.9	995.5 ± 3.9	143.4 ± 1.4	1.22
18 GUBA-C	0.1507	2309.3 ± 1.9	42.2 ± 3.1	146.2 ± 1.3	0.011185 ± 0.000049	10098 ± 739	1,069.1 ± 4.9	1,068.7 ± 4.9	999.9 ± 4.9	146.7 ± 1.3	1.22
18 GUBA-D	0.15200	2071.6 ± 2.1	51.4 ± 3.1	142.3 ± 1.3	0.005385 ± 0.000027	3576 ± 213	515.3 ± 2.7	514.7 ± 2.7	445.6 ± 2.7	142.5 ± 1.3	1.22
18 KAWA-A	0.15070	2443.3 ± 2.7	132.3 ± 3.1	145.4 ± 1.4	0.004263 ± 0.000018	1298 ± 31	406.6 ± 1.8	405.3 ± 1.9	336.2 ± 1.9	145.6 ± 1.4	1.70
18 KAWA-B	0.14770	2108.3 ± 2.3	123.3 ± 3.1	145.6 ± 1.3	0.003290 ± 0.000018	928 ± 24	313.6 ± 1.7	312.3 ± 1.9	243.2 ± 1.9	145.8 ± 1.3	1.78
18 KAWA-C	0.15240	2274.0 ± 2.4	588.7 ± 3.1	145.2 ± 1.4	0.028242 ± 0.000089	1799 ± 11	2,721.6 ± 9.3	2,715.6 ± 9.7	2,646.5 ± 9.7	146.3 ± 1.4	1.67
18 KAWA-D	0.1475	2121.7 ± 1.6	299.4 ± 3.2	145.9 ± 1.5	0.008111 ± 0.000049	948 ± 12	774.5 ± 4.8	771.2 ± 5.0	702.4 ± 5.0	146.2 ± 1.5	1.26
18 KAWA-F	0.1568	2481.1 ± 2.1	350.1 ± 3.1	144.6 ± 1.5	0.028353 ± 0.000082	3313 ± 30	2,733.9 ± 8.8	2,730.7 ± 8.9	2,661.8 ± 8.9	145.7 ± 1.5	5.63
18 KAWA-G	0.14980	2295.9 ± 2.5	134.3 ± 3.1	145.1 ± 1.4	0.024676 ± 0.000057	6954 ± 161	2,374.5 ± 6.3	2,373.2 ± 6.3	2,304.1 ± 6.3	146.1 ± 1.4	4.63
18 KAWA-H	0.1560	2257.1 ± 1.9	150.9 ± 3.0	144.7 ± 1.4	0.024507 ± 0.000068	6042 ± 121	2,358.9 ± 7.2	2,357.4 ± 7.3	2,288.5 ± 7.3	145.7 ± 1.4	3.86
18 NADE-A	0.14770	2320.3 ± 2.2	659.1 ± 3.5	145.2 ± 1.3	0.003571 ± 0.000056	2073 ± 3.4	340.5 ± 5.4	334.0 ± 6.3	264.8 ± 6.3	145.4 ± 1.3	1.36
18 NADE-AA	0.1517	2305.7 ± 1.9	45.2 ± 3.1	142.2 ± 1.4	0.06967 ± 0.00015	58601 ± 3971	6,854 ± 17	6,854 ± 17	6,785 ± 17	144.9 ± 1.4	7.31
18 NADE-AB	0.1546	2395.2 ± 2.3	58.7 ± 3.0	142.1 ± 1.5	0.05583 ± 0.00014	37555 ± 1924	5,460 ± 16	5,459 ± 16	5,390 ± 16	144.3 ± 1.5	7.31
18 NADE-B	0.1590	2568.7 ± 2.4	39.8 ± 2.9	145.3 ± 1.7	0.003541 ± 0.000028	3765 ± 278	337.6 ± 2.7	337.3 ± 2.7	268.4 ± 2.7	145.5 ± 1.7	1.27
18 NADE-D	0.15120	3555.2 ± 3.4	160.6 ± 3.1	146.7 ± 1.2	0.005221 ± 0.000021	1906 ± 37	497.6 ± 2.1	496.5 ± 2.2	427.4 ± 2.2	146.9 ± 1.2	1.21
18 NADE-E	0.14990	3143.2 ± 3.2	573.2 ± 3.2	147.5 ± 1.3	0.004724 ± 0.000021	427.1 ± 3.0	449.8 ± 2.0	445.6 ± 2.9	376.5 ± 2.9	147.7 ± 1.3	1.21
18 NADE-F	0.1465	3139.7 ± 3.2	328.7 ± 3.2	143.2 ± 1.5	0.031385 ± 0.000088	4942 ± 51	3,034 ± 10	3,032 ± 10	2,963 ± 10	144.4 ± 1.5	3.55
18 NADE-G	0.15190	2048.6 ± 2.2	36.0 ± 3.1	144.0 ± 1.3	0.029186 ± 0.000065	27417 ± 2331	2,816.7 ± 7.2	2,816.3 ± 7.2	2,747.2 ± 7.2	145.1 ± 1.3	3.53
18 NADE-H	0.1489	3.2692 ± 0.0047	150.5 ± 3.1	139.0 ± 1.9	0.029393 ± 0.000088	10529 ± 221	2,850 ± 10	2,849 ± 10	2,779 ± 10	140.1 ± 1.9	3.43
18 NADE-J	0.1553	3091.8 ± 2.7	449.0 ± 3.1	144.3 ± 1.4	0.040687 ± 0.000090	4619 ± 34	3,945 ± 10	3,942 ± 10	3,873 ± 10	145.9 ± 1.4	6.24
18 NADE-K	0.1506	2110.5 ± 1.7	150.1 ± 3.1	144.6 ± 1.3	0.03994 ± 0.00011	9256 ± 193	3,870 ± 12	3,868 ± 12	3,800 ± 12	146.2 ± 1.3	6.24
18 NADE-L	0.1524	2.9608 ± 0.0038	55.0 ± 3.0	146.7 ± 1.8	0.04034 ± 0.00011	35798 ± 1985	1,645.7 ± 8.9	1,637 ± 10	1,568 ± 10	148.3 ± 1.8	6.24
18 NADE-P	0.1479	3.1586 ± 0.0033	1187.2 ± 3.9	143.9 ± 1.7	0.017140 ± 0.000088	751.8 ± 4.5	1,765.2 ± 5.4	1,764.3 ± 5.4	1,695.2 ± 5.4	145.6 ± 1.7	3.00
18 NADE-S	0.15210	2138.4 ± 2.8	86.8 ± 3.1	144.8 ± 1.7	0.018389 ± 0.000048	7466 ± 263	1,765.2 ± 5.4	1,764.3 ± 5.4	1,695.2 ± 5.4	145.6 ± 1.7	3.25
18 NADE-T	0.1562	2256.6 ± 2.0	10.3 ± 3.0	144.4 ± 1.4	0.016430 ± 0.000059	59316 ± 17102	1,576.4 ± 6.0	1,576.3 ± 6.0	1,507.4 ± 6.0	145.1 ± 1.4	3.00
18 NADE-U	0.15210	2658.8 ± 3.1	228.3 ± 3.1	142.9 ± 1.4	0.07010 ± 0.00012	13461 ± 181	6,893 ± 15	6,891 ± 15	6,822 ± 15	145.7 ± 1.4	9.28
18 NADE-V	0.14770	2383.0 ± 2.3	10.8 ± 3.1	144.8 ± 1.3	0.04684 ± 0.00012	171029 ± 49947	4,551 ± 13	4,551 ± 13	4,482 ± 13	146.7 ± 1.3	6.57
18 NADE-W	0.15020	2440.4 ± 2.6	781.4 ± 2.1	142.7 ± 1.4	0.04061 ± 0.00034	209.1 ± 1.8	3,943 ± 34	3,869 ± 50	3,800 ± 50	144.3 ± 1.4	6.57
18 NADE-X	0.1552	2477.4 ± 2.1	53.2 ± 3.0	145.0 ± 1.4	0.03504 ± 0.00010	26916 ± 1517	3,387 ± 11	3,387 ± 11	3,318 ± 11	146.4 ± 1.4	4.71
18 NADE-Y	0.1512	2084.3 ± 1.7	32.9 ± 3.1	145.6 ± 1.4	0.03666 ± 0.00011	38250 ± 3568	3,545 ± 12	3,544 ± 12	3,476 ± 12	147.1 ± 1.4	4.75
18 NADE-Z	0.1566	2298.3 ± 2.1	1476.1 ± 4.4	143.9 ± 1.5	0.05553 ± 0.00019	1425.4 ± 6.4	5,421 ± 21	5,406 ± 22	5,337 ± 22	146.1 ± 1.5	7.31
18 PORO-A2	0.1490	2222.2 ± 2.1	30.6 ± 3.1	147.1 ± 1.4	0.004919 ± 0.000032	5887 ± 600	468.6 ± 3.1	468.3 ± 3.1	399.4 ± 3.1	147.3 ± 1.4	1.37
18 PORO-B2	0.14830	2293.9 ± 2.5	719.1 ± 3.3	145.7 ± 1.4	0.004741 ± 0.000030	249.4 ± 1.9	452.1 ± 2.9	444.9 ± 4.6	375.8 ± 4.6	145.9 ± 1.4	1.37
18 PORO-C	0.1602	2356.3 ± 2.3	203.6 ± 2.9	143.2 ± 1.4	0.004063 ± 0.000028	775 ± 12	388.2 ± 2.7	386.2 ± 2.9	317.4 ± 2.9	143.4 ± 1.4	1.47
18 PORO-K	0.1507	2419.7 ± 2.1	83.4 ± 3.1	142.7 ± 1.4	0.018526 ± 0.000073	8858 ± 329	1,781.8 ± 7.4	1,781.0 ± 7.4	1,712.1 ± 7.4	143.4 ± 1.4	4.69
18 PORO-L	0.1491	2646.0 ± 2.7	121.1 ± 3.1	145.4 ± 1.7	0.018965 ± 0.000070	6835 ± 178	1,820.1 ± 7.3	1,819.0 ± 7.3	1,750.2 ± 7.3	146.1 ± 1.7	4.69
18 WAGI-C	0.1498	2479.9 ± 2.3	196.8 ± 3.1	143.8 ± 1.5	0.019902 ± 0.000074	4134 ± 67	1,913.5 ± 7.6	1,911.7 ± 7.7	1,842.8 ± 7.7	144.5 ± 1.5	3.52
18 WAGI-D	0.1558	2167.8 ± 1.8	11.4 ± 3.0	145.3 ± 1.4	0.020793 ± 0.000080	65184 ± 17032	1,997.1 ± 8.2	1,997.0 ± 8.2	1,928.2 ± 8.2	146.2 ± 1.4	3.80

Table C.2. Th/U isotopic results from ICPMS analysis of coral samples. Analytical errors are 2σ of the mean. ^a $[^{238}\text{U}] = [^{235}\text{U}] \times 137.77 (\pm 0.11\%)$ (Hiess et al., 2012); $\delta^{234}\text{U} = ([^{234}\text{U}/^{238}\text{U}]_{\text{activity}} - 1) \times 1000$. ^b $\delta^{234}\text{U}_{\text{initial}}$ corrected was calculated based on ^{230}Th age (T), i.e., $\delta^{234}\text{U}_{\text{initial}} = \delta^{234}\text{U}_{\text{measured}} X e^{\lambda^{234}T}$, and T is corrected age. ^c $[^{230}\text{Th}/^{238}\text{U}]_{\text{activity}} = 1 - e^{-\lambda^{230}T} + (\delta^{234}\text{U}_{\text{measured}}/1000)[\lambda_{230}/(\lambda_{230} - \lambda_{234})](1 - e^{-(\lambda_{230} - \lambda_{234})T})$, where T is the age. Decay constants are $9.1705 \times 10^{-6} \text{ yr}^{-1}$ for ^{230}Th , $2.8221 \times 10^{-6} \text{ yr}^{-1}$ for ^{234}U (Cheng et al., 2013), and $1.55125 \times 10^{-10} \text{ yr}^{-1}$ for ^{238}U . ^dAge corrections, relative to chemistry date on October 31st, 2018, were calculated using an estimated atomic $^{230}\text{Th}/^{232}\text{Th}$ ratio of $4 (\pm 2) \times 10^{-6}$.

APPENDIX D: SUPPLEMENTARY MATERIAL FOR CHAPTER 5

D.1. GPS uncertainty calculations

Formal uncertainties for GPS velocities, particularly from campaign observations, tend to underestimate their true uncertainty (e.g., Zhang et al., 1997; Williams et al., 2004). To correct for underestimated uncertainties, a random-walk noise component is commonly incorporated into the final uncertainties. This correction scales with the inverse of the square root of the observation period, given in Zhang et al. (1997) as:

$$\sigma_{RWN} = \frac{A_{RWN}}{\sqrt{T}} \quad (D.1)$$

where T is the time series duration and A_{RWN} is the amplitude of the random walk noise. Following Koulali et al. (2015)'s study of Papua New Guinea GPS velocities, we use random walk noise increments of $0.3 \text{ mm}/\sqrt{\text{yr}}$ for continuous sites and $1.0 \text{ mm}/\sqrt{\text{yr}}$ for campaign sites. Formal and corrected uncertainties are shown in Table D.2 columns 8-11.

D.2. Earthquake offset corrections

Static elastic coseismic displacements due to far-field ($\sim 100 - 1,000 \text{ km}$) large earthquakes range from $< 1 \text{ mm}$ to 10 's of mm (e.g., Banerjee et al., 2005; Tregoning et al., 2013) depending on the distance from the hypocenter, the regional crustal elastic stratification, the spatial distribution of slip, and slip characteristics such as rake and total slip (Pollitz et al., 1996). Tregoning et al. (2013) showed that $M_w > 8.0$ earthquakes caused mm -scale offsets within $\sim 1000 \text{ km}$ of their epicenters. Correcting for such offsets is especially important in studies where the velocity signal of interest is small (mm -scale), as is the case for velocities across the Mai'iu fault. Therefore, we calculate coseismic corrections for all $M_w \geq 6.9$ (based on USGS catalogue magnitudes) earthquakes with hypocentral depths $< 100 \text{ km}$ located within 700 km of our Mai'iu fault network (Figure D.1) from 2008 to June 2018.

We use a spherical layered Earth model (Pollitz, 1996) of harmonic degree 1 to 1500 with PREM elastic stratification (Dziewonski & Anderson, 1981) to calculate surface displacements at our GPS sites due to uniform slip on prescribed fault source models. For the 2016 $M_w 7.9$ Solomon

Islands earthquake (~725 km from our network), we use two fault planes to approximate the composite megathrust source model of Lee et al. (2018), which matches observed teleseismic waveforms better than other proposed source models. This source model ascribes all coseismic slip to patches of the curved subduction megathrust and hence predicts larger horizontal displacements at our GPS sites than source models with rupture of an intraslab fault (Lay et al., 2017; USGS finite fault model). We find that surface displacements predicted by the model of Lee et al. (2018) best match those estimated from time-series analysis of continuous GPS data from site PNGM, the nearest continuous GPS site with similar azimuth to the hypocenter as our sites.

For other nearby 2008-2018 $M_w \geq 6.9$ earthquakes (~350 – 825 km from our network), we approximate the USGS finite fault models (Hayes, 2017; U.S. Geological Survey, 2019) as finite planes with uniform slip. For the few events without published finite fault models, we estimate slip planes based on hypocentral depth, focal mechanism solutions, regional tectonics and nearby event characteristics constrained by typical subduction zone earthquake length-width ratios from Strasser et al. (2010), as most of these events were subduction thrust events near the New Britain and San Cristobal trenches. The earthquake closest to our network was the 2010 M 6.9 New Britain event (~350 km away), while the earthquake with the largest static coseismic offsets at our sites was the 2016 M 7.9 New Britain event (~700 km away). We also reevaluate and correct for coseismic offsets due to the 2 April 2007 M_w 8.1 Solomon Islands earthquake using the coseismic slip model of Wallace et al. (2015), which was developed by jointly inverting horizontal GPS displacements and vertical displacements from coseismically emerged coral reefs in the Solomon Islands (Taylor et al., 2008) (Figure D.2). All slip models are tuned to approximately match the seismologically inferred M_w using a shear modulus of 25 GPa, and the details of each are listed in Table D.4. GPS positions are corrected by adding static offset corrections equal and opposite to the modeled coseismic offsets during the GLOBK stage of processing.

D.3. Block modeling (TDEFNODE)

Using the preferred block and fault configuration (Figures 5.2a, D.3; Table D.5), we perform inversions with different constraints on fault locking to explore how model constraints influence preferred locking distributions and data misfits. For example, the best-fit model (Figure 5.2) results from inversions where the coupling ratio (Φ) is required to decrease with increasing depth for all faults. We also test models where Φ is free to increase or decrease with depth (Figure D.4a), as well as models where the Mai'iu fault is prescribed to be fully creeping ($\Phi = 0$) or fully locked ($\Phi = 1$) at all depths (Figures D.4b, D.4c, respectively), or fully locked at the surface (Figure D.4d) or from the surface to 2, 4, 9, or 14 km depth (Figures D.4e, D.4f, D.4g, D.4h, respectively).

D.4. Dislocation modeling of vertical velocities

Vertical velocities can also be valuable for investigating fault locking processes (e.g., Segall, 2010). However, because horizontal displacements are larger than vertical displacements for LANFs and vertical GPS uncertainties are typically 3–5 times larger than horizontal ones (e.g., Bennett et al., 2007; Serpelloni et al., 2013), we first consider only the strike-perpendicular horizontal velocities. Vertical velocities also suffer from an indeterminate reference frame problem and can be influenced by regional-scale uplift or subsidence processes unrelated to fault slip. Horizontal velocities can be tied to the rigid block motion of adjacent crustal blocks to isolate the components related to fault slip or locking. To address these issues, some authors select the site least likely to be affected by vertical tectonic motions and use its vertical velocity as the vertical reference frame (e.g., Beavan et al., 2010). Even with this method and high-precision continuous GPS observations, it is necessary to arbitrarily adjust all velocities by a baseline value in order to compare them to analytical physical models of crustal deformation (Beavan et al., 2010).

Vertical velocities across the fault show a sharp change on the order of 5 mm/yr from subtle footwall subsidence to hanging wall uplift near the fault trace, decaying to hanging wall subsidence with distance from the trace. At face value, the wavelength of vertical velocity change across the

hanging wall suggests deeper locking than the horizontal velocities alone. Including both horizontal and vertical velocities in models with locking to the surface, the best-fit ($\chi^2 = 2.41$) model fault dips 32° and slips at 13.5 mm/yr below a locking depth of 13 km. However, addressing the vertical reference frame ambiguity by allowing for a uniform modeled vertical velocity shifts across all sites of -5 to +5 mm/yr leads to a best-fit ($\chi^2 = 1.53$) model fault dipping 28° and slipping 10 mm/yr below a locking depth of 3 km, similar to the best-fitting model from horizontal velocities alone, with -3 mm/yr uniform vertical velocity shift. As with buried dislocation models based solely on horizontal velocities (section 5.2.4.2), the data fit improves by treating site YAMS as part of the footwall: total χ^2 based on horizontal and vertical velocities decreases from 2.44 with YAMS in the hanging wall to 2.06 with YAMS in the footwall.

D.5. Quantitative X-ray diffraction methods

Eight fault rock samples (Table D.6) were analyzed by X-Ray Diffraction by Mark Raven at CSIRO Land and Water Flagship, Mineral Resources Flagship, at the Centre for Australian Forensic Soil Science (CAFSS), in Urrbrae, South Australia. From these samples, 1.5 g sub-samples were ground for 10 minutes in a McCrone micronizing mill under ethanol. The resulting slurries were oven dried at 60°C then thoroughly mixed in an agate mortar and pestle before being lightly pressed into aluminum sample holders for X-ray diffraction analysis. XRD patterns from the micronized materials showed variable hydration of the interlayer which causes problems with quantification. Because the samples did not appear to contain any water-soluble phases, they were calcium saturated, and the data were re-analyzed. XRD patterns were recorded with a PANalytical X'Pert Pro Multi-purpose Diffractometer using Fe filtered Co Ka radiation, auto divergence slit, 2° anti-scatter slit and fast X'Celerator Si strip detector. The diffraction patterns were recorded in steps of $0.016^\circ 2\theta$ with a 0.4 second counting time per step, and logged to data files for analysis. XPLOT and HighScore Plus (PANalytical) search and match software were used to perform qualitative analysis. The abundance of identified mineral phases was then determined using

SIROQUANT software from Sietronics Pty Ltd. Results are normalized to 100% and do not include unidentified or amorphous phases. Table D.6 lists each sample’s mineral phases and their relative proportion.

D.6. Hydrothermal Friction Experiments

Complete hydrothermal friction results can be found in Supplementary Dataset S1 of Biemiller et al. (2020b). The text file contains data in tab delimited columns arranged by experiment (see Table 5.1 for experiment details). Lower case “d” denotes displacement (mm) and μ denotes the corrected coefficient of friction. Acquired raw torque and normal force data were processed to obtain shear stress and normal stress measurements respectively. Raw, externally measured, torque data were corrected for fluid pressure and shear displacement-dependent friction of the Teflon-coated O-ring seals using calibration values obtained in runs with a dummy sample of carbon-coated PolyEtherEtherKeton with a known sliding friction; seal friction is typically around 0.03 kN (equivalent to ~ 1.5 MPa shear stress). The contribution of the Molykote-coated confining rings to the measured friction is negligible (see also den Hartog et al., 2012a). The applied normal stress was corrected for the stress supported by the internal seals, the level of which is clearly visible during initial loading and was generally around 0.5 kN (equivalent to ~ 2 MPa normal stress acting on the sample). All experimental conditions are listed in Table 5.1.

The friction rate parameter (a–b) was quantified using an iterative least-squares method incorporating the Dieterich (1979) rate-and-state friction equation:

$$\mu = \mu_0 + a \ln\left(\frac{v}{v_0}\right) + b_i \ln\left(\frac{v_0 \theta_i}{D_{c_i}}\right), \text{ with } \frac{d\theta_i}{dt} = 1 - \frac{v \theta_i}{D_{c_i}} \quad (\text{D.2})$$

Here, μ is the instantaneous friction coefficient, μ_0 is a reference friction coefficient at velocity V_0 , θ is a state variable, a and b are constants, and D_c is the critical slip distance. The subscripts for b , θ , and D_c represent separate evolution processes (Marone, 1998). The inversion was performed using the XLook code developed at the Pennsylvania State University. The inversion scheme is fully documented in Reinen & Weeks (1993) and Ikari et al. (2009).

At steady-state, the friction rate parameter ($a-b$) is defined in terms of the logarithmic velocity-dependence of friction following:

$$(a - b) = \frac{\partial \mu_{ss}}{\partial \ln V} \quad (D.3)$$

Positive ($a-b$) values indicate that a material is rate-strengthening and intrinsically stable. Negative ($a-b$) values indicate that a material is rate-weakening and can nucleate a frictional instability if fault stiffness (k) is less than a critical stiffness (k_c):

$$k_c = \frac{-(a-b)\sigma'_n}{D_c} \quad (D.4)$$

In general, most fault gouges strengthen with increasing simulated depth (i.e. increasing temperature, effective normal stress, and fluid pressure) during an individual experiment. In some experiments, strengthening is the result of a long-term displacement-dependent increase in friction (e.g. Figure 5.5c), whereas in other experiments strengthening is abrupt and is the result of increased simulated depth (e.g. Figure 5.5b). The repeat experiment pairs u368+u370, u369+u371 and u546+u547 (note that a different velocity profile was applied in experiments u368 and u369) show good reproducibility in terms of the general evolution of friction with displacement, the level of friction and the velocity dependence of friction. Variability in friction is less than 0.05 in all cases and less than 0.02 in most cases. Unstable sliding (stick-slips) is encountered in only a few experiments, typically at a temperature range between 250 °C and 350 °C at low sliding velocity (< 30 $\mu\text{m/s}$) for samples with a friction coefficient of at least 0.6 (Figures 5.5b,d). Some history dependence (i.e. displacement dependence) is seen in the experiments performed at the highest temperatures (i.e., 300-350-400-450 °C), in which the first series of velocity steps reproduces the temperature conditions of the last series of velocity steps performed in the low temperature experiment (Table 5.1). The friction coefficient recorded at low displacements at 300°C is consistently lower than that recorded at high displacements at 300 °C, except for experiment u775. It should be noted that both effective normal stress and fluid pressure are considerably lower in the low-displacement 300 °C steps (120 vs. 180 MPa and 80 vs. 180 MPa, respectively), which might explain the difference.

D.7. Supplementary Figures

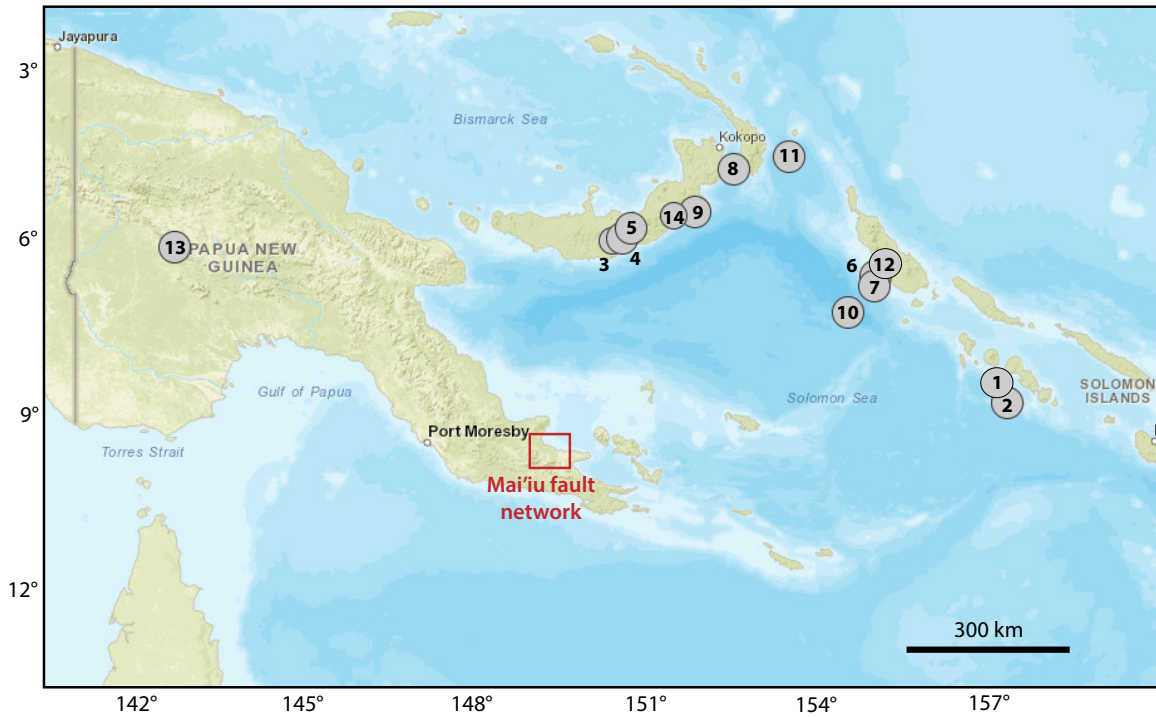


Figure D.1. Regional earthquakes of $M \geq 6.9$ corrected for using STATIC1D (Section D.2; U.S. Geological Survey, 2019). See Table D.4 and Section D.2 for a list and description of these events. Labeled numbers refer to event numbers in Table D.4.

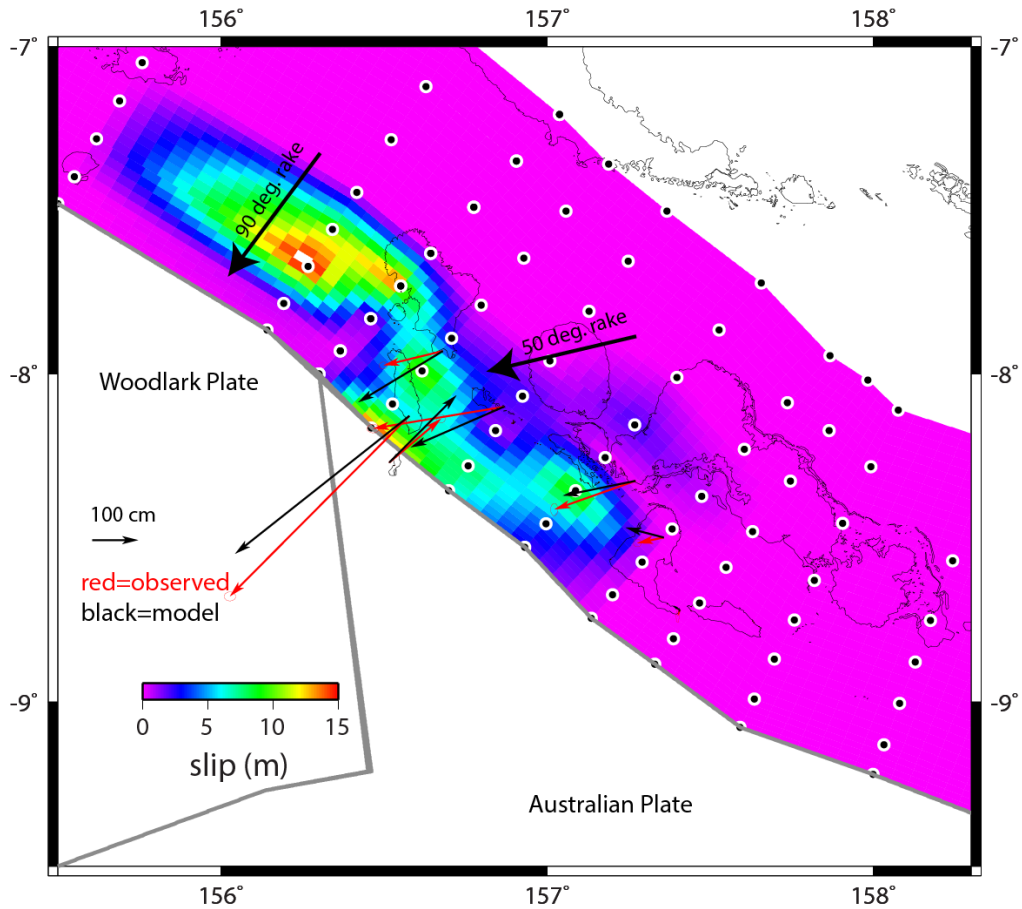


Figure D.2. Slip distribution for the 2007 M 8.1 Solomon Islands earthquakes from joint inversion of campaign GPS displacements (red vectors) and coastal uplift/subsidence recorded by coral reef platforms (Taylor et al., 2008; Wallace et al., 2015). Black vectors show the modeled fit to the horizontal component of GPS velocities. Larger black vectors show the rake of slip.

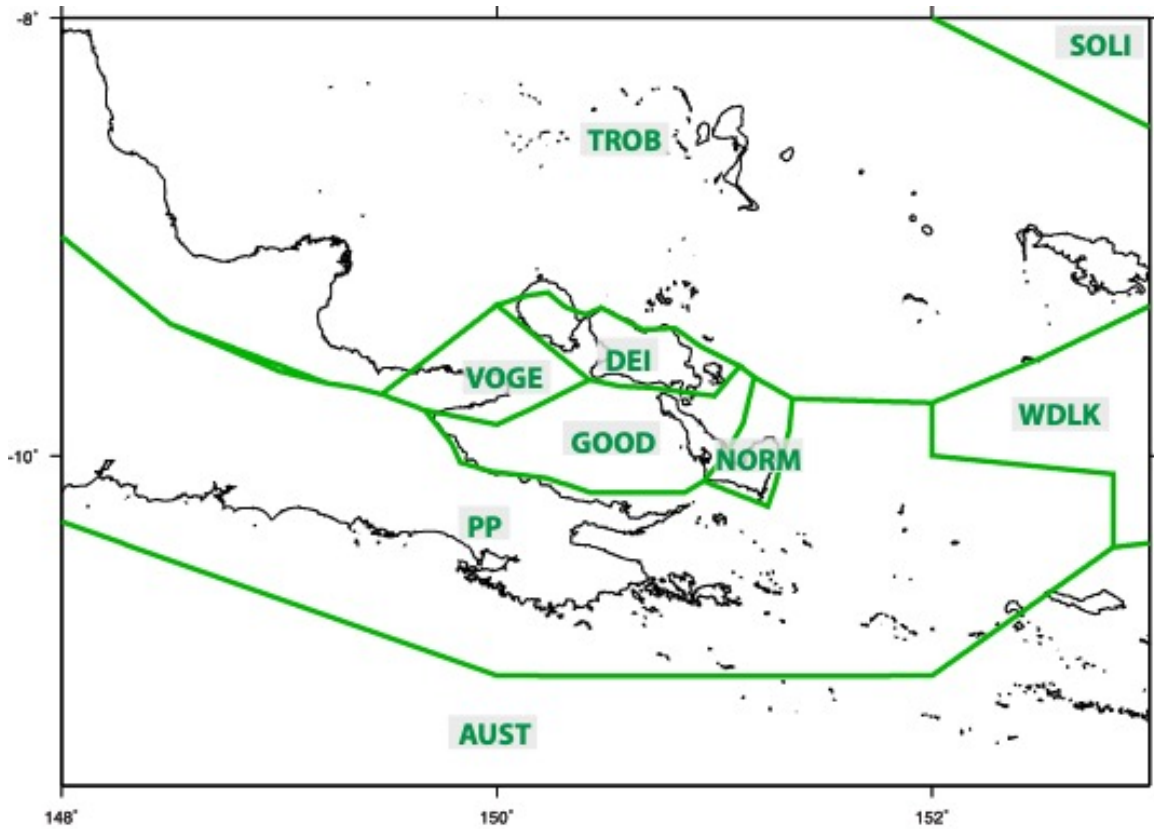


Figure D.3. Individual blocks tested for independence. F tests cannot statistically distinguish between models where VOG and GOOD are considered individual blocks and ones where they are one unified block (Table D.5). Therefore, we treat them as one block in subsequent TDEFNODE block models (configuration 2 in Table D.5). TROB = Trobriand Islands block; SOLI = Solomon Islands block; WDLK = Woodlark Plate block; DEI = D'Entrecasteaux Islands block (Goodenough & Fergusson Islands); NORM = Normanby Island block; VOG = Cape Vogel block; GOOD = Goodenough Basin block; PP = Papuan Peninsula block; AUST = Australian Plate block.

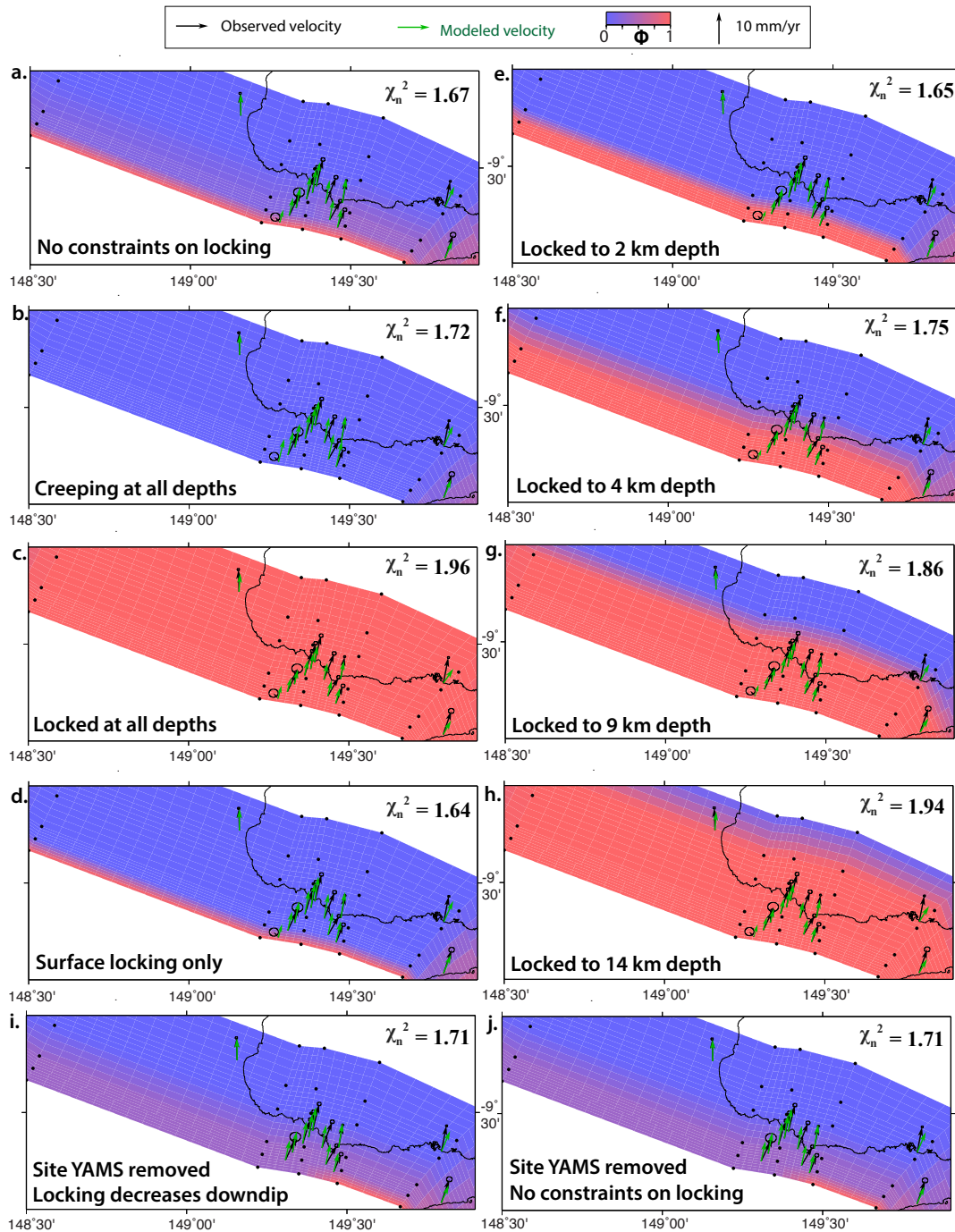


Figure D.4. Mai'iu fault locking results for different inversion constraints and locking depths in the elastic block models. We test models where the kinematic coupling ratio, Φ , is free to increase or decrease with depth (a), as well as models where the Mai'iu fault is prescribed to be fully creeping ($\Phi = 0$) or fully locked ($\Phi = 1$) at all depths (b, c, respectively), or fully locked at the surface (d) or from the surface to 2, 4, 9, or 14 km depth (e, f, g, h, respectively). We also test models that exclude the velocity at site YAMS: i.) coupling is required to decrease with depth; and j.) no prescribed spatial constraints on coupling.

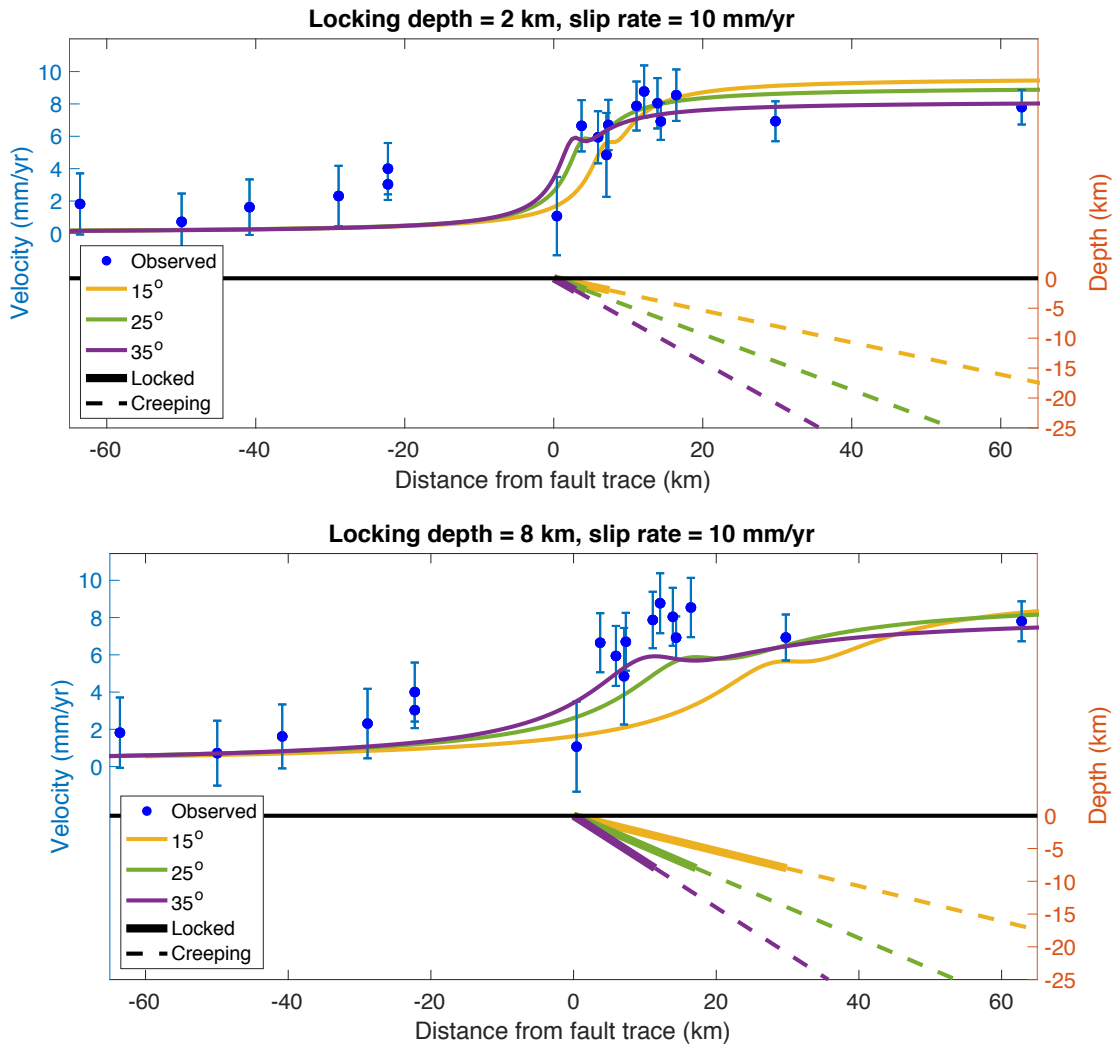


Figure D.5. Illustrated example of tradeoffs between locking depth, fault dip and predicted velocities for planar dislocation models with locking at the surface. Observed velocities are parallel to profile X-X' of Figure 5.1a and are relative to a fixed Australian plate. Fault dip has less effect on velocities for shallowly locked faults than for more deeply locked faults.

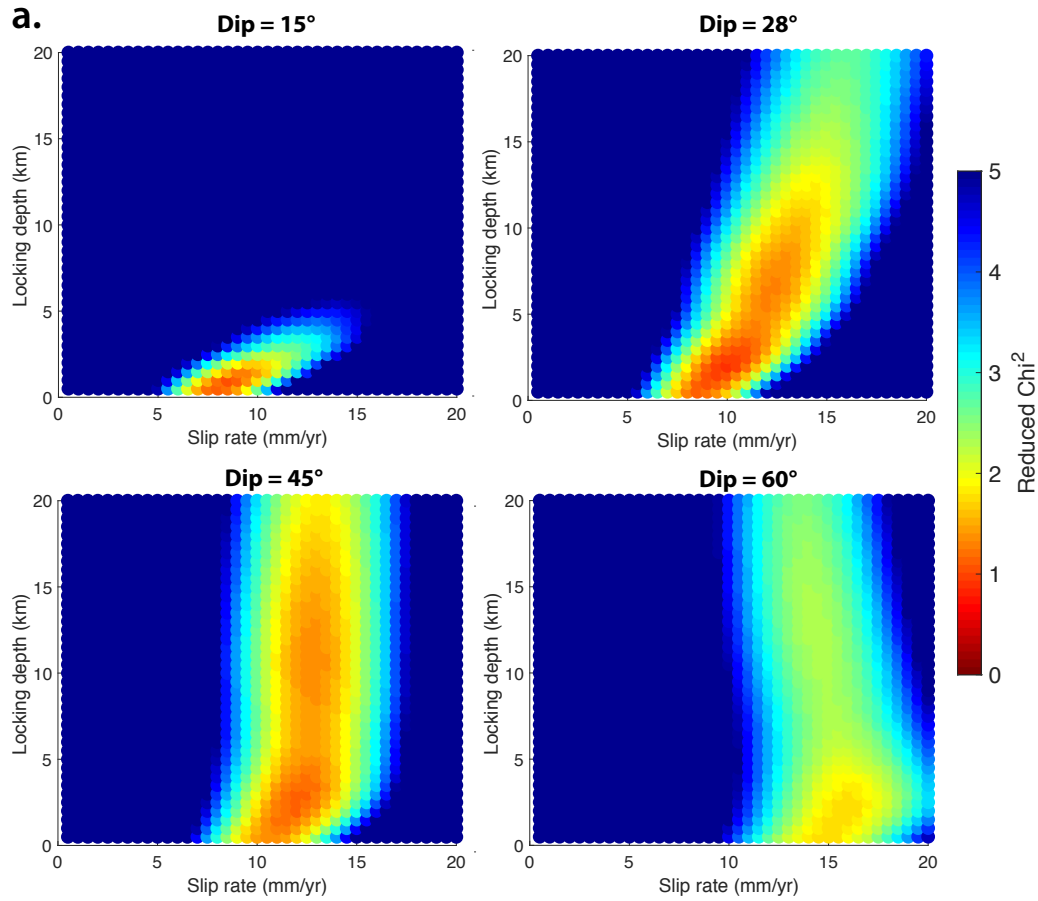


Figure D.6. Parameter sensitivity plots for locked-to-surface dislocation models showing data misfit (reduced χ^2) tradeoffs between: a.) slip rate and locking depth for dips of 15° , 28° , 45° , and 60° ; b.) dip angle and slip rate for locking depths of 0.5, 2, 5, and 15 km; c.) dip angle and locking depth for slip rates of 8, 10, 12, and 14 mm/yr.

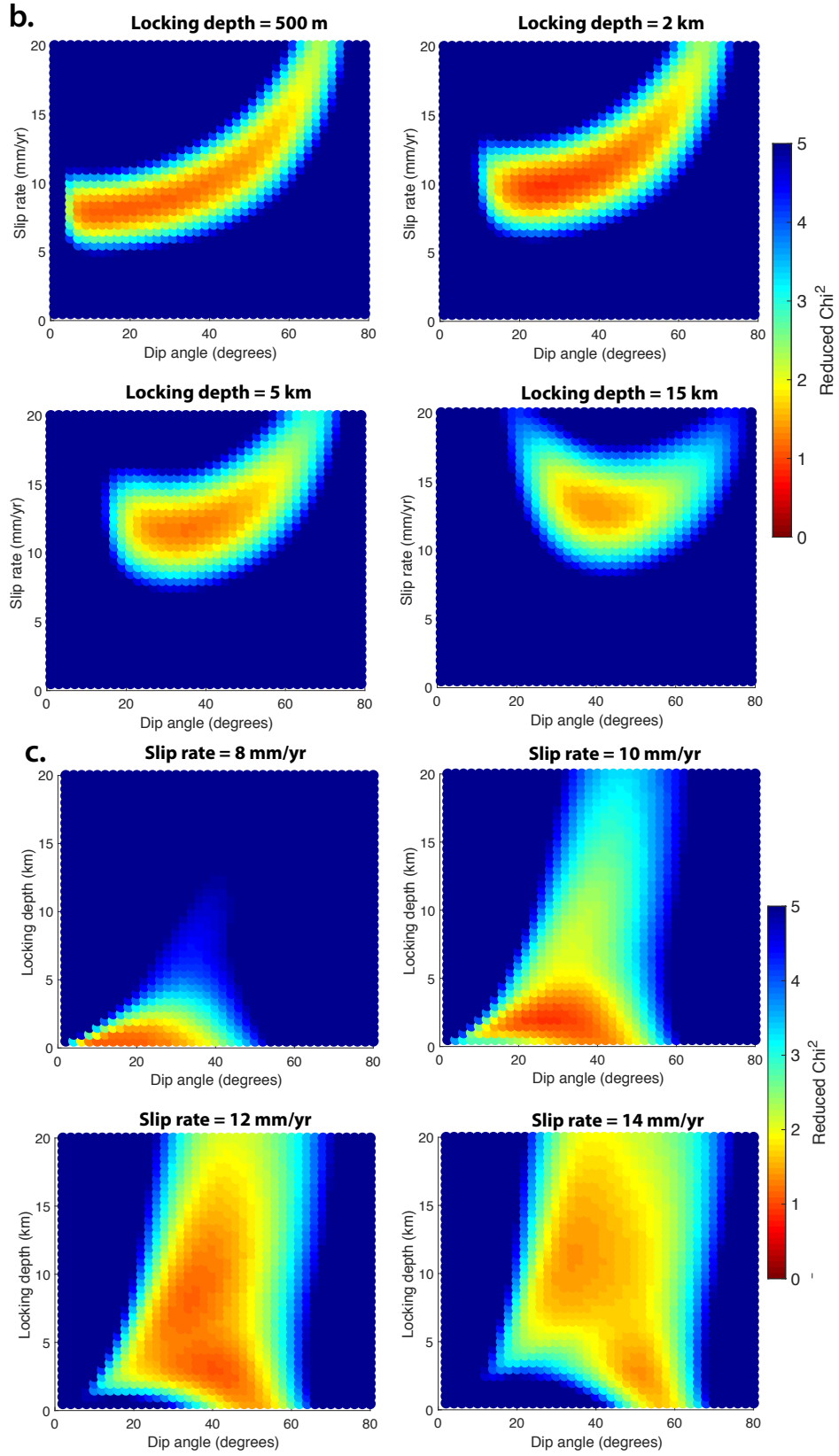


Figure D.6 b & c.

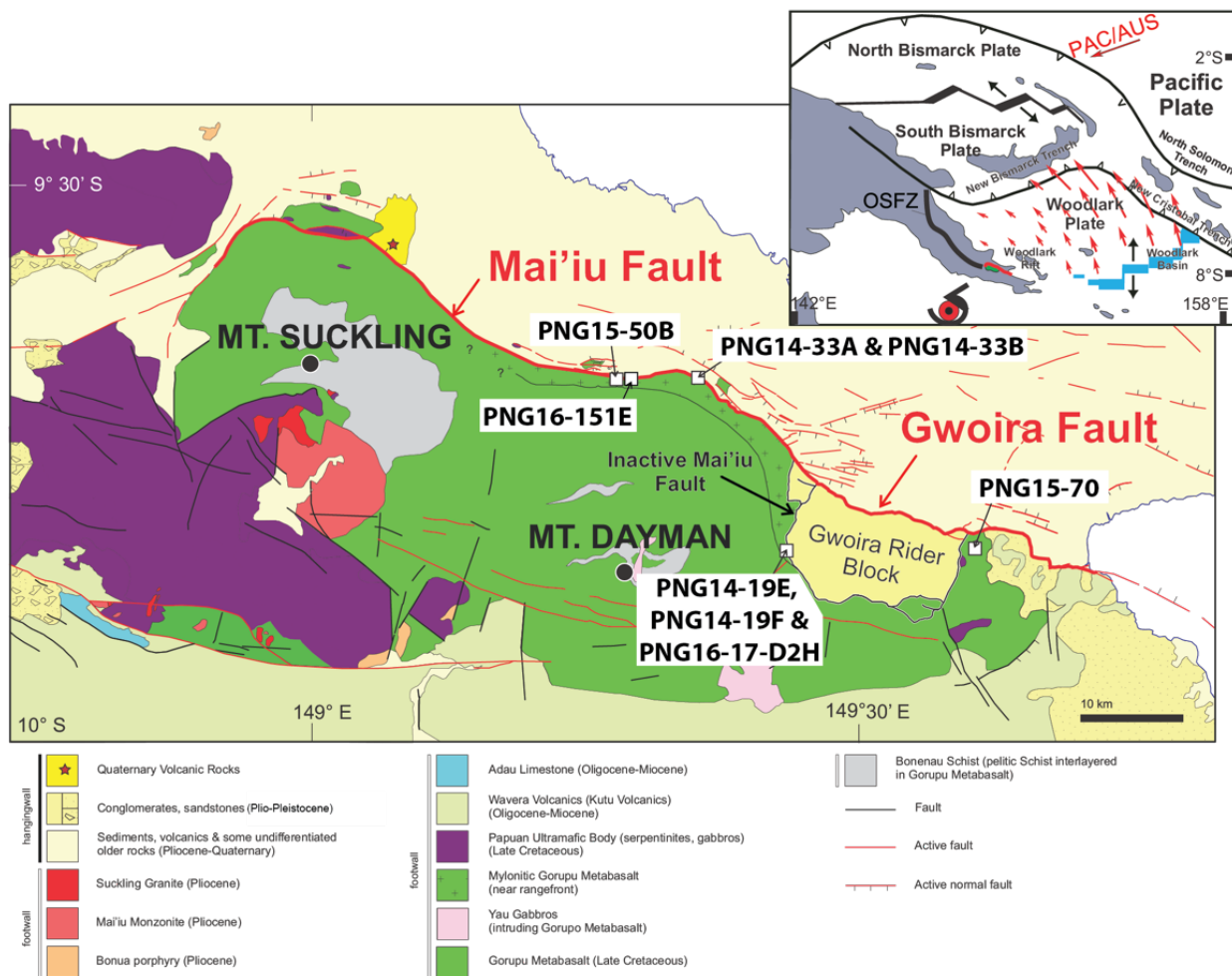


Figure D.7. Tectonic setting (inset) and geological map showing the active and inactive strands of the Mai'iu Fault and the location of the fault rocks analyzed. Each fault rock is identified by its field sample number. Map after Little et al. (2019) and Mizera et al (2020).

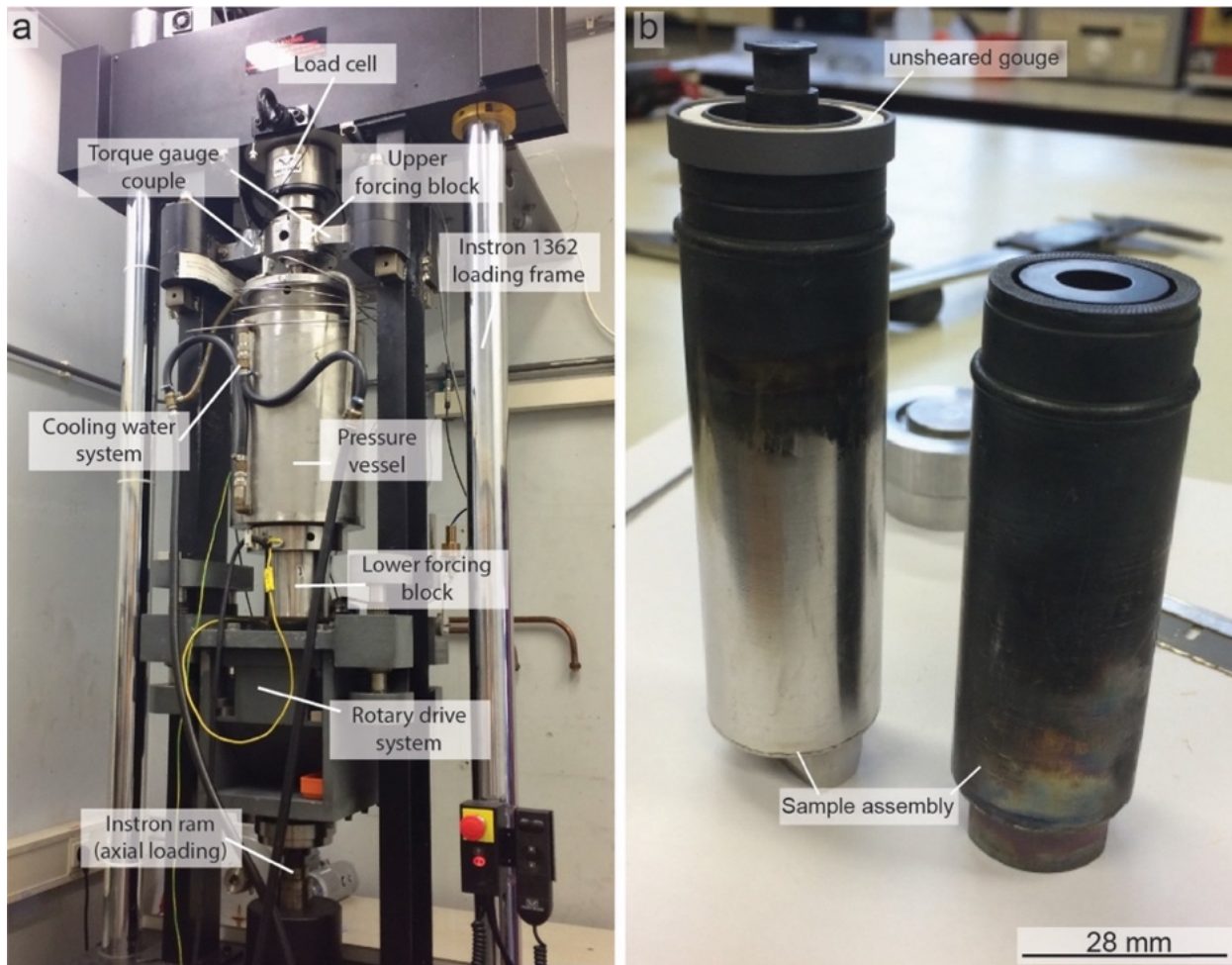


Figure D.8. Images of the High Temperature and Pressure (HPT) Lab, Utrecht University, hydrothermal ring shear apparatus used to measure the frictional properties of Mai'iu fault rock samples. (a) is a labelled photograph of the apparatus, and (b) depicts the two pistons which, fitted together with an annulus of gouge between them, are inserted into the pressure vessel and sheared under controlled conditions of temperature, effective normal stress, and velocity.

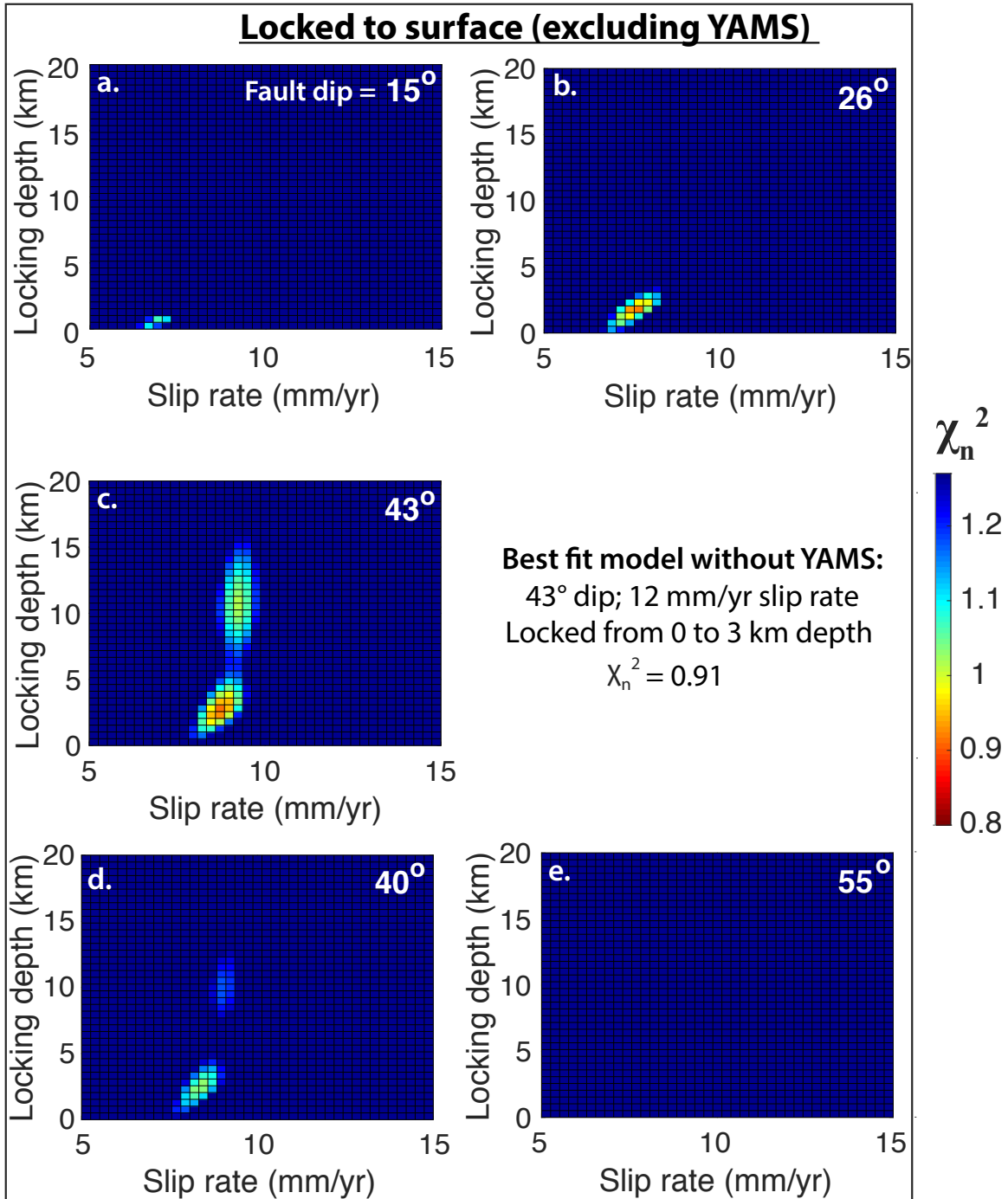


Figure D.9. Parameter sensitivity plots for models with locking to the surface excluding the velocity at site YAMS. a-e.) Tradeoffs between locking depth and slip rate for locked from surface to depth models with different dip angles of 15° , 26° , 43° (best-fit), 40° and 55° , respectively.

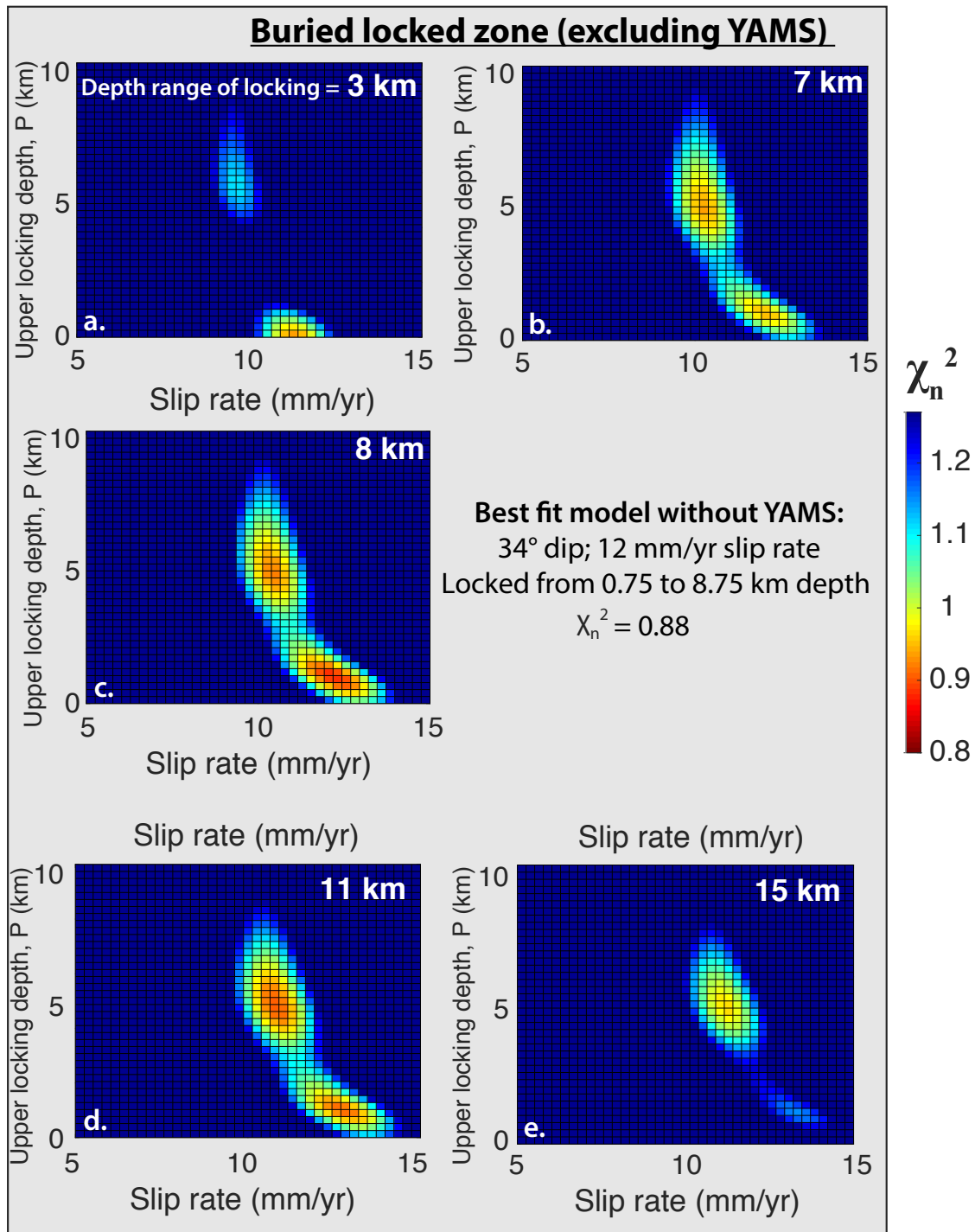


Figure D.10. Parameter sensitivity plots for buried dislocation models excluding the velocity at site YAMS. Buried-dislocation models show tradeoffs between the updip depth of locking (depth P, Figure 5.3f) and slip rate with different depth ranges of locking (depth D, Figure 5.3f). Fault dip shown here is fixed to the best-fitting value of 34°; however, P, D, slip rate, and dip were all varied in grid searches. a-e.) Sensitivity plots for total depth ranges of locking of 3 km, 7 km, 8 km (best-fit), 11 km, and 15 km, respectively.

D.8. Supplementary Tables

Table D.1. GPS sites and observation years used in this study (below).

Site	2002	2004	2005	2006	2008	2009	2010	2012	2015	2016	2018
AGAN									x		x
ALT2	x	x				x	x	x			
BASM						x	x	x			
BAYA						x	x	x	x		
BINI									x	x	x
BORO									x	x	x
BWAR						x	x	x			
DAIO						x	x	x			
DARB						x	x	x			
DD01									x	x	
DIGA						x	x	x			
ESAA		x			x		x	x			
GIWA						x	x	x			
GONO									x	x	x
GOUR									x	x	x
GUA1		x					x				
GUMA						x	x	x			
HEHE						x	x	x			
JONE						x	x	x			
KABU									x	x	
KALO						x	x	x			x
KAWA						x	x	x			
KEIA						x	x	x			
KIBU									x	x	x
KILI						x	x	x			x
KURA						x	x	x			
KWAN						x	x	x			
KWAT						x	x	x			
LELE						x	x	x			
LOS2		x					x	x			
MAAP						x	x	x			
MENA						x	x	x			
MORA						x	x	x			x
MORB									x	x	x

NUBE						x	x	x			
PEMM						x	x	x		x	
RAB2							x				x
RABA						x	x	x			x
RAKO									x	x	x
SALM		x				x	x	x			
SIBA						x	x	x			
SIRI						x	x	x			
SMRI						x	x	x			
STRA						x	x	x			
TUF2						x	x	x	x		x
TUFI		x	x	x							
UAMA						x	x	x			
VAKU						x	x	x			
VIVI					x		x				
WAIB						x	x	x			x
WANI						x	x	x		x	
WAPO						x	x	x			
WATL		x			x		x	x			
YAMS									x	x	
YANA						x	x	x			

Table D.1. (continued)

Table D.2. (below) Coordinates, velocities, and uncertainties for each GPS site. V_N^{IT14} and V_E^{IT14} are the North and East components of velocity in the ITRF14 reference frame. V_N^{AUS} and V_E^{AUS} are the North and East components of velocity relative to the Australian Plate. σ_N^f and σ_E^f are the formal uncertainties for the North and East velocity components. σ_N^{rwn} and σ_E^{rwn} are the uncertainties of the North and East velocity components after correcting for random-walk noise (Section D.1).

Site	Longitude °	Latitude °	V_N^{IT14} mm/yr	V_E^{IT14} mm/yr	V_N^{AUS} mm/yr	V_E^{AUS} mm/yr	σ_N^f mm/yr	σ_E^f mm/yr	σ_N^{rwn} mm/yr	σ_E^{rwn} mm/yr
AGAN	149.387	-9.93	34.21	59.4	3.90	1.01	0.63	0.74	1.20	1.31
ALT2	150.338	-10.31	35.05	57.54	2.41	2.20	0.14	0.16	0.45	0.47
BASM	150.833	-9.466	34.85	68.54	13.60	1.66	0.76	0.87	1.33	1.44
BAYA	149.474	-9.608	34.6	62.4	6.93	1.26	0.23	0.27	0.63	0.67
BINI	149.308	-9.648	36.19	61.57	6.04	2.84	0.61	0.73	1.20	1.32
BORO	149.459	-9.684	35.57	60.97	5.50	2.27	0.64	0.78	1.23	1.37
BWAR	151.185	-9.94	36.04	58.13	3.34	3.15	0.88	1.00	1.46	1.58
DAIO	150.427	-10.408	34.12	57.06	1.96	1.34	1.08	1.25	1.65	1.82
DARB	151.015	-9.927	33.86	57.98	3.12	0.93	0.97	1.06	1.55	1.64
DD01	149.289	-9.835	35.91	54.54	-1.00	2.65	1.60	1.88	2.57	2.85
DIGA	151.204	-10.2	34.67	58.42	3.63	1.91	1.53	1.55	2.11	2.13
ESAA	150.812	-9.739	37.41	59.87	4.93	4.35	0.34	0.42	0.70	0.78
GIWA	149.794	-9.78	35.74	62.69	7.35	2.54	1.12	1.33	1.70	1.91
GONO	149.434	-9.661	36.73	61.35	5.87	3.41	0.56	0.68	1.15	1.27
GOUR	149.362	-9.597	35.69	63.05	7.54	2.33	0.51	0.61	1.10	1.20
GUA1	152.944	-9.225	36.57	83.52	29.47	3.58	0.37	0.45	0.77	0.85
GUMA	150.865	-9.21	32.55	70.84	15.92	-0.76	0.80	0.93	1.38	1.51
HEHE	150.874	-10.226	34.28	58.02	3.10	1.48	1.07	1.27	1.65	1.85
JONE	150.102	-10.095	34.97	58.02	2.79	1.97	0.77	0.87	1.34	1.44
KABU	149.33	-9.624	34.24	60.38	4.86	0.89	2.05	2.64	3.07	3.66
KALO	150.43	-9.414	34.54	63.94	8.84	1.26	0.22	0.24	0.55	0.57
KAWA	150.299	-8.522	26.69	69.17	14.02	-7.05	0.96	1.07	1.53	1.64
KEIA	150.554	-10.213	34.66	57.22	2.17	1.80	0.83	0.93	1.40	1.50
KIBU	149.381	-9.577	34.9	63.53	8.03	1.53	0.57	0.68	1.16	1.27
KILI	150.292	-9.496	34.91	63.94	8.79	1.65	0.23	0.26	0.56	0.59
KURA	151.036	-10.11	34.59	56.13	1.28	1.76	1.10	1.09	1.68	1.67
KWAN	151.274	-9.923	33.01	58.92	4.16	0.12	0.88	1.05	1.46	1.63
KWAT	150.712	-9.311	32.68	70.48	15.50	-0.61	0.72	0.80	1.30	1.38
LELE	150.728	-10.302	33.53	55.36	0.38	0.75	0.93	1.04	1.50	1.61
LOS2	151.125	-8.535	28.31	72.08	17.26	-5.30	0.25	0.31	0.61	0.67
MAAP	150.4374	-9.6104	35.55	62.5	7.41	2.37	0.39	1.12	1.18	1.70

MENA	149.936	-9.757	34.91	62.25	6.96	1.72	1.01	1.13	1.59	1.71
MORA	150.187	-9.432	33.51	64.14	8.95	0.20	0.22	0.24	0.55	0.57
MORB	149.422	-9.61	36.56	63.65	8.16	3.21	0.63	0.79	1.22	1.38
NUBE	149.867	-10.399	33.91	55.7	0.38	1.03	0.90	0.99	1.47	1.56
PEMM	149.795	-9.621	34.84	63.35	8.01	1.56	0.27	0.32	0.65	0.70
RABA	149.834	-9.972	35.44	58.79	3.46	2.34	0.10	0.12	0.37	0.39
RAKO	149.393	-9.557	35.43	63.86	8.36	2.05	0.61	0.75	1.20	1.34
SALM	150.796	-9.663	37.72	65.59	10.64	4.62	0.21	0.24	0.57	0.60
SIBA	150.268	-10.684	32.83	57.05	1.89	0.16	1.24	1.18	1.81	1.75
SIRI	149.708	-9.841	36.52	58.04	2.66	3.33	1.34	1.42	1.92	2.00
SMRI	150.662	-10.613	32.96	56.62	1.62	0.32	0.87	0.93	1.44	1.50
STRA	151.868	-10.225	34.72	58.69	4.18	2.09	0.82	0.90	1.40	1.48
TUF2	149.318	-9.079	32.1	63.18	7.65	-1.52	0.23	0.25	0.56	0.58
TUFI	149.323	-9.08	30.51	63.96	8.44	-3.10	0.95	1.09	1.65	1.79
UAMA	150.953	-9.452	33.38	70.92	16.03	0.20	1.16	1.35	1.73	1.92
VAKU	151.184	-8.853	30.03	72.51	17.72	-3.42	0.66	0.73	1.23	1.30
VIVI	150.324	-9.31	33.28	64.98	9.84	-0.07	0.97	1.12	1.68	1.83
WAIB	150.139	-9.245	33.73	66.61	11.40	0.32	0.24	0.26	0.57	0.59
WANI	149.157	-9.338	33.34	62.52	6.93	-0.18	0.35	0.42	0.73	0.80
WAPO	150.532	-9.355	32.76	69.06	14.00	-0.53	1.12	1.31	1.70	1.89
WATL	150.243	-9.211	32.89	66.21	11.04	-0.52	0.35	0.43	0.71	0.79
YAMS	149.279	-9.7	31.93	57.23	1.69	-1.41	2.18	2.50	2.77	3.09
YANA	151.897	-9.271	33.51	74.89	20.39	0.38	1.00	1.20	1.59	1.79

Table D.2. (continued)

Plate	Longitude (°)	Latitude (°)	Rotation Rate (°/Myr)	Major Axis Uncertainty (Distance in °)	Minor Axis Uncertainty (Distance in °)	Orientation of Major Axis (° East of North)
WDLK	148.92	-10.97	2.81 ± 0.40	0.77	0.19	82
TROB	147.75	-9.33	2.67 ± 0.23	0.42	0.19	75
DEI	147.90	-8.95	2.04 ± 1.11	1.93	0.34	104
GOOD	175.79	-18.84	-0.16 ± 1.00	102.36	3.54	107
NORM	150.42	-9.70	1.64 ± 0.28	0.68	0.52	151
PP	149.23	-9.40	0.73 ± 0.28	0.91	0.6	128

Plate	Ω_x	Ω_y	Ω_z	σ_x	σ_y	σ_z	cov(x,y)	cov(x,z)	cov(y,z)
WDLK	-2.36	1.43	-0.54	0.35	0.18	0.07	-0.0646	0.0255	-0.0132
TROB	-2.23	1.41	-0.43	0.20	0.11	0.03	-0.021	0.0066	-0.0036
DEI	-1.71	1.07	-0.32	0.95	0.54	0.18	-0.5127	0.1745	-0.0998
GOOD	0.15	-0.01	0.05	0.96	0.55	0.19	-0.5264	0.1775	-0.102
NORM	-1.41	0.80	-0.28	0.24	0.14	0.05	-0.0329	0.0125	-0.0072
PP	-0.62	0.37	-0.12	0.24	0.14	0.05	-0.0331	0.0119	-0.0069

Table D.3. Poles of rotation of crustal blocks relative to the Australian Plate. Cartesian coordinates are shown in the lower section. Ω_x , Ω_y , and Ω_z are the Cartesian angular velocity vector components; σ_x , σ_y , and σ_z are the uncertainties of the respective components. The final columns give the covariances of component pairs. WDLK = Woodlark Plate; TROB = Trobriand Block; DEI = D’Entrecasteaux Islands block; GOOD = Goodenough Bay block; NORM = Normanby Island block; PP = Papuan Peninsula block.

#	Year	Event name	d_h km	Lat. °	Lon. °	d_1 km	d_2 km	Str. °	Dip °	L km	Rake °	Slip m	dE mm	dN mm	D km
1	2007	M 8.1 Solomon Isl.	24*												
2	2010	M 7.1 Solomon Isl.	10	-8.67	157.30	5	15	326	15	45	94	0.8			
3	2010	M 6.9 New Britain 1	28	-6.37	150.35	25	45	185	50	45	75	0.6			
4	2010	M 7.3 New Britain	35	-6.00	150.20	25	35	257	24	70	102	1.2			
5	2010	M 7.0 New Britain	44	-5.70	150.65	16	40	240	31	60	60	0.25			
6	2014	M 7.1 Bougainville 1	61	-6.39	154.97	50	75	310	45	50	80	0.7			
7	2014	M 7.5 Bougainville	43	-6.36	154.90	15	45	315	33	49	95	1.5			
8	2015	M 7.5 New Britain 1	41*												
		Segment 1		-5.40	152.25	12	17	252	44	120	61	0.3			
		Segment 2		-5.19	152.91	17	28	252	33	120	90	0.8			
		Segment 3		-5.08	152.16	28	43	252	24	120	65	0.5			
		Segment 4		-4.80	152.64	43	57	252	13	40	90	0.3			
9	2015	M 7.5 New Britain 2	55	-5.38	151.71	26	56	244	29	70	65	1			
10	2015	M 7.1 Bougainville 2	10	-7.54	154.87	0	16	125	67.5	80	270	1.2			
11	2016	M 7.9 New Britain 1	95*										7.90	7.62	725
		Segment 1		-5.00	153.00	0	50	313	27.9	260	90	1			
		Segment 2		-4.50	153.50	50	100	313	65	100	90	1			
12	2017	M 7.9 Bougainville	135	-6.70	155.20	136	166	135	55	50	90	8	3.16	1.98	750
13	2018	M 7.5 Highlands	25	-5.80	142.20	1	30	308	33	100	90	1	0.02	0.03	825
14	2018	M 6.9 New Britain 2	35	-5.82	151.07	25	45	244	45	45	82	0.6	0.04	0.55	500

Table D.4. Events and fault parameters used in regional earthquake corrections, based on USGS finite fault models (U.S. Geological Survey, 2019). Latitude and longitude are given for the lower corner of the fault farthest along the strike direction. d_h is the hypocentral depth. d_1 and d_2 are the upper and lower depths of the fault, respectively. Str is the fault strike. L is the along-strike length of the slipping fault and slip is the total slip. For the events from 2016-2018 (during our Mai’iu fault campaign experiment), D is the approximate distance from the earthquake to our GPS sites near the Mai’iu fault, dE is the average magnitude of the eastward offset at our campaign sites due to each event, and dN is the average magnitude of the northward offset at our campaign sites due to each event. Red events had no available USGS finite fault model as of publication. * = events with non-planar or multi-segment sources (Section D.2). Individual fault segment parameters are listed below these events, except for the 2007 Solomon Islands earthquake, for which the modeled slip distribution from Wallace et al. (2015) is shown in Figure D.2.

Config.	Description	N _{data}	N _{params}	DOF	χ^2	F test probability	Is (1) better?
1	Best fit	255	46	209	1.65		
2	VOGE + GOOD	255	43	212	1.69	57	No
3	VOGE + DEI + GOOD	255	39	216	1.93	87	Probably
4	GOOD + NORM	255	42	213	2.02	93	Probably
5	GOOD + NORM + DEI	255	38	217	1.95	89	Probably
6	DEI + TROB	255	38	217	1.82	76	Probably

Table D.5. Results of F test for block independence based on GPS velocities in Table D.2 and block boundary configurations in Figure D.3. N_{data} = number of data; N_{params} = number of free parameters; DOF = degrees of freedom. ‘VOGE + DEI + GOOD’ refers to models where Cape Vogel (VOGE), Goodenough Bay (GOOD), and D’Entrecasteaux Islands (DEI) blocks are treated as one unified block rotating about one pole. F tests cannot statistically distinguish between models where VOG and GOOD are considered individual blocks (configuration 1) and ones where they are one unified block (configuration 2). Therefore, we treat them as one block in all TDEFNODE block models.

CSIRO ID	Field Sample #	Fault rock	Lat. (°S), Long (°E) (WGS84)	Quantitative mineralogy
42351	PNG14-19E	upper gouge	-9.82862, 149.44082	Corrensite/Saponite (65%), Augite (13%), Kaolin (8%), Amphibole (6%), Plagioclase (4%), Quartz (2%), Calcite (2%)
42352	PNG14-19F	lower gouge	-9.82862, 149.44082	Corrensite/Saponite (49%), Amphibole (18%), Augite (17%), Plagioclase (8%), Kaolin (4%), Quartz (1%), Calcite (3%)
42358	PNG14-33B	upper mafic gouge	-9.67726, 149.35904	Corrensite/Saponite (21%), Calcite (21%), Montmorillonite (11%), Plagioclase (11%), Epidote (9%), Kfeldspar (7%), Amphibole (5%), Quartz (5%), Chlorite (4%), Dolomite/Ankerite (3%), White mica (3%)
42357	PNG14-33A	lower mafic gouge	-9.67726, 149.35904	Plagioclase (30%), Epidote (18%), Amphibole (16%), Corrensite/Saponite (8%), Chlorite (7%), Titanite (6%), Stilpnomelane (6%), Quartz (3%), Calcite (3%), Kfeldspar (2%)
52980	PNG16-17-D2H	foliated cataclasite	-9.8297, 149.4403	Epidote (26%), Plagioclase (19%), Quartz (20%), Calcite (12%), Amphibole (9%), Corrensite/Saponite (8%), Chlorite (3%), Titanite (3%)
52979	PNG16-151E	foliated cataclasite	-9.6790, 149.2941	Amphibole (37%), Plagioclase (29%), Epidote (22%), Chlorite (5%), Titanite (3%), Calcite (2%), White mica (2%), Quartz (<1%)
45071	PNG15-70	serpentinite	-9.82863, 149.61246	Lizardite Serpentine (82%), Magnesite (12%), Saponite (4%), Maghemite (1%), Quartz (<1%), Calcite (<1%), Dolomite/Ankerite (<1%)
45070	PNG15-50B	ultracataclasite	-9.67778, 149.28669	Corrensite (25%), Kfeldspar (22%), Plagioclase (20%), Amphibole (16%), Augite (12%), Chlorite (2%), Calcite (2%), Quartz (1%)

Table D.6. Description and quantitative mineralogy of fault rock samples.

References

- Abers, G. A., Eilon, Z., Gaherty, J. B., Jin, G., Kim, Y., Obrebski, M., & Dieck, C. (2016). Southeast Papuan crustal tectonics: Imaging extension and buoyancy of an active rift. *Journal of Geophysical Research: Solid Earth*, *121*(2), 951–971. <https://doi.org/10.1002/2015JB012621>
- Abers, G. a. (2001). Evidence for seismogenic normal faults at shallow dips in continental rifts. *Geological Society, London, Special Publications*, *187*(1), 305–318. <https://doi.org/10.1144/GSL.SP.2001.187.01.15>
- Abers, G. A., Ferris, A., Craigi, M., Daviest, H., Lerner-Lam, A. L., Mutter, J. C., & Taylor, B. (2002). Mantle compensation of active metamorphic core complexes at Woodiark rift in Papua New Guinea. *Nature*, *418*(6900)(August), 862.
- Abers, G. A. (2009). Slip on shallow-dipping normal faults. *Geology*, *37*(8), 767–768. <https://doi.org/10.1130/focus082009.1>
- Abers, G. A. (1991). Possible seismogenic shallow-dipping normal faults in the Woodlark-D'Entrecasteaux extensional province, Papua New Guinea. *Geology*, *19*(12), 1205–1208. [https://doi.org/10.1130/0091-7613\(1991\)019<1205:pssdnf>2.3.co;2](https://doi.org/10.1130/0091-7613(1991)019<1205:pssdnf>2.3.co;2)
- Abers, G. A., Mutter, C. Z., & Fang, J. (1997). Shallow dips of normal faults during rapid extension: Earthquakes in the Woodlark-D'Entrecasteaux rift system, Papua New Guinea. *Journal of Geophysical Research: Solid Earth*, *102*(B7), 15301–15317. <https://doi.org/10.1029/97jb00787>
- Almeida, R., Lindsey, E. O., Bradley, K., Hubbard, J., Mallick, R., & Hill, E. M. (2018). Can the Updip Limit of Frictional Locking on Megathrusts Be Detected Geodetically? Quantifying the Effect of Stress Shadows on Near-Trench Coupling. *Geophysical Research Letters*, *45*(10), 4754–4763. <https://doi.org/10.1029/2018GL077785>
- Anderlini, L., Serpelloni, E., & Belardinelli, M. E. (2016). Creep and locking of a low-angle normal fault: Insights from the Altotiberina fault in the Northern Apennines (Italy). *Geophysical Research Letters*, *43*(9), 4321–4329. <https://doi.org/10.1002/2016GL068604>
- Anzidei, M., Boschi, E., Cannelli, V., Devoti, R., Esposito, A., Galvani, A., ... Serpelloni, E. (2009). Coseismic deformation of the destructive April 6, 2009 L'Aquila earthquake (central Italy) from GPS data. *Geophysical Research Letters*, *36*(17). <https://doi.org/10.1029/2009GL039145>
- Araki, E., Saffer, D. M., Kopf, A. J., Wallace, L. M., Kimura, T., Machida, Y., ... Davis, E. (2017). Recurring and triggered slow-slip events near the trench at the Nankai Trough subduction megathrust. *Science*, *356*(6343), 1157–1160. <https://doi.org/10.1126/science.aan3120>

- Avouac, J.-P. (2015). From Geodetic Imaging of Seismic and Aseismic Fault Slip to Dynamic Modeling of the Seismic Cycle. *Annual Review of Earth and Planetary Sciences*, 43(1), 233–271. <https://doi.org/10.1146/annurev-earth-060614-105302>
- Axen, G. J. (1992). Pore pressure, stress increase, and fault weakening in low-angle normal faulting. *Journal of Geophysical Research*, 97(B6), 8979–8991.
- Axen, G. J., & Bartley, J. M. (1997). Implications for Extensional Tectonics, 102.
- Axen, G. J. (2004). Mechanics of Low-Angle Normal Faults. In *Rheology and Deformation of the Lithosphere at Continental Margins*. Columbia University Press. <https://doi.org/10.7312/karn12738-004>
- Axen, G. J. (2020). How a strong low-angle normal fault formed: The Whipple detachment, southeastern California. *Bulletin of the Geological Society of America*, 132(9–10), 1817–1828. <https://doi.org/10.1130/B35386.1>
- Balázs, A., Burov, E., Matenco, L., Vogt, K., Francois, T., & Cloetingh, S. (2017). Symmetry during the syn- and post-rift evolution of extensional back-arc basins: The role of inherited orogenic structures. *Earth and Planetary Science Letters*, 462, 86–98. <https://doi.org/10.1016/J.EPSL.2017.01.015>
- Baldwin, S. L., Fitzgerald, P. G., & Webb, L. E. (2012). Tectonics of the New Guinea Region. *Annual Review of Earth and Planetary Sciences*, 40(1), 495–520. <https://doi.org/10.1146/annurev-earth-040809-152540>
- Baldwin, S. L., Lister, G. S., Hill, E. J., Foster, D. A., & McDougall, I. (1993). Thermochronologic constraints on the tectonic evolution of active metamorphic core complexes, D'entrecasteaux Islands, Papua New Guinea. *Tectonics*, 12(3), 611–628. <https://doi.org/10.1029/93TC00235>
- Baldwin, S. L., Webb, L. E., & Monteleone, B. D. (2008). Late Miocene coesite-eclogite exhumed in the Woodlark Rift. *Geology*, 36(9), 735–738. <https://doi.org/10.1130/G25144A.1>
- Banerjee, P., Pollitz, F. F., & Bürgmann, R. (2005). The Size and Duration of the Sumatra-Andaman Earthquake from Far-Field Static Offsets. *Science*, 308(5729).
- Barbot, S., Lapusta, N., & Avouac, J. P. (2012). Under the hood of the earthquake machine: Toward predictive modeling of the seismic cycle. *Science*, 336(6082), 707–710. <https://doi.org/10.1126/science.1218796>
- Beaumont, C., Jamieson, R. A., Butler, J. P., & Warren, C. J. (2009). Crustal structure: A key constraint on the mechanism of ultra-high-pressure rock exhumation. *Earth and Planetary Science Letters*, 287(1–2), 116–129. <https://doi.org/10.1016/j.epsl.2009.08.001>

- Beavan, J., Denys, P., Denham, M., Hager, B., Herring, T., & Molnar, P. (2010). Distribution of present-day vertical deformation across the Southern Alps, New Zealand, from 10 years of GPS data. *Geophysical Research Letters*, *37*(16), n/a-n/a. <https://doi.org/10.1029/2010GL044165>
- Beavan, J., Moore, M., Pearson, C., Henderson, M., Parsons, B., Bourne, S., ... Hodgkinson, K. (1999). Crustal deformation during 1994-1998 due to oblique continental collision in the central Southern Alps, New Zealand, and implications for seismic potential of the Alpine fault. *Journal of Geophysical Research: Solid Earth*, *104*(B11), 25233–25255. <https://doi.org/10.1029/1999jb900198>
- Beavan, J., Wallace, L. M., Palmer, N., Denys, P., Ellis, S., Fournier, N., ... Denham, M. (2016). New Zealand GPS velocity field: 1995–2013. *New Zealand Journal of Geology and Geophysics*, *59*(1), 5–14. <https://doi.org/10.1080/00288306.2015.1112817>
- Behr, W. M., Kotowski, A. J., & Ashley, K. T. (2018). Dehydration-induced rheological heterogeneity and the deep tremor source in warm subduction zones. *Geology*, *46*(5), 475–478. <https://doi.org/10.1130/G40105.1>
- Benedetti, L., Manighetti, I., Gaudemer, Y., Finkel, R., Malavieille, J., Pou, K., ... Keddadouche, K. (2013). Earthquake synchrony and clustering on Fucino faults (Central Italy) as revealed from in situ ³⁶Cl exposure dating. *Journal of Geophysical Research: Solid Earth*, *118*(9), 4948–4974. <https://doi.org/10.1002/jgrb.50299>
- Bennett, R. A., Wernicke, B. P., Niemi, N. A., Friedrich, A. M., & Davis, J. L. (2003). Contemporary strain rates in the northern Basin and Range province from GPS data. *Tectonics*, *22*(2). <https://doi.org/10.1029/2001TC001355>
- Bennett, R. A., Hreinsdóttir, S., Velasco, M. S., & Fay, N. P. (2007). GPS constraints on vertical crustal motion in the northern Basin and Range. *Geophysical Research Letters*, *34*(22), L22319. <https://doi.org/10.1029/2007GL031515>
- Berdin, R. D., Siringan, F. P., & Maeda, Y. (2004). Holocene sea-level highstand and its implications for the vertical stability of Panglao Island, southwest Bohol, Philippines. *Quaternary International*, *115–116*, 27–37. [https://doi.org/10.1016/S1040-6182\(03\)00094-6](https://doi.org/10.1016/S1040-6182(03)00094-6)
- Biemiller, J., Wallace, L. M., Ellis, S. M., Little, T. A., Lavier, L., Mizera, M., ... Webber, S. M. (2018). Short- and Long-term Deformation Styles on an Active Low-angle Normal Fault: Mai'iu Fault, Papua New Guinea. *AGUFM*, *2018*, T33D-0430.
- Biemiller, J., Taylor, F., Lavier, L., Yu, T. L., Wallace, L., & Shen, C. C. (2020a). Emerged Coral Reefs Record Holocene Low-Angle Normal Fault Earthquakes. *Geophysical Research Letters*, *47*(20), 1–12. <https://doi.org/10.1029/2020GL089301>

- Biemiller, J., Boulton, C., Wallace, L., Ellis, S., Little, T., Mizera, M., ... Lavier, L. (2020b). Mechanical Implications of Creep and Partial Coupling on the World's Fastest Slipping Low-Angle Normal Fault in Southeastern Papua New Guinea. *Journal of Geophysical Research: Solid Earth*, 125(10), 1–24. <https://doi.org/10.1029/2020JB020117>
- Biemiller, J., Ellis, S., Mizera, M., Little, T., Wallace, L., & Lavier, L. (2019). Tectonic Inheritance Following Failed Continental Subduction: A Model for Core Complex Formation in Cold, Strong Lithosphere. *Tectonics*, 1742–1763. <https://doi.org/10.1029/2018TC005383>
- Biemiller, J., & Lavier, L. (2017). Earthquake supercycles as part of a spectrum of normal fault slip styles. *Journal of Geophysical Research: Solid Earth*, 122(4), 3221–3240. <https://doi.org/10.1002/2016JB013666>
- Bostock, M. G., Christensen, N. I., & Peacock, S. M. (2019). Seismicity in Cascadia. *Lithos*, 332–333, 55–66. <https://doi.org/10.1016/j.lithos.2019.02.019>
- Bottrill, A. D., Van Hunen, J., Cuthbert, S. J., Brueckner, H. K., & Allen, M. B. (2014). Plate rotation during continental collision and its relationship with the exhumation of UHP metamorphic terranes: Application to the Norwegian Caledonides. *Geochemistry, Geophysics, Geosystems*, 15(5), 1766–1782. <https://doi.org/10.1002/2014GC005253>
- Boulton, C., Barth, N. C., Moore, D. E., Lockner, D. A., Townend, J., & Faulkner, D. R. (2018). Frictional properties and 3-D stress analysis of the southern Alpine Fault, New Zealand. *Journal of Structural Geology*, 114, 43–54. <https://doi.org/10.1016/j.jsg.2018.06.003>
- Brozzetti, F., Boncio, P., Lavecchia, G., & Pace, B. (2009). Present activity and seismogenic potential of a low-angle normal fault system (Città di Castello, Italy): Constraints from surface geology, seismic reflection data and seismicity. *Tectonophysics*, 463(1–4), 31–46. <https://doi.org/10.1016/j.tecto.2008.09.023>
- Bruhn, R. L., Parry, W. T., Yonkee, W. A., & Thompson, T. (1994). Fracturing and hydrothermal alteration in normal fault zones. *Pure and Applied Geophysics PAGEOPH*, 142(3–4), 609–644. <https://doi.org/10.1007/BF00876057>
- Brun, J.-P., Sokoutis, D., & Van Den Driessche, J. (1994). Analogue modeling of detachment fault systems and core complexes. *Geology*, 22(4), 319–322. [https://doi.org/10.1130/0091-7613\(1994\)022<0319:AMODFS>2.3.CO;2](https://doi.org/10.1130/0091-7613(1994)022<0319:AMODFS>2.3.CO;2)
- Brun, J.-P., Sokoutis, D., Tirel, C., Gueydan, F., Van Den Driessche, J., & Beslier, M.-O. (2018). Crustal versus mantle core complexes. *Tectonophysics*, 746, 22–45. <https://doi.org/10.1016/J.TECTO.2017.09.017>
- Buck, W. R. (1988). Flexural Rotation of Normal Faults. *Tectonics*, 7(5), 959–973.

- Buck, W. R. (1991). Modes of Continental Lithospheric Extension. *Journal of Geophysical Research*, 96, 20161. <https://doi.org/10.1029/91JB01485>
- Buck, W. R. (1997). Bending thin lithosphere causes localized “Snapping” and not distributed “crunching”: Implications for Abyssal Hill Formation. *Geophysical Research Letters*, 24(20), 2531–2534. <https://doi.org/10.1029/97GL02640>
- Buck, W. R. (1993). Effect of lithospheric thickness on the formation of high- and low-angle normal faults. *Geology*, 21(10), 933–936. [https://doi.org/10.1130/0091-7613\(1993\)021<0933:EOLTOT>2.3.CO;2](https://doi.org/10.1130/0091-7613(1993)021<0933:EOLTOT>2.3.CO;2)
- Buck, W. R., Lavier, L. L., & Poliakov, A. N. B. (1999). How to make a rift wide. *Philosophical Transactions of the Royal Society A: Mathematical, Physical and Engineering Sciences*, 357(1753), 671–693. <https://doi.org/10.1098/rsta.1999.0348>
- Buiter, S., & Ellis, S. (2012). SULEC: Benchmarking a new ALE finite-element code. *EGU General Assembly 2012, Held 22-27 April, 2012 in Vienna, Austria.*, p.7528, 14, 7528. Retrieved from <http://adsabs.harvard.edu/abs/2012EGUGA..14.7528B>
- Bürgmann, R., Schmidt, D., Nadeau, R. M., D’Alessio, M., Fielding, E., Manaker, D., ... Murray, M. H. (2000). Earthquake potential along the Northern Hayward fault, California. *Science*, 289(5482), 1178–1182. <https://doi.org/10.1126/science.289.5482.1178>
- Bürgmann, R. (2018). The geophysics, geology and mechanics of slow fault slip. *Earth and Planetary Science Letters*, 495, 112–134. <https://doi.org/10.1016/j.epsl.2018.04.062>
- Bürgmann, R., Pollard, D. D., & Martel, S. J. (1994). Slip distributions on faults: effects of stress gradients, inelastic deformation, heterogeneous host-rock stiffness, and fault interaction. *Journal of Structural Geology*, 16(12), 1675–1690. [https://doi.org/10.1016/0191-8141\(94\)90134-1](https://doi.org/10.1016/0191-8141(94)90134-1)
- Butler, J. P., Beaumont, C., & Jamieson, R. A. (2015). Paradigm lost: Buoyancy thwarted by the strength of the Western Gneiss Region (ultra)high-pressure terrane, Norway. *Lithosphere*, 7(4), 379–407. <https://doi.org/10.1130/L426.1>
- Chamoli, A., Lowry, A. R., & Jeppson, T. N. (2014). Implications of transient deformation in the northern Basin and Range, western United States. *Journal of Geophysical Research: Solid Earth*, 119(5), 4393–4413. <https://doi.org/10.1002/2013JB010605>
- Chappell, J., & Polach, H. A. (1976). Holocene sea-level change and coral-reef growth at Huon Peninsula, Papua New Guinea. *GSA Bulletin*, 87(2), 235–240. [https://doi.org/10.1130/0016-7606\(1976\)87<235:hscacg>2.0.co;2](https://doi.org/10.1130/0016-7606(1976)87<235:hscacg>2.0.co;2)
- Chen, J., Niemeijer, A. R., & Spiers, C. J. (2017). Microphysically Derived Expressions for Rate-and-State Friction Parameters, a , b , and D_c . *Journal of Geophysical Research: Solid Earth*, 122(12), 9627–9657. <https://doi.org/10.1002/2017JB014226>

- Cheng, H., Lawrence Edwards, R., Shen, C. C., Polyak, V. J., Asmerom, Y., Woodhead, J., ... Calvin Alexander, E. (2013). Improvements in ^{230}Th dating, ^{230}Th and ^{234}U half-life values, and U-Th isotopic measurements by multi-collector inductively coupled plasma mass spectrometry. *Earth and Planetary Science Letters*, 371–372, 82–91. <https://doi.org/10.1016/j.epsl.2013.04.006>
- Chester, F. M., & Higgs, N. G. (1992). Multimechanism friction constitutive model for ultrafine quartz gouge at hypocentral conditions. *Journal of Geophysical Research: Solid Earth*, 97(B2), 1859–1870. <https://doi.org/10.1029/91JB02349>
- Chiaraluce, L., Chiarabba, C., Collettini, C., Piccinini, D., & Cocco, M. (2007). Architecture and mechanics of an active low-angle normal fault: Alto Tiberina Fault, northern Apennines, Italy. *Journal of Geophysical Research*, 112(B10), B10310. <https://doi.org/10.1029/2007JB005015>
- Chiaraluce, L., Amato, A., Carannante, S., Castelli, V., Cattaneo, M., Cocco, M., ... Valoroso, L. (2014). The alto Tiberina near fault observatory (northern Apennines, Italy). *Annals of Geophysics*, 57(3). <https://doi.org/10.4401/ag-6426>
- Choi, E., & Buck, W. R. (2012). Constraints on the strength of faults from the geometry of rider blocks in continental and oceanic core complexes. *Journal of Geophysical Research: Solid Earth*, 117(B4), n/a-n/a. <https://doi.org/10.1029/2011JB008741>
- Choi, E., Buck, W. R., Lavier, L. L., & Petersen, K. D. (2013). Using core complex geometry to constrain fault strength. *Geophysical Research Letters*, 40(15), 3863–3867. <https://doi.org/10.1002/grl.50732>
- Church, J. A., & White, N. J. (2011). Sea-Level Rise from the Late 19th to the Early 21st Century. *Surveys in Geophysics*, 32(4–5), 585–602. <https://doi.org/10.1007/s10712-011-9119-1>
- Cloos, M., Weiland, R. J., Warren, P. Q., & McMahon, T. P. (2005). The geotectonics of subducting slab breakoff. *Geological Society of America Special Paper*, 400, 1–51. <https://doi.org/10.1130/2005.2400>
- Collettini, C., & Barchi, M. R. (2004). A comparison of structural data and seismic images for low-angle normal faults in the Northern Apennines (Central Italy): Constraints on activity. *Geological Society Special Publication*, 224, 95–112. <https://doi.org/10.1144/GSL.SP.2004.224.01.07>
- Collettini, C., Tesei, T., Scuderi, M. M., Carpenter, B. M., & Viti, C. (2019). Beyond Byerlee friction, weak faults and implications for slip behavior. *Earth and Planetary Science Letters*, 519, 245–263. <https://doi.org/10.1016/j.epsl.2019.05.011>

- Collettini, C. (2011). The mechanical paradox of low-angle normal faults: Current understanding and open questions. *Tectonophysics*, 510(3–4), 253–268. <https://doi.org/10.1016/j.tecto.2011.07.015>
- Collettini, C., Niemeijer, A., Viti, C., & Marone, C. (2009b). Fault zone fabric and fault weakness. *Nature*, 462(7275), 907–910. <https://doi.org/10.1038/nature08585>
- Collettini, C., & Sibson, R. H. (2001). Normal faults, normal friction? *Geology*, 29(10), 927. [https://doi.org/10.1130/0091-7613\(2001\)029<0927:NFNF>2.0.CO;2](https://doi.org/10.1130/0091-7613(2001)029<0927:NFNF>2.0.CO;2)
- Collettini, C., Viti, C., Smith, S. A. F., & Holdsworth, R. E. (2009a). Development of interconnected talc networks and weakening of continental low-angle normal faults. *Geology*, 37(6), 567–570. <https://doi.org/10.1130/G25645A.1>
- Cowie, P. A., & Roberts, G. P. (2001). Constraining slip rates and spacings for active normal faults. *Journal of Structural Geology*, 23(12), 1901–1915. [https://doi.org/10.1016/S0191-8141\(01\)00036-0](https://doi.org/10.1016/S0191-8141(01)00036-0)
- Crow, R., Karlstrom, K., Asmerom, Y., Schmandt, B., Polyak, V., & DuFrane, S. A. (2011). Shrinking of the Colorado plateau via lithospheric mantle erosion: Evidence from Nd and Sr isotopes and geochronology of Neogene basalts. *Geology*, 39(1), 27–30. <https://doi.org/10.1130/G31611.1>
- Cummins, P. R., Pranantyo, I. R., Pownall, J. M., Griffin, J. D., Meilano, I., & Zhao, S. (2020). Earthquakes and tsunamis caused by low-angle normal faulting in the Banda Sea, Indonesia. *Nature Geoscience*. <https://doi.org/10.1038/s41561-020-0545-x>
- Cundall, P. A. (1989). Numerical experiments on localization in frictional materials. *Ingenieur-Archiv*, 59(2), 148–159. <https://doi.org/10.1007/BF00538368>
- Daczko, N. R., Caffi, P., Halpin, J. A., & Mann, P. (2009). Exhumation of the Dayman dome metamorphic core complex, eastern Papua New Guinea. *Journal of Metamorphic Geology*, 27(6), 405–422. <https://doi.org/10.1111/j.1525-1314.2009.00825.x>
- Daczko, N. R., Caffi, P., & Mann, P. (2011). Structural evolution of the Dayman dome metamorphic core complex, eastern Papua New Guinea. *Geological Society of America Bulletin*, 123(11–12), 2335–2351. <https://doi.org/10.1130/B30326.1>
- Daniell, J. E., Khazai, B., Wenzel, F., Daniell, J. E., Khazai, B., & Wenzel, F. (2013). Article in Natural hazards and earth system sciences · May. *Nat. Hazards Earth Syst. Sci. Discuss*, 1. <https://doi.org/10.5194/nhessd-1-1913-2013>
- Davies, H. L. (1980). Folded thrust fault and associated metamorphics in the Suckling-Dayman massif, Papua New Guinea, 280A, 171–191.

- Davies, H. L., & Jaques, A. L. (1984). Emplacement of ophiolite in Papua New Guinea. *Geological Society, London, Special Publications*, 13(1), 341–349. <https://doi.org/10.1144/GSL.SP.1984.013.01.27>
- Davies, H. L., & Smith, I. E. (1971). Geology of eastern Papua. *Bulletin of the Geological Society of America*, 82(12), 3299–3312. [https://doi.org/10.1130/0016-7606\(1971\)82\[3299:GOEP\]2.0.CO;2](https://doi.org/10.1130/0016-7606(1971)82[3299:GOEP]2.0.CO;2)
- Huw Davies, J., & von Blanckenburg, F. (1995). Slab breakoff: A model of lithosphere detachment and its test in the magmatism and deformation of collisional orogens. *Earth and Planetary Science Letters*, 129(1–4), 85–102. [https://doi.org/10.1016/0012-821X\(94\)00237-S](https://doi.org/10.1016/0012-821X(94)00237-S)
- Davis, G. A., Anderson, J. L., Frost, E. G., & Shackelford, T. J. (1980). Mylonitization and detachment faulting in the Whipple-Buckskin-Rawhide Mountains terrane, southeastern California and western Arizona. In *Cordilleran Metamorphic Core Complexes* (p. 79).
- Den Hartog, S. A. M., & Spiers, C. J. (2013). Influence of subduction zone conditions and gouge composition on frictional slip stability of megathrust faults. *Tectonophysics*, 600, 75–90. <https://doi.org/10.1016/j.tecto.2012.11.006>
- Dickinson, W. R. (2009). Pacific atoll living: How long already and until when? *GSA Today*, 19(3), 4–10. <https://doi.org/10.1130/GSATG35A.1>
- Dieterich, J. H. (1979). Modeling of rock friction: 1. Experimental results and constitutive equations. *Journal of Geophysical Research*, 84(B5), 2161. <https://doi.org/10.1029/JB084iB05p02161>
- Dieterich, J. H. (1981). Constitutive Properties of Faults With Simulated Gouge (pp. 103–120). American Geophysical Union (AGU). <https://doi.org/10.1029/GM024p0103>
- Dolan, J. F., Bowman, D. D., & Sammis, C. G. (2007). Long-range and long-term fault interactions in Southern California. *Geology*, 35(9), 855–858. <https://doi.org/10.1130/G23789A.1>
- Duretz, T., & Gerya, T. V. (2013). Slab detachment during continental collision: Influence of crustal rheology and interaction with lithospheric delamination. *Tectonophysics*, 602, 124–140. <https://doi.org/10.1016/j.tecto.2012.12.024>
- Duretz, T., Schmalholz, S. M., & Gerya, T. V. (2012). Dynamics of slab detachment. *Geochemistry, Geophysics, Geosystems*, 13(3). <https://doi.org/10.1029/2011GC004024>
- Duretz, T., Gerya, T. V., & May, D. A. (2011). Numerical modelling of spontaneous slab breakoff and subsequent topographic response. *Tectonophysics*, 502(1–2), 244–256. <https://doi.org/10.1016/j.tecto.2010.05.024>

- Dziewonski, A. M., & Anderson, D. L. (1981). *Preliminary reference Earth model* *. *Preliminary reference Earth model Phys. Earth Planet. Inter* (Vol. 25).
- Eberhard, B. M. O., Baldrige, S., Marshall, J., Mooney, W., Rix, G. J., & Survey, U. S. G. (2010). The Mw 7.0 Haiti earthquake of January 12, 2010 : USGS / EERI advance reconnaissance team report. *U.S. Geological Survey*, 1–57.
- Eilon, Z., Abers, G. A., Gaherty, J. B., & Jin, G. (2015). Imaging continental breakup using teleseismic body waves: The Woodlark Rift, Papua New Guinea. *Geochemistry, Geophysics, Geosystems*, *16*(8), 2529–2548. <https://doi.org/10.1002/2015GC005835>
- Eilon, Z., Abers, G. A., & Gaherty, J. B. (2016). A joint inversion for shear velocity and anisotropy: the Woodlark Rift, Papua New Guinea. *Geophysical Journal International*, *206*(2), 807–824. <https://doi.org/10.1093/gji/ggw177>
- Ellis, S. M., Little, T. A., Wallace, L. M., Hacker, B. R., & Buitter, S. J. H. (2011). Feedback between rifting and diapirism can exhume ultrahigh-pressure rocks. *Earth and Planetary Science Letters*, *311*(3–4), 427–438. <https://doi.org/10.1016/j.epsl.2011.09.031>
- Evans, J. P. (1990). Textures, deformation mechanisms, and the role of fluids in the cataclastic deformation of granitic rocks. *Geological Society Special Publication*, *54*(1), 29–39. <https://doi.org/10.1144/GSL.SP.1990.054.01.03>
- Fagereng, Å., & Sibson, R. H. (2010). Mélange rheology and seismic style. *Geology*, *38*(8), 751–754. <https://doi.org/10.1130/G30868.1>
- Ferris, A., Abers, G. A., Zelt, B., Taylor, B., & Roecker, S. (2006). Crustal structure across the transition from rifting to spreading: The Woodlark rift system of Papua New Guinea. *Geophysical Journal International*, *166*(2), 622–634. <https://doi.org/10.1111/j.1365-246X.2006.02970.x>
- Fitz, G. (2011). *Offshore mapping and modeling of Miocene-Recent extensional basins adjacent to metamorphic gneiss domes of the D'Entrecasteaux Islands, eastern Papua New Guinea*. University of Texas at Austin.
- Fitz, G., & Mann, P. (2013b). Evaluating upper versus lower crustal extension through structural reconstructions and subsidence analysis of basins adjacent to the D'Entrecasteaux Islands, eastern Papua New Guinea. *Geochemistry, Geophysics, Geosystems*, *14*(6), 1800–1818. <https://doi.org/10.1002/ggge.20123>
- Fitz, G., & Mann, P. (2013a). Tectonic uplift mechanism of the Goodenough and Fergusson Island gneiss domes, eastern Papua New Guinea: Constraints from seismic reflection and well data. *Geochemistry, Geophysics, Geosystems*, *14*(10), 3969–3995. [https://doi.org/10.1002/GGGE.20208@10.1002/\(ISSN\)1525-2027.LITHOS1](https://doi.org/10.1002/GGGE.20208@10.1002/(ISSN)1525-2027.LITHOS1)

- Fletcher, J. M., Oskin, M. E., & Teran, O. J. (2016). The role of a keystone fault in triggering the complex El Mayor-Cucapah earthquake rupture. *Nature Geoscience*, 9(4), 303–307. <https://doi.org/10.1038/ngeo2660>
- Fletcher, J. M., Teran, O. J., Rockwell, T. K., Oskin, M. E., Hudnut, K. W., Mueller, K. J., ... González-García, J. (2014). Assembly of a large earthquake from a complex fault system: Surface rupture kinematics of the 4 April 2010 El Mayor-Cucapah (Mexico) Mw 7.2 earthquake. *Geosphere*, 10(4), 797–827. <https://doi.org/10.1130/GES00933.1>
- Floyd, J. S., Mutter, J. C., Goodliffe, A. M., & Taylor, B. (2001). Evidence for fault weakness and fluid flow within an active low-angle normal fault. *Nature*, 411(6839), 779–783. <https://doi.org/10.1038/35081040>
- Friedrich, A. M., Wernicke, B. P., Niemi, N. A., Bennett, R. A., & Davis, J. L. (2003). Comparison of geodetic and geologic data from the Wasatch region, Utah, and implications for the spectral character of Earth deformation at periods of 10 to 10 million years. *Journal of Geophysical Research: Solid Earth*, 108(B4). <https://doi.org/10.1029/2001jb000682>
- Garcés, M., & Gee, J. S. (2007). Paleomagnetic evidence of large footwall rotations associated with low-angle faults at the Mid-Atlantic Ridge. *Geology*, 35(3), 279–282. <https://doi.org/10.1130/G23165A.1>
- Gold, R. D., & Cowgill, E. (2011). Deriving fault-slip histories to test for secular variation in slip, with examples from the Kunlun and Awatere faults. *Earth and Planetary Science Letters*, 301(1–2), 52–64. <https://doi.org/10.1016/j.epsl.2010.10.011>
- Goodwin, I. D., & Harvey, N. (2008). Subtropical sea-level history from coral microatolls in the Southern Cook Islands, since 300 AD. *Marine Geology*, 253(1–2), 14–25. <https://doi.org/10.1016/j.margeo.2008.04.012>
- Grossman, E. E., Fletcher, C. H., & Richmond, B. M. (1998). The Holocene sea-level highstand in the equatorial Pacific: Analysis of the insular paleosea-level database. *Coral Reefs*, 17(3), 309–327. <https://doi.org/10.1007/s003380050132>
- Gu, J. C., Rice, J. R., Ruina, A. L., & Tse, S. T. (1984). Slip motion and stability of a single degree of freedom elastic system with rate and state dependent friction. *Journal of the Mechanics and Physics of Solids*, 32(3), 167–196. [https://doi.org/10.1016/0022-5096\(84\)90007-3](https://doi.org/10.1016/0022-5096(84)90007-3)
- Haines, S., Marone, C., & Saffer, D. (2014). Frictional properties of low-angle normal fault gouges and implications for low-angle normal fault slip. *Earth and Planetary Science Letters*, 408, 57–65. <https://doi.org/10.1016/j.epsl.2014.09.034>
- Hales, T. C., Abt, D. L., Humphreys, E. D., & Roering, J. J. (2005). A lithospheric instability origin for Columbia River flood basalts and Willowa Mountains uplift in northeast Oregon. *Nature*, 438(7069), 842–845. <https://doi.org/10.1038/nature04313>

- Harris, R. A. (2017, March 1). Large earthquakes and creeping faults. *Reviews of Geophysics*. Blackwell Publishing Ltd. <https://doi.org/10.1002/2016RG000539>
- Harris, R. A. (2017). Large earthquakes and creeping faults. *Reviews of Geophysics*, 55(1), 169–198. <https://doi.org/10.1002/2016RG000539>
- Harris, R. A., & Simpson, R. W. (1998, October 10). Suppression of large earthquakes by stress shadows: A comparison of Coulomb and rate-and-state failure. *Journal of Geophysical Research: Solid Earth*. Blackwell Publishing Ltd. <https://doi.org/10.1029/98jb00793>
- Hayes, G. P. (2017). The finite, kinematic rupture properties of great-sized earthquakes since 1990. *Earth and Planetary Science Letters*, 468, 94–100. <https://doi.org/10.1016/j.epsl.2017.04.003>
- He, C., Luo, L., Hao, Q.-M., & Zhou, Y. (2013). Velocity-weakening behavior of plagioclase and pyroxene gouges and stabilizing effect of small amounts of quartz under hydrothermal conditions. *Journal of Geophysical Research: Solid Earth*, 118(7), 3408–3430. <https://doi.org/10.1002/jgrb.50280>
- Herrendörfer, R., Van Dinther, Y., Gerya, T., & Dalguer, L. A. (2015). Earthquake supercycle in subduction zones controlled by the width of the seismogenic zone. *Nature Geoscience*, 8(6), 471–474. <https://doi.org/10.1038/NGEO2427>
- Herring, T. A., Floyd, M. A., King, R. W., & McClusky, S. C. (2015). GLOBK Reference Manual. Massachusetts Institute of Technology.
- Herring, T. A., King, R. W., Floyd, M. A., & McClusky, S. C. (2018). GAMIT Reference Manual. Massachusetts Institute of Technology.
- Herring, T. A., Melbourne, T. I., Murray, M. H., Floyd, M. A., Szeliga, W. M., King, R. W., ... Wang, L. (2016). Reviews of Geophysics data analysis methods and geodetic products. *Reviews of Geophysics*, 759–808. <https://doi.org/10.1002/2016RG000529>
- Hetzl, R., & Hampel, A. (2005). Slip rate variations on normal faults during glacial-interglacial changes in surface loads. *Nature*, 435(7038), 81–84. <https://doi.org/10.1038/nature03562>
- Heuret, A., Lallemand, S., Funiciello, F., Piromallo, C., & Faccenna, C. (2011). Physical characteristics of subduction interface type seismogenic zones revisited. *Geochemistry, Geophysics, Geosystems*, 12(1), 1–26. <https://doi.org/10.1029/2010GC003230>
- Hillers, G., Ben-Zion, Y., & Mai, P. M. (2006). Seismicity on a fault controlled by rate- and state-dependent friction with spatial variations of the critical slip distance. *Journal of Geophysical Research*, 111(B1), B01403. <https://doi.org/10.1029/2005JB003859>

- Hirose, H., & Obara, K. (2005). Repeating short- and long-term slow slip events with deep tremor activity around the Bungo channel region, southwest Japan. *Earth, Planets and Space*, 57(10), 961–972. <https://doi.org/10.1186/BF03351875>
- Hirth, G., & Kohlstedt, D. L. (2003). Rheology of the Upper Mantle and the Mantle Wedge : A View from the Experimentalists upper mantle . We first analyze experimental data to provide a critical review of flow. *Geophysical Monograph Series*, 138, 83–105. <https://doi.org/10.1029/138GM06>
- Holm, R. J., Rosenbaum, G., & Richards, S. W. (2016). Post 8 Ma reconstruction of Papua New Guinea and Solomon Islands: Microplate tectonics in a convergent plate boundary setting. *Earth-Science Reviews*, 156, 66–81. <https://doi.org/10.1016/J.EARSCIREV.2016.03.005>
- Hreinsdóttir, S., & Bennett, R. A. (2009). Active aseismic creep on the Alto Tiberina low-angle normal fault, Italy. *Geology*, 37(8), 683–686. <https://doi.org/10.1130/G30194A.1>
- Huet, B., Le Pourhiet, L., Labrousse, L., Burov, E. B., & Jolivet, L. (2011a). Formation of metamorphic core complex in inherited wedges: A thermomechanical modelling study. *Earth and Planetary Science Letters*, 309(3–4), 249–257. <https://doi.org/10.1016/j.epsl.2011.07.004>
- Huet, B., Le Pourhiet, L., Labrousse, L., Burov, E., & Jolivet, L. (2011b). Post-orogenic extension and metamorphic core complexes in a heterogeneous crust: The role of crustal layering inherited from collision. Application to the Cyclades (Aegean domain). *Geophysical Journal International*, 184(2), 611–625. <https://doi.org/10.1111/j.1365-246X.2010.04849.x>
- Huisman, R. S., & Beaumont, C. (2007). Roles of lithospheric strain softening and heterogeneity in determining the geometry of rifts and continental margins. *Geological Society, London, Special Publications*, 282(1), 111–138. <https://doi.org/10.1144/SP282.6>
- Huisman, R. S., & Beaumont, C. (2003). Symmetric and asymmetric lithospheric extension: Relative effects of frictional-plastic and viscous strain softening. *Journal of Geophysical Research: Solid Earth*, 108(B10), 1–22. <https://doi.org/10.1029/2002JB002026>
- Ide, S., Beroza, G. C., Shelly, D. R., & Uchide, T. (2007). A scaling law for slow earthquakes. *Nature*, 447(7140), 76–79. <https://doi.org/10.1038/nature05780>
- Ikari, M. J., & Kopf, A. J. (2017). Seismic potential of weak, near-surface faults revealed at plate tectonic slip rates. *Science Advances*, 3(11), e1701269. <https://doi.org/10.1126/sciadv.1701269>
- Ikari, M. J., Marone, C., & Saffer, D. M. (2011). On the relation between fault strength and frictional stability. *Geology*, 39(1), 83–86. <https://doi.org/10.1130/G31416.1>

- Ikari, M. J., Saffer, D. M., & Marone, C. (2009). Frictional and hydrologic properties of clay-rich fault gouge. *Journal of Geophysical Research: Solid Earth*, *114*(5).
<https://doi.org/10.1029/2008JB006089>
- Ito, Y., Obara, K., Shiomi, K., Sekine, S., & Hirose, H. (2007). Slow earthquakes coincident with episodic tremors and slow slip events. *Science*, *315*(5811), 503–506.
<https://doi.org/10.1126/science.1134454>
- Jackson, J. A. (1987). Active normal faulting and crustal extension. *Geological Society Special Publication*, *28*, 3–17. <https://doi.org/10.1144/GSL.SP.1987.028.01.02>
- Jackson, J. A., & White, N. J. (1989). Normal faulting in the upper continental crust: observations from regions of active extension. *Journal of Structural Geology*, *11*(1–2), 15–36. [https://doi.org/10.1016/0191-8141\(89\)90033-3](https://doi.org/10.1016/0191-8141(89)90033-3)
- Jackson, J., & McKenzie, D. (1983). The geometrical evolution of normal fault systems. *Journal of Structural Geology*, *5*(5), 471–482. [https://doi.org/10.1016/0191-8141\(83\)90053-6](https://doi.org/10.1016/0191-8141(83)90053-6)
- Jammes, S., Lavier, L. L., & Reber, J. E. (2015). Localization and delocalization of deformation in a biminerale material. *Journal of Geophysical Research: Solid Earth*, *120*(5), 3649–3663. <https://doi.org/10.1002/2015JB011890>
- Jaoul, O., Tullis, J., & Kronenberg, A. (1984). The effect of varying water contents on the creep behavior of Heavitree quartzite. *Journal of Geophysical Research: Solid Earth*, *89*(B6), 4298–4312. <https://doi.org/10.1029/JB089iB06p04298>
- Japan, N. P. A. of. (2020). *Police Countermeasures and Damage Situation associated with 2011 Tohoku district - off the Pacific Ocean Earthquake*.
- Jolivet, L., Lecomte, E., Huet, B., Denèle, Y., Lacombe, O., Labrousse, L., ... Mehl, C. (2010). The North Cycladic Detachment System. *Earth and Planetary Science Letters*, *289*(1–2), 87–104. <https://doi.org/10.1016/j.epsl.2009.10.032>
- Kirby, S. H., & Kronenberg, A. K. (1987). Rheology of the lithosphere: Selected topics. *Reviews of Geophysics*, *25*(7), 1219–1244. <https://doi.org/10.1029/RG021i006p01458>
- Kopp, R. E., Kemp, A. C., Bittermann, K., Horton, B. P., Donnelly, J. P., Gehrels, W. R., ... Rahmstorf, S. (2016). Temperature-driven global sea-level variability in the Common Era. *Proceedings of the National Academy of Sciences of the United States of America*, *113*(11), E1434–E1441. <https://doi.org/10.1073/pnas.1517056113>
- Kostoglodov, V., Singh, S. K., Santiago, J. A., Franco, S. I., Larson, K. M., Lowry, A. R., & Bilham, R. (2003). A large silent earthquake in the Guerrero seismic gap, Mexico. *Geophysical Research Letters*, *30*(15). <https://doi.org/10.1029/2003GL017219>

- Koulali, A., Tregoning, P., McClusky, S., Stanaway, R., Wallace, L., & Lister, G. (2015). New Insights into the present-day kinematics of the central and western Papua New Guinea from GPS. *Geophysical Journal International*, 202(2), 993–1004. <https://doi.org/10.1093/gji/ggv200>
- Labrousse, L., Huet, B., Le Pourhiet, L., Jolivet, L., & Burov, E. (2016). Rheological implications of extensional detachments: Mediterranean and numerical insights. *Earth-Science Reviews*, 161, 233–258. <https://doi.org/10.1016/j.earscirev.2016.09.003>
- Lambert, V., & Barbot, S. (2016). Contribution of viscoelastic flow in earthquake cycles within the lithosphere-asthenosphere system. *Geophysical Research Letters*, 43(19), 10,142–10,154. <https://doi.org/10.1002/2016GL070345>
- Lapusta, N., & Barbot, S. (2012). Models of earthquakes and aseismic slip based on laboratory-derived rate-and-state friction laws. In A. Bizzarri & H. S. Bhat (Eds.), *The Mechanics of Faulting: From Laboratory to Real Earthquakes* (pp. 153–207).
- Lapusta, N., & Liu, Y. (2009). Three-dimensional boundary integral modeling of spontaneous earthquake sequences and aseismic slip. *Journal of Geophysical Research*, 114(B9), B09303. <https://doi.org/10.1029/2008JB005934>
- Lapusta, N., Rice, J. R., Ben-Zion, Y., & Zheng, G. (2000). Elastodynamic analysis for slow tectonic loading with spontaneous rupture episodes on faults with rate- and state-dependent friction. *Journal of Geophysical Research: Solid Earth*, 105(B10), 23765–23789. <https://doi.org/10.1029/2000jb900250>
- Lavier, L. L., Bennett, R. A., & Duddu, R. (2013). Creep events at the brittle ductile transition. *Geochemistry, Geophysics, Geosystems*, 14(9), 3334–3351. <https://doi.org/10.1002/ggge.20178>
- Lavier, L. L., Buck, W. R., & Poliakov, A. (1999). Self-consistent rolling-hinge model for the evolution of large-onset low-angle normal faults. *Geology*, 27(12), 1127–1130. [https://doi.org/10.1130/0091-7613\(1999\)027<1127:SCRHMF>2.3.CO;2](https://doi.org/10.1130/0091-7613(1999)027<1127:SCRHMF>2.3.CO;2)
- Lavier, L. L., & Buck, W. R. (2002). Half graben versus large-offset low-angle normal fault: Importance of keeping cool during normal faulting. *Journal of Geophysical Research*, 107(B6), 2122. <https://doi.org/10.1029/2001JB000513>
- Lavier, L. L., Buck, W. R., & Poliakov, A. N. B. (2000). Factors controlling normal fault offset in an ideal brittle layer. *Journal of Geophysical Research: Solid Earth*, 105(B10), 23431–23442. <https://doi.org/10.1029/2000JB900108>
- Lavier, L. L., & Manatschal, G. (2006). A mechanism to thin the continental lithosphere at magma-poor margins. *Nature*, 440(7082), 324–328. <https://doi.org/10.1038/nature04608>

- Lay, T., Kanamori, H., Ammon, C. J., Koper, K. D., Hutko, A. R., Ye, L., ... Rushing, T. M. (2012). Depth-varying rupture properties of subduction zone megathrust faults. *Journal of Geophysical Research: Solid Earth*, *117*(4), 1–21. <https://doi.org/10.1029/2011JB009133>
- Lay, T., Ye, L., Ammon, C. J., & Kanamori, H. (2017). Intraslab rupture triggering megathrust rupture coseismically in the 17 December 2016 Solomon Islands M_w 7.9 earthquake. *Geophysical Research Letters*, *44*(3), 1286–1292. <https://doi.org/10.1002/2017GL072539>
- Le Pourhiet, L., Burov, E., & Moretti, I. (2004). Rifting through a stack of inhomogeneous thrusts (the dipping pie concept). *Tectonics*, *23*(4). <https://doi.org/10.1029/2003TC001584>
- Lee, S., Lin, T., Feng, K., & Liu, T. (2018). Composite Megathrust Rupture From Deep Interplate to Trench of the 2016 Solomon Islands Earthquake. *Geophysical Research Letters*, *45*(2), 674–681. <https://doi.org/10.1002/2017GL076347>
- Leech, M. L., Singh, S., Jain, A. K., Klemperer, S. L., & Manickavasagam, R. M. (2005). The onset of India-Asia continental collision: Early, steep subduction required by the timing of UHP metamorphism in the western Himalaya. *Earth and Planetary Science Letters*, *234*(1–2), 83–97. <https://doi.org/10.1016/j.epsl.2005.02.038>
- Leeman, J. R., Saffer, D. M., Scuderi, M. M., & Marone, C. (2016). Laboratory observations of slow earthquakes and the spectrum of tectonic fault slip modes. *Nature Communications*, *7*(1), 1–6. <https://doi.org/10.1038/ncomms11104>
- Leonard, M. (2010). Earthquake fault scaling: Self-consistent relating of rupture length, width, average displacement, and moment release. *Bulletin of the Seismological Society of America*, *100*(5 A), 1971–1988. <https://doi.org/10.1785/0120090189>
- Levander, A., Schmandt, B., Miller, M. S., Liu, K., Karlstrom, K. E., Crow, R. S., ... Humphreys, E. D. (2011). Continuing Colorado plateau uplift by delamination-style convective lithospheric downwelling. *Nature*, *472*(7344), 461–465. <https://doi.org/10.1038/nature10001>
- Li, D., & Liu, Y. (2016). Spatiotemporal evolution of slow slip events in a nonplanar fault model for northern Cascadia subduction zone. *Journal of Geophysical Research: Solid Earth*, *121*(9), 6828–6845. <https://doi.org/10.1002/2016JB012857>
- Liao, J., Malusà, M. G., Zhao, L., Baldwin, S. L., Fitzgerald, P. G., & Gerya, T. (2018). Divergent plate motion drives rapid exhumation of (ultra)high pressure rocks. *Earth and Planetary Science Letters*, *491*, 67–80. <https://doi.org/10.1016/J.EPSL.2018.03.024>
- Lister, G. S., & Davis, G. A. (1989). The origin of metamorphic core complexes and detachment faults formed during Tertiary continental margins. *Geology*, *14*(1), 246–250. [https://doi.org/10.1016/0191-8141\(89\)90036-9](https://doi.org/10.1016/0191-8141(89)90036-9)

- Little, T. A., Hacker, B. R., Gordon, S. M., Baldwin, S. L., Fitzgerald, P. G., Ellis, S., & Korchinski, M. (2011). Diapiric exhumation of Earth's youngest (UHP) eclogites in the gneiss domes of the D'Entrecasteaux Islands, Papua New Guinea. *Tectonophysics*, *510*(1–2), 39–68. <https://doi.org/10.1016/j.tecto.2011.06.006>
- Little, T. A., Baldwin, S. L., Fitzgerald, P. G., & Monteleone, B. (2007). Continental rifting and metamorphic core complex formation ahead of the Woodlark spreading ridge, D'Entrecasteaux Islands, Papua New Guinea. *Tectonics*, *26*(1), 1–26. <https://doi.org/10.1029/2005TC001911>
- Little, T. A., Webber, S. M., Mizera, M., Boulton, C., Oesterle, J., Ellis, S., ... Wallace, L. (2019). Evolution of a rapidly slipping, active low-angle normal fault, Suckling-Dayman metamorphic core complex, SE Papua New Guinea. *GSA Bulletin*. <https://doi.org/10.1130/B35051.1>
- Liu, Y., McGuire, J. J., & Behn, M. D. (2012). Frictional behavior of oceanic transform faults and its influence on earthquake characteristics. *Journal of Geophysical Research: Solid Earth*, *117*(B4), n/a-n/a. <https://doi.org/10.1029/2011JB009025>
- Liu, Y., & Rice, J. R. (2005). Aseismic slip transients emerge spontaneously in three-dimensional rate and state modeling of subduction earthquake sequences. *Journal of Geophysical Research: Solid Earth*, *110*(8), 1–14. <https://doi.org/10.1029/2004JB003424>
- Liu, Y., & Rice, J. R. (2009). Slow slip predictions based on granite and gabbro friction data compared to GPS measurements in northern Cascadia. *Journal of Geophysical Research*, *114*(B9), B09407. <https://doi.org/10.1029/2008JB006142>
- Liu, Y., & Rice, J. R. (2007). Spontaneous and triggered aseismic deformation transients in a subduction fault model. *Journal of Geophysical Research: Solid Earth*, *112*(9). <https://doi.org/10.1029/2007JB004930>
- Lockner, D. A., Morrow, C., Moore, D., & Hickman, S. (2011). Low strength of deep San Andreas fault gouge from SAFOD core. *Nature*, *472*(7341), 82–86. <https://doi.org/10.1038/nature09927>
- Machette, M. N., Personius, S. F., Nelson, A. R., Schwartz, D. P., & Lund, W. R. (1991). The Wasatch fault zone, Utah—segmentation and history of Holocene earthquakes. *Journal of Structural Geology*, *13*(2), 137–149. [https://doi.org/10.1016/0191-8141\(91\)90062-N](https://doi.org/10.1016/0191-8141(91)90062-N)
- Malservisi, R., Furlong, K. P., & Gans, C. R. (2005). Microseismicity and creeping faults: Hints from modeling the Hayward fault, California (USA). *Earth and Planetary Science Letters*, *234*(3–4), 421–435. <https://doi.org/10.1016/j.epsl.2005.02.039>
- Manatschal, G., Lavier, L., & Chenin, P. (2015). The role of inheritance in structuring hyperextended rift systems: Some considerations based on observations and numerical modeling. *Gondwana Research*, *27*(1), 140–164. <https://doi.org/10.1016/j.gr.2014.08.006>

- Mann, P., Horton, B. K., Taylor, F. W., Shen, C., Lin, K., Renema, W., ... Renema, W. (2009). Uplift patterns of reef terraces and sedimentary rocks constrain tectonic models for metamorphic core complexes in eastern Papua New Guinea. *AGUFM, 2009*, G33B-0642.
- Mann, P., & Taylor, F. W. (2002). Emergent Late Quaternary Coral Reefs of Eastern Papua New Guinea Constrain the Regional Pattern of Oceanic Ridge Propagation. *AGUFM, 2002*, T52C-1206.
- Mann, P., Taylor, F. W., Gahagan, L., Watson, L., Mann, P., Taylor, F. W., ... Watson, L. (2004). Rapid Kinematic and Tectonic Variations Along the 1400-km-long Australia-Woodlark Plate Boundary Zone, Papua New Guinea and Woodlark Basin. *AGUFM, 2004*, T41C-1209.
- Manning, A. H., & Bartley, J. M. (1994). Postmylonitic deformation in the Raft River metamorphic core complex, northwestern Utah: Evidence of a rolling hinge. *Tectonics, 13*(3), 596–612. <https://doi.org/10.1029/93TC03321>
- Marone, C. (1998). Laboratory-Derived Friction Laws and their Application to Seismic Faulting. *Annual Review of Earth and Planetary Sciences, 26*(1), 643–696. <https://doi.org/10.1146/annurev.earth.26.1.643>
- Martinez, F., Goodliffe, A. M., & Taylor, B. (2001). Metamorphic core complex formation by density inversion and lower-crust extension. *Nature, 411*(June), 930–934.
- McCaffrey, R. (2009). Time-dependent inversion of three-component continuous GPS for steady and transient sources in northern Cascadia. *Geophysical Research Letters, 36*(7), n/a-n/a. <https://doi.org/10.1029/2008GL036784>
- McCalpin, J. P., & Nishenko, S. P. (1996). Holocene paleoseismicity, temporal clustering, and probabilities of future large ($M > 7$) earthquakes on the Wasatch fault zone, Utah. *Journal of Geophysical Research: Solid Earth, 101*(B3), 6233–6253. <https://doi.org/10.1029/95jb02851>
- Miller, E. L., Gans, P. B., & Garing, J. (1983). The Snake Range Décollement: An exhumed Mid-Tertiary ductile-brittle transition. *Tectonics, 2*(3), 239–263. <https://doi.org/10.1029/TC002i003p00239>
- Miller, S. R., Baldwin, S. L., & Fitzgerald, P. G. (2012). Transient fluvial incision and active surface uplift in the Woodlark Rift of eastern Papua New Guinea. *Lithosphere, 4*(2), 131–149. <https://doi.org/10.1130/L135.1>
- Misra, A. A., & Mukherjee, S. (2015). *Tectonic Inheritance in Continental Rifts and Passive Margins*. <https://doi.org/10.1007/978-3-319-20576-2>
- Mizera, M., Little, T. A., Biemiller, J., Ellis, S., Webber, S., & Norton, K. P. (2019). Structural and Geomorphic Evidence for Rolling-Hinge Style Deformation of an Active Continental

- Low-Angle Normal Fault, SE Papua New Guinea. *Tectonics*, 38(5), 1556–1583.
<https://doi.org/10.1029/2018TC005167>
- Mizera, M., Little, T., Boulton, C., Prior, D., Watson, E., Biemiller, J., ... Shigematsu, N. (2020). Slow-to-Fast Deformation in Mafic Fault Rocks on an Active Low-Angle Normal Fault, Woodlark Rift, SE Papua New Guinea. *Geochemistry, Geophysics, Geosystems*, 21(11).
<https://doi.org/10.1029/2020gc009171>
- Monteleone, B. D., Baldwin, S. L., Webb, L. E., Fitzgerald, P. G., Grove, M., & Schmitt, A. K. (2007). Late Miocene-Pliocene eclogite facies metamorphism, D'Entrecasteaux Islands, SE Papua New Guinea. *Journal of Metamorphic Geology*, 25(2), 245–265.
<https://doi.org/10.1111/j.1525-1314.2006.00685.x>
- Montgomery-Brown, E. K., Segall, P., & Miklius, A. (2009). Kilauea slow slip events: Identification, source inversions, and relation to seismicity. *Journal of Geophysical Research*, 114(B6). <https://doi.org/10.1029/2008jb006074>
- Moore, D. E., Lockner, D. A., Ma, S., Summers, R., & Byerlee, J. D. (1997). Strengths of serpentinite gouges at elevated temperatures. *Journal of Geophysical Research: Solid Earth*, 102(B7), 14787–14801. <https://doi.org/10.1029/97jb00995>
- Moore, D. E. (2014). Comparative mineral chemistry and textures of SAFOD fault gouge and damage-zone rocks. *Journal of Structural Geology*, 68(PA), 82–96.
<https://doi.org/10.1016/j.jsg.2014.09.002>
- Moore, D. E., & Lockner, D. A. (2013). Chemical controls on fault behavior: Weakening of serpentinite sheared against quartz-bearing rocks and its significance for fault creep in the San Andreas system. *Journal of Geophysical Research: Solid Earth*, 118(5), 2558–2570.
<https://doi.org/10.1002/jgrb.50140>
- Moresi, L., Dufour, F., & Mühlhaus, H.-B. (2003). A Lagrangian integration point finite element method for large deformation modeling of viscoelastic geomaterials. *Journal of Computational Physics*, 184(2), 476–497. [https://doi.org/10.1016/S0021-9991\(02\)00031-1](https://doi.org/10.1016/S0021-9991(02)00031-1)
- Morris, A., Gee, J. S., Pressling, N., John, B. E., MacLeod, C. J., Grimes, C. B., & Searle, R. C. (2009). Footwall rotation in an oceanic core complex quantified using reoriented Integrated Ocean Drilling Program core samples. *Earth and Planetary Science Letters*, 287(1–2), 217–228. <https://doi.org/10.1016/j.epsl.2009.08.007>
- Murphy, M. A., & Copeland, P. (2005). Transtensional deformation in the central Himalaya and its role in accommodating growth of the Himalayan orogen. *Tectonics*, 24(4), 1–19.
<https://doi.org/10.1029/2004TC001659>
- Nicol, A., Walsh, J. J., Manzocchi, T., & Morewood, N. (2005). Displacement rates and average earthquake recurrence intervals on normal faults. *Journal of Structural Geology*, 27(3), 541–551. <https://doi.org/10.1016/j.jsg.2004.10.009>

- Niemeijer, A. R., Boulton, C., Toy, V. G., Townend, J., & Sutherland, R. (2016). Large-displacement, hydrothermal frictional properties of DFDP-1 fault rocks, Alpine Fault, New Zealand: Implications for deep rupture propagation. *Journal of Geophysical Research: Solid Earth*, *121*(2), 624–647. <https://doi.org/10.1002/2015JB012593>
- Niemeijer, A. R., Spiers, C. J., & Peach, C. J. (2008). Frictional behaviour of simulated quartz fault gouges under hydrothermal conditions: Results from ultra-high strain rotary shear experiments. *Tectonophysics*, *460*(1–4), 288–303. <https://doi.org/10.1016/j.tecto.2008.09.003>
- Niemeijer, A. R., & Collettini, C. (2014). Frictional Properties of a Low-Angle Normal Fault Under In Situ Conditions: Thermally-Activated Velocity Weakening. *Pure and Applied Geophysics*, *171*(10), 2641–2664. <https://doi.org/10.1007/s00024-013-0759-6>
- Niemi, N. A., Wernicke, B. P., Friedrich, A. M., Simons, M., Bennett, R. A., & Davis, J. L. (2004). BARGEN continuous GPS data across the eastern Basin and Range province, and implications for fault system dynamics. *Geophysical Journal International*, *159*(3), 842–862. <https://doi.org/10.1111/j.1365-246X.2004.02454.x>
- Numelin, T., Marone, C., & Kirby, E. (2007b). Frictional properties of natural fault gouge from a low-angle normal fault, Panamint Valley, California. *Tectonics*, *26*(2), n/a-n/a. <https://doi.org/10.1029/2005TC001916>
- Numelin, T., Kirby, E., Walker, J. D., & Didericksen, B. (2007a). Late Pleistocene slip on a low-angle normal fault, Searles Valley, California. *Geosphere*, *3*(3), 163–176. <https://doi.org/10.1130/GES00052.1>
- Obara, K. (2002). Nonvolcanic deep tremor associated with subduction in southwest Japan. *Science*, *296*(5573), 1679–1681. <https://doi.org/10.1126/science.1070378>
- Okada, Y. (1985). Surface deformation due to shear and tensile faults in a half-space. *Bulletin of the Seismological Society of America*, *75*(4), 1135–1154.
- Okamoto, A. S., Niemeijer, A. R., Takeshita, T., Verberne, B. A., & Spiers, C. J. (2020). Frictional properties of actinolite-chlorite gouge at hydrothermal conditions. *Tectonophysics*, *779*, 228377. <https://doi.org/10.1016/j.tecto.2020.228377>
- Okamoto, A. S., Verberne, B. A., Niemeijer, A. R., Takahashi, M., Shimizu, I., Ueda, T., & Spiers, C. J. (2019). Frictional Properties of Simulated Chlorite Gouge at Hydrothermal Conditions: Implications for Subduction Megathrusts. *Journal of Geophysical Research: Solid Earth*, *124*(5), 4545–4565. <https://doi.org/10.1029/2018JB017205>
- Ollier, C. D., & Pain, C. F. (1980). Actively rising surficial gneiss domes in Papua New Guinea. *Journal of the Geological Society of Australia*, *27*(1–2), 33–44. <https://doi.org/10.1080/00167618008729116>

- Osmundsen, P. T., & Péron-Pinvidic, G. (2018). Crustal-Scale Fault Interaction at Rifted Margins and the Formation of Domain-Bounding Breakaway Complexes: Insights From Offshore Norway. *Tectonics*, 37(3), 935–964. <https://doi.org/10.1002/2017TC004792>
- Österle, J. E., Little, T. A., Seward, D., Stockli, D. F., & Gamble, J. (2020a). The petrology, geochronology and tectono-magmatic setting of igneous rocks in the Suckling-Dayman metamorphic core complex, Papua New Guinea. *Gondwana Research*. <https://doi.org/10.1016/j.gr.2020.01.014>
- Österle, J. E., Stockli, D. F., Seward, D., & Little, T. A. (2020b). Dating of young (<1 Ma) tephra: Using U-Pb (zircon) and (U-Th[-Sm])/He (zircon, apatite, magnetite) chronometers to unravel the eruption age of a tephra in the Woodlark Rift of Papua New Guinea. *Terra Nova*, 32(5), 345–354. <https://doi.org/10.1111/ter.12464>
- Parry, W. T., & Bruhn, R. L. (1986). Pore fluid and seismogenic characteristics of fault rock at depth on the Wasatch Fault, Utah. *Journal of Geophysical Research*, 91(B1), 730. <https://doi.org/10.1029/JB091iB01p00730>
- Parry, W. T., & Bruhn, R. L. (1987). Fluid inclusion evidence for minimum 11 km vertical offset on the Wasatch fault, Utah. *Geology*, 15(1), 67–70. [https://doi.org/10.1130/0091-7613\(1987\)15<67:FIEFMK>2.0.CO;2](https://doi.org/10.1130/0091-7613(1987)15<67:FIEFMK>2.0.CO;2)
- Parry, W. T., & Bruhn, R. L. (1990). Fluid pressure transients on seismogenic normal faults. *Tectonophysics*, 179(3–4), 335–344. [https://doi.org/10.1016/0040-1951\(90\)90299-N](https://doi.org/10.1016/0040-1951(90)90299-N)
- Peng, Z., & Gombert, J. (2010). An integrated perspective of the continuum between earthquakes and slow-slip phenomena. *Nature Geoscience*, 3(9), 599–607. <https://doi.org/10.1038/ngeo940>
- Petersen, K. D., & Schiffer, C. (2016). Wilson cycle passive margins: Control of orogenic inheritance on continental breakup. *Gondwana Research*, 39, 131–144. <https://doi.org/10.1016/J.GR.2016.06.012>
- Petersen, K. D., & Buck, W. R. (2015). Eduction, extension, and exhumation of ultrahigh-pressure rocks in metamorphic core complexes due to subduction initiation. *Geochemistry, Geophysics, Geosystems*, 16(8), 2564–2581. <https://doi.org/10.1002/2015GC005847>
- Pirazzoli, P. A. (1986). Marine notches. *Sea-Level Research*, 361–400. https://doi.org/10.1007/978-94-009-4215-8_12
- Platt, J. P., Behr, W. M., & Cooper, F. J. (2017). Metamorphic core complexes: Windows into the mechanics and rheology of the crust. *Journal of the Geological Society*, 174(1), 9–27. <https://doi.org/10.1144/jgs2014-036>

- Pollitz, F. F. (1996). Coseismic Deformation From Earthquake Faulting On A Layered Spherical Earth. *Geophysical Journal International*, 125(1), 1–14. <https://doi.org/10.1111/j.1365-246X.1996.tb06530.x>
- Prante, M. R., Evans, J. P., Janecke, S. U., & Steely, A. (2014). Evidence for paleoseismic slip on a continental low-angle normal fault: Tectonic pseudotachylyte from the West Salton detachment fault, CA, USA. *Earth and Planetary Science Letters*, 387, 170–183. <https://doi.org/10.1016/j.epsl.2013.10.048>
- Price, J. B., Wernicke, B. P., Cosca, M. A., & Farley, K. A. (2018). Thermochronometry Across the Austroalpine-Pennine Boundary, Central Alps, Switzerland: Orogen-Perpendicular Normal Fault Slip on a Major “Overthrust” and Its Implications for Orogenesis. *Tectonics*, 37(3), 724–757. <https://doi.org/10.1002/2017TC004619>
- Qiu, Q., Hill, E. M., Barbot, S., Hubbard, J., Feng, W., Lindsey, E. O., ... Tapponnier, P. (2016). The mechanism of partial rupture of a locked megathrust: The role of fault morphology. *Geology*, 44(10), 875–878. <https://doi.org/10.1130/G38178.1>
- Ranalli, G. (1995). *Rheology of the Earth*. Springer Science & Business Media.
- Reber, J. E., Lavier, L. L., & Hayman, N. W. (2015). Experimental demonstration of a semi-brittle origin for crustal strain transients. *Nature Geoscience*, 8(9), 712–715. <https://doi.org/10.1038/ngeo2496>
- Reinen, L. A., & Weeks, J. D. (1993). Determination of rock friction constitutive parameters using an iterative least squares inversion method. *Journal of Geophysical Research*, 98(B9), 15937–15950. <https://doi.org/10.1029/93jb00780>
- Rice, J. R., & Ruina, A. L. (1983). Stability of steady frictional slipping. *Journal of Applied Mechanics, Transactions ASME*, 50(2), 343–349. <https://doi.org/10.1115/1.3167042>
- Rice, J. R. (1993). Spatio-temporal complexity of slip on a fault. *Journal of Geophysical Research*, 98(B6), 9885. <https://doi.org/10.1029/93JB00191>
- Rice, J. R., & Tse, S. T. (1986). Dynamic motion of a single degree of freedom system following a rate and state dependent friction law. *Journal of Geophysical Research*, 91(B1), 521. <https://doi.org/10.1029/JB091iB01p00521>
- Rosenbaum, G., Regenauer-Lieb, K., & Weinberg, R. (2005). Continental extension: From core complexes to rigid block faulting. *Geology*, 33(7), 609. <https://doi.org/10.1130/G21477.1>
- Rosenbaum, G., Weinberg, R. F., & Regenauer-Lieb, K. (2008). The geodynamics of lithospheric extension. *Tectonophysics*, 458(1–4), 1–8. <https://doi.org/10.1016/j.tecto.2008.07.016>

- Rubin, A. M. (2008). Episodic slow slip events and rate-and-state friction. *Journal of Geophysical Research: Solid Earth*, 113(11). <https://doi.org/10.1029/2008JB005642>
- Ruina, A. (1983). Slip instability and state variable friction laws. *Journal of Geophysical Research: Solid Earth*, 88(B12), 10359–10370. <https://doi.org/10.1029/JB088iB12p10359>
- Ruppel, C. (1995). Extensional processes in continental lithosphere. *Journal of Geophysical Research*, 100(B12). <https://doi.org/10.1029/95jb02955>
- Ruprecht, P., Plank, T. A., Jin, G., & Abers, G. A. (2013). Rifting and UHP exhumation in Eastern Papua New Guinea: Temperature and pressure constraints from primitive magmas. *American Geophysical Union, Fall Meeting 2013, Abstract Id. T21B-2559*. Retrieved from <http://adsabs.harvard.edu/abs/2013AGUFM.T21B2559R>
- Saffer, D. M., & Wallace, L. M. (2015). The frictional, hydrologic, metamorphic and thermal habitat of shallow slow earthquakes. *Nature Geoscience*, 8(8), 594–600. <https://doi.org/10.1038/ngeo2490>
- Salazar-Mora, C. A., Huisman, R. S., Fossen, H., & Eglydio-Silva, M. (2018). The Wilson Cycle and Effects of Tectonic Structural Inheritance on Rifted Passive Margin Formation. *Tectonics*, 37(9), 3085–3101. <https://doi.org/10.1029/2018TC004962>
- Salerno, V. M., Capitanio, F. A., Farrington, R. J., & Riel, N. (2016). The role of long-term rifting history on modes of continental lithosphere extension. *Journal of Geophysical Research: Solid Earth*, 121(12), 8917–8940. <https://doi.org/10.1002/2016JB013005>
- Savage, M. K. (1999). Seismic anisotropy and mantle deformation: What have we learned from shear wave splitting? *Reviews of Geophysics*, 37(1), 65–106. <https://doi.org/10.1029/98RG02075>
- Schenker, F. L., Gerya, T., & Burg, J. P. (2012). Bimodal behavior of extended continental lithosphere: Modeling insight and application to thermal history of migmatitic core complexes. *Tectonophysics*, 579, 88–103. <https://doi.org/10.1016/j.tecto.2012.07.002>
- Scholz, C. H. (2002). *The Mechanics of Earthquakes and Faulting* (2nd ed.). Cambridge: Cambridge University Press. [https://doi.org/DOI: 10.1017/9781316681473](https://doi.org/DOI:10.1017/9781316681473)
- Schwartz, S., Guillot, S., Reynard, B., Lafay, R., Debret, B., Nicollet, C., ... Auzende, A. L. (2013). Pressure-temperature estimates of the lizardite/antigorite transition in high pressure serpentinites. *Lithos*, 178, 197–210. <https://doi.org/10.1016/j.lithos.2012.11.023>
- Schwartz, S. Y., & Rokosky, J. M. (2007). Slow slip events and seismic tremor at circum-Pacific subduction zones. *Reviews of Geophysics*, 45(3), n/a-n/a. <https://doi.org/10.1029/2006RG000208>

- Segall, P. (2010). *Earthquake and volcano deformation*. Princeton, New Jersey, USA: Princeton University Press.
- Segall, P., & Bradley, A. M. (2012). Slow-slip evolves into megathrust earthquakes in 2D numerical simulations. *Geophysical Research Letters*, *39*(18).
<https://doi.org/10.1029/2012GL052811>
- Serpelloni, E., Faccenna, C., Spada, G., Dong, D., & Williams, S. D. P. (2013). Vertical GPS ground motion rates in the Euro-Mediterranean region: New evidence of velocity gradients at different spatial scales along the Nubia-Eurasia plate boundary. *Journal of Geophysical Research: Solid Earth*, *118*(11), 6003–6024. <https://doi.org/10.1002/2013JB010102>
- Shelton, G., & Tullis, J. (1981). Experimental flow laws for crustal rocks. *Eos, Trans - Am. Geophys. Union*, *62*(17), 396.
- Shen, C. C., Wu, C. C., Cheng, H., Lawrence Edwards, R., Hsieh, Y. Te, Gallet, S., ... Spötl, C. (2012). High-precision and high-resolution carbonate ²³⁰Th dating by MC-ICP-MS with SEM protocols. *Geochimica et Cosmochimica Acta*, *99*, 71–86.
<https://doi.org/10.1016/j.gca.2012.09.018>
- Sibson, R. H. (1985). A note on fault reactivation. *Journal of Structural Geology*, *7*(6), 751–754.
[https://doi.org/10.1016/0191-8141\(85\)90150-6](https://doi.org/10.1016/0191-8141(85)90150-6)
- Sibson, R. H. (2000). Fluid involvement in normal faulting. *Journal of Geodynamics*, *29*(3–5), 469–499. [https://doi.org/10.1016/S0264-3707\(99\)00042-3](https://doi.org/10.1016/S0264-3707(99)00042-3)
- Sieh, K., Natawidjaja, D. H., Meltzner, A. J., Shen, C. C., Cheng, H., Li, K. S., ... Edwards, R. L. (2008). Earthquake supercycles inferred from sea-level changes recorded in the corals of west Sumatra. *Science*, *322*(5908), 1674–1678. <https://doi.org/10.1126/science.1163589>
- Singleton, J. S., Wong, M. S., & Johnston, S. M. (2018). The role of calcite-rich metasedimentary mylonites in localizing detachment fault strain and influencing the structural evolution of the Buckskin-Rawhide metamorphic core complex, west-central Arizona. *Lithosphere*, *10*(2), 172–193. <https://doi.org/10.1130/L699.1>
- Skarbek, R. M., Rempel, A. W., & Schmidt, D. A. (2012). Geologic heterogeneity can produce aseismic slip transients. *Geophysical Research Letters*, *39*(21), n/a-n/a.
<https://doi.org/10.1029/2012GL053762>
- Skarbek, R. M., & Rempel, A. W. (2016). Dehydration-induced porosity waves and episodic tremor and slip. *Geochemistry, Geophysics, Geosystems*, *17*(2), 442–469.
<https://doi.org/10.1002/2015GC006155>
- Smith, R. B., & Bruhn, R. L. (1984). Intraplate extensional tectonics of the eastern basin-range: inferences on structural style from seismic reflection data, regional tectonics, and thermal-

- mechanical models of brittle- ductile deformation (USA). *Journal of Geophysical Research*, 89(B7), 5733–5762. <https://doi.org/10.1029/JB089iB07p05733>
- Smith, S. A. F., & Faulkner, D. R. (2010). Laboratory measurements of the frictional properties of the Zuccale low-angle normal fault, Elba Island, Italy. *Journal of Geophysical Research*, 115(B2), B02407. <https://doi.org/10.1029/2008JB006274>
- Sone, H., Shimamoto, T., & Moore, D. E. (2012). Frictional properties of saponite-rich gouge from a serpentinite-bearing fault zone along the Gokasho-Arashima Tectonic Line, central Japan. *Journal of Structural Geology*, 38, 172–182. <https://doi.org/10.1016/j.jsg.2011.09.007>
- Spencer, J. E. (2010). Structural analysis of three extensional detachment faults with data from the 2000 Space-Shuttle Radar Topography Mission. *GSA Today*, 20(8), 4–10. <https://doi.org/10.1130/GSATG59A.1>
- Stamps, D. S., Calais, E., Saria, E., Hartnady, C., Nocquet, J. M., Ebinger, C. J., & Fernandes, R. M. (2008). A kinematic model for the East African Rift. *Geophysical Research Letters*, 35(5). <https://doi.org/10.1029/2007GL032781>
- Strasser, F. O., Arango, M. C., & Bommer, J. J. (2010). Scaling of the source dimensions of interface and intraslab subduction-zone earthquakes with moment magnitude. *Seismological Research Letters*, 81(6), 941–950. <https://doi.org/10.1785/gssrl.81.6.941>
- Tamisiea, M. E., & Mitrovica, J. X. (2011). The Moving boundaries of Sea Level Change. *Oceanography*, 24(Sea Level), 24–39. <https://doi.org/10.5670/oceanog.2011.25.COPYRIGHT>
- Taylor, B., Goodliffe, A. M., & Martinez, F. (1999). How continents break up: Insights from Papua New Guinea. *Journal of Geophysical Research: Solid Earth*, 104(B4), 7497–7512. <https://doi.org/10.1029/1998jb900115>
- Taylor, F. W., Isacks, B. L., Jouannic, C., Bloom, A. L., & Dubois, J. (1980). Coseismic and Quaternary vertical tectonic movements, Santo and Malekula Islands, New Hebrides Island Arc. *Journal of Geophysical Research*, 85(B10), 5367. <https://doi.org/10.1029/JB085iB10p05367>
- Taylor, F. W., Jouannic, C., & Bloom, A. L. (1985). Quaternary uplift of the Torres Islands, northern New Hebrides frontal arc: comparison with Santo and Malekula Islands, central New Hebrides frontal arc. *Journal of Geology*, 93(4), 419–438. <https://doi.org/10.1086/628964>
- Taylor, F. W., Mann, P., Bevis, M. G., Edwards, R. L., Cheng, H., Cutler, K. B., ... Recy, J. (2005). Rapid forearc uplift and subsidence caused by impinging bathymetric features: Examples from the New Hebrides and Solomon arcs. *Tectonics*, 24(6), n/a-n/a. <https://doi.org/10.1029/2004TC001650>

- Taylor, F. W., Briggs, R. W., Frohlich, C., Brown, A., Hornbach, M., Papabatu, A. K., ... Billy, D. (2008). Rupture across arc segment and plate boundaries in the 1 April 2007 Solomons earthquake. *Nature Geoscience*, 1(4), 253–257. <https://doi.org/10.1038/ngeo159>
- Taylor, F. W., Edwards, R. L., Wasserburg, G. J., & Frohlich, C. (1990). Seismic recurrence intervals and timing of aseismic subduction inferred from emerged corals and reefs of the Central Vanuatu (New Hebrides) Frontal Arc. *Journal of Geophysical Research*, 95(B1), 393. <https://doi.org/10.1029/JB095iB01p00393>
- Taylor, F. W., Frohlich, C., Lecolle, J., & Strecker, M. (1987). Analysis of partially emerged corals and reef terraces in the central Vanuatu Arc: Comparison of contemporary coseismic and nonseismic with quaternary vertical movements. *Journal of Geophysical Research*, 92(B6), 4905. <https://doi.org/10.1029/jb092ib06p04905>
- Tetreault, J. L., & Buitter, S. J. H. (2012). Geodynamic models of terrane accretion: Testing the fate of island arcs, oceanic plateaus, and continental fragments in subduction zones. *Journal of Geophysical Research: Solid Earth*, 117(8), 1–23. <https://doi.org/10.1029/2012JB009316>
- Tetreault, J. L., & Buitter, S. J. H. (2017). The influence of extension rate and crustal rheology on the evolution of passive margins from rifting to break-up. *Tectonophysics*. <https://doi.org/10.1016/J.TECTO.2017.08.029>
- Thatcher, W. (2009). How the Continents Deform: The Evidence From Tectonic Geodesy. *Annual Review of Earth and Planetary Sciences*, 37(1), 237–262. <https://doi.org/10.1146/annurev.earth.031208.100035>
- Thirumalai, K., Taylor, F. W., Shen, C. C., Lavier, L. L., Frohlich, C., Wallace, L. M., ... Papabatu, A. K. (2015). Variable Holocene deformation above a shallow subduction zone extremely close to the trench. *Nature Communications*, 6(May), 1–6. <https://doi.org/10.1038/ncomms8607>
- Tirel, C., Brun, J.-P., & Burov, E. (2008). Dynamics and structural development of metamorphic core complexes. *Journal of Geophysical Research*, 113(B4), B04403. <https://doi.org/10.1029/2005JB003694>
- Tjhin, K. T. (1976). Trobriand Basin Exploration, Papua New Guinea. *The APPEA Journal*, 16(1), 81. <https://doi.org/10.1071/aj75008>
- Tregoning, P., Burgette, R., McClusky, S. C., Lejeune, S., Watson, C. S., & McQueen, H. (2013). A decade of horizontal deformation from great earthquakes. *Journal of Geophysical Research: Solid Earth*, 118(5), 2371–2381. <https://doi.org/10.1002/jgrb.50154>
- U.S. Geological Survey. (2019). Earthquake Hazards Program.
- Valoroso, L., Chiaraluce, L., Di Stefano, R., & Monachesi, G. (2017). Mixed-Mode Slip Behavior of the Altotiberina Low-Angle Normal Fault System (Northern Apennines, Italy)

- through High-Resolution Earthquake Locations and Repeating Events. *Journal of Geophysical Research: Solid Earth*, 122(12), 10,220-10,240. <https://doi.org/10.1002/2017JB014607>
- van Hunen, J., & Allen, M. B. (2011). Continental collision and slab break-off: A comparison of 3-D numerical models with observations. *Earth and Planetary Science Letters*, 302(1–2), 27–37. <https://doi.org/10.1016/j.epsl.2010.11.035>
- Veedu, D. M., & Barbot, S. (2016). The Parkfield tremors reveal slow and fast ruptures on the same asperity. *Nature*, 532(7599), 361–365. <https://doi.org/10.1038/nature17190>
- Velasco, M. S., Bennett, R. A., Johnson, R. A., & Hreinsdóttir, S. (2010). Subsurface fault geometries and crustal extension in the eastern Basin and Range Province, western U.S. *Tectonophysics*, 488(1–4), 131–142. <https://doi.org/10.1016/j.tecto.2009.05.010>
- Vidale, J. E., & Houston, H. (2012). Slow slip: A new kind of earthquake. *Physics Today*, 65(1), 38–43. <https://doi.org/10.1063/PT.3.1399>
- Wallace, L. M., Taylor, F. W., Bevis, M. G., Phillips, D. A., Walter, J. I., Kendrick, E. C., ... Papabatu, A. K. (2015). Interseismic, coseismic, postseismic, and slow slip event deformation above a shallow subduction thrust in the western Solomon Islands. *AGUFM*, 2015, T44B-07.
- Wallace, L. M., Beavan, J., Bannister, S., & Williams, C. (2012). Simultaneous long-term and short-term slow slip events at the Hikurangi subduction margin, New Zealand: Implications for processes that control slow slip event occurrence, duration, and migration. *Journal of Geophysical Research B: Solid Earth*, 117(11). <https://doi.org/10.1029/2012JB009489>
- Wallace, L. M., Ellis, S., Little, T., Tregoning, P., Palmer, N., Rosa, R., ... Kwazi, J. (2014). Continental breakup and UHP rock exhumation in action: GPS results from the Woodlark Rift, Papua New Guinea. *Geochemistry, Geophysics, Geosystems*, 15(11), 4267–4290. <https://doi.org/10.1002/2014GC005458>
- Wallace, L. M., Stevens, C., Silver, E., McCaffrey, R., Loratung, W., Hasiata, S., ... Taugaloidi, J. (2004). GPS and seismological constraints on active tectonics and arc-continent collision in Papua New Guinea: Implications for mechanics of microplate rotations in a plate boundary zone. *Journal of Geophysical Research: Solid Earth*, 109(5), 1–16. <https://doi.org/10.1029/2003JB002481>
- Wallace, R. (1987). Grouping and migration of surface faulting and variations in slip rates on faults in the Great Basin province. *Bulletin of the Seismological Society of America*, 77(3), 868–876.
- Wang, Z. (2008). A preliminary report on the Great Wenchuan Earthquake. *Earthquake Engineering and Engineering Vibration*, 7(2), 225–234. <https://doi.org/10.1007/s11803-008-0856-1>

- Watson, E., & Emma. (2019). Using paleomagnetism to test rolling hinge behaviour of an active low angle normal fault, Papua New Guinea. Retrieved from <http://researcharchive.vuw.ac.nz/handle/10063/8252>
- Webb, L. E., Baldwin, S. L., Little, T. A., & Fitzgerald, P. G. (2008). Can microplate rotation drive subduction inversion. *Geology*, *36*(10), 823. <https://doi.org/10.1130/G25134A.1>
- Webber, S., Little, T. A., Norton, K. P., Österle, J., Mizera, M., Seward, D., & Holden, G. (2020). Progressive back-warping of a rider block atop an actively exhuming, continental low-angle normal fault. *Journal of Structural Geology*, *130*, 103906. <https://doi.org/10.1016/j.jsg.2019.103906>
- Webber, S., Norton, K. P., Little, T. A., Wallace, L. M., & Ellis, S. (2018). How fast can low-angle normal faults slip? Insights from cosmogenic exposure dating of the active Mai'iu fault, Papua New Guinea. *Geology*, *46*(3), 227–230. <https://doi.org/10.1130/G39736.1>
- Webber, S. M. (2017). Using Structural Geology and Cosmogenic Nuclide Dating to Infer the Slip Rate and Frictional Strength of the Active Mai'iu Low-Angle Normal Fault , Eastern Papua New Guinea By. *Thesis*.
- Wei, M., Kaneko, Y., Liu, Y., & McGuire, J. J. (2013). Episodic fault creep events in California controlled by shallow frictional heterogeneity. *Nature Geoscience*, *6*(7), 566–570. <https://doi.org/10.1038/ngeo1835>
- Weinberg, R. F., Regenauer-Lieb, K., & Rosenbaum, G. (2007). Mantle detachment faults and the breakup of cold continental lithosphere. *Geology*, *35*(11), 1035. <https://doi.org/10.1130/G23918A.1>
- Weldon, R., Scharer, K., Fumal, T., & Biasi, G. (2004). Wrightwood and the earthquake cycle: What a long recurrence record tells us about how faults work. *GSA Today*, *14*(9), 4–10. [https://doi.org/10.1130/1052-5173\(2004\)014<4:WATECW>2.0.CO;2](https://doi.org/10.1130/1052-5173(2004)014<4:WATECW>2.0.CO;2)
- Wernicke, B. (1995). Low-angle normal faults and seismicity: A review. *Journal of Geophysical Research: Solid Earth*, *100*(B10), 20159–20174. <https://doi.org/10.1029/95JB01911>
- Whitney, D. L., Teyssier, C., Rey, P., & Roger Buck, W. (2013). Continental and oceanic core complexes. *Bulletin of the Geological Society of America*, *125*(3–4), 273–298. <https://doi.org/10.1130/B30754.1>
- Widlansky, M. J., Timmermann, A., & Cai, W. (2015). Future extreme sea level seesaws in the tropical Pacific. *Science Advances*, *1*(8), 1–9. <https://doi.org/10.1126/sciadv.1500560>
- Williams, S. D. P., Bock, Y., Fang, P., Jamason, P., Nikoladi, R., Prawirodirdjo, L., ... Johnson, D. (2004). Error analysis of continuous GPS position time series. *Journal of Geophysical Research*, *109*(B3). <https://doi.org/10.1029/2003jb002741>

- Wolfson-Schwehr, M., & Boettcher, M. S. (2019). Global Characteristics of Oceanic Transform Fault Structure and Seismicity. In *Transform Plate Boundaries and Fracture Zones* (pp. 21–59). Elsevier. <https://doi.org/10.1016/b978-0-12-812064-4.00002-5>
- Wong A Ton, S. Y. M., & Wortel, M. J. R. (1997). Slab detachment in continental collision zones: An analysis of controlling parameters. *Geophysical Research Letters*, *24*(16), 2095–2098. <https://doi.org/10.1029/97GL01939>
- Wu, G., & Lavier, L. L. (2016). The effects of lower crustal strength and preexisting midcrustal shear zones on the formation of continental core complexes and low-angle normal faults. *Tectonics*, *35*(9), 2195–2214. <https://doi.org/10.1002/2016TC004245>
- Wu, G., Lavier, L. L., & Choi, E. (2015). Modes of continental extension in a crustal wedge. *Earth and Planetary Science Letters*, *421*, 8997. <https://doi.org/10.1016/j.epsl.2015.04.005>
- Yang, H., Liu, Y., & Lin, J. (2012). Effects of subducted seamounts on megathrust earthquake nucleation and rupture propagation. *Geophysical Research Letters*, *39*(24), 2012GL053892. <https://doi.org/10.1029/2012GL053892>
- Yang, H., Liu, Y., & Lin, J. (2013). Geometrical effects of a subducted seamount on stopping megathrust ruptures. *Geophysical Research Letters*, *40*(10), 2011–2016. <https://doi.org/10.1002/grl.50509>
- Yi, S., Wang, Q., & Sun, W. (2016). Journal of Geophysical Research : Solid Earth. *Journal of Geophysical Research: Solid Earth*, 3782–3803. <https://doi.org/10.1002/2015JB012608>.Received
- Yuan, X. P., Olive, J. A., & Braun, J. (2020). Partially Locked Low-Angle Normal Faults in Cohesive Upper Crust. *Tectonics*, *39*(2). <https://doi.org/10.1029/2019TC005753>
- Zachariassen, J., Sieh, K., Taylor, F. W., & Hantoro, W. S. (2000). Modern vertical deformation above the Sumatran subduction zone: Paleogeodetic insights from coral microatolls. *Bulletin of the Seismological Society of America*, *90*(4), 897–913. <https://doi.org/10.1785/0119980016>
- Zachariassen, J., Sieh, K., Taylor, F. W., Edwards, R. L., & Hantoro, W. S. (1999). Submergence and uplift associated with the giant 1833 Sumatran subduction earthquake: Evidence from coral microatolls. *Journal of Geophysical Research: Solid Earth*, *104*(B1), 895–919. <https://doi.org/10.1029/1998jb900050>
- Zhang, J., Bock, Y., Johnson, H., Fang, P., Williams, S., Genrich, J., ... Behr, J. (1997). Southern California permanent GPS geodetic array: Error analysis of daily position estimates and site velocities. *Journal of Geophysical Research: Solid Earth*, *102*(B8), 18035–18055. <https://doi.org/10.1029/97jb01380>

Zoback, M. Lou. (1983). Structure and Cenozoic tectonism along the Wasatch fault zone, Utah. *Memoir of the Geological Society of America*, 157(1), 3–27.
<https://doi.org/10.1130/MEM157-p3>